ADDIS ABABA UNIVERSITY

ADDIS ABABA INSTITUTE OF TECHNOLOGY SCHOOL OF CIVIL AND ENVIRONMENTAL ENGINEERING

Site Response Analysis of Selected Sites of Adama City

A Thesis in Geotechnical Engineering

By Temesgen Abiy

September 2021

Addis Ababa

Advisor: Dr.-Ing. Asrat Worku

Co-Advisor: Prof. Atalay Ayele

A Thesis

Submitted in Partial Fulfillment of the Requirements for the Degree of Master of Science

UNDERTAKING

I certify that this research work titled "Site Response Analysis of Selected Sites of Adama City" is my work. The work has not been presented elsewhere for assessment. Where material has been used from other sources, it has been properly acknowledged /referred.

Temesegen Abiy

ABSTRACT

The local soil deposits found in Adama area have the potential of seismic site amplification. Site response analysis of the study area is mainly motivated by the presence of thick local soil deposits in a seismic prone area. Compressional (P-wave), horizontally polarized shear (S_H-wave) and surface waves was acquired at four sites in the study area. Multichannel Analysis of Surface Wave (MASW) and Micrometer Analysis Measurements (MAM) were used to evaluate the shear waves from the surface waves and refraction time term inversion, to evaluate shear waves from body waves. The Poisson's ratio and anisotropy of the site have been calculated using the P-wave, S_V-wave and S_H-wave results.

Using the results of the average shear wave velocity for a depth of 30 m (V_{S30}), the sites were characterized as site class C according to EN 1998:2015 and site class D according to National Earthquake Hazards Reduction Program (NEHRP). The geotechnical data collected from different private and government organizations have also been used to characterize additional five sites and to generate dynamic properties such as the modulus reduction and material damping curves. The input ground motions from the Pacific Earthquake Engineering Research Center (PEER) database were selected using several criteria such as magnitude, site conditions, and target spectrum. These are then scaled to the site PGA value of 0.15g as established based on Global Seismic Hazard Assessment Program (GSHAP).

One-dimensional site response analyses have been conducted by adapting equivalent linear analysis (EQL), nonlinear analysis with Modified Kondner-Zelasko (MKZ) and General Quadratic/Hyperbaric (GQ/H) model at nine sites in the study area. The results have been presented in terms of peak ground acceleration (PGA) profiles, displacement profiles, strain profiles, and response spectra. The area shows an amplification between 1.30 and 3.73, 1.15 and 2.00, 1.25 and 2.36 in PGA value for EQL, MKZ and GQ/H models. The results indicate that the current code design spectra (EN 1998:2015) for the site class C underestimates the shaking intensity of the sites.

ACKNOWLEDGMENTS

I would like to express my appreciation and respect for my advisor, Dr.-Ing Asrat Worku, for his guidance and support throughout the period of study. His critiques and investment of time and energy in the support of this research have been a source of professional and personal inspiration. I would like to extend my appreciation to Professor Atalay Ayele Director of Institute of Geophysics, Space Science and Astronomy (IGSSA) who has provided immense value to this work through acquisition of the geophysical data, and licensed software and guidance in the analysis of the data. He also provided logistics support during the field data acquisition. I would like to forward my appreciation to the Ministry of Education for sponsoring my study through Wachemo University. The author wishes to express his profound gratitude and sincere appreciation to the consulting companies: Addis Geosystems plc, ARCON Design Build plc, Best Consulting Engineers plc, Ethiopian Construction Design and Supervision Works Corporation, Radice Engineering plc, SG Consulting plc, Jeroccia Geotechnical Engineering plc and Ethiopian Institute of Architecture, Building Construction and City Development for providing the geotechnical data of the study area. I would like to express my deepest gratitude for Mr. Belay K. of METEC, who helped me a lot in the preparation of the seismic wave source. I would like to express my sincere gratitude to the developer team of DEEPSOIL at the University of Illinois, Urbana Champagne (UIUC), for providing free access to the software to carry out this research.

TABLE OF CONTENTS

LIST OF TABLES

LIST OF FIGURES

LIST OF SYMBOLS

c	Rayleigh wave phase velocity
d	Depth
d_t	Sampling interval
d_x	Receiver spacing
e	Void ratio
ϕ	Friction Angle
f	Frequency
γ	Shear strain
γ	Unit weight of soil
$\gamma_{d,max}$	Maximum dry unit weight
G_{max}	Small strain shear modulus
G_{sec}	Secant shear modulus
η	Velocity of the daspot or damping correlation factor
h	Layer thickness vector
h_i	Thickness of the i-th layer
h_{min}	Minimum thickness of the top layer
h_{min}	Minimum layer thickness
K	System stiffness matrix
L	Length of receiver spread
λ	Wave length
λ_{max}	Maximum Rayleigh wave wavelength.
M_W	Earthquake moment magnitude
N	Number of geophones
ν	Poisson's ratio
N	Number of Cycles
Pwave	Compressional wave (primary wave)
ρ	Material density
S_H	Horizontal Shear wave
S_V	Vertical Shear wave
σ'_V	Vertical effective stress
τ	Shear Strength
$V_{s,d}$	Average shear wave velocity of the uppermost d meters
V_{S30}	Time-averaged shear wave velocity in the top 30 m of a site
ω	Angular frequency.
ξ	Material damping
X_1	Source offset
Z_{max}	Maximum investigation depth

LIST OF ABBREVIATIONS

CTP	Cone Penetration Test
DFT	Discrete Fourier Transform
EC8	Eurocode 8
Eq./Eqs.	Equation/Equations
EQL	Equivalent Linear
FAS	Fourier Amplitude Spectrum
FFT	Fast Fourier Transform
GMPE	Ground-Motion Prediction Equation
GQ/H	General Quadratic/Hyperbaric
GSHAP	Global Seismic Hazard Assessment Program
ICSU	International Council of Scientific Unions
IGSSA	Institute of Geophysics, Space Science and Astronomy
ILP	International Lithosphere Program
MAM	Microtremor Analysis Measurement
MASW	Multichannel Analysis of Surface Waves
MER	Main Ethiopian Rift
MKZ	Modified Kondner-Zelasko
NEHRP	National earthquake hazard reduction program
NEHRP	National Earthquake Hazard Reduction Program
NGA	Next Generation Attenuation Relations
NL	Nonlinear
OCR	Overconsolidation Ratio
PEER	Pacific Earthquake Engineering Research Center
PGA	Peak Ground Acceleration
PGD	Peak Ground Displacement
PI	Plasticity index
PSA	Pseudo-spectral Acceleration
RMS	Root mean square
SASW	Spectral Analysis of Surface Waves
SCS	Seismodule Controller Software
SPAC	Spatial Autocorrelation
SPT	Standard penetration test
SPT	Standard Penetration Test
UN/IDNDR	United Nations international decade for natural disaster reduction
USCS	Unified Soil Classification System
UTM	Universal Transverse Mercator
WFB	Wonji Fault Belt

CHAPTER 1
INTRODUCTION

1.1 Background

Numerous past researchers have shown the amplification potential of local site effects. A number of researchers worked on the estimation of surface ground motions by considering a column of soil to be excited by strong bedrock ground motions (Celebi et al., 1987; Stone et al., 1987; Seed et al., 1990). Seismic areas of moderate seismicity such as Adama can be significantly affected by the site soil amplification (Worku, 2011).

Geotechnical earthquake engineers have evaluated this aspect by performing site response analysis in order to observe the influences on the three important characteristics of seismic ground motion; 1) amplitude, 2) frequency content and 3) duration of the motion (Kramer, 1996) at any depth of interest. One of the most popular techniques in site response analysis is the equivalent linear (EQL) approach because it only requires relatively straightforward soil properties. Meanwhile, nonlinear (NL) analyses have recently gained more popularity since they are able to predict the nonlinear soil behavior during cyclic loading with more accuracy. The pioneering program SHAKE (Schnabel et al., 1972) implemented the one-dimensional equivalent linear method. Since then, many packages are available for one-dimensional analysis, such as SHAKE, DEEPSOIL, EDUSHAKE, PROSHAKE, etc. DEEPSOIL, which was originally developed at the University of Illinois to predict the seismic site response of multi-layered thick soil deposits, is developed with a clear and friendly user interface that is capable of performing both the EQL and NL representation.

1.2 Statement of the Problem

The present area of study, Adama, is one of the fastest-growing cities in Ethiopia. It is found in the central part of the Main Ethiopian Rift (MER), is vulnerable to earthquakes. Adama had been struck by a moderate earthquake of 5.0 magnitude in 1993 and its epicenter located at 8.3°N, 39.3°E, which has caused several adobe buildings to collapse and was also felt as far as Debre Zeit and Addis Ababa (Asfaw, 1998). Geological and geotechnical reports

showed that there is a thick sediment deposit in the city which influences the site response during shaking.

The city's administration has drafted a new master plan that will expand size of the city from the current 13,000 hectares to 33,000 hectares. This will attract more population to the city. Developments in the city involving engineering structures and population centers could aggravate the damages from earthquake hazards. This calls for comprehensive studies of local site effects and the use of the results for updating the current local seismic code for the safe design of structures.

1.3 Objectives of the Study

General objective

This study aims to assess the engineering geological, geophysical, and geotechnical characteristics and perform site response studies for selected sites of Adama.

Specific objective

- To do the detailed geophysical and geotechnical characterization based on the soil properties and prepare the detailed soil profiles of representative areas of the city.
- To estimate the characteristics of the ground motion parameters like the surface peak ground acceleration of likely earthquake by the equivalent linear analysis and nonlinear analysis.
- To prepare design response spectra for Adama city from clusters of individual spectra and compare them with design response spectra specified in the current seismic code for the area.

1.4 Scope of the Study

Due to practical constraints, this paper does not provide a comprehensive study of city-wide site characterization and shear wave velocity measurement; only selected sites have been studied. To supplement the geophysical data, geotechnical reports conducted by other organizations were used. As Ethiopia has no recorded strong ground motion data in form of acceleration time history, globally available recorded time histories are selected and adjusted to the local conditions. The scaled time histories compatible with the 475-year return period for the respective sites were assigned as input bedrock motions. Site effects

are also causative of liquefaction. However, the sites are characterized by a deep-water table, and liquefaction may not be a major concern, so liquefaction is not a part of the study.

It is beyond the scope of this study to conduct laboratory tests for capturing some of the properties of soils, though geotechnical borehole data collected from various organizations are used.

1.5 Outline of Thesis

The research presented in this thesis is divided into five chapters: Chapter 2 reviews the relevant literature about soil behavior during cyclic loading, site response analysis and geophysical investigations. Chapter 3 presents the procedure for the site response analyses,, the description of the study area, seismicity of the study area, discusses site characterization from the result of geophysical and geotechnical investigations and input motions used in the analyses. The inputs used for DEEPSOIL analyses such as shear modulus reduction and damping curves and shear strength are discussed in this chapter. The results of the site response analyses are presented and discussed in Chapter 4. Finally, conclusions are drawn and recommendations for future research are presented in Chapter 5.

CHAPTER 2
REVIEW OF PERTINENT LITERATURE

A thorough literature review on soil behavior during cyclic loading, site response analysis and geophysical investigations was presented in this chapter.

2.1 Soil Behavior During Cyclic Loading

This section gives a brief overview of soil behavior during cyclic loading as commonly adopted in site response analysis. The direct simple shear concept which provides shear strain distortion rather than horizontal displacement is widely used for representing the cyclic behavior of soil. The soil medium is assumed to behave as a Kelvin-Voigt solid, in which the dynamic response of the soil medium can be described using an elastic spring and a viscous (dashpot) resistance (Kramer, 1996) is given in Eq. (2-1) and illustrated in Figure 2-1. The shear stress and strain response of this material is shown in Figure 2-2, where secant shear modulus (G_{sec}) and material damping ratio (ξ) represent, respectively, the elastic stiffness and the viscous resistance.

$$\tau = G\gamma + \eta \frac{\partial \gamma}{\partial t} \tag{2-1}$$

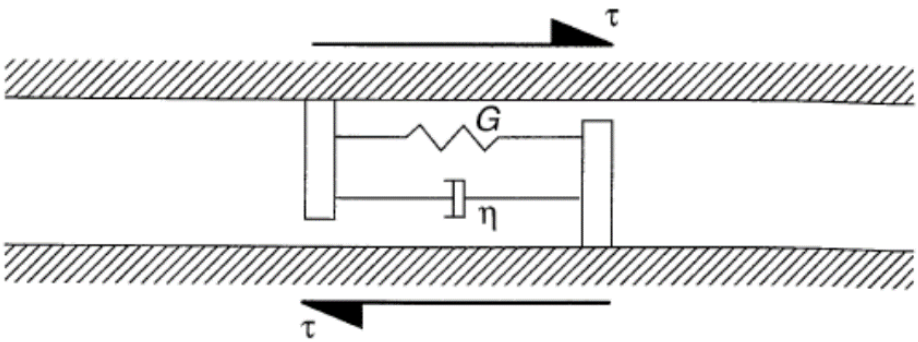

Figure 2-1: Kelvin-Voigt model includes spring constant (G) and dashpot coefficient (η) in the soil skeleton and deformed shape illustration during loading.

The viscous resistance represents the ability of a material to dissipate energy in the soil mass under cyclic loading. Material damping ratio, ξ, is defined as the ratio of the dissipated energy over the maximum strain energy during each cycle at a given strain amplitude as shown in Figure 2-2. In Figure 2-2 the gray area within the hysteresis loop (A_L) represents

the energy dissipated over a loading cycle; and the triangular area (A_T), calculated using peak shear stress and peak shearing strain, represents the maximum retained strain energy.

Material damping ratio is a result of friction between soil particles, strain rate effects and nonlinearity of the stress strain relationship in soils.

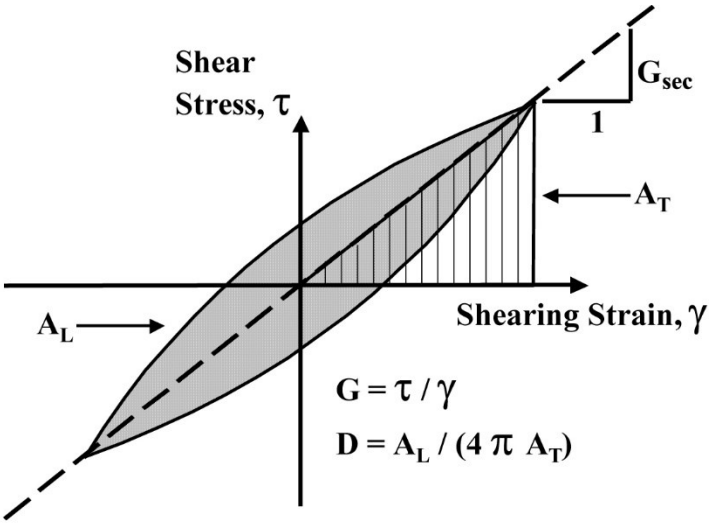

Figure 2-2: Illustration to estimate the secant shear modulus (G_{sec}) and material damping ratio (ξ) during cyclic loading.

The damping ratio is calculated as:

$$\xi = \frac{A_L}{4\pi A_T} \tag{2-2}$$

where A_L is the energy dissipated in each cycle of motion, and the strain energy stored in each cycle of loading as represented by the triangular area (A_T). The secant shear modulus for each cycle of loading is determined by calculating the slope of the line that connects the extreme points of the hysteresis loop as illustrated in Figure 2-3.

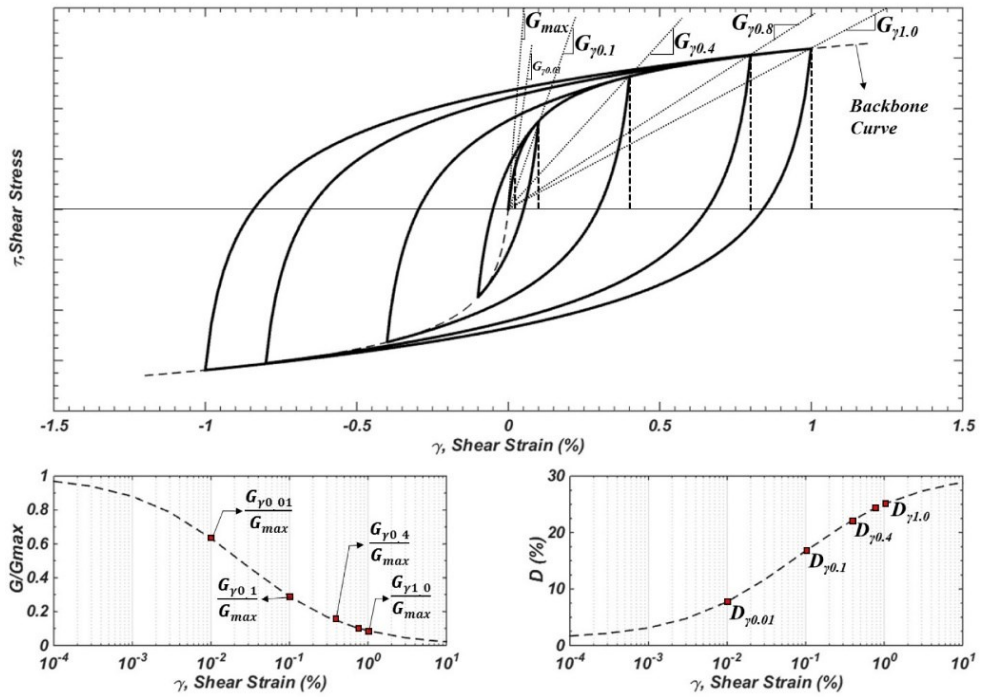

Figure 2-3: Cyclic stress-strain behavior and two important dynamic properties (G/G_{max} and Damping Ratio) of soil during cyclic loading (Kramer, 1996).

Figure 2-3 shows the stress-strain behavior of soils under strain controlled cyclic loading test. The maximum shear modulus, G_{max}, taken as the value on the shear modulus reduction curve at a very small strain ($\gamma \approx 10^{-4}$ %) and can be related to the shear wave velocity and density of the soil ($G_{max} = \rho \times V_S^2$). As the strain increases, the shear modulus curve decreases, while material damping increases as illustrated in Figure 2-3 on left and right respectively. The modulus reduction and damping curves describe the most important dynamic soil properties during cyclic loading and they are important parameters in site response analysis.

Numerous researchers have developed curves for modulus reduction and damping curves for different soils. Seed et al. (1986) by analyzing the test results from numerous researchers, and proposed modulus reduction and damping curves, together with the upper and lower bounds for sands and gravels shown in Figure 2-4. The authors concluded that the G/G_{max} versus shear strain curve shown in Figure 2-4 (a) is generally representative of most sands, but the curve will be somewhat flatter than for the silty sands and gravels.

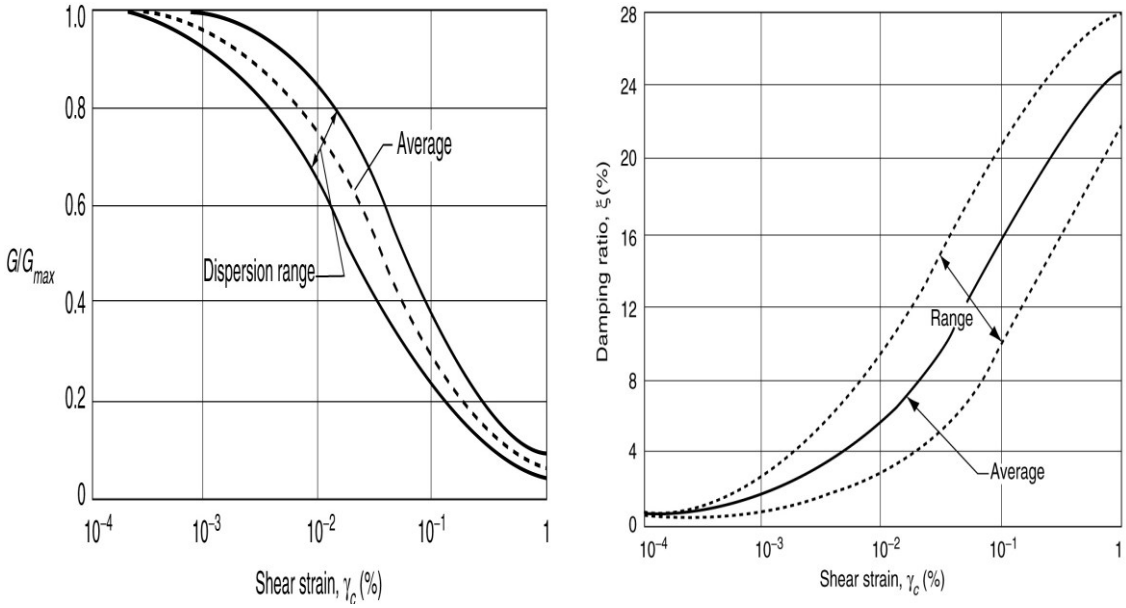

(a) **(b)**

Figure 2-4: Variation of (a) normalized shear modulus with shear strain (b) of damping ratio with shear strain for sands.

Vucetic and Dobry (1991) reported that the plasticity index (PI) is the main factor controlling the modulus reduction and damping curves. With increasing PI value, the shear modulus reduction was increased, while the material damping was decreased (Figure 2-5). The proposed curves agree quite well with curves published by Seed et al. (1986) for PI=0.

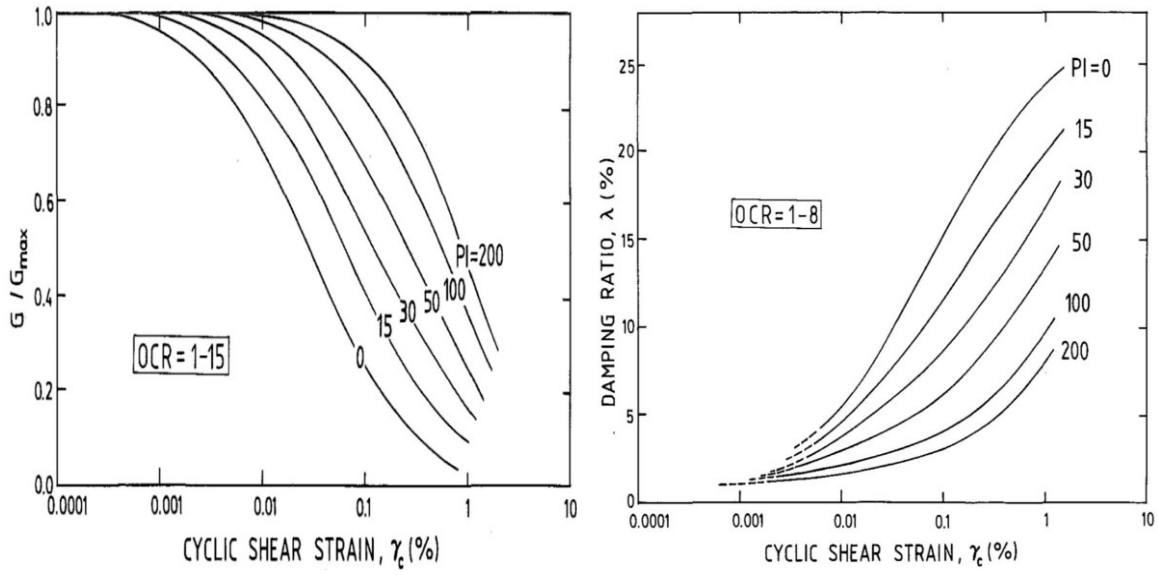

(a) **(b)**

Figure 2-5: Relations between (a) G/G_{max} versus shear strain (b) Damping ratio versus shear strain curves for different soil plasticity for normally and over consolidated clays (Vucetic and Dobry, 1991).

Darendeli (2001) concluded that plasticity index, strain amplitude and mean effective confining pressure are very important parameters that control nonlinear soil behavior at various strain levels as shown in Figure 2-7 and Figure 2-8. Darendeli (2001) developed an empirical model for shear modulus reduction and material damping curves. The proposed curve agrees with the Vucetic and Dobry (1991) curve but the effect of soil plasticity presented by the latter model is more pronounced than the Darendeli (2001) model as shown in Figure 2-6. Additionally, the Vucetic and Dobry (1991) failed to capture the damping ratio curve for small-strain with increasing soil plasticity. Darendeli (2001) claimed that this was due to accuracy problems in damping measurements which arise from the use of inaccurate and old generation equipment.

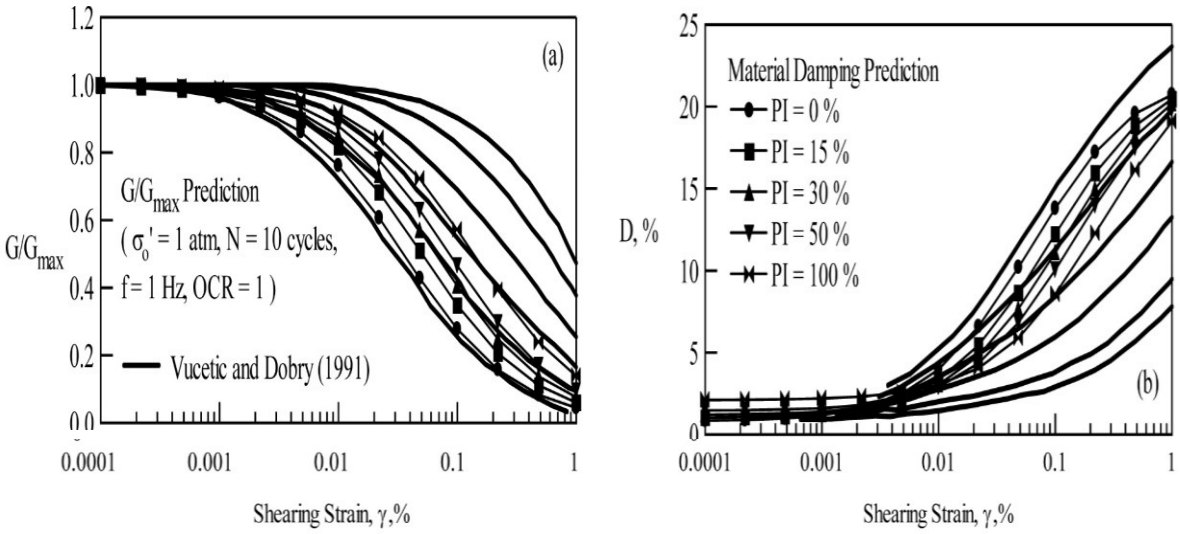

(a) **(b)**

Figure 2-6: Comparison of the effect of soil plasticity on nonlinear soil behavior predicted by the calibrated model and empirical curves proposed by Vucetic and Dobry (1991) (Darendeli, 2001).

The differences among these models are summarized in Table 2-1.

Table 2-1: Prediction parameters for mostly used models in practice

Model	**Darendeli (2001)**	**Vucetic & Dobry (1991)**	**Seed et.al. (1986)**
Prediction basis Confinement (depth dependence): Soil type:	 Yes Yes	 No Yes	 No Yes
Model for soil type	Continuous function = f(PI, OCR)	6 Discrete Groups = f(PI)	Range for Sands
Model for confinement	Continuous function of effective Stress	Na	Na

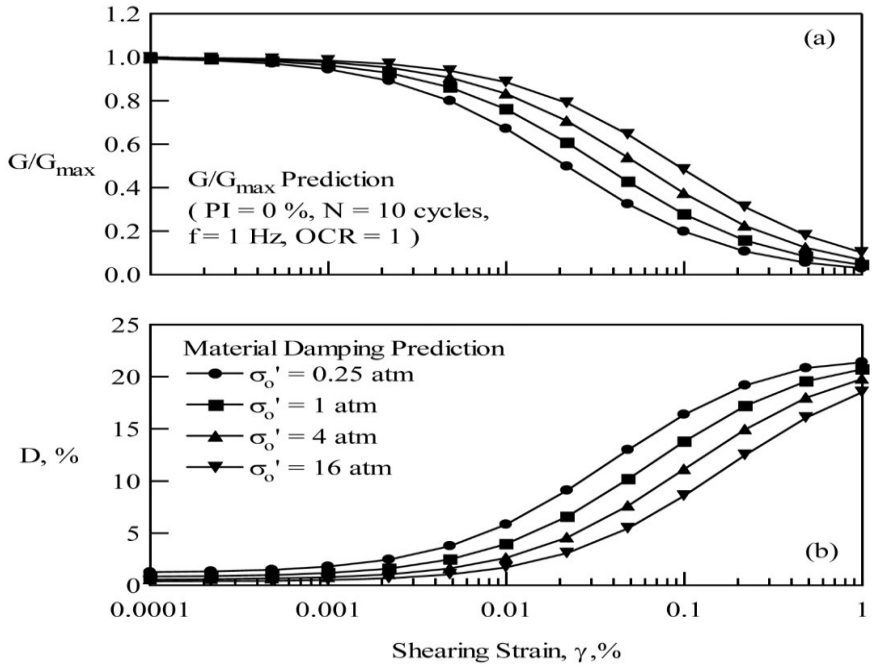

Figure 2-7: Effect of confining pressure on (a) normalized modulus reduction and (b) material damping curves (Darendeli, 2001).

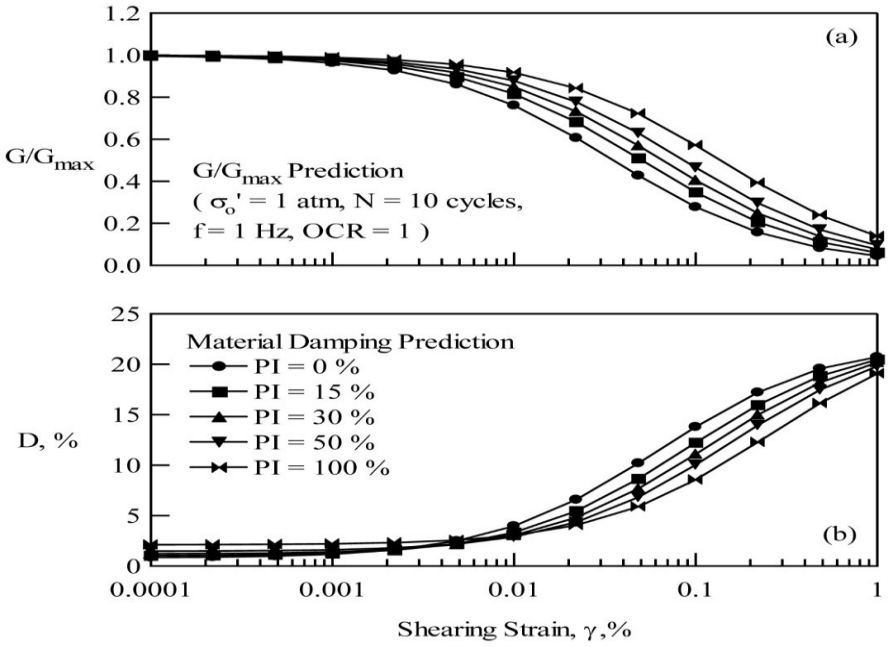

Figure 2-8: Effect of soil plasticity on (a) normalized modulus reduction and (b) material damping curves (Darendeli, 2001).

2.2 Site Response Analysis

2.2.1 Applicability of One-, Two-, and Three-Dimensional Site Response Analysis

One-dimensional site response analysis is usually chosen for its simplicity, where it is reasonable to assume that the soil layers extend infinitely in the horizontal direction and the incident earthquake motions are mainly controlled by vertically propagating, horizontally polarized shear waves. These assumptions are mostly true due to the fact that soil properties generally vary more rapidly vertically than horizontally. Generally, the velocity of waves decrease with distance from the earth's interior to the surface, and hence stress waves propagating into an earth medium are bent by successive refractions and produces a nearly vertical path near the ground surface (Kramer, 1996). The one-dimensional site analysis can be performed based on the solution of one-dimensional wave equation with the assumptions described above. One has to keep in mind that the results based on this analysis could lead to more conservative results because the soil column move freely in one dimensional analysis whereas in multi-dimensional analyses are constrained not to move freely by neighboring soil column. Structures designed based on this method are capable of withstanding the seismic loads during the major earthquake events. One-dimensional site response analysis can be carried out by a number of programs such as DEEPSOIL (Hashash et al., 2020).

The one-dimensional site analysis is mostly used in engineering practice, however there were exceptional situations. The transmission of seismic waves is affected by a variety of factors, such as topographic and subsurface irregularity. Special modeling techniques such as two-dimensional or even three-dimensional modeling are required in order to obtain the relevant site seismic responses when topographic and subsurface irregularity are significant. These special modeling techniques can also capture both types of seismic waves propagation that are body wave and surface wave. The two-dimensional or three-dimensional site-response analysis is usually performed using finite element analysis.

One dimensional analysis is usually performed using S_H-wave than S_V-wave and P-wave for the reason that ground accelerations are usually dominated by S_H-waves. However, for site with topographic and subsurface irregularity and many geotechnical structures, the second dimension is also of significant importance, and two- and three-dimensional analysis must be carried out to account for S_V-wave, P-wave and Rayleigh wave propagation as well. Chávez-García and Faccioli (2000) investigated the effects of sedimentary basin by

neglecting the topographic site effects using two-dimensional analysis and the result obtained from this analysis has two times response spectra than that of one-dimensional and recommended the current building codes to include basin effects.

Building Research Institute and Japan Society of Construction Engineering (1997) as cited by Yoshida (2015) suggested a correction factor for one dimensional analysis result for sites that found near the cliff. Yoshida (2015) reported the one-dimensional analysis is sufficient without any need of multi-dimensional analysis or correction factor if the following conditions are satisfied.

1. Slope angle of a cliff is less than or equal to 15^0.
2. Height of a cliff is less than or equal to 4 m.
3. Site is apart from the cliff by six times of the height of the cliff.

The selected sites on this study satisfied the above criteria and possible to conduct one dimensional analysis.

2.2.2 One Dimensional Site Response Analysis

The methods of analysis can be broadly categorized as follows: (a) Linear analysis (b) Equivalent linear analysis and (c) Nonlinear analysis. This study was performed using equivalent linear analysis and nonlinear analysis.

2.2.2.1 Linear analysis

The linear approach assumes that the soil behaves as a Kelvin-Voigt material with the shear modulus is a constant maximum value, G_{max}, and the damping is a constant minimum value, $\xi_{min.}$ This method is used to evaluate the response of various parameters to an input of motions using transfer functions. However, the method is limited to analysis of linear behavior because it is based on the superposition principle. The approach might be suitable for very small strain problems, but incorrect for higher strain problems. Equivalent linear analysis is used to approximate the nonlinear soil properties by using an iterative procedure.

2.2.2.2 Equivalent linear analysis

Schnabel et al. (1972) proposed the Equivalent-linear (EQL) approach by modifying the linear approach, and it provides a reasonable estimation of site response. Principally, the linear approach uses transfer functions that determine how each frequency in the input motion is amplified or deamplified by the soil column (Kramer, 1996).

Once the transfer function is established, the input earthquake motion in the time domain is converted to frequency domain using Fast Fourier Transform algorithm (FFT). The FFT will transform the input motion into Fourier Amplitude Spectrum (FAS) at various frequencies where the summation would be the original time history. Each term in the Fourier series of the input motion is then multiplied by the transfer function to produce the Fourier series of the output motion (surface motion). In order to obtain the time history of the output motion, the output Fourier series is then transformed back to the time domain using inverse FFT algorithm. Transfer functions are dependent on frequency and the stiffness, damping, and density properties of the soil column (Kramer, 1996).

For wave propagation in an infinite viscoelastic medium, the following linear second-order differential equations can be written as:

$$\rho \frac{\partial^2 u}{\partial t^2} = G \frac{\partial^2 u}{\partial z^2} + \eta \frac{\partial^3 u}{\partial z^2 \partial t} \qquad (2\text{-}3)$$

which can be solved by assuming a harmonic response of $u(z,t)=U(z)\ e^{iwt}$. Because earthquake motions are not harmonic, time histories of input motions are converted to the frequency domain by summing up harmonic response under different frequencies.

The transfer functions are used to predict the response of the soil at different layers from input bedrock motions which propagated through different soil layers. The formation of transfer function depends mainly on the boundary conditions of the base and have two types within and outcrop as illustrated in Figure 2-9.

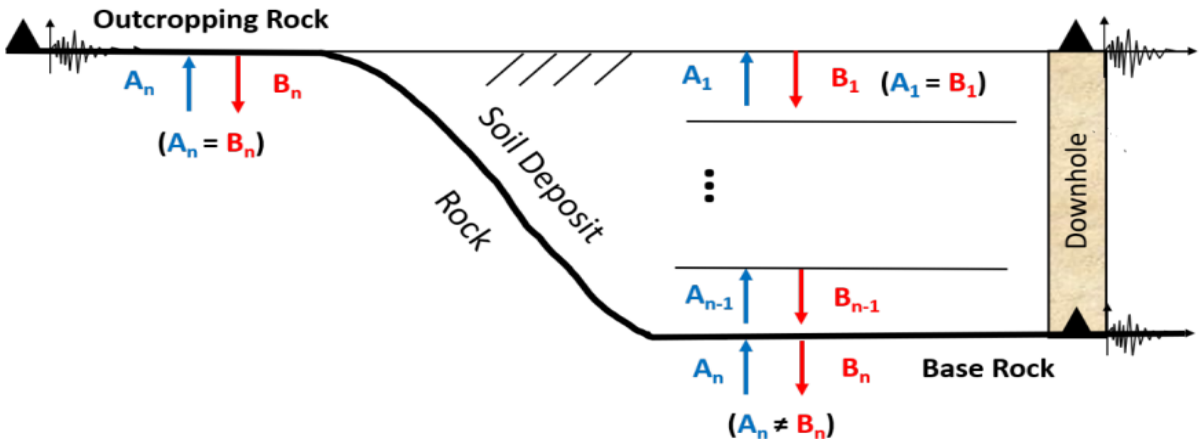

Figure 2-9: Boundary conditions and wave amplitudes considered in one-dimensional site response analysis (Kramer, 1996).

A layered soil comprise upward and downward waves for each layer and is underlain by a rock half-space that contains both upward and downward waves. Almost all site response analyses were performed by using outcropping motions, and at this location, because of the free surface effect, the upward and downward motions are equal ($A_n = B_n$). However, when analyzing a downhole array, in within motion, the upward and downward waves are not the same ($A_n \neq B_n$).

A two-layer simplified interpretation technique was used to find a solution assuming the half-space as second layer for within the subsurface profile and outcrop as a surface for outcropping layer. For each frequency on a layer *i* A_i and B_i are defined for upward wave and downward wave, respectively. The displacements in each layer for harmonic motion can be expressed as after Kramer (1996):

$$u_1(z_1,t) = (A_1 e^{ik^*_1 z_1} + B_1 e^{-ik^*_1 z_1})^* e^{i\omega t} \quad (2\text{-}4)$$

$$u_2(z_2,t) = (A_2 e^{ik^*_2 z_2} + B_2 e^{-ik^*_2 z_2})^* e^{i\omega t} \quad (2\text{-}5)$$

where is ω angular frequency, t is time, z_i is the depth below the top layer i, and k_i^* is the complex wave number in layer i ($k^* = \omega / v_s^*$)

The compatibility of displacements and continuity of stress at the layer interface lead to (Kramer, 1996):

$$A_2 = \frac{1}{2} A_1 \left[(1+\alpha^*_{12}) e^{ik^*_1 H_1} + (1-\alpha^*_{12}) e^{-ik^*_1 H_1} \right] \quad (2\text{-}6)$$

$$B_2 = \frac{1}{2} A_1 \left[(1-\alpha^*_{12}) e^{ik^*_1 H_1} + (1+\alpha^*_{12}) e^{-ik^*_1 H_1} \right] \quad (2\text{-}7)$$

where α^*_{12} represents the complex impedance ratio (i.e., $\alpha^*_{12} = \rho_1 Vs_1^* / \rho_2 Vs_2^*$) and H_1 represents the thickness of layer 1. Substituting Eqs. (2-6) and (2-7) into Eq. (2-5) and substituted $Z_2=0$ to calculate the amplitude at the top of layer 2 and yields

$$A_2 + B_2 = A_1 \left[e^{ik^*_1 H_1} + e^{-ik^*_1 H_1} \right] \quad (2\text{-}8)$$

However, if layer 2 is outcropping with $B_2 = A_2$, then the amplitude at the top of layer 2 become:

$$2A_2 = A_1 \left[(1+\alpha^*_{12}) e^{ik^*_1 H_1} + (1-\alpha^*_{12}) e^{-ik^*_1 H_1} \right] \quad (2\text{-}9)$$

The wave amplitude at the top of within profile (i.e., $z_1 = 0$) is $2A_1$.

The transfer function (TF) is defined as the ratio between the top of within profile and the top of layer 2 for TF_{within} and ratio of the outcrop to the base of the rock for $TF_{outcrop}$.

$$TF_{within} = \frac{2A_1}{A_2 + B_2} = \frac{2A_1}{A_1(e^{ik^*_1 H_1} + e^{-ik^*_1 H_1})} = \frac{2}{(e^{ik^*_1 H_1} + e^{-ik^*_1 H_1})} \quad (2\text{-}10)$$

$$TF_{outcrop} = \frac{2A_1}{2A_2} = \frac{2A_1}{A_1\left[(1+\alpha^*_{12})e^{ik^*_1 H_1} + (1-\alpha^*_{12})e^{-ik^*_1 H_1})\right]} \quad (2\text{-}11)$$

$$= \frac{2}{(1+\alpha^*_{12})e^{ik^*_1 H_1} + (1-\alpha^*_{12})e^{-ik^*_1 H_1})}$$

The two-layer derivation for transfer functions can easily be extended into layered soils using the recursion formula. The transfer function relating the displacement at layer i to that and layer j is given by Kramer (1996).

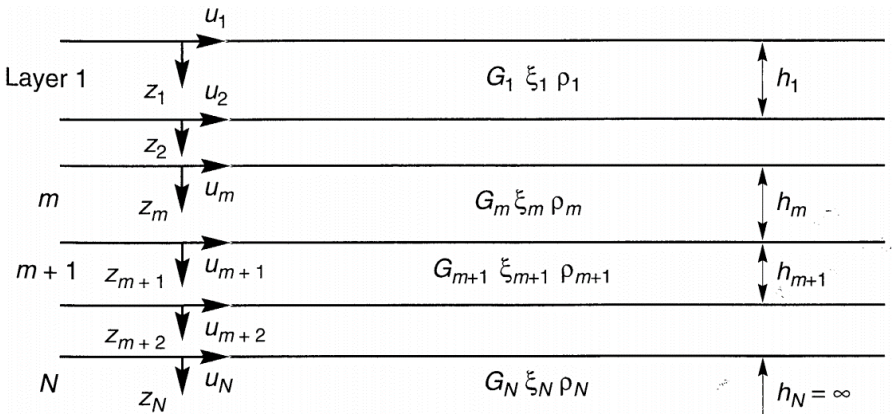

Figure 2-10: Layered soil deposit on elastic bedrock for equivalent linear method (Kramer, 1996).

$$F_{ij}(\omega) = \frac{|u_i|}{|u_j|} = \frac{a_i(\omega) + b_i(\omega)}{a_j(\omega) + b_j(\omega)} \quad (2\text{-}12)$$

EQL site response analysis is based on one-dimensional, linear elastic wave propagation through layered media, but incorporates soil nonlinearity through the use of strain compatible soil properties (i.e., shear modulus, G, and damping ratio, ξ) for each soil layer. The key to the EQL approach is the selection of soil properties (G and ξ) for each soil layer that are consistent with the shear strain level induced in the soil during seismic loading.

Development of strain-compatible properties requires an iterative approach in which the strains are computed, the properties are revised based on the strains, and revised strains are computed based on the updated properties. These iterations continue until the properties assigned to each layer in the wave-propagation analyses are consistent with the strains generated in each layer. The strain level used to select the strain-compatible properties is

not the peak time domain shear strain, but rather an effective shear strain (γ_{eff}) that usually is 65% of the peak shear strain. The computation process is repeated until the convergence limit is below 5% between two successive shear strain values.

The EQL approach uses the same stiffness and damping properties for the entire duration of analysis. This leads to under prediction of the stiffness and over prediction of the damping when the peak shear strain is much larger than the shear strains at other time intervals and vice versa when the shear strain is nearly uniform with time. And also, the stiffness and damping do not change with time, resonances could occur at natural frequency of the soil column which do not occur at actual soils (Kramer, 1996).

Another shortcoming of EQL approach is its analysis conducted in terms of total stress and therefore makes it impossible to assess the effects of pore pressure generation and cyclic degradation that could significantly decrease the stress and stiffness of soils layers, resulting in liquefaction for cohesionless soils and failure for cohesive soils. Finally, EQL analyses cannot predict accurately the response of soils at large shear strains because soil response at large strains are highly nonlinear and the dynamic properties change significantly over the duration of the shaking.

Kaklamanos et al. (2013) conducted numerous site response analyses and concludes that if the shear strain is between 0.1% - 0.4% the EQL analysis improves the accuracy of site response predictions as shown in Figure 3-11. Furthermore, if the induced shear strain is greater than 0.4% the NL approach is needed because EQL results in under prediction of surface motion.

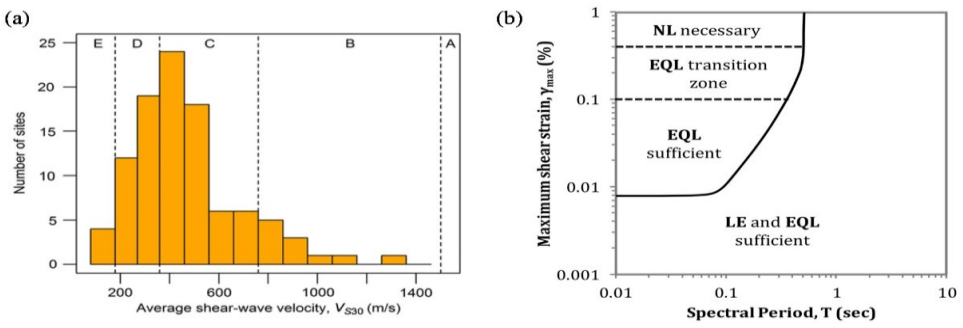

Figure 2-11: a) range of data within KiK-net downhole array, (b) the threshold of shear strain and period that predicts at which strain level the accuracy of equivalent linear approach is no longer accurate (Kaklamanos et al., 2013).

Despite these limitations, the most common site response analysis method continues to be the equivalent linear method. The EQL approach is commonly used in practice because it requires straight forward readily obtainable soil properties and low computational requirements since the computation process is performed in the frequency domain (Hashash et al, 2010). This makes EQL analysis a very efficient technique for site response calculations. For the present study, the program DEEPSOIL (Hashash et al., 2020) was used for all EQL analyses.

2.2.2.3 Nonlinear Method

The program DEEPSOIL uses the lumped mass equation of motion. In the lumped mass system, mass, nonlinear spring, and dashpot is used to represent each soil in the system as shown in Figure 2-12. The nonlinear response analysis is performed by writing the global equations of motion (Eq. (2-13)) from each node of the system.

$$[M]\{\ddot{u}\}+[C]\{\dot{u}\}+[K]\{u\}=-[M]\{I\}\ddot{u}_g \qquad (2\text{-}13)$$

where M is the mass matrix, C is the viscous damping matrix, K is the stiffness matrix. Eq. (2-13) is solved numerically using a time integration method such as Newmark (1959) β-method for each time step.

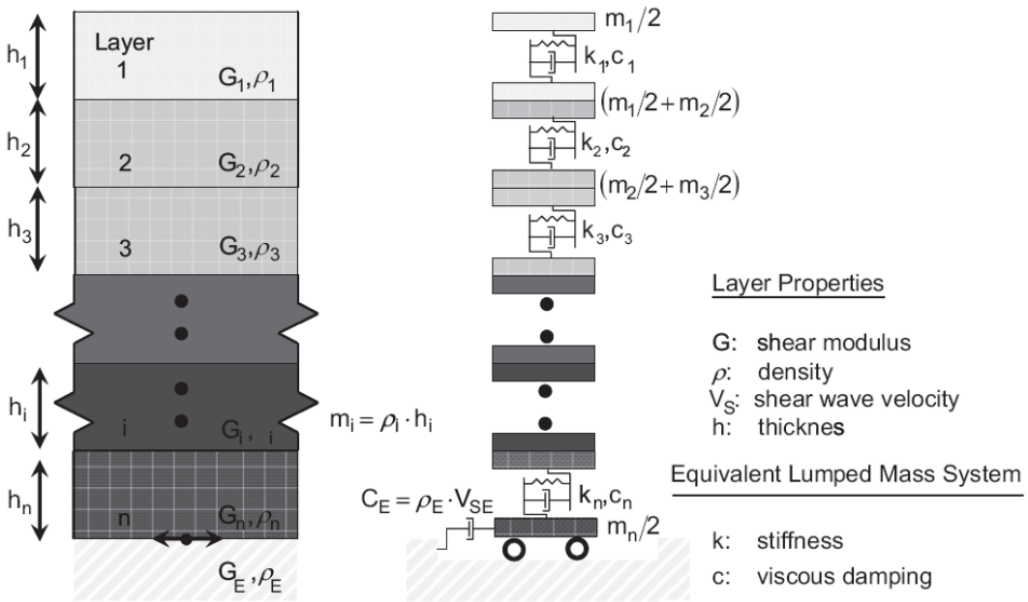

Figure 2-12: Graphical representation of a lumped mass system (Phillips and Hashash, 2009).

A lumped mass is used to construct the soil mass matrix [M]. Rayleigh damping or frequency independent approach suggested by Phillips and Hashash (2009) is used to

construct the soil viscous damping matrix [C]. The key of NL approach is the construction of the soil stiffness matrix, [K], that is continuously updated at each time increment. The [K] will adopt a cyclic non-linear soil model (i.e., (Matasovic, 1993; Groholski et al., 2016).

The calculation process for a nonlinear model is as follows (Kramer 1996): The input acceleration time series is used to determine the motion at the base of the soil profile. Then, the motion at each layer boundary is calculated moving from the bottom of the soil profile to the top. Using the displacements at each layer boundary the shear strain in each layer is calculated. The shear stress for each layer is estimated from the shear strain using a specified constitutive model. This process is repeated for the next time step until the end of shaking.

Nonlinear soil models are expected to capture: 1) definition of the backbone curve; 2) rules to characterize unloading and reloading behavior (Hysteretic damping) (3) the peak shear strength of the soil; 4) pore water pressure generation (for effective stress analysis model).

2.2.2.3.1 Backbone curves

a) Kondner-Zelasko (KZ) model

Different soil models have been suggested to date that aimed to capture the backbone curve of a soil. The earliest constitute model was Kondner-Zelasko (KZ) model (Kondner and Zelasko, 1963) which relates shear stress to shear strain using a hyperbolic function:

$$\tau = \frac{G_{max}\gamma}{1+\frac{G_{max}\gamma}{\tau_{max}}} = \frac{G_{max}\gamma}{1+\frac{\gamma}{\gamma_r}} \quad (2\text{-}14)$$

which provides the shear modulus reduction curve as

$$\frac{G}{G_{max}} = \frac{1}{1+\frac{G_{max}\gamma}{\tau_{max}}} = \frac{1}{1+\frac{\gamma}{\gamma_r}} \quad (2\text{-}15)$$

where τ= shear stress, γ= shear strain, G_{max}= initial shear modulus, τ_{max}= shear strength, and a reference shear strain equivalent to τ_{max}/G_{max}. The reference shear strain is the shear strain at which failure would occur if a soil were to behave elastically. Alternatively from Eqs. (2-14) and (2-15), the reference shear strain is the shear strain at which $\tau = \tau_{max}/2$ and $G/G_{max}=0.5$.

Eqs. (2-14) and (2-15) show that γ_r is the only modifiable parameter and that changing this parameter has two effects: (1) it sets the limit of Eq. (2-14) to $\tau=G_{max}\gamma_r/2=\tau_{max}$, and

(2) it translates the G/G_{max} curve of Eq. (2-15) along the γ-axis. Even though the KZ model is simple and easy to use, it lacks the ability to model small-strain soil behavior.

b) Modified Kondner-Zelasko (MKZ) model

Matasovic (1993) modified the KZ model by adding two new curve fitting parameters in order to improve the small strain accuracy and introduced the Modified Kondner-Zelasko (MKZ) model.

$$\tau = \frac{G_{\max}\gamma}{1+\beta\left(\frac{G_{\max}\gamma}{\tau_{\max}}\right)^{s}} = \frac{G_{\max}\gamma}{1+\beta\left(\frac{\gamma}{\gamma_r}\right)^{s}} \tag{2-16}$$

which provides the shear modulus reduction curve as

$$\frac{G}{G_{\max}} = \frac{1}{1+\beta\left(\frac{G_{\max}\gamma}{\tau_{\max}}\right)^{s}} = \frac{1}{1+\beta\left(\frac{\gamma}{\gamma_r}\right)^{s}} \tag{2-17}$$

where β and s are non-zero positive values in addition to the single KZ model parameter , γ_r.

Adding the parameter s, helps the model to capture the small strain behavior of the soil, though when the s<1 there might arise cases, in which the shear stress become greater than the shear strength of the soil. Some site response programs capped the shear stress not to be larger than the shear strength of the soil.

Hashash and Park (2001) extended the MKZ model to account for the influence of large confining pressure on modulus reduction and damping. The suggested formulation of the reference strain which include the influence of confining pressure on modulus reduction is shown Eq. (2-18).

$$\gamma_r = a\left(\frac{\sigma'}{\sigma_{ref}}\right)^{b} \tag{2-18}$$

where *a* and *b* are curve fitting parameters and σ_{ref} is a reference confining pressure of 0.18 MPa.

c) General Quadratic/ Hyperbolic (GQ/H) Model

Darendeli (2001) used the resonant column test and the torsional shear test to collect small strain and medium strain data respectively. In his experiment large strain level data was

obtained using extrapolation which may underestimate or overestimate the shear strength at large strains. Groholski et al. (2016) proposed a new approach, the General Quadratic/ Hyperbolic (GQ/H) model which has a curve fitting scheme that correct the reference curves (Darendeli, 2001) automatically based on the specified shear strength at the large strains. The model satisfies both the small-strain and large-strain modeling of the backbone curve of soils which exhibit strain-hardening behavior.

The material model uses the shear stress at failure (τ_{max}), maximum shear modulus (G_{max}), and curve-fitting constants (θ_1 through θ_5) to construct the shear strength-shear strain curve using the following functions:

$$\theta_\tau = \theta_1 + \theta_2 \frac{\theta_4 \left(\frac{\gamma}{\gamma_r}\right)^{\theta_5}}{\theta_3^{\theta_5} + \theta_4 \left(\frac{\gamma}{\gamma_r}\right)^{\theta_5}} \leq 1 \quad (2\text{-}19)$$

where, γ_r is the reference strain and is calculated as $\gamma_r = \tau_{max}/G_{max}$. Once θ_τ the is determined, the shear strength- shear strain curve is constructed as follows:

$$\tau = \tau_{max} \left(\frac{1 + \left(\frac{\gamma}{\gamma_r}\right) - \sqrt{\left[1 + \left(\frac{\gamma}{\gamma_r}\right)\right]^2 - 4\theta_\tau \left(\frac{\gamma}{\gamma_r}\right)}}{2\theta_\tau} \right) \quad (2\text{-}20)$$

Whereas the GQ/H model will always be asymptotic to τ_{max} at infinite shear strain, Groholski et al. (2016) suggested to fit the Darendeli (2001) reference curve for shear strain range up to 0.1% under the condition that the shear stresses reach 95% of the maximum at γ=10% (i.e. the implied shear strength at 10% shear strain should be 95% of the asymptotic shear strength).

2.2.2.3.2 Small Strain and Hysteretic Damping

Small strain damping

Hysteretic damping predicts nearly zero damping at small strain which contradicts with experimental results. To overcome this issue, viscous damping (frequency independent and Rayleigh damping) is recommended at small strain levels. Experimental data show a dependence of soil damping at very small strains on confining pressure. Eq. (2-21) showed

the zero-strain damping ratio which also depends on the confining pressure (Phillips and Hashash, 2009) .

$$\xi = \frac{c}{(\sigma')^d} \tag{2-21}$$

where c and d are curve fitting parameters.

Frequency independent viscous damping shown in Eq. (2-21) was used for this study.

Hysteretic damping

The unloading and reloading rules used to construct the hysteretic material damping behavior follow the Masing rules. The second part of the soil model consists of rules to characterize unloading and reloading behavior. The Masing criteria (Masing, 1926) and extended Masing criteria (Pyke, 1979) are commonly used to define unloading-reloading criteria and behavior under general cyclic loading conditions (Figure 2-13). The Masing criteria and extended Masing criteria are the following:

1. For initial loading, the stress-strain curve follows the backbone curve.
2. The unloading and reloading curve can be defined using the backbone curve as:

$$\frac{\tau - \tau_{rev}}{2} = F_{bb}\left(\frac{\gamma - \gamma_{rev}}{2}\right) \tag{2-22}$$

   where τ_{rev} is the shear stress at reversal, γ_{rev} is the shear strain at reversal, and F_{bb} is the backbone curve function.

3. If the unloading and reloading curve exceeds the maximum past shear strain and intersects the backbone curve, it follows the backbone curve until the next shear stress reversal.
4. If an unloading or reloading curve crosses an unloading or reloading curve from the previous cycle, the stress-strain curve follows that of the previous cycle.

Extended masing model follow the four criteria updating the criteria 1 and 2 of the masing criteria. However, the model still overestimates the hysteretic damping at large shear strains. Phillips and Hashash (2009) came up with an idea to avoid this and proposed an expression that modifies the Masing unloading-reloading rules and provides better agreement with the damping curves at large shear strains, commonly called the modulus reduction and damping factor (MRDF) approach. The Phillips and Hashash (2009) MRDF reduction factor is given by

$$F(\gamma_{max}) = p_1 - p_2(1 - \frac{G_{\gamma max}}{G_{max}})^{p3} \quad (2\text{-}23)$$

in which p_1, p_2, and p_3 are nondimensional parameters selected to obtain the best fit with the target damping curve. Eq. (2-23) shows that the reduction factor is dependent on the normalized modulus reduction curve. Thus, the user should first determine the constitutive model parameters which provide the best fit to the backbone curve. Then, the reduction factor parameters p_1, p_2, and p_3 can be selected to provide the best fit of the damping curve without modification of the fit to the backbone curve. The MRDF approach is implemented in the 1D nonlinear site response analysis program DEEPSOIL by including the reduction factor $F(\gamma_{max})$.

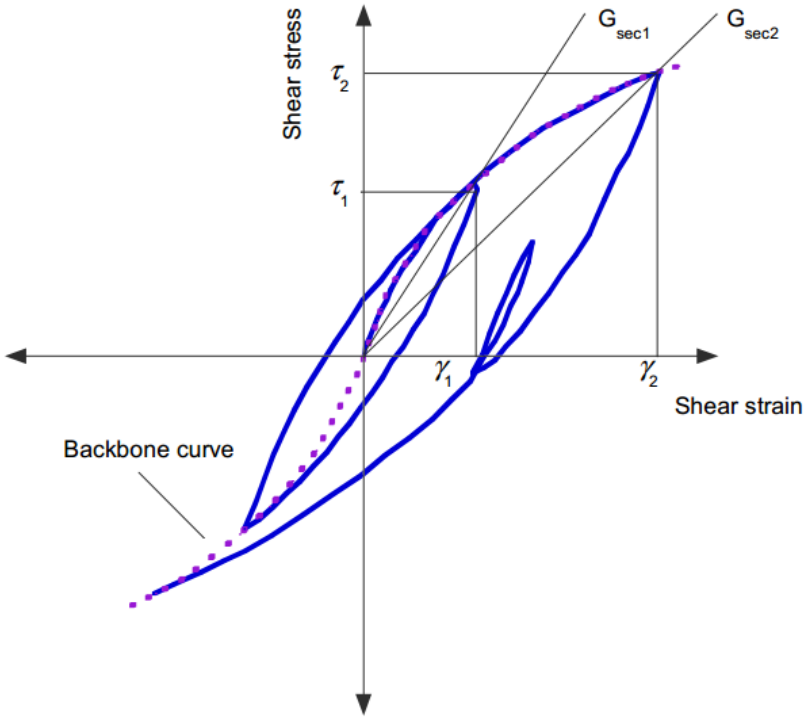

Figure 2-13: Hyperbolic nonlinear soil model with extended Masing rules to define loading and unloading behavior (Phillips and Hashash, 2009).

2.2.2.3.3 Layer Thickness

In time domain analyses, the maximum frequency that can be propagated through a soil layer is given by (Kramer, 1996):

$$f_{max,i} = \frac{V_{s,i}}{4H_i} \quad (2\text{-}24)$$

where $f_{max,i}$ is the maximum frequency that layer i can propagate, $V_{s,i}$ is the shear wave velocity of layer *i*, and H_i is the height of layer *i*. It is recommended that the maximum cut-

off frequency for any given layer be no less than 25-30 Hz, but may be larger as governed by the frequency content of the input motion and the level of strains anticipated in the soil profile. Soil profiles in this study were subdivided such that the maximum frequency of the soil profile was 50 Hz.

2.2.2.3.4 Definition of Input Motion and Half Space (Base)

Stewart (2008) compared the response of time domain analyses with elastic material properties to frequency domain analyses, which provide an exact solution for linear material properties. They looked at all four parameter combinations; within motion and rigid base, within motion and elastic base, outcropping motion and rigid base, and outcropping motion with an elastic base. Stewart (2008) recommend that when the input motion is an outcropping motion, the time series should be applied without modification using an elastic base, and if the input motion is a within motion taken from a vertical array or a down-hole recording, then the within motion should be used without modification using a rigid base. All of the motions used in this study are surface recordings. Therefore, this study used the ground motions outlined in the next chapter without modification in conjunction with an elastic base.

2.3 Geophysical Investigations

Geophysical testing is a widely used method for subsurface imaging and characterization of subsurface properties. It saves costs by providing the aforementioned properties of subsurface prior to design and construction. The geophysical tests are non-destructive, it is rapid in execution, allowing large areas to be surveyed quickly at relatively low costs, make it preferable for subsurface investigation. The geophysical methods include the measurement of mechanical waves and electromagnetic techniques. The mechanical waves measurements were done in this study and included the following measurements: MASW and MAM using Rayleigh wave and seismic refraction using P-wave and S-wave. Before proceeding to a discussion of these methods, let me first discuss the seismic waves.

2.3.1 Seismic Waves

Two main types of waves are generated following a seismic disturbance; body waves and surface waves (Aki and Richards, 1980).

2.3.1.1 Body waves

Body waves consist of shear (S-wave) waves and compressional (P-wave) waves that propagate through the earth's inside. The particle motions associated with these waves are parallel to the direction of wave propagation for compressional waves through compression and dilation causing changes in elementary volume particles while for shear waves are perpendicular to the direction of wave propagation causing shear deformations (Aki and Richards, 1980), as illustrated in Figure 2-14 and Figure 2-15.

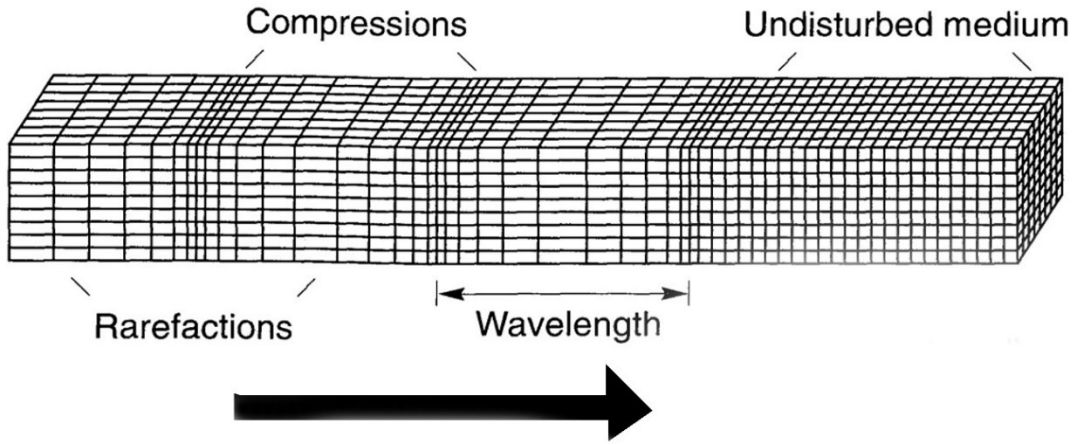

Figure 2-14: Particle motion associated with compressional waves (Kramer, 1996).

The S-wave is polarized in two perpendicular planes, the vertically polarized components (particle motion acting on a vertical plane), S_V and the horizontally polarized components (Particle motion moving in a horizontal plane), S_H (Aki and Richards, 1980; Kramer, 1996) (see Figure 2-15).

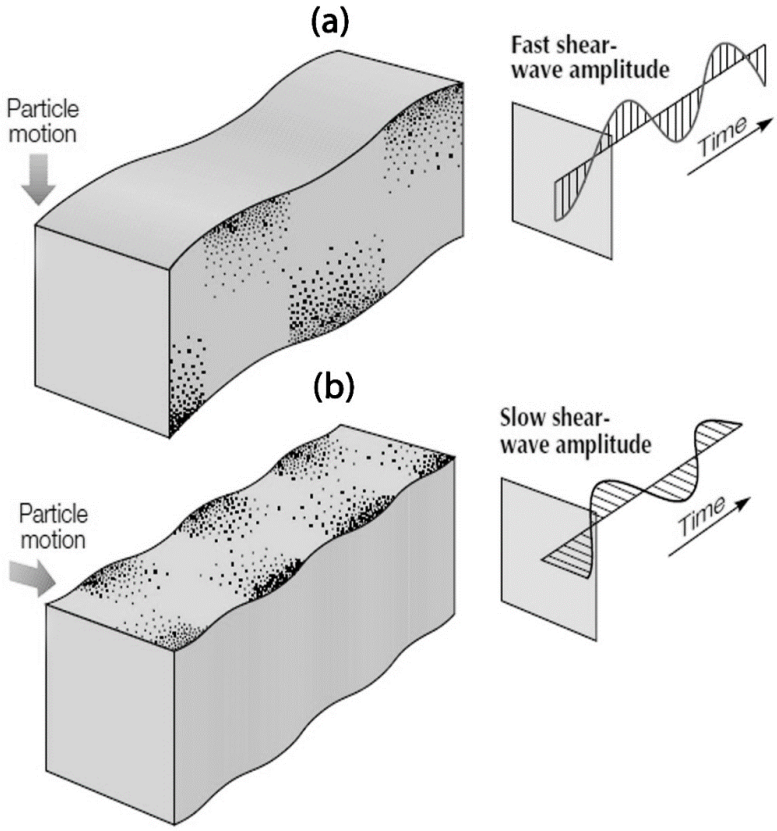

Figure 2-15: Particle motion associated with (a) vertical shear wave, (b) horizontal shear wave (Aki and Richards, 1980; Kramer, 1996).

2.3.1.2 Surface waves

Surface waves are propagated along a boundary between two different media, such as along the earth's surface. The two types of surface waves, known as Love waves and Rayleigh waves are of the main interest for engineering applications (Kramer, 1996). Rayleigh waves are the result of the interaction between the two waves (i.e P and S_V) with the earth's free surface (Aki and Richards, 1980). At the surface, the waves are elliptical in motion and retrograde (anticlockwise) with respect to the direction of propagation but become prograde (clockwise) at deeper depths.

Love waves are resulting from the interaction of horizontal shear waves (S_H) with surficial soft (low velocity) soil layer (Aki and Richards, 1980). The particle motions associated with Love waves are horizontal and transverse with respect to the direction of wave propagation shown in Figure 2-16.

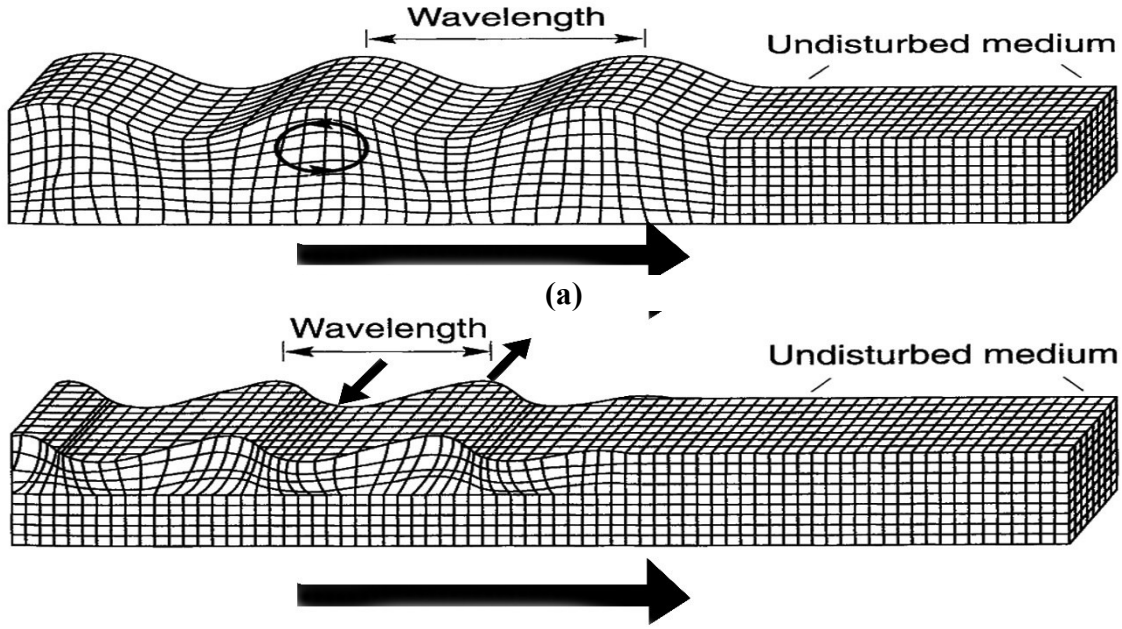

Figure 2-16: Particle motion associated with (a) Rayleigh wave (b) Love wave (Kramer, 1996).

2.3.2 Rayleigh Waves in Homogeneous Elastic Half-space

There are three waves generated when an impact is applied on the surface of an isotropic, homogeneous, elastic half-space: compressional waves (P-waves), shear waves (S-waves), and Rayleigh waves. Two-third of the total seismic energy (about 67%) generated in a seismic survey from an impact source is imparted into Rayleigh waves, while about 26% into shear waves and only a small amount of energy (7%) into compressional waves (Richart et al. 1970).

The variation of seismic wave velocities with Poisson's ratio are presented in Figure 2-17, and the waves are normalized by the shear wave.

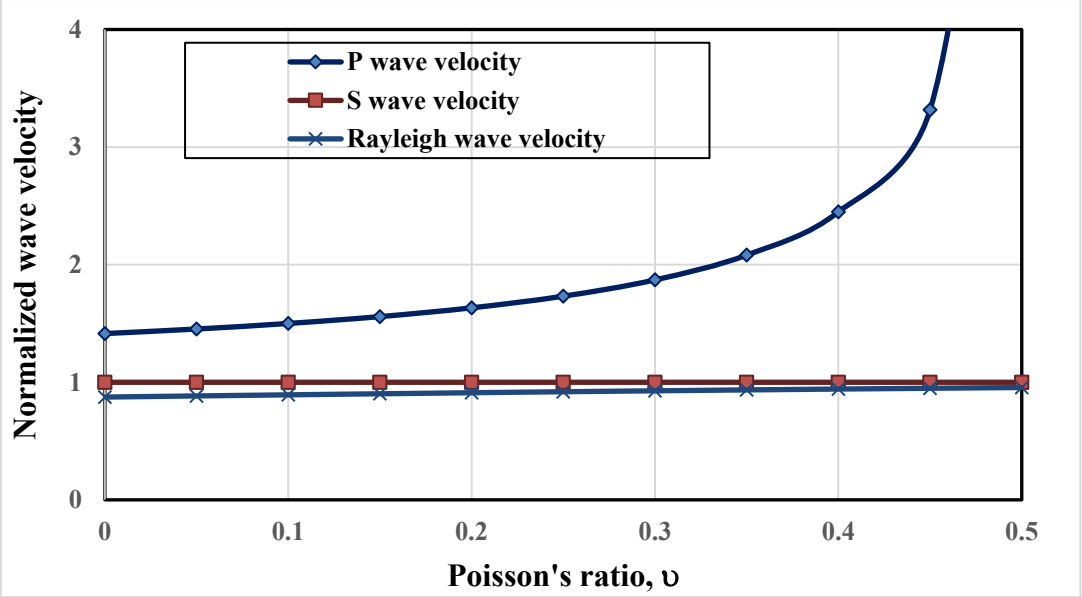

Figure 2-17 Variation of compressional, shear and Rayleigh wave propagation velocities in a homogeneous medium with Poisson's ratio (Richart et al., 1970).

2.3.3 Seismic Refraction

2.3.3.1 Theoretical background

Seismic refraction is the most widely used geophysical technique used to investigate the subsurface layering and/or local anomalies. The seismic method utilizes the propagation of elastic waves (sound waves) through the earth. It is based on the following fundamental assumptions: (a) the waves are propagated through different geological strata with different velocities (b) there must be a significant velocity contrast and (c) the layers velocities are increasing with depth. Departures from the assumed velocity conditions make it difficult or even impossible to provide a reliable estimation of velocity. Fortunately, however, the departures occur rarely (Sjogren, 1984).

Seismic waves can be generated by impacts (striking a steel plate with a hammer or falling weight drop) or detonating explosives charges. Geophones which are sensitive to vibration will record the arrival of the waves that propagate through the earth. The velocity of a wave in a particular layer can be determined by knowing the distance and travel times between the source point and receiving stations.

The seismic fieldwork is generally carried out with the impact points and detectors placed in a straight line and by keeping a regular distance between the geophones, which is called

in-line profiling system, which has the advantage of simplifying both fieldwork and interpretation.

The method makes use of waves traveling along the ground surface and of waves refracted from a higher velocity layer underlain by a lower velocity layer. Ground surface waves are the first to arrive in the vicinity of the source point. At a certain distance from the source point, the waves following the longer but faster paths in the underlying layers overtake the ground surface waves as shown in Figure 2-18. The distances from the source point to the points where the refracted waves are recorded as first arrivals are a function of the strata velocities and depths.

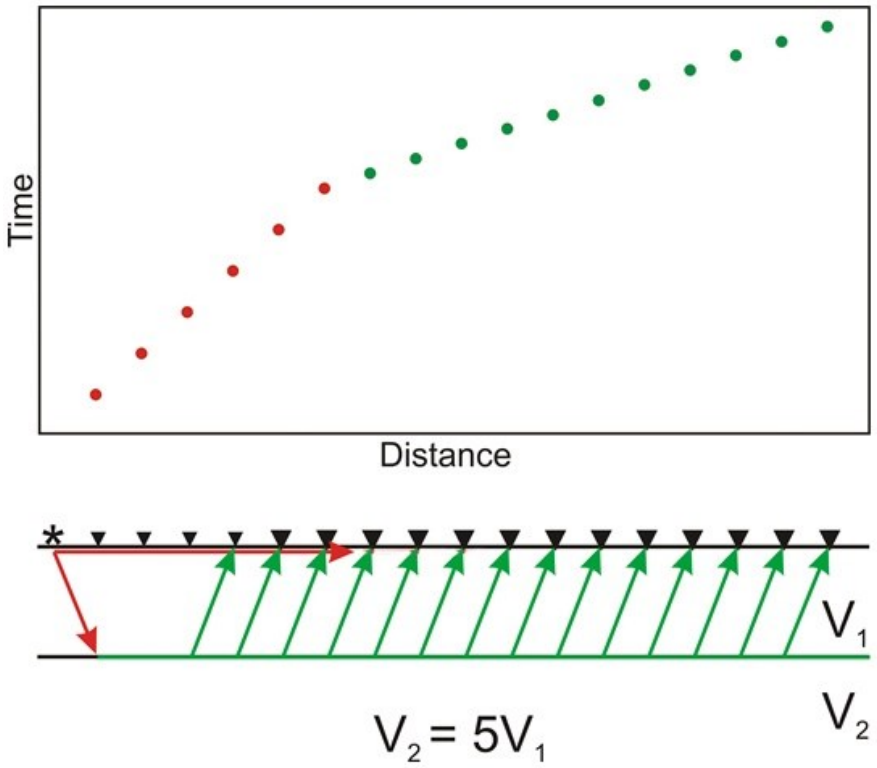

Figure 2-18: Schematic of seismic refraction survey.

The interpretation gives the velocity of different layers and their respective depth can be carried out manually or by processing software. The reliability in the determination of the depths and layer velocities increases if the signals are recorded with multiple shots, including forward, middle, and reverse shots which are, respectively, at the beginning, middle, and end of a survey line along the spread length.

A seismic survey yields essential information like compressional wave and shear wave which will properly delineate the shallow subsurface layering as well as used to determine other parameters such as Poisson's Ratio, Young's modulus, and shear modulus.

For our purpose, the seismic waves may be considered to be transmitted according to the same laws as for ray optics. The two basic concepts, namely Huygens' principle, Snell's law are governing principles for refracted waves across which there is a marked contrast in physical properties.

2.3.3.1.1 Huygens' principle

The principle states that each point on a wave surface acts as a source for an expanding spherical wave and after a certain time lapse the envelope of all the wavelets defines the new wavefront.

2.3.3.1.2 Snell's law

The refraction that a seismic pulse undergoes when passing between two different material depends upon the ratio of the velocity of the two materials. Snell's law is the fundamental law that properly describes the refraction of waves and together with the "critical incidence" phenomenon can be considered as the foundation of seismic refraction surveys.

First Snell's law and critical incidence are illustrated in Figure 2-19, which shows a medium with a velocity V_1, underlain by a medium with a higher velocity V_2.

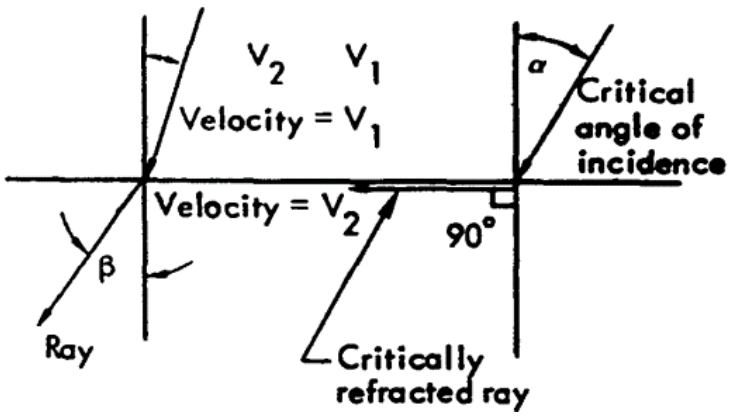

Figure 2-19: Snell's Law and refraction of ray transmitted across boundary between two media with different velocities (V_2=2V_1).

Any wave meeting an interface between media of differing velocities is partly reflected and partly refracted.

$$\sin\theta_1 / V_1 = \sin\theta_2 / V_2 \quad (Snell's\ Law) \tag{2.25}$$

This equation is known as Snell's law or the law of refraction. The angle θ_2 is called the angle of refraction and θ_1 the angle of incidence. Since V_2 in this case is greater than V_1, θ_2 is greater than θ_1. When θ_1 increases there is a unique case where the angle of refraction θ_2 is 90° and sin θ_2 = 1. Therefore, in this particular case

$$\sin\theta_1 = \frac{V_1}{V_2} = \sin\theta_{12} \tag{2.26}$$

The angle i_{12} is called the critical angle of incidence. For incidence angles greater than θ_{12}, the energy is totally reflected into the upper layer. Snell's law cannot be satisfied since sin θ_2 cannot exceed unity.

The two-layer case shown in Figure 2-20 will be used to explain some fundamental principles. From the source point B, the waves spread out in accordance with the seismic laws into the two media composing the subsurface.

In the vicinity of point B, the waves travel in the upper layer with velocity V_1, and on reaching the second layer they propagate with the higher velocity V_2. These latter waves return to the surface as plane waves making the angle θ_{12} with the interface. The corresponding ray paths, shown in the cross-section (b), make the angle θ_{12} with the normal to the interface.

At large distances from B, the waves that travel along the longer but faster path in the second medium will overtake those that follow the ground surface. Therefore, there must exist a point along the surface where the times for the arrival of the direct waves and refracted waves are equal.

If the first arrivals of the elastic waves are recorded by geophones planted in the ground, the times from the impact instant to the geophones can be plotted on a time-distance graph as shown by the dots in the upper part of Figure 2-18. The slopes of the lines obtained by connecting these dots yield the reciprocal of the velocities, namely l/V. Therefore, the lower the velocity, the steeper the slope of the time-distance line.

The intersection, 'break-point', between the two velocity lines is obviously the point where the times are equal. The distance between the impact point B and the break-point is called the critical distance.

For calculating the depth at an impact point two different approaches are available using either the intercept or the critical distance. Both intercept time and critical distance approaches are discussed here.

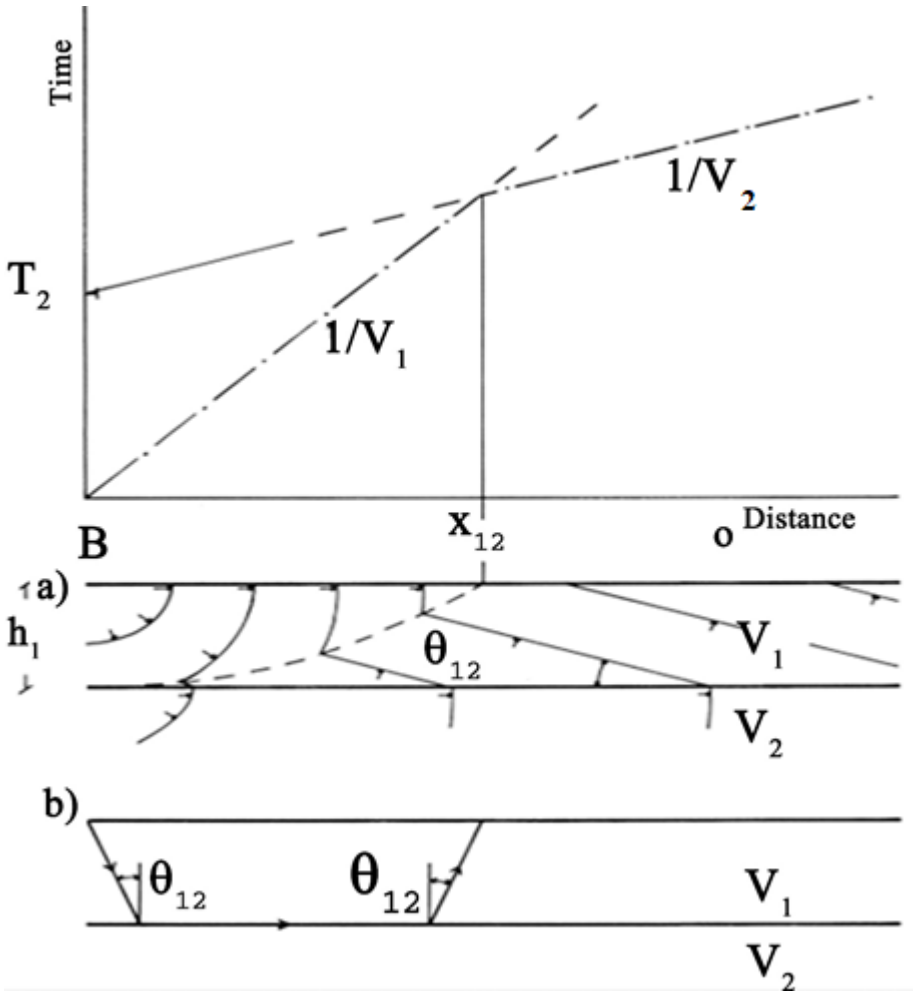

Figure 2-20: Fundamental principle of refraction shooting.

2.3.3.1.3 Intercept time

The equation for the arrival time T_1 of the direct surface waves is

$$T_1 = \frac{x}{V_1} \tag{2.27}$$

which is the equation for a straight line through the impact point with slope $1/V_1$.

For the arrival time T_2 of the refracted waves we have

$$T_2 = \frac{2h_1}{V_1 \cos\theta_{12}} + \frac{x_{12} - 2h_1 \tan\theta_{12}}{V_2} \quad (2.28)$$
$$= \frac{2h_1}{V_1 \cos\theta_{12}} - \frac{2h_1 \sin\theta_{12} \sin\theta_{12}}{V_1 \cos\theta_{12}} + \frac{x}{V_2}$$
$$= \frac{x}{V_2} + \frac{2h_1 \cos\theta_{12}}{V_1}$$

which is the equation of a straight line with slope $1/V_2$ and an intercept on the time axis through the impact point (i.e. the time for x = 0) equal to

$$T_2 = \frac{2h_1 \cos\theta_{12}}{V_1} \quad (2.29)$$

From this we get

$$h_1 = \frac{T_2 V_1}{2\cos\theta_{12}} \quad (2.30)$$

The formula can also be expressed in terms of V_1 and V_2 as

$$h_1 = \frac{T_2 V_1 V_2}{2\sqrt{V_2^2 - V_1^2}} \quad \text{since} \quad \cos\theta_{12} = \sqrt{1 - V_1^2 / V_2^2} \quad (2.31)$$

2.3.3.1.4 Critical distance

The intersection of the two time-distance lines in Figure 2-20 is the critical distance X_{12} at which $T_1 = T_2$. Thus

$$\frac{2h_1}{V_1 \cos\theta_{12}} + \frac{x_{12} - 2h_1 \tan\theta_{12}}{V_2} = \frac{x_{12}}{V_1} \quad (2.32)$$
$$\frac{2h_1}{V_1 \cos\theta_{12}} - \frac{2h_1(1 - \cos^2\theta_{12})}{V_2 \cos\theta_{12}} = x_{12}\left(\frac{1}{V_1} - \frac{1}{V_2}\right)$$

Using the relation $V_1 / V_2 = \sin\theta_{12}$

$$h_1 = \frac{x_{12}(1 - \sin\theta_{12})}{2\cos\theta_{12}} \quad (2.33)$$

In terms of the velocities instead of the critical angle θ_{12}, we have

$$h_1 = \frac{x_{12}}{2}\sqrt{\frac{V_2 - V_1}{V_2 + V_1}} \quad (2.34)$$

The critical distance and intercept time formulae can be extended for any desired number of layers as long as the velocities increase with depth.

2.3.3.1.5 Dipping layers

If the boundaries between interfaces are nonparallel (i.e., if there are dipping interfaces), a plot of arrival times versus distance will give only apparent velocities for the refracting layers, and the use of these apparent velocities will result in erroneous depths. To avoid such kind of problems, a computer program SeisImager using time term inversion was used to calculate depths, dip angles, and true velocity.

2.3.4 Shear Waves

In examining the behavior of the shear wave, further attention must be given to the direction of the particle motion within the plane perpendicular to the direction of the wave advance. It will be assumed that interfaces between layers in the medium are horizontal. The particle displacement in the shear wave can then be resolved into horizontal and vertical components that are respectively parallel and perpendicular to the interfaces, and the two components can be examined separately. As illustrated in Figure 2-21, the horizontally polarized shear wave, or S_H-wave shown as a first component and vertically polarized shear wave, or S_V-wave appeared as a second component.

In principle, for an anisotropic medium, a consequence of which would be that the S_V - and S_H -waves would be propagated at different velocities and thus would arrive at a geophone at different times.

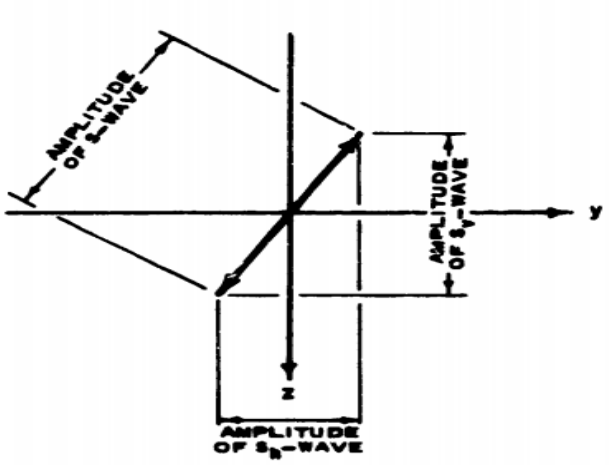

Figure 2-21: Resolution of S-wave into S_V-wave and S_H-wave components.

2.3.4.1 Measurement of horizontal shear waves

The P-wave is relatively easy to measure because the wave overtakes all other waves and arrive first at the geophone. On the other hand, the shear wave travels slower than P-wave which makes it difficult to measure because that they will be imbedded in seismograph somewhere after the P-wave arrival. To overcome this difficulty, we use a seismic energy source that generates mostly shear waves and geophones that only detect shear waves.

The radiation pattern generated by an impulsive source is shown in Figure 2-22, P- and S_V -waves are also generated by such a source and propagate most strongly in the direction parallel to the impulse. A nearly pure S_H-wave is propagated in a direction perpendicular to the direction of the impulse (Woods, 1978).

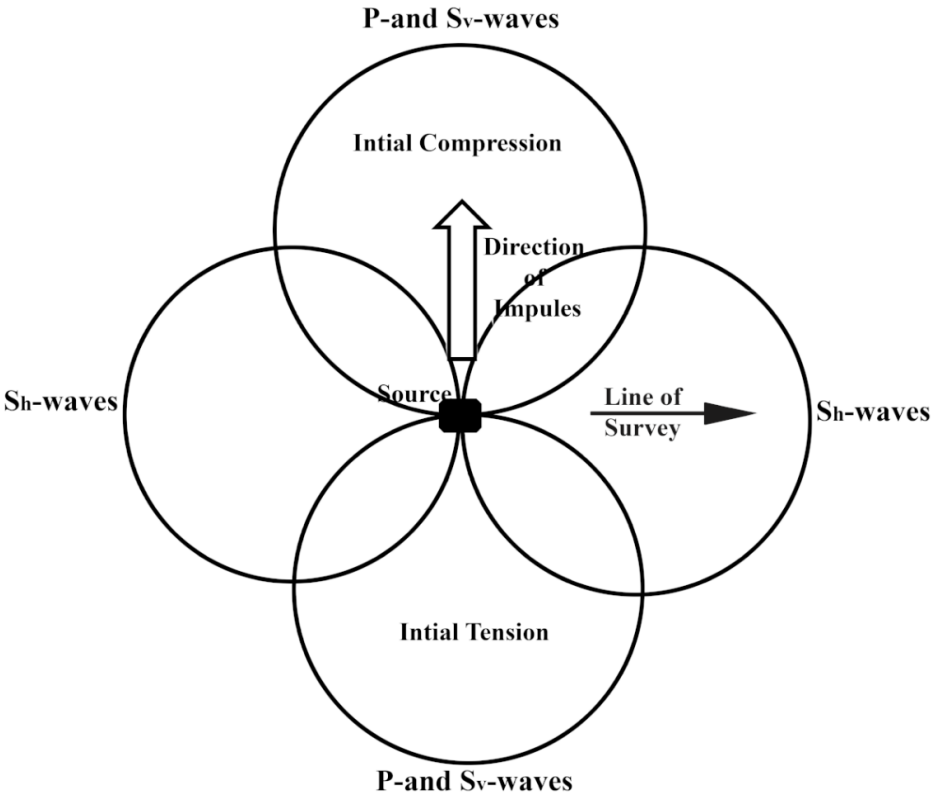

Figure 2-22: Radiation pattern for an impulsive surface traction source (Woods, 1978).

Considerable success has been obtained with the use of source that is made for this purpose, which must be held in contact with the ground surface by weight and struck at one end with a sledgehammer. The source is weighted by a standing person who strikes the hammer. To reduce slippage between the source and the ground, spikes are attached to the bottom of the source.

Horizontal geophones are used for the survey, they are sensitive to horizontal plane motions. The horizontal geophone oriented parallel with the long axis of the source, in the same axis as the particle motion. It will be more sensitive to shear waves and less sensitive to compressional waves.

Consequently, discrimination of the S_H-wave from the P-wave can be improved by interpretation methods that make use of the reversal of phase of the S_H-wave. Horizontal shear waves (S_H) are preferable for this type of application because they do not convert to compressional or vertical shear at planar refraction boundaries. Two shot records are obtained from the same location where hammer strike alternately at opposite ends of the source. Then, appending the two end shots using a computer program and the first point the two wiggles coincide is the first shear wave arrival as shown in Figure 2-23.

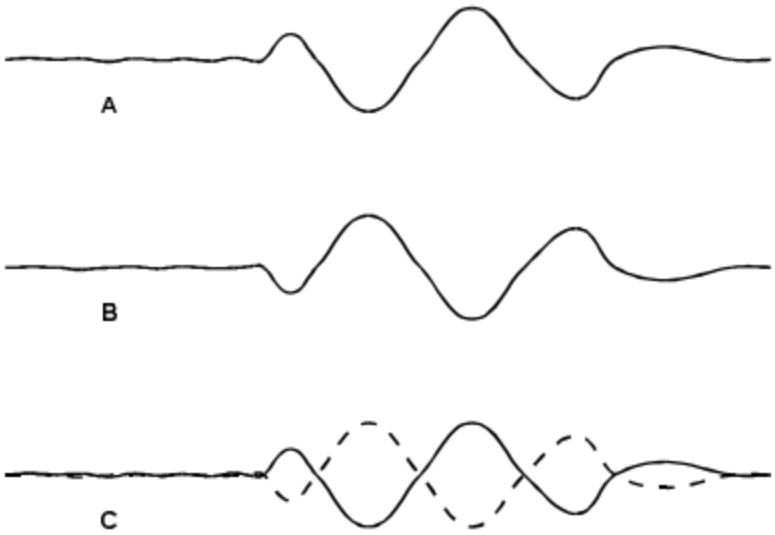

Figure 2-23: Shear wave shot from (a) left (b) right end and (c) appending of the left and right shots.

2.3.4.2 Soil and stress anisotropy

Another cause of variation is material (and stress) anisotropy. When the medium is anisotropic, S_V and S_H wave velocities are not identical; therefore, horizontally and vertically traveling P waves are not the same. As a result, horizontal wave propagation and vertical propagation could have different velocities, despite both measuring P- and S-wave velocities (Lee, 1993). Typically, these effects will introduce a 10 to 15% variation in velocity under the best conditions. As the soil profile becomes more varied or as the care and experience of the investigator decreases, the amount of variation is expected to increase.

The ratio of S_V- arid S_H-wave velocities, is one measure of soil anisotropy. A shear wave velocity ratio of less than unity implies a stiffer soil in the horizontal direction than in the vertical direction. Conversely, when $(S_V/S_H)>1$, the soil is stiffer in the vertical direction. Gibbs et al. (1992) performed crosshole seismic test at the Gilory 2 and Treasure island site to measure the shear (S_V and S_H) wave velocities. Shear wave measurements at Gilory site indicate higher stiffness in the horizontal direction than in the vertical direction at most depths between 35 ft and 100 ft (10.7 m and 30.5 m) as shown in Figure 2-24-a. Shear wave measurements at Treasure island indicate higher stiffness in the vertical direction than in the horizontal direction at depths between 20 ft and 60 ft (9.1 m and 18.3 m) as shown in Figure 2-24-b.

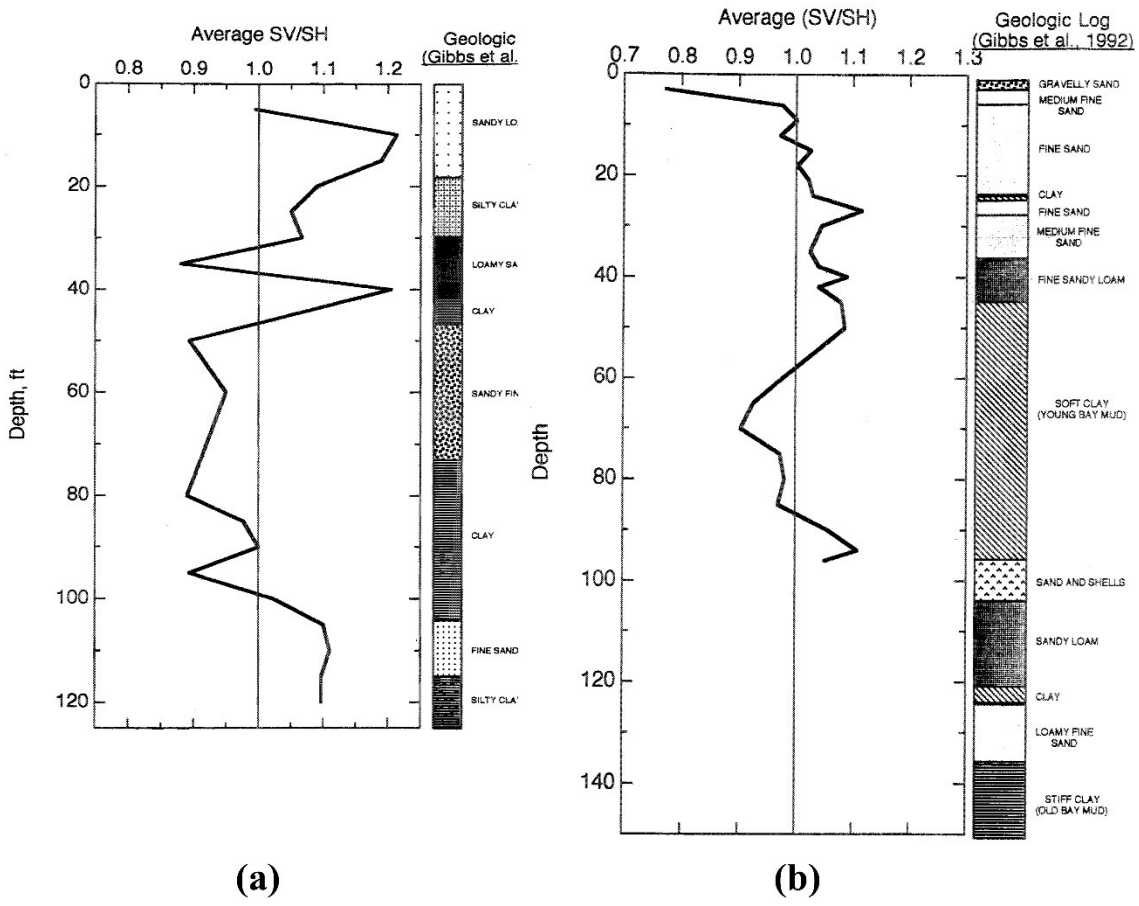

Figure 2-24: (a) Average shear wave velocity ratio (S_V/S_H) at Gilroy 2 (b) average shear wave velocity ratio (S_V/S_H) at Treasure island (Gibbs et al., 1992).

2.3.5 Multichannel Analysis of Surface Waves (MASW)

Surface wave methods are used to determine the shear wave velocity profile of the uppermost soil layers by generating dispersion curves from the surface waves records. Numerous methods exist, the most popular being Spectral Analysis of Surface Waves (SASW) and Multichannel Analysis of Surface Waves (MASW). The Multichannel Analysis of Surface Waves (MASW) was first introduced by Park et al. (1999) and was developed to overcome the problems associated with the SASW.

The MASW method has become increasingly popular in the geophysics and civil engineering in the last 20 years. The method has become more preferable to other surface wave methods for shear wave velocity profiles estimation because of their non-invasive, non-destructive, efficient, and low-cost advantages (Xia, 2014). From the results found by Xia et al. (2002), the relative difference of V_{S30} from MASW and direct borehole measurements is less than 15%.

Ground roll is a particular type of Rayleigh that travels along or near the surface of the ground. It is usually characterized by relatively low velocity, low frequency, and high amplitude (Sheriff, 1991). The Rayleigh waves with long wavelengths will be influenced by the elastic properties of the deeper layers and also exhibit greater phase velocities. In contrast, short wavelengths are more controlled by physical properties of the surface layers and exhibit slower phase velocities. Based on this reasoning a particular mode of surface wave will possess a unique phase velocity for each unique wavelength, leading to the dispersion of the seismic signal (Xia et al., 1999). The three steps of processing scheme for Multichannel Analysis of Surface Waves data: acquisition, processing and inversion is shown in Figure 2-25.

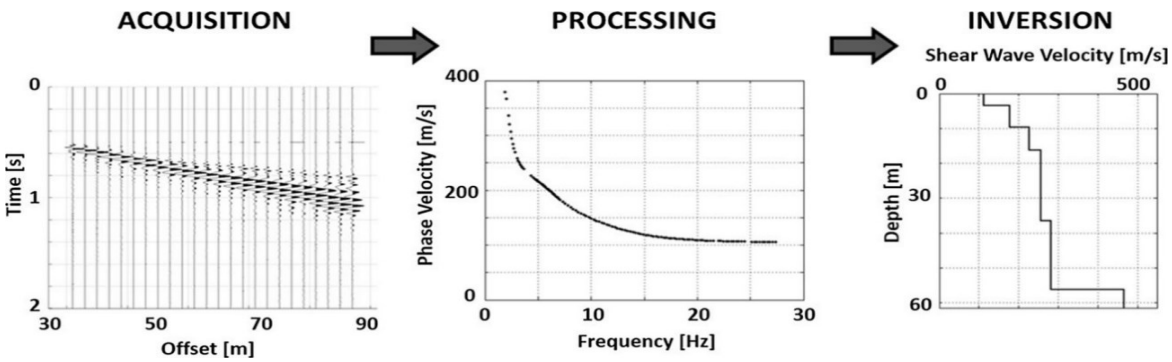

Figure 2-25: A three step processing scheme for Multichannel Analysis of Surface Waves data.

2.3.5.1 MASW data acquisition

The first step in the MASW process is data acquisition in the field. The purpose of this is to acquire broadband high frequency planar fundamental-mode Rayleigh wave records. There are two types of sources: active and passive sources, both sources are used for all surveys conducted as part of this study. Active MASW is similar to that used in refraction surveys, a sledgehammer is used as the active seismic source and low-frequency geophone lined up with equal spacing in a straight line.

The number of samples recorded per unit time, i.e. the sampling rate in Hertz [Hz], is denoted by f_S. In terms of angular frequency, the sampling rate (ω_s) is

$$\omega = 2\pi f_s \tag{2-35}$$

Park (2019) suggested that MASW surveys should be sampled at 1000 Hz i.e, the corresponding sampling interval (dt) of 1 msec for total recording time of one second.

Park et al. (1999) recommended using twelve or more vertical geophones with a natural frequency of not more than 10 Hz. It has been suggested that heavy sources like weight drop that are capable of delivering more impact into the ground can improve the low frequency and longer wavelengths of Rayleigh waves (Park et al., 2002). Moreover, the use of a plastic base plate also does the same effect. An 10 kg sledgehammer and a plastic plate were chosen as the seismic source and the signal recorded with a 24-channel array of 4.5 Hz vertical geophones, which are suitable for materials in the upper 30 m (Park et al., 2002).

2.3.5.2 Configuration of the measurement profile

2.3.5.2.1 Spread length

The maximum investigation depth (Z_{max}) will be determined by the longest wavelength (Rayleigh wave), a widely adopted empirical relation (Park and Carnevale, 2010) is that

$$z_{max} = 0.5\lambda_{max} \tag{2-36}$$

In 2010, Park & Carnevale (2010) reported that the spread length (L) is approximately equal to the longest wavelength, by utilizing Eq. (2-36) the maximum investigation depth related to the spread length (L), can be written as

$$z_{max} = 0.5L \tag{2-37}$$

Consequently, the optimum spread length for practice use has been suggested to lie within this interval (Park, 2019)

$$z_{max} \leq L \leq 3z_{max} \quad (2\text{-}38)$$

with $L = 2z_{max}$ generally recommended (e.g., Xia et al., 2009).

2.3.5.2.2 Receiver spacing

The receiver (geophone) spacing (dx) should not be larger than half the length of shortest wavelength to avoid spatial aliasing, which caused a misrepresentation of a measured signal (Xia et al., 2009).

$$dx \leq 0.5\lambda_{min} \quad (2\text{-}39)$$

Furthermore, the receiver spacing also used to determine the minimum thickness (h_{min}) of the upper layer (Park et al., 1999; Xia et al., 1999).

$$h_{min} = dx \quad (2\text{-}40)$$

2.3.5.2.3 Source offset

The non-planar surface waves cannot be picked by the geophones unless proper choice of distance between the source and nearest receiver is made and the effects are called near-field effects. As noted earlier, minimum source offset (x_1) required to avoid near-field effects depends on the longest wavelength (λ_{max}) is generally considered to be half of the longest wavelength measured (Park et al., 1999). Hence,

$$x_1 \geq 0.5L \quad \text{when} \quad L=\lambda_{max} \quad (2\text{-}41)$$

A long source offset, i.e $x_1 \geq L$, enhances the energy of long-wavelength wave components, which however would also lead to the lack of short-wavelength components (Park and Shawver, 2009; Park and Carnevale, 2010)

The minimum ($x_{1,\,min}$) and maximum ($x_{1,\,max}$) source offsets for use in practice have been suggested as (Park, 2019)

$$x_{1,min} = 0.2L \quad \text{and} \quad x_{1,max} = L \quad (2\text{-}42)$$

2.3.5.3 Summary of recommended profile-setup parameters

The measurement profile setup parameters discussed above are summarized in Table 2-2. The Spread length (L) and the source offset length (x_1) are given within a range, as indicated by Eq. (2-38) and Eq. (2-42), respectively. Assuming the number of receivers (N) is 24, then the receiver spacing is calculated and this was used for data acquisition.

Table 2-2: Summary of data acquisition parameters for active MASW surveys (Park, 2019)

Depth Z_{max} (m)	Maximum wavelength λ_{max} (m)	Length of receiver spread L (m)	Source offset x_1 (m)	Receiver spacing (24 geophones) dx (m)
5	10	(5-15) 10	(1-15) 5	(0.2-0.7) 0.4
15	30	(15-45) 30	(3-45) 15	(0.7-2) 1.3
25	50	(25-75) 50	(5-75) 25(*)	(1.1-3.3) 2.17
30	60	(30-90) 60	(6-90) 30(*)	(1.3-3.9) 2.6

(*) A 10 m source offset was found to be sufficient to assure surface wave propagation that extends to a longer wavelength up to 60 m (Park et al., 2002).

2.3.5.4 Topographical conditions

Topography can also have influence on the quality of the recorded surface wave data, steeper topography will result in a lower quality dispersion image (Zeng et al., 2012). Zeng et al. (2012) on their numerical investigations suggested that the topographic slope along the survey line (θ) should preferably be lower than 10 and for steeper topography (slope angle $\theta > 10$) errors on the dispersion image are significant (greater than 4%).

2.3.5.5 Passive surface wave

In active MASW the investigated depth might not be deep to 30 m due to either the nature of near surface material or the energy of the source. To overcome this problem, weight drop sources are invented; they are expensive and inconvenient which will discourage its use in seismic surveys. Passive surface waves generated by noises are nowadays chosen to filling the gap as their long wavelength assure to reach below the maximum depth attained by an active survey (Park et al., 2005).

The passive survey captured the lower frequency range (2 Hz-15 Hz), while the active survey captured the higher frequency range (15 Hz-40 Hz), by combing the two dispersion curves and inverting the results it is possible to obtain the shear wave profile for a wide depth range.

Micrometer Analysis Measurements (MAM) was used for the passive investigation, Park et al. (2005) suggested that mostly fundamental mode is obtained from the MAM analysis although confirmation is needed by tied up the two active and passive modes.

2.3.5.5.1 MAM data acquisition

In microtremor analyses, the signal should be planar and coming from all directions. SeisImager/SW has a built-in feature called SPAC (spatial autocorrelation) which will be used to avoid the problem associated with source location and orientation. From all available orientations (Linear, Circular, L-shape and Triangle), the L-shape was used which has an advantage to capture the signal from both directions NS and EW as well as not being time-consuming to set the orientation in the field. The dispersion curve processed from MAM was then combined with the dispersion curve from MASW, producing one dispersion curve with a wide range of frequency.

2.3.5.6 Dispersion analysis

The main aim of this step is to obtain Rayleigh wave dispersion curves from the raw surface wave data using either of the two methods i.e, swept frequency approach and phase shift method. The fundamental mode should be dominant in dispersion curve. The resolution of the dispersion image generated by the phase-shift method is superior to those obtained by swept frequency method (Park et al., 1998). Therefore, this method was used to develop dispersion images for all of the acquired field data throughout the paper.

2.3.5.6.1 Phase shift method

The phase shift method, first described by Park et al. (1998), used to image and extract dispersion curves for given seismic records and transforms the waveforms from the distance-time into the phase velocity-frequency domain. In general, surface waves propagate in several modes, which means that each mode has its own frequency content and characteristic phase velocity values at each of their respective frequencies. The desired fundamental mode of Rayleigh wave dispersion curve is extracted from the obtained dispersion image for further analyses.

The phase shift method can be divided into three main steps:

a) Fourier transformation and amplitude normalization.
b) Dispersion imaging.
c) Extraction of dispersion curves.

2.3.5.7 Inversion analysis

The inversion analysis is used to develop the shear wave profile by back calculating the shear wave velocity and their respective depths from the experimental dispersion curve using an inversion process. An earth model with plane layers assumption is made for computations of Rayleigh wave propagation.

Inversion problem must be solved by iterative methods to properly acquired a realistic layered earth model from the nonlinear Rayleigh wave dispersion data. To extract the theoretical fundamental mode dispersion curve, a mathematical model is needed that uses a set of given input parameters. Different sets of layer parameters are updated throughout of the inversion until the theoretical dispersion curve perfectly matches the observed experimental dispersion curve (Park et al., 1998; 1999). An acceptable shear wave profile acquired through multi-parameter optimization targeted to minimize the difference between the theoretical dispersion curves and the experimental one.

Based on the described above, three major components are included in the inversion analysis software. The first one is an algorithm that is used to estimate the initial set of model parameters. The second one is the mathematical model based on the stiffness matrix, the concept was developed by Kausel and Roësset (1981), which compute theoretical dispersion curves from the assumed soil profiles. The third one is evaluating and minimizing the misfit between the theoretical fundamental mode dispersion curve and experimental one using algorithms.

CHAPTER 3
MATERIALS AND METHODS

A number of analytical models and computational procedures have been developed to predict and evaluate site response due to seismic excitation. This chapter presents a review of the current methods for modeling and analysis of the seismic site response of soil deposits.

3.1 Procedure of Seismic Site Response Analysis

Flow of the one dimensional seismic site response analysis using DEEPSOILv7 is schematically shown in Figure 3-1.

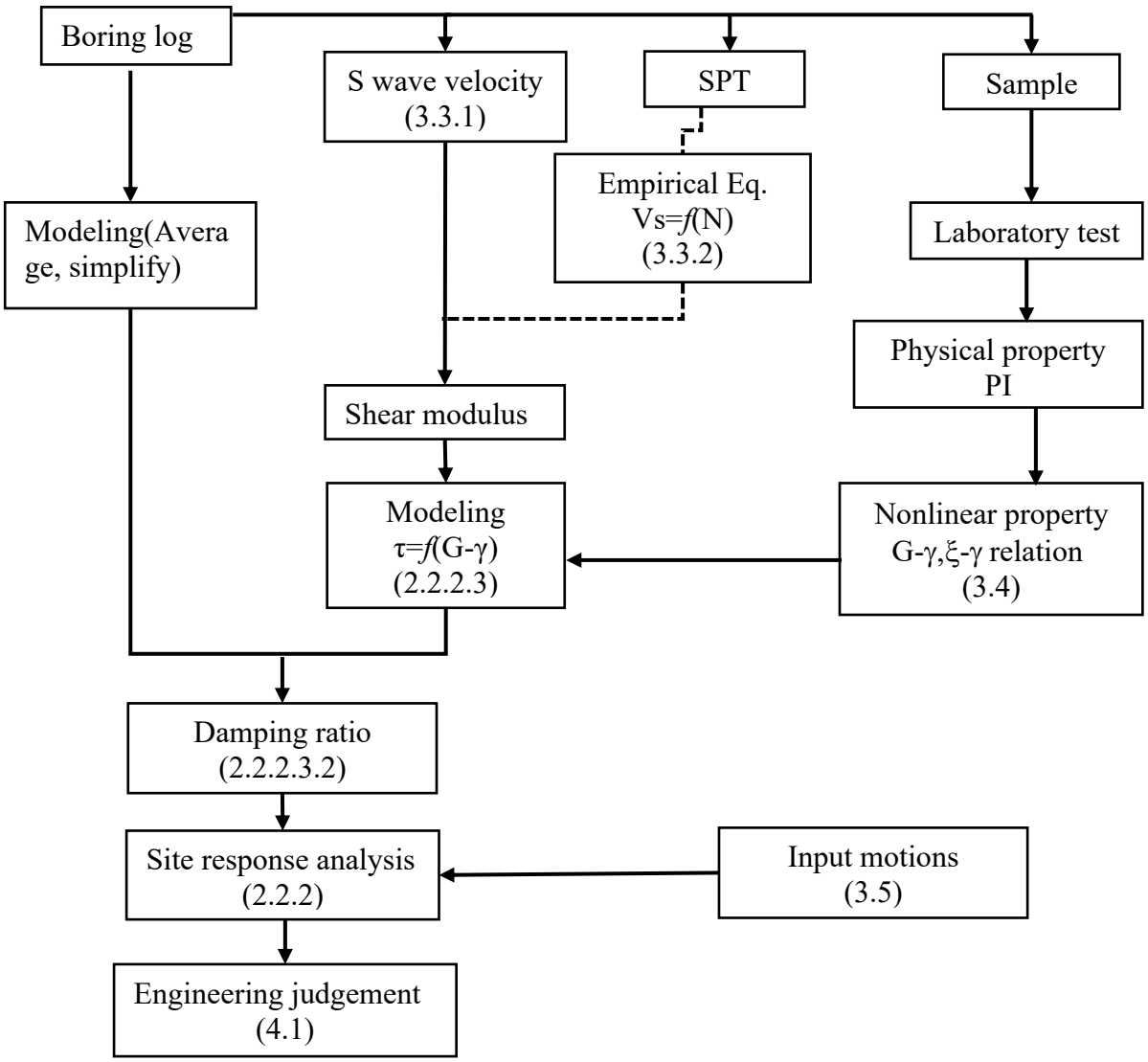

Figure 3-1: Flow of the seismic site response analysis.

The procedure consists of the following steps: (1) collect data, (2) model them for computer programs, (3) to execute computer program, and (4) to interpret the results. Several input data are required in the seismic site response analysis. They are classified into four categories:

- Measured or estimated shear wave velocity
- Mechanical properties
- Input motions
- Parameters to control the flow of the computer program or the method of the analysis

Among these input data, measured or estimated shear wave velocity will be discussed in section 3.3, under geophysical and geotechnical site characterization. Shear modulus reduction curve and damping curves that represent the dynamic properties of the soil layer will be estimated in section 3.4 and input earthquake motions that were used to excite the soil column will be discussed in section 3.5. Site response analysis and parameters that control the analysis will be described in section 2.2.2. First, the geology and seismicity of the study area have been discussed.

In Figure 3-1, numbers in parenthesis are section numbers where related descriptions are given. The total stress analysis have been conducted for the reason that the site characterized by deep water table.

3.2 Geology and Seismicity of the Study Area

3.2.1 Description of the Study Area

3.2.1.1 Location

The study area, formerly known by the Nazreth and currently by Adama, is located about 100 km southeast of Addis Ababa. Adama roughly outlined by the geographical coordinates of 8° 30' 46.081" to 8° 35' 39.146" latitude, and 39° 16' 21.305" to 39° 20' 10.274" longitude. The city is the Oromia region's largest urban area with a population exceeding 324 thousand inhabitants (Central Statistical Authority, 2012) and is categorized in the East Shoa Zone.

Adama is a modern city crossed by a major national trunk road and a railway line leading to the port city of Djibouti. All these natural and manmade attributes make Adama and its

surroundings a base for investment in several sectors, such as hotels, recreation centers, small and heavy industries, etc. For this reason, Adama is considered as one of the fastest-growing cities of the country. Furthermore, pressure from other natural developments, the staggering population growth of the country being a primary one, continue to force rapid implementation of large-scale engineering infrastructure works such as mass settlement, water supply, power generation, etc.

3.2.1.2 Geomorphology

In general, the entire area, in which Adama is located can be characterized as a flat landscape surrounded by ridges. Different geomorphologic processes have occurred in the area. These are production, movement and deposition of sediments. The primary driving forces for these processes are rain splash, wind erosion and flooding etc. These factors influence and greatly impact modern geomorphology and processes. For this reason, the plain land is covered by thick lacustrine sediments and reworked volcanic rocks. In contrast, the ridges are made of volcanic rocks. Sediments deposited are mostly of lacustrine and fluvial origin and are intercalated with volcanic extrusions. In sum, the landscape of Adama city consists of mostly a flat land covered with sediments and surrounded by ridges.

3.2.2 Regional Geology

Adama is located in the northern Main Ethiopian rift (MER); the dominant formation appears to be loose Quaternary deposits (Wolfenden et al., 2004; Furi et al., 2011).

The Main Ethiopian Rift comprises the Northern, Central, Southern MER, and Wonji fault belt (WFB) system. Several deformations due to faulting affected the rift floor of the MER along the Wonji fault belt (WFB) (Wolfenden et al., 2004). The study area is found within this broad range of faulting structures and WFB systems.

The Wonji fault belt (WFB) was formed some 2 My ago, which is a recent development in terms of geological time. There are four WFB segments near the study area Gedems, Boseti, Kone and Fantale–Dofen. The WFB is the youngest feature of MER which responsible for active faulting and volcanism in the floor of the rift (Mohr, 1963; Boccaletti et al., 1998).

The topography of the Adama is mainly flat and predominately constituted by lacustrine sediments, and the remaining parts are covered by ignimbrite, ash flow tuffs and unwelded tuffs, rhyolite domes and flows, and basalt (Alula, 1992). The Nazreth and Wonji groups topographic highs such as Mt. Bosset, and near palace and Mt Dengrotio area are underlain

by rocks of Nazreth groups consisting of ignimbrite, trachytes & ryolites and Mt Battu Deggaga. are underlain by rocks of Wonji groups consisting of Pleistocene- recent basalt can be observed with an age from Neogene to Quaternary in the study area as shown in Figure 3-2.

Alula (1992) divided the Nazreth-Dera area regional geology into eight major units: Eastern Margin Unit (EMU), Dera-Nazret Unit, Keleta Unit, Boku Unit, Dera-Sodere Unit, Gedemsa Unit and Melkasa Unit.

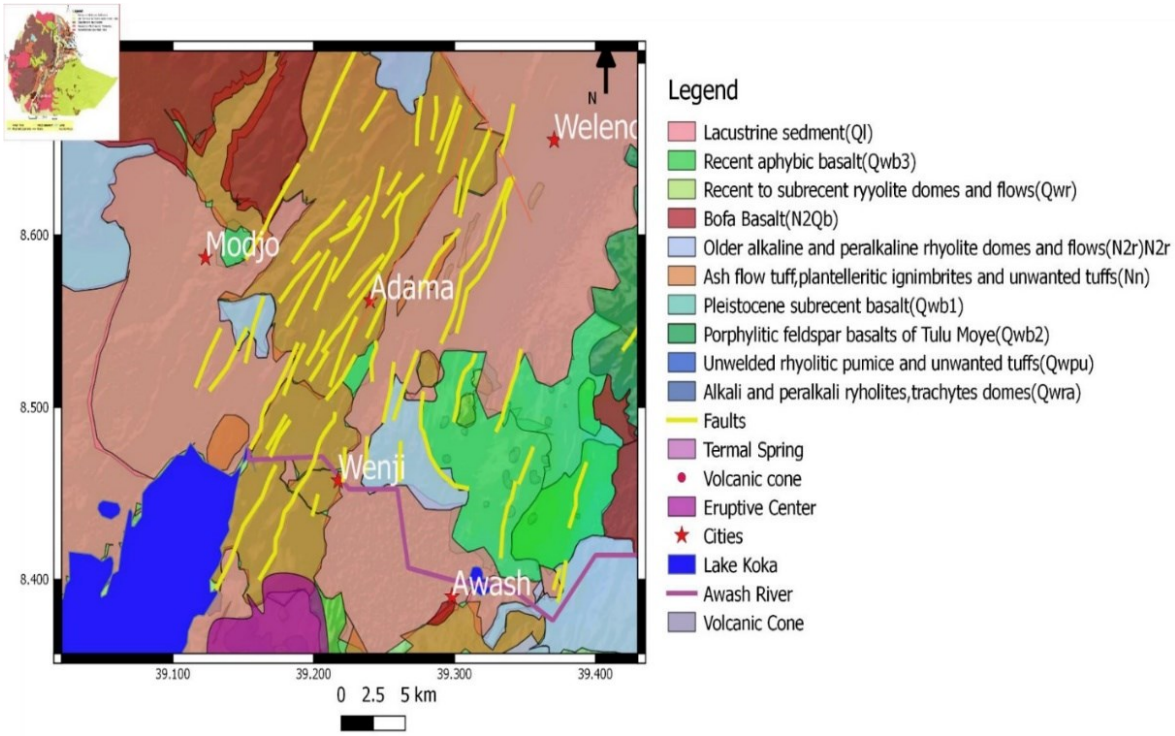

Figure 3-2: Geology of the study area (Alula, 1992).

3.2.3 Geological Soil Classification

Most soils of Adama and its environs soils are alluvial, residual, and lacustrine soils.

3.2.3.1 Alluvial soils

Alluvial soils are aggrading deposits of gravel and clay by a stream issuing from a hill onto a surface or valley floor. Getahun (1987) summarized the Holocene veneer of alluvial sediments in Metahara and Abadir as 40 m thick and in Arerty as 20 m thick.

3.2.3.2 Residual soils

Residual soils are formed in situ by mechanical and chemical decomposition of parent rock on which it lies. In the study area, residual soil occurs around Mechara, Gololcha, Rimeti,

and Gadulo derived from sandstone, and at Chole the source rock is completely a weathered basalt. The residual soil that occurs around Mechara, Gololcha, and Gadulo is reddish, less dense, dry, fine to medium-grained, less plastic sandy soil whereas the residual soil around Chole (Hagere- Sernay) is red, moderately dense and firm, massive, slightly moist, fine to medium-grained and moderately plastic silty/clay soil.

3.2.3.3 Lacustrine sediments

Lacustrine soils occupy the areas northeast of Daubreeite, between Mojo and Koka, between Nazareth and Welenchiti, Wonji, Dera, and Abura. In the Wonji area, it is about 50 m thick clayey at the top and sandy to gravel and pebble rich sand at the bottom. At the Wadecha area, the lacustrine sediment is about 62 m thick and composed of coarse sand with pebbles. In the Dera area, the lacustrine sediment comprises of fined-grained clayey sand. The lacustrine sediments in the rift proper comprise clay, silt, tuff, travertine, diatomite with intercalation of pumice. They are deposited from extensive lakes during Pleistocene pluvial, and are Pleistocene to Holocene in age. They are exposed in Nazareth, Welenchit, Wonji, and Koka up to Goriya Mountain, having a thickness ranging from 30-40 m. The thickness of lacustrine sediments is about 200 m around Dera, and 41 m around Wadecha area, northeast of Debrezeit (Getahun, 1987). About 40 hand dug wells, and 30 bore wells have been drilled in different places of the Wonji area. In this part of the study area, about 50 m thick lacustrine deposit with clay and silt at the top, sandy to gravel, and pebble at the bottom were reported.

3.2.3.4 Volcanic ash

Volcanic ashes are products of quaternary volcanic. It is mainly exposed around Methara and Melka Djilo. It is yellowish in color, soft (less consistent), has low density, dry, massive, fine-grained with coarse particles, less plastic volcanic ash.

The major part of the study area is topographically flat and is covered by lacustrine sediments. Whereas some parts are covered by ignimbrite, ash flow tuffs and unwelded tuffs, rhyolite domes and flows, and basalt unit.

The thickness of the lacustrine sediments reaches up to 40 m in the eastern and South eastern parts. This unit covers about 60% of the area. The rhyolite domes and flows are exposed in the central and northern parts of the study area. This unit covers a small part of the study area (about 15%). Ignimbrite, Ash flow Tuffs and Unwelded Tuffs are exposed in the

southern and northern parts of the study area. This unit covers up to 15% of the total area. The basalt unit is exposed in the southern part of the study area, and this unit covers the smallest part of the study area, 5% (Getahun, 1987).

3.2.4 Water Level Depth

The depth of the water level in the study area is deep. Depth to the water table is reported to be approximately 100 m below ground level as shown in Table 3-1. Hence, a total stress site response analysis is possible because the depth of water level is deep.

Table 3-1: Boreholes in the Adama area (Getahun, 1987)

Site name	Altitude (masl)	Year	UTM_E	UTM_N	Well depth (m)	Ground water table (m)
Nazreth Tankegna	1,640	1953	531000	946200	128	108.0
Nazreth ETCA	1,620	1957	530000	943000	205	116.0
Nazreth WSSA	1,720	1959	532500	950500	199	172.7
Nazerath Itegu hotel	1,650	1961	536000	944200	120	100.0
Nazerath Military camp	1,600	1969	535100	952300	128	108.0
Nazreth ETCA	1,620	1997	530000	943000	187	116.0

3.2.5 Seismic Hazard of Adama City

The Ethiopian rift System, which is part of East African Rift system, passes through the middle of the country, making it one of the most seismically active regions in the world. Thus, significant and damaging earthquakes have been reported and recorded in the past in this region. Of these, the 1906 Langano earthquake with magnitude 6.8 , the 1961 Kara Kore earthquake magnitude 6.4, which caused damage to manmade structures (destroyed the town of Majete) and alterations in the landscape, and the 1969 Serdo earthquake magnitude 6.5 are significant ones (Kebede and van Eck, 1997).

Adama has been struck by a moderate earthquake of 5.0 magnitude in 1993, which has caused several adobe buildings to collapse and was also felt as far as Debre Zeit and Addis Ababa (Asfaw, 1998). Several codes have been discussed to get the PGA value of the study area.

3.2.5.1 Ethiopian Building Code Standard, EBCS 8, 1995

The code has made an improvement over previous codes (CP1-78 and ESCP1-83) based on new recorded earthquakes and an expanded earthquake database in the horn of Africa region.

Although an attempt has been made to address the site-soil effects, it is still failing to capture all site-soil classes in the current codes. This code defines four seismic hazard zones which are based on return periods of around 100 years (corresponding to a 50% probability of exceedance in 50 years) in contrast with a 475 years return-period which is adopted by international codes (Worku, 2011). According to the hazard map, each seismic zone of 1 to 4 is assigned a constant bedrock acceleration, a_g, of 0.03g, 0.05g, 0.07g or 0.1g, whereas zone 0 is considered seismic free. Adama, the study area, located at 8° 30' 52.1172" N and 39° 16' 9.3252" E, belongs to Zone 4 with a_g = 0.1g.

The code in itself is now obsolete and the third generation of Ethiopian seismic hazard maps was released in 2015 as basis for updated seismic provisions of ES EN 1998:2015-1. Most of the buildings prior to the updated version designed with peak ground acceleration by almost half as compared to the current seismic code, remedial measures such as retrofitting might be needed.

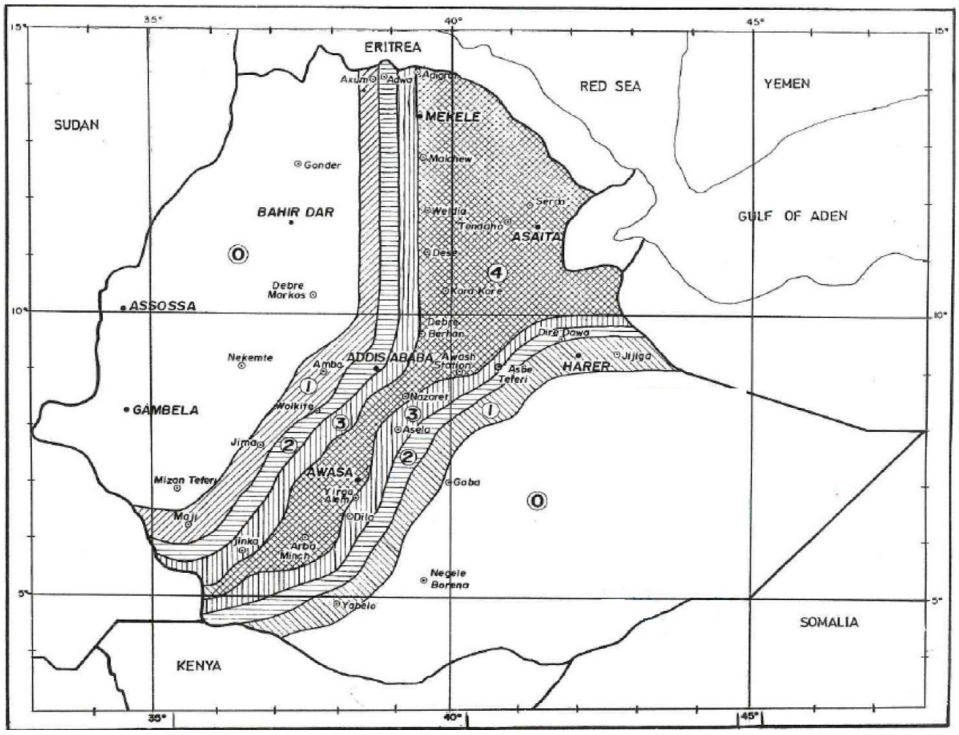

Figure 3-3: Seismic hazard map of Ethiopia as per EBCS-8 for 100-year return period EBCS 8 (EBCS-8, 1995).

3.2.5.2 Ethiopian Building Code Standard, ES EN 1998:2015

The current seismic code is based on the Eurocode, which has provided new seismic coefficients and a site classification system. ES EN 1998:2015 provides peak ground

acceleration (PGA) map for 10% probability of exceedance in 50 years (i.e., return period of 475 years). The seismic hazard map divides the country into five zones; the hazard in these zones is given based on the ratio of the design bedrock acceleration to the acceleration of gravity (α_o) and indicated in Table 3-2. It also provides the seismic hazard maps shown in Figure 3-4.

Table 3-2: Bedrock Acceleration Ratio α_o (ES EN 1998:2015)

Zone	5	4	3	2	1	0
$\alpha_o=a_g/g$	0.20	0.15	0.10	0.07	0.04	0

The seismic code provisions are thought to overcome some of the limitations of the previous code, though it has its drawbacks and limitations. There are significant discrepancies between the values obtained from PGA maps and tabular listing. The study area, Adama is one such place, the value read from the hazard map is 0.08g, while it belongs to zone 4 with a PGA of 0.15g in the table.

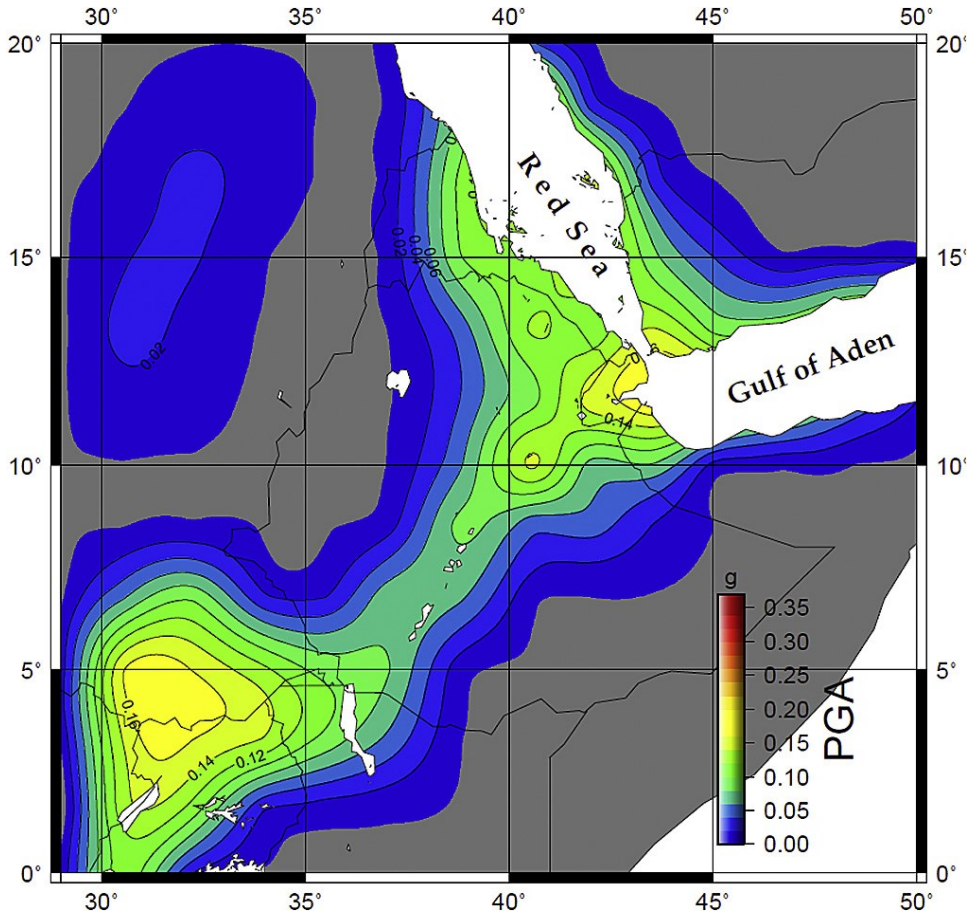

Figure 3-4: Seismic Hazard Map along the Horn of Africa for 475-year return period (ES EN 1998:2015).

3.2.5.3 The Global Seismic Hazard Assessment Program (GSHAP)

The GSHAP was designed to provide a useful global seismic hazard framework and serve as basis for further detailed studies in many national or regional agencies. The report accompanies the publication of the GSHAP, compiled by joining the regional maps produced for different GSHAP regions and test areas.

The GSHAP depicts Peak Ground Acceleration (PGA) with a 10% chance of exceedance in 50 years, corresponding to a return period of 475 years. The map colors chosen to delineate the hazard roughly correspond to the actual level of the hazard. The warm colors correspond to high levels of hazard and the cool colors correspond to low levels of hazard.

The hazard map extracted from GSHAP data is shown in Figure 3-5. The Adama's PGA value can be read as 0.15g from the GSHAP hazard map and this PGA value is employed in the subsequent sections of this study.

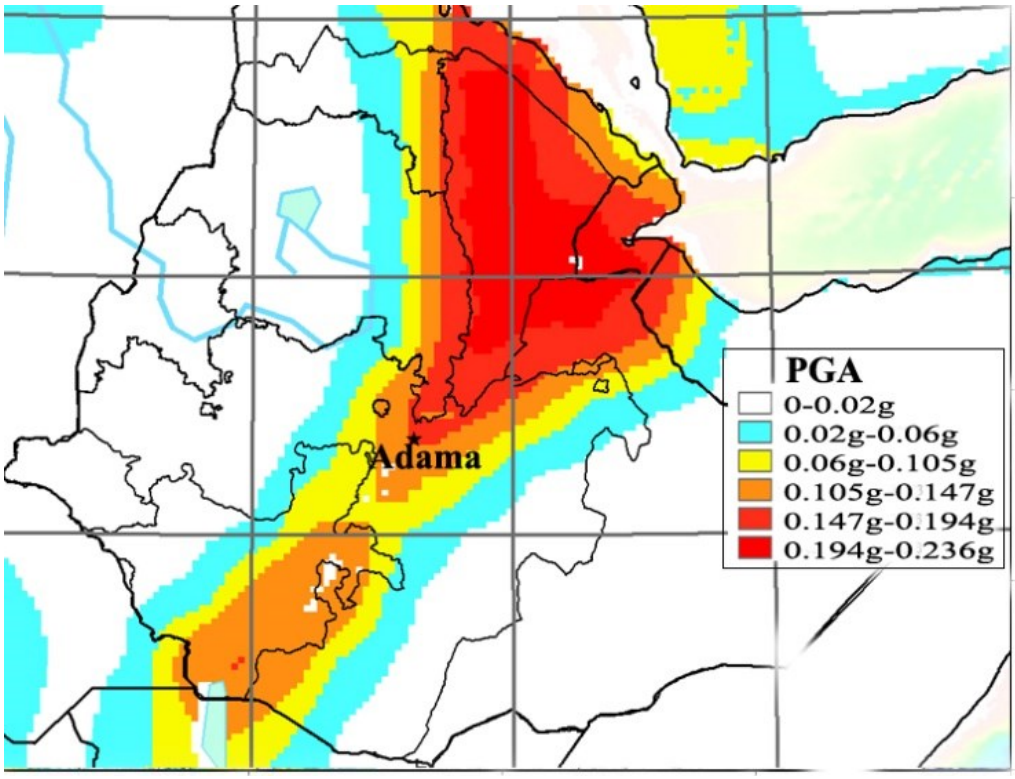

Figure 3-5: Seismic hazard map of Ethiopia based on the GSHAP data for a return period of 475 years (Giardini, 1999).

3.3 Geophysical and Geotechnical Site Characterization

Characterization of the selected sites of Adama city is done using the primary geophysical data and geotechnical data collected from various organization and the results are discussed here.

3.3.1 Data from Geophysical Investigation

3.3.1.1 Equipment and field procedure

The necessary equipment to undertake the seismic refraction and MASW surveys are as follows: the seismograph, hammer and strike plate, horizontal shear wave source, geophones, spread cable, battery, and trigger cable.

Seismograph

The seismograph is, fundamentally, a device that gives the time of the impact moment and the times of the arrivals of the waves at each geophone. In this study, refraction and MASW data were recorded using a 24-channel Geode seismograph manufactured by Geometrics Inc shown in Figure 3-6. The Geode is controlled by a personal computer running Seismodule Controller Software (SCS).

Figure 3-6: Geode Seismograph.

Geophones and spread cable

The arrivals of the various seismic waves from the impacts are detected by geophones placed in a straight line through the impact points. The geophones consist of a bar magnet which is surrounded by a coil. The coil is free to oscillate either along a vertical axis or horizontal

axis that depends on the target of interest (P-wave or S-wave), and the magnet is anchored to the housing of the geophone. The arrivals of the various seismic waves from the impacts are detected by geophones placed in a straight line through the impact points. The geophones transform the mechanical energy into a small electric current, which is transmitted by cables to a recording unit where it is amplified before the signals are recorded directly. Geophones equipped with spikes have to be firmly planted into the ground to increase the reception capacity. If necessary, the uppermost loose soil layer should be removed. Besides, the disturbance due to wind is reduced if the geophones are placed in small holes. The cable which connects geophones to the seismograph is known as a spread cable and shown Figure 3-8. The seismograph has one takeout cable to connect geophones. The cable has 24 takeouts, allowing for a maximum of 24 geophones to be connected at one time. Spread cables carry the geophone current (or ground-motion signal) to the seismograph. Both horizontal and vertical geophones were employed to allow sensitivity for several different types of waves and directions of motion and shown in Figure 3-7.

(a) (b) (c)

Figure 3-7:Geophones (a) vertical (14 Hz) (b) vertical (4.5 Hz) (c) horizontal (14 Hz).

Figure 3-8: Spread Cable.

Hammer and strike plate

In seismic work, the selection of seismic sources depends on the depth of investigation and geological conditions. There are many different energy sources that are used for seismic refraction and MASW surveys, including sledgehammers, mechanical weight drops, explosives, and projectile (gun) sources. For the current survey, A sledgehammer (10 kg) was used to generate the seismic P-waves and MASW. Zero-time for the seismic record is initiated by a switch that is attached with tape along the length of the handle, a few inches from the hammer head. A plastic plate (20×20 cm^2) was used to receive the sledgehammer strikes and to improve the coupling of energy from the hammer to the soil.

Figure 3-9: Hammer and Strike plate.

Horizontal shear wave source

The horizontal polarized shear wave is generated by horizontal hammer impacts of a rigid object on both left and right sides which is coupled to the ground surface. Several different horizontal sources have been used by a number of different workers over the years.

Hasbrouck (1983) describes what is often referred to as a golf shoe (Figure 3-10-a); it is made of steel, has a spike at the base, and has good repeatability. It weighs around 40 kg and thus leads to being difficult to transport during the fieldwork. Additionally, the vertical impact face makes it difficult to swing for a person hitting the source and consequently reduces the data quality and strike-to-strike repeatability.

Various workers have used a wooden beam with steel end caps that are coupled to the ground by parking the front wheels of the field vehicle (pickup) on the top of the beam (Figure 3-10-b). The beam wears out after a few shots which will limit the use of the source for an extended field survey.

Haines (2007) designed a source made of aluminum and weighs approximately 25 kg and was designed to provide a comfortable strike stance for the hammer swinger, which leads to improved repeatability and overall data quality (Figure 3-10-c). It has withstood approximately 10,000 impacts and remains functional. Loriaux (personal communication, August 21, 2019) designed a source similar to the one in Haines but with a minor modification adding a steel plate which will reduce the stress on the bolt which makes it more durable (Figure 3-10-d).

(a)

(c)

(b)

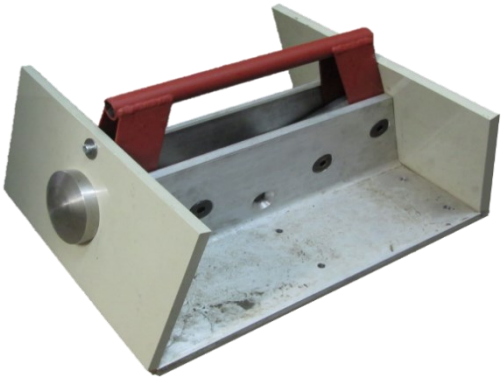

(d)

Figure 3-10: (a) The steel golf shoe source (b) the wooden beam source (c) aluminum source by Haines (2007) and (d) aluminum source by Loriaux.

Source design

I designed the source by utilizing the advantages of the Haines (2007) and Loriaux sources and also considering the locally available materials.

The source was built from a 2-cm thick aluminum plate with 6061-T6 material grade, and was bent to create an L-shape. Holes were drilled on one side of the plate to make contact with a ground surface for the ground-coupling spikes. The holes are counter-sunk on the bottom, to create a depression around the hole for the nuts that attach to the spikes. The other side of the plate provides rigid support and retention for the impact plates.

The impact plates must be made of thicker material in order to withstand a long period of use and exploitation. Although steel has a higher strength than aluminum, aluminum was chosen as the impact plate for the reason that it rings less when struck with a hammer and will avoid an inconvenience that can become more of a major issue over the course of an extended survey. A 10 x 10 x 20 cm aluminum block, machined to shape, has proven effective and long-lasting. These blocks are bolted to the one side of the plate using M16 bolts with class 8.8, in order to facilitate the replacement of the impact plates. A steel shield was introduced between the aluminum plate and impact plate for the reduction of stress. Finally, a CHS with side plate was welded in the steel shield to provide a carrying handle. The source is shown in Figure 3-11.

Figure 3-11: Horizontal shear wave source.

3.3.1.2 Data acquisition

3.3.1.2.1 Refraction acquisition

Seismic refraction data acquisitions for all selected sites were accomplished using a 24-channel Geometrics Geode seismograph. Two different types of geophones were used for collecting seismic-refraction data. P-wave data were collected using an array of 14-Hz vertical geophones; S_H-wave data were collected coincident to the P-wave survey lines using 14-Hz horizontal geophones.

Primarily, 14-Hz vertical geophones were used to acquire the P-wave data. Horizontal shear wave data were acquired using 14-Hz horizontal geophones. The horizontal geophones are horizontally polarized, leveled, and oriented in the same direction to particle motion and orthogonal to the direction of wave propagation during acquisition. The P-wave and S_H-wave were generated using a 10 kg hammer. The hammer struck against a 20 x 20 cm plastic plate for compressional wave acquisition and a source made for this purpose pictured in Figure 3-11 for the horizontal shear wave production surveys.

For S_H-wave surveys, the geophones are aligned parallel to the direction of the hammer swing and perpendicular to the direction of wave propagation (Figure 3-12). In order to enhance the signal to noise ratio, multiple stacks (or hammer blows) were done at each shot

point. In order to decimate P-wave contamination, the two acquired data from the left and right shot will append together, thus constructively interfering with the S_H-wave generation. A total of 10 stacks were made per each shot for P-wave and 10 stacks were made alternately on the left and right side of the S_H source per each shot for S_H-wave. This was found to be sufficient using a signal enhancement seismograph.

As a rule of thumb around 4000 samples per trace is sufficient to acquire the refraction data (Geometrics manual,2016). A recording length of 0.5 sec with a corresponding 0.125 msec sampling interval was used to satisfy the 4000 samples per trace rule of thumb for both P-wave and S_H-wave acquisition. Each profile extends a total spread length of 69 m, and a 3 m fixed geophone spacing was used for both P-wave and S_H-wave survey. Shot points were located at five positions, including near and far offset of 5 m, at 16.5 m and 52.5 m from the first geophone and at the center of the geophone line to account for possible dipping of sub-layers. A summary of data acquisition parameters used in this study is presented in Table 3-3.

Table 3-3: Acquisition parameters for P-wave and S_H-wave.

	P-wave	**S_H-wave**
Source Type	10 kg hammer	10 kg hammer
Stacks	10 times	10 times (each)
Geophone Frequency	14-Hz vertical geophone	14-Hz horizontal geophone
Sample Interval	0.125 msec	0.125 msec
Geophone Interval	3 m	3 m
Offset	±5 m	±5 m
Record Length	500 msec	500 msec

Four seismic refraction profiles were conducted at representative sites of the study area.

Figure 3-12: The typical set-up for shear-wave refraction acquisition.

3.3.1.2.2 MASW acquisition

MASW data acquisitions for all selected sites were accomplished using a 24-channel Geometrics Geode seismograph. Geophones with a natural frequency of 4.5 Hz were used for collecting surface waves data. The surface waves were generated using a 10 kg hammer. The hammer struck against a 20 x 20 cm^2 plastic plate for MASW acquisition. A total of 10 stacks were made per each together with using a signal enhancement seismograph to enhance the data quality. For recording, a sampling rate (fs) of 4000 Hz was used, corresponding to a sampling interval (dt) of 0.5 msec. The total recording time for each measurement (T) was 2 sec. Each profile extends a total spread length of 69 m and a 3 m fixed geophone spacing was used for MASW survey. Shot points were located at three positions and two near offset and one far offset at -10 m, -25 m and 94 m from the first geophone.

3.3.1.2.3 MAM acquisition

MAM data acquisitions for all selected sites were accomplished with Linear and L-shape SPAC (spatial autocorrelation) using Geometrics Geode seismograph. Twenty-four geophones for linear array and eleven geophones for L-shape array with a natural frequency of 4.5 Hz were used for collecting surface waves data and the cultural noises used for surface wave generation. For the data acquisition, the following parameter are used.

Table 3-4: Acquisition parameters for passive surface wave.

Parameter	Setting
Spread configuration	L-shape (L11) and Linear (24)
Array size	50 m (L-shape) and 69 m (Linear)
Geophone interval	10 m (L-shape) and 3 m (Linear)
Total number of geophones	11 (L-shape) and 24 (Linear)
Geophone type	4.5 Hz vertical geophones
Trigger	Manual keyboard trigger
Sample interval	2 msec
Record length	32 sec for each record, A total of 60 records

3.3.1.3 Field tests

Surface wave and seismic refraction field measurements were concurrently carried out at two locations during the summer of 2020. Additional seismic refraction measurements were carried out at two more locations during the spring of 2019. The location of the four sites is shown Figure 3-13.

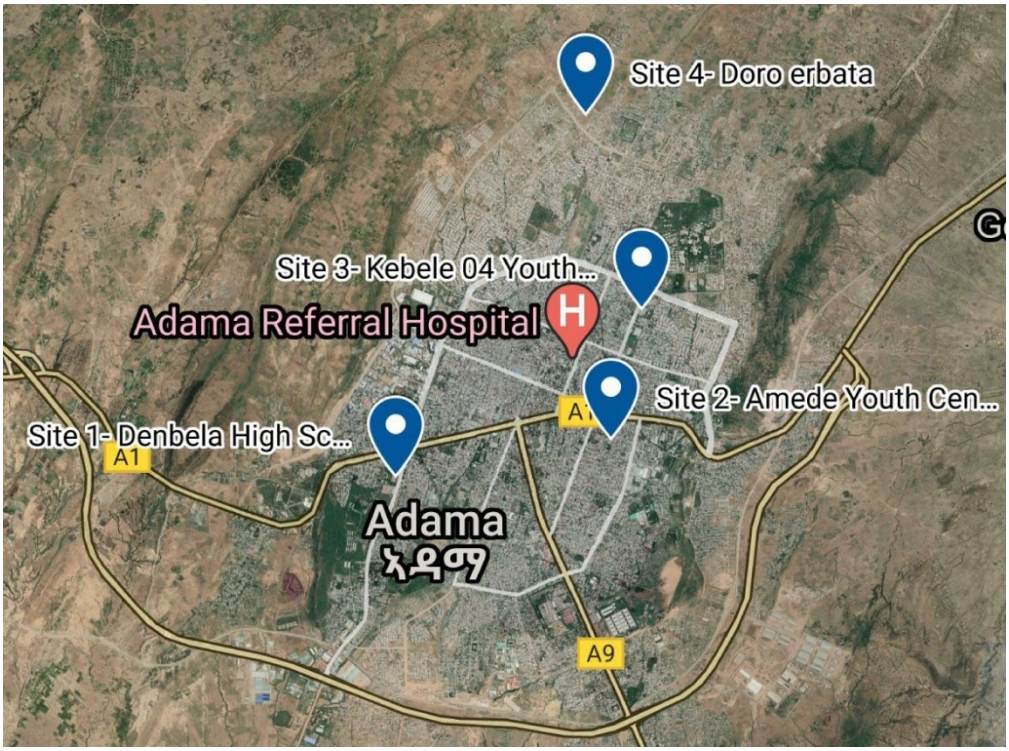

Figure 3-13: Locations of the four sites.

3.3.1.3.1 Site 1: Denbela High School site

Surface wave and seismic refraction field measurements were carried out inside the Denbela High School on the football field in the west of Adama on the 26th of August 2020 and the site is shown in Figure 3-14 . Both seismic refraction (P-wave and S_H-wave) and surface wave (MASW and MAM) data were acquired, and the S_H-wave field measurement was the first in Ethiopia.

Figure 3-14: Site 1: Denbela High School site.

(a) P-wave result

Refraction models were created using two programs within the SeisImager software suite. Pickwin version 5.2.1.3 was used to pick first arrivals and to determine travel-time curves and Plotrefa 3.1.0.5 was used to analyze the travel-time curves and to determine the final velocities. All collected seismic data were analyzed using SeisImager/2D licensed at the Institute of Geophysics, Space Science and Astronomy (IGSSA), Addis Ababa University. The geometry must be set for the data, either during acquisition in the field using the seismograph or in the Pickwin program. The first step in the seismic-refraction processing is identifying and digitally picking the first break seismic arrivals. Figure 3-15 shows that the picking of first arrivals for forward shot using Pickwin software. The first arrival of the P-wave was properly picked with high care and attention.

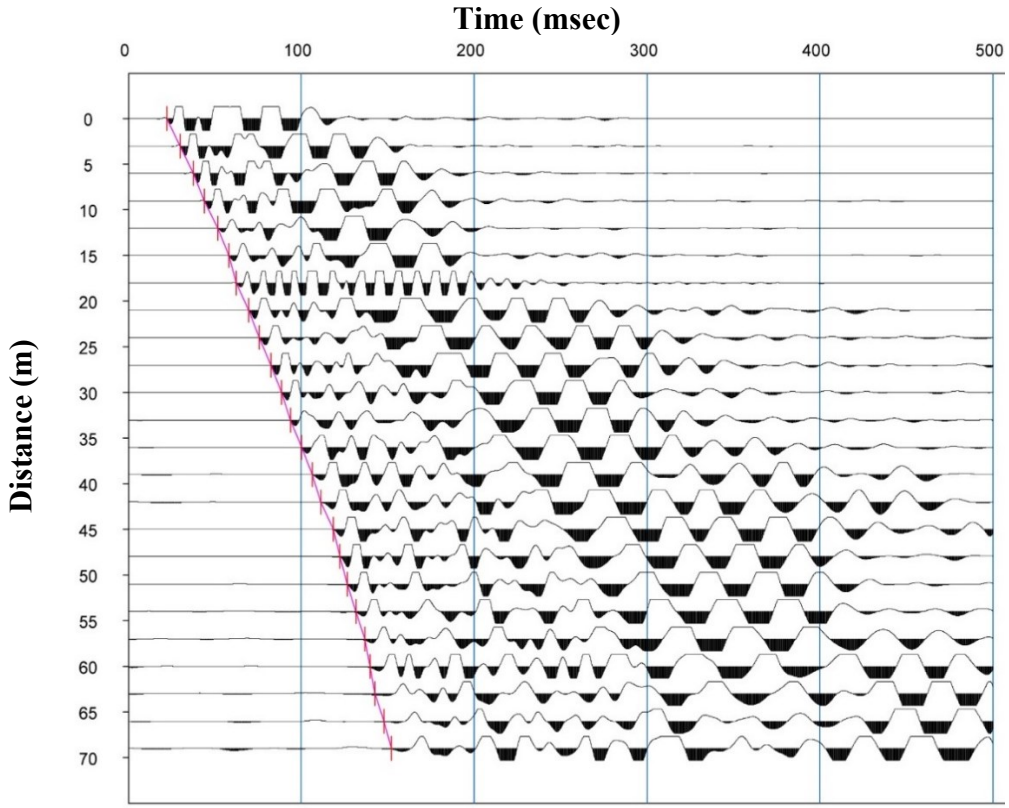

Figure 3-15: First-arrival picks represented by red lines for the shot location at 5 m.

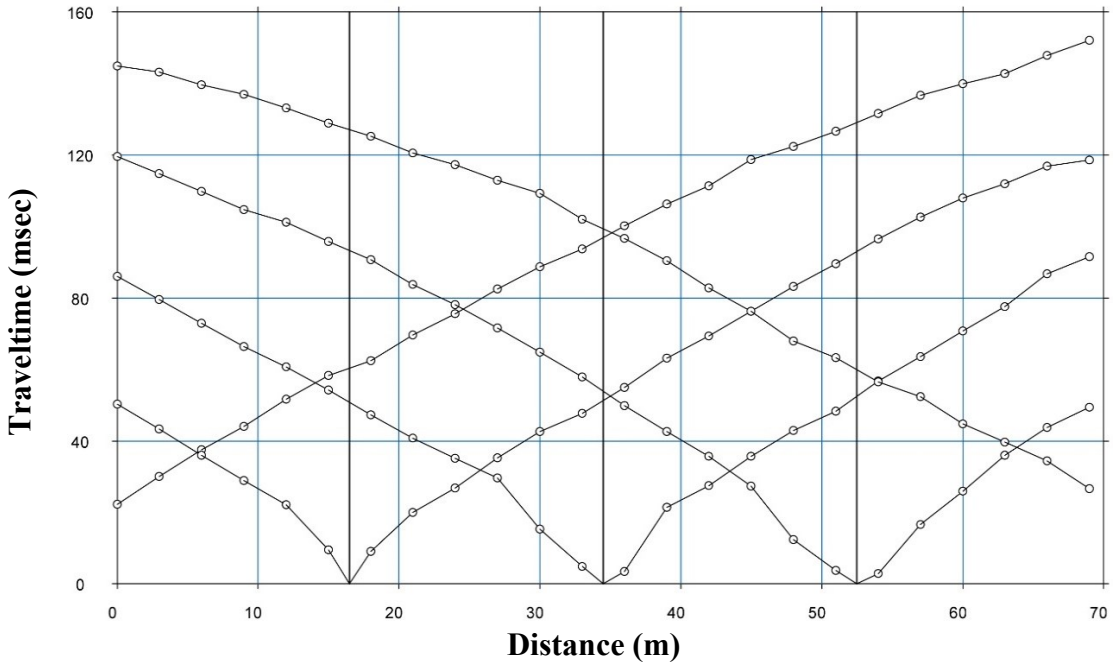

Figure 3-16: Travel time curves of P-wave for all field shots at Site 1: Denbela High School.

All of the picks from the five shots shown in Figure 3-16,were combined to produce the compressional wave velocities of the site. The time-term inversion method was applied to produce the subsurface velocities.

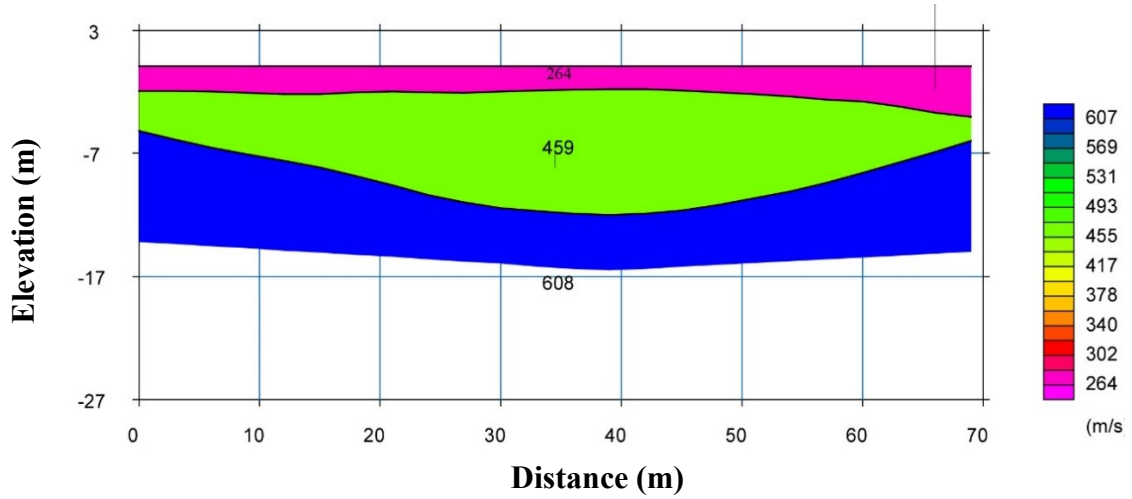

Figure 3-17: P-wave velocity of Site 1: Denbela High School site using time-term inversion.

The results from time-term inversion shown in Figure 3-17 have given three layers The first layer has an average thickness of 2 m and a velocity of 264 m/sec. The second layer has a velocity of 459 m/sec with thickness ranging from 2 to 12 m in the middle of the survey line. The third layer ranges in thickness from 12 to 16.5 m, and the velocity associated with this layer is 608 m/sec. The root mean square **(**RMS) error is 1.21 msec which was less than the recommended limit by the SeisImager manual which is 1.5 msec. The results show that there is a low-velocity soil medium, which is consistent with the corresponding available adjacent boreholes. The site is located between two borehole locations that are both 500 m far from the survey line, the boreholes show a soil deposit up to the depth of investigation (20 m).

(b) S_H-wave result

The left and right shots of S_H-wave were appended together to properly pick the first shear wave arrivals. SeisImager has a tool to append the two shots with transparent copy, and one can see the different colors of these two shots with blue and black colors (Figure 3-18). The first point where the blue and black waves start mirroring each other is the first arrival of S_H-wave. The first arrival of the S_H-wave was properly picked with high care and attention and shown with a red line in Figure 3-18. Plotrefa was used for refraction velocity analyses.

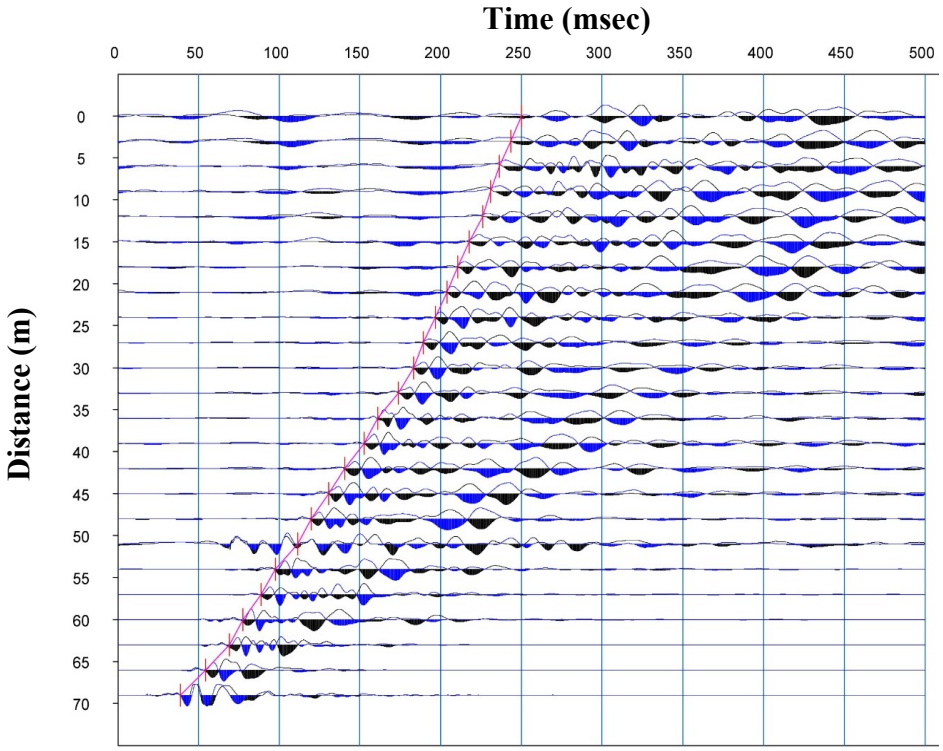

Figure 3-18: Appended data of left and right shots at 74 m from the first geophone.

The travel-time curves of the five shots is shown in Figure 3-19. All of the five shots picks are combined to produce the horizontal shear wave velocities of the site shown in Figure 3-20. The inversion of the S_H-wave is similar to P-wave and the time-term inversion method is applied to obtain the velocity of the layers.

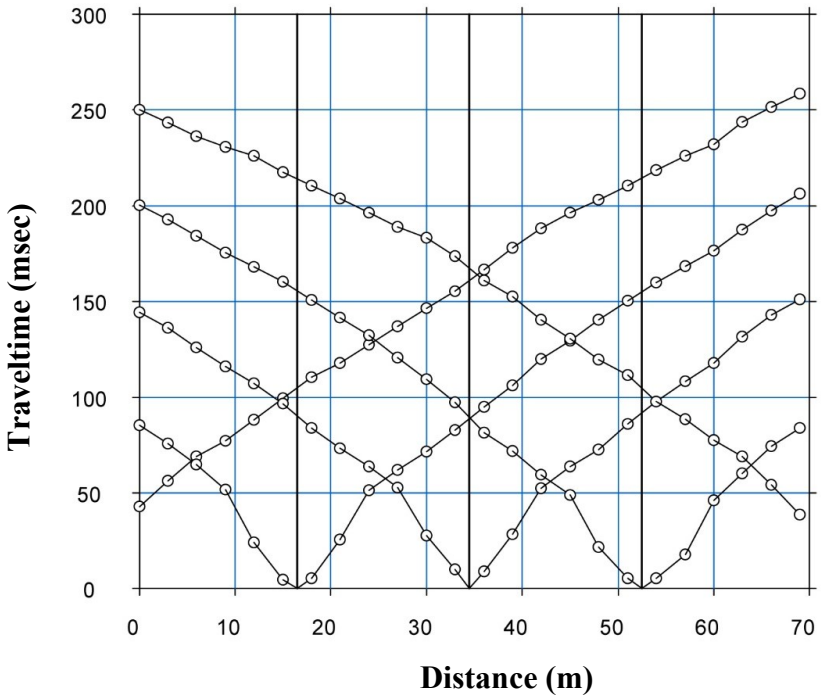

Figure 3-19: Travel time curves of S_H-wave for all field shots at Site 1: Denbela High School.

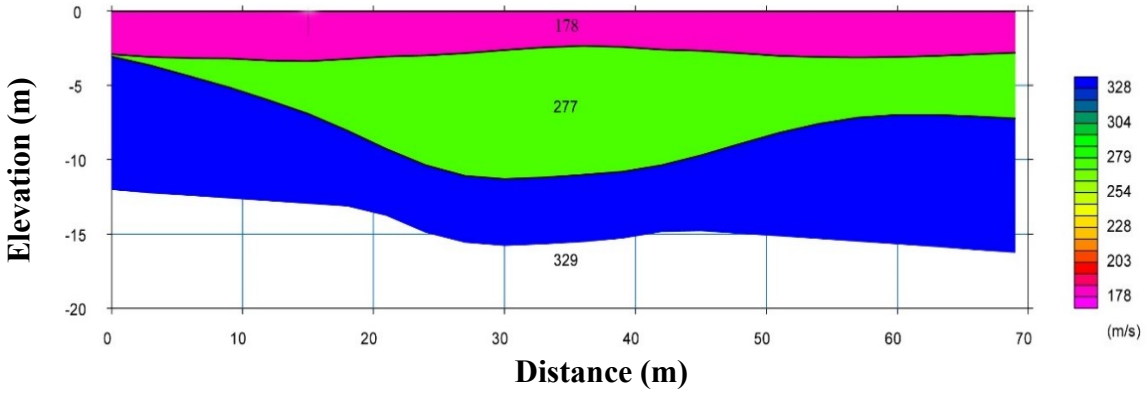

Figure 3-20: S_H-wave velocity of Site 1: Denbela High School site using time inversion.

The results from time-term inversion shown in Figure 3-20 have given three layers and the first layer with an average thickness of 2.5 m and a velocity of 178 m/sec. The second layer has a velocity of 277 m/sec with a thickness ranging from 2.5 to 11 m in the middle of the survey line. The third layer ranges in thickness from 11 to 15.5 m, and the velocity associated with this layer is 329 m/sec. The RMS error was 1.41 msec. The results show that there is a low-velocity soil medium, which is consistent with the corresponding available adjacent boreholes.

(c) Surface wave results

One active (MASW) and two passive (MAM) measurements have been measured on Site 1. The center of the three measurements has been aligned to acquire a deep velocity profile by utilizing the advantages of the three measurements. First, a dispersion curve was extracted from the three surface measurements and combined the individual curves to obtain one dispersion curve with a wide range of frequencies. Pickwin (the surface wave tool) was used for dispersion curve image generation and WaveEq 4.0.1.0 was used for inversion to shear wave velocity.

MASW result

From all offset shots the one with less high-mode energy was selected for dispersion curve extraction.

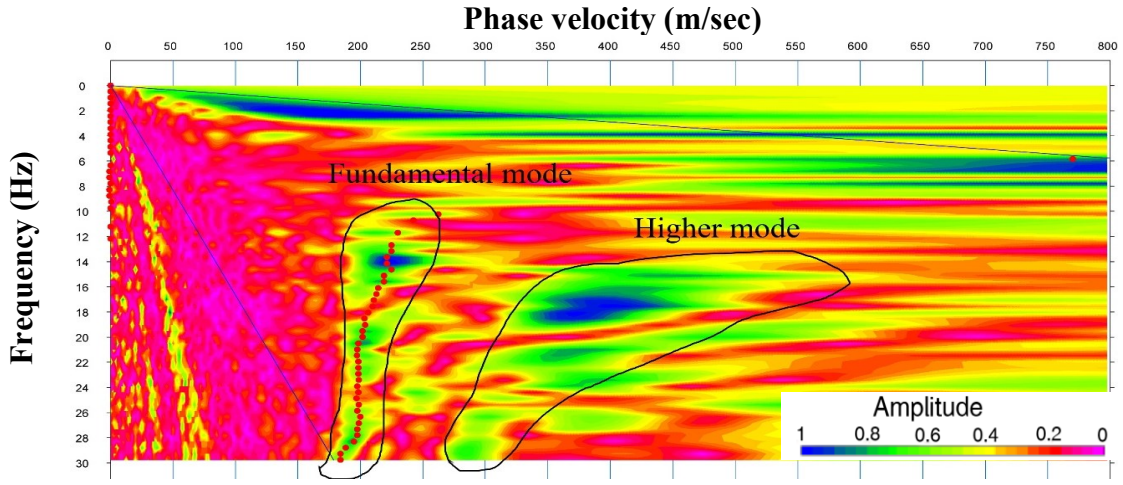

Figure 3-21: Dispersion image of Site 1: Denbela High School using MASW.

As illustrated in Figure 3-21, both fundamental and higher mode appeared on MASW dispersion image. The fundamental mode has a lower velocity than the higher model. The dispersion curve which was extracted from the fundamental mode was used for inversion. SeisImager automatically picks points on the dispersion curve by identifying points with the highest amplitude. The fundamental mode can be picked with confidence between 10 and 30 Hz but between 15 and 18 Hz the amplitude of the higher mode is higher than the fundamental so manual picking was done for this range. The phase velocity shows a little increment with the frequency ranging from 30 to 10 Hz which indicates that at these frequencies the corresponding wavelengths are not long enough to go deeper.

Linear MAM result

A linear array of 24 geophones was used to collect the ambient noise and the dispersion curve extracted from the measurement is shown in Figure 3-22.

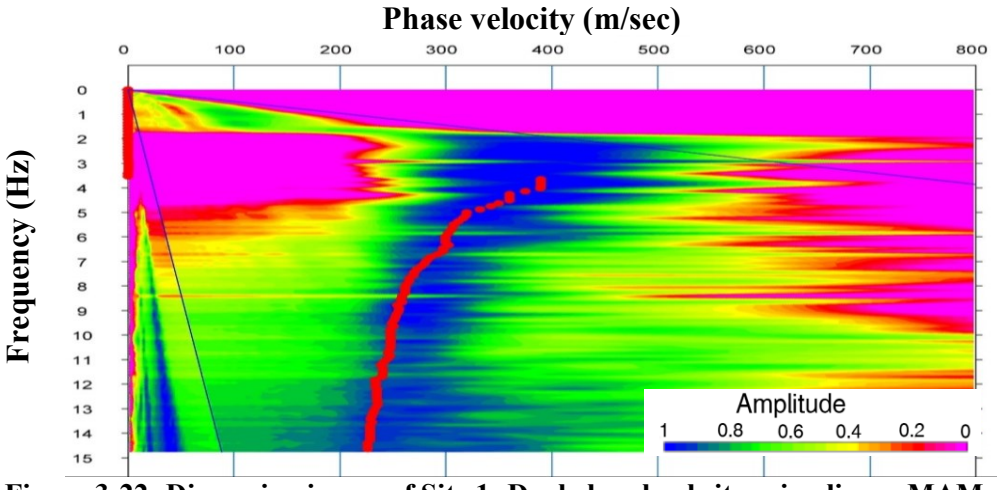

Figure 3-22: Dispersion image of Site 1: Denbela school site using linear MAM.

The fundamental mode can be picked with confidence between 3 and 18 Hz. Automatic picking was applied. The phase velocity is lower at high frequencies and higher at low frequencies. It implies that the soil stiffness increases with depth.

L-shape MAM result

The L-shape is commonly deployed at street intersections to acquire ambient noise from the two roads. An 11- channel L-shaped array with 4.5 Hz geophones was used for this survey. The fundamental mode can be picked with confidence between 2.5 and 11 Hz (Figure 3-23.). The dispersion curve of the L-shaped array was extracted for inversion. The phase velocity is lower at high frequencies and higher at low frequencies. It once again implies that the soil stiffness increases with depth.

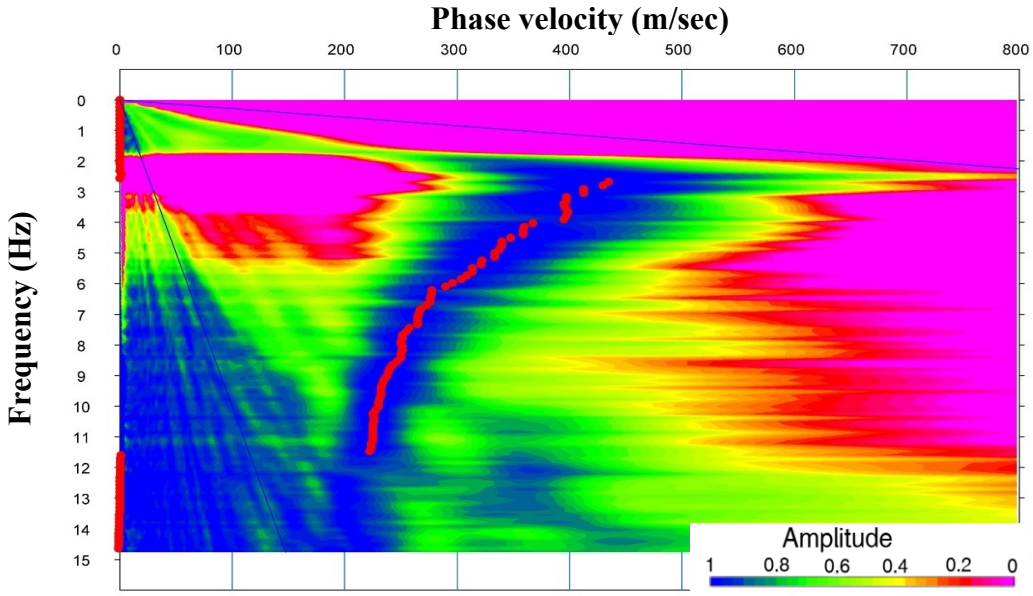

Figure 3-23: Dispersion image of Site 1: Denbela High School using L-shape MAM.

The survey was done by targeting the center of the three arrays to align with one another. The dispersion curves of the three measurements are combined to make one dispersion curve with wide ranges of frequencies. The three dispersion curves were combined by averaging their velocity over a range of frequencies. One can see from the Figure 3-24 that there is a minor difference among the dispersion curves.

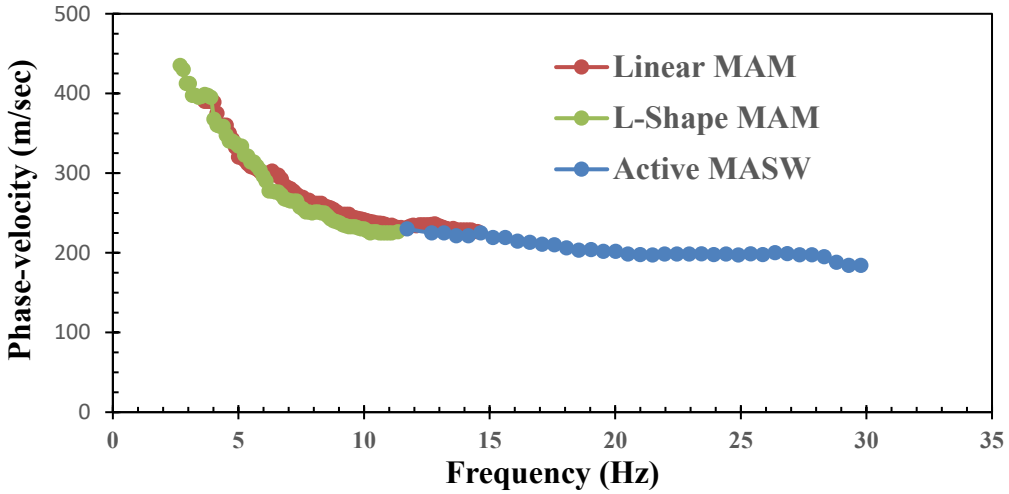

Figure 3-24: Dispersion curve of active MASW, linear MAM and L-shape MAM.

The combined dispersion curve is inverted using an initial model of 15 layers. The layer thickness in the model gradually increased from 1 to 5 m. The root-mean-square (RMS) error between the theoretical and experimental dispersion curves converged to within 1.092% after ten iterations which is less than the recommended limit by the SeisImager manual which is 5%. For the inversion the value of both P-wave velocity and density are needed for each initial model layer and twice the magnitude of shear velocity is used for P-wave and density varies from 1.6 to 2 g/cc from the top layer to bottom. The one-dimensional shear-wave velocity profile is obtained by inversion, which is shown in Figure 3-25.

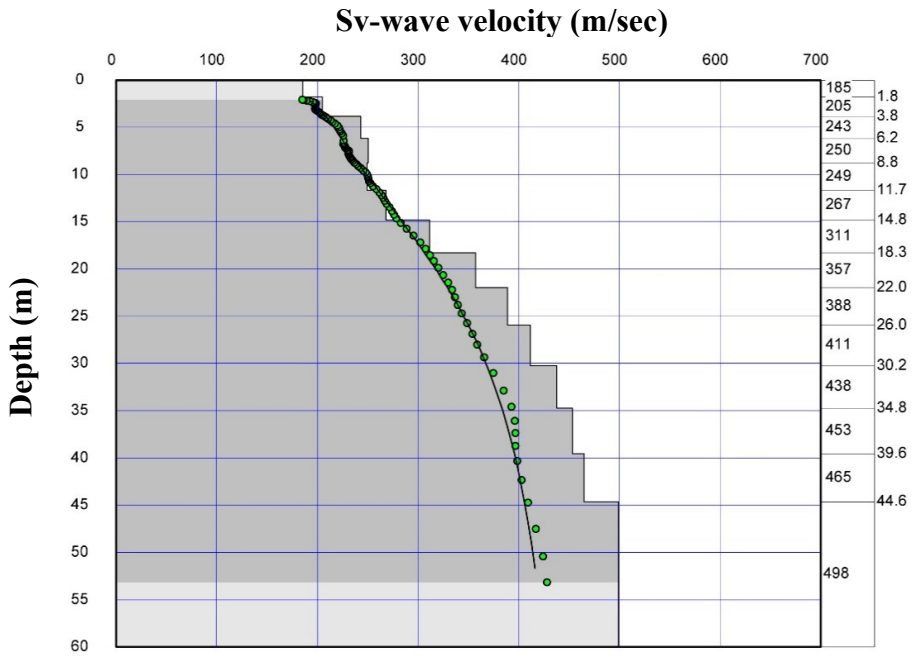

Figure 3-25: Shear wave velocity profiles obtained from the combined dispersion curves.

The velocity of the site increases gradually from 185 to 498 m/sec. The average shear wave velocity over the uppermost 30m of depth (V_{S30}) of the site is 288.6 m/sec and is classified as the site classes C according to the Eurocode 8 and site class D according to the NEHRP. According to the Eurocode 8, the site class C V_{S30} ranges from 180 m/sec to 360 m/sec , which is the range for site class D according to the NEHRP:2015.

The ratio between P-wave and Sv-wave is calculated. In this comparison, the Sv-wave is averaged with the depth level that matches with P-wave. The P-wave and Sv-wave velocities are shown in Figure 3-26.

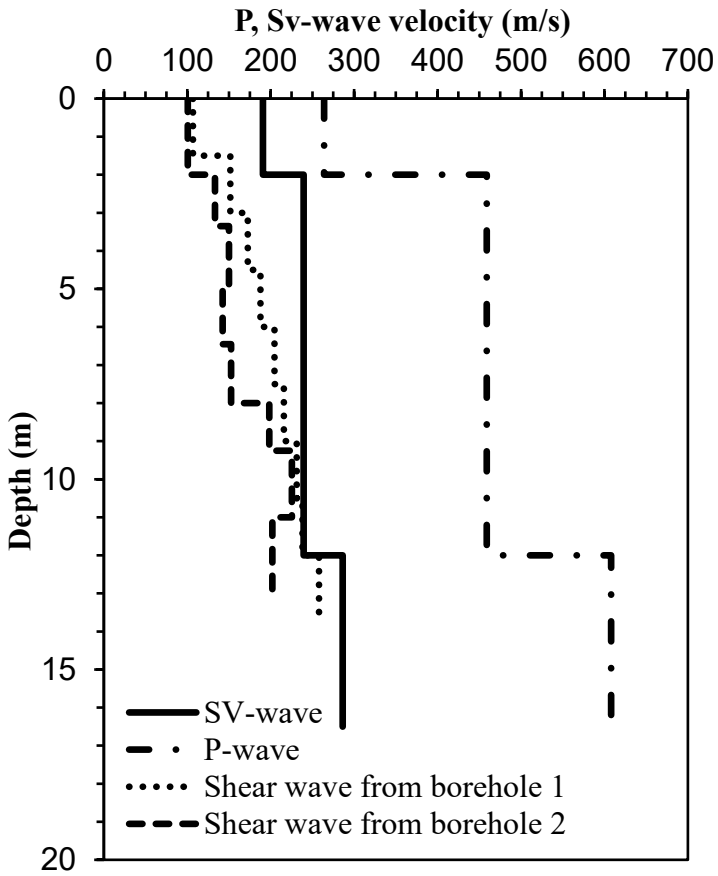

Figure 3-26: P-wave and Sv-wave comparison for Site 1: Denbela High School.

The ratio between P and Sv-waves between 2 and 12 m is 1.917, and the corresponding Poisson's ratio found as 0.315. Between 12 and 16.5 m the ratio is 2.12 with the corresponding Poisson's ratio of 0.35. Two borehole locations were found at the top and bottom of the survey and show that the soil found in that area is sandy silt up to their drilled depths (20 m). The correlated shear wave velocity profiles from the SPT value using the formula on section (3.3.2.1) for the two borehole is shown in Figure 3-26. Acceptable agreement has been found between the correlated shear wave velocity from boreholes SPT

values and the measured shear wave velocity as depth go deeper, borehole one is more agree with the measured shear wave velocity. Silt soil's Poisson's ratio lies with a range of 0.3-0.35 (Sharma et al., 1990). The calculated Poisson's ratio using P-wave and S-wave results lies within this range and agrees with the soil classification results from the borehole logs which classified the soil as silt soils.

The ratio between S_H-wave and S_V-wave is calculated and the S_V-wave is averaged with depth level that matches with S_H-wave. The S_H-wave and S_V-wave velocity is shown in Figure 3-27.

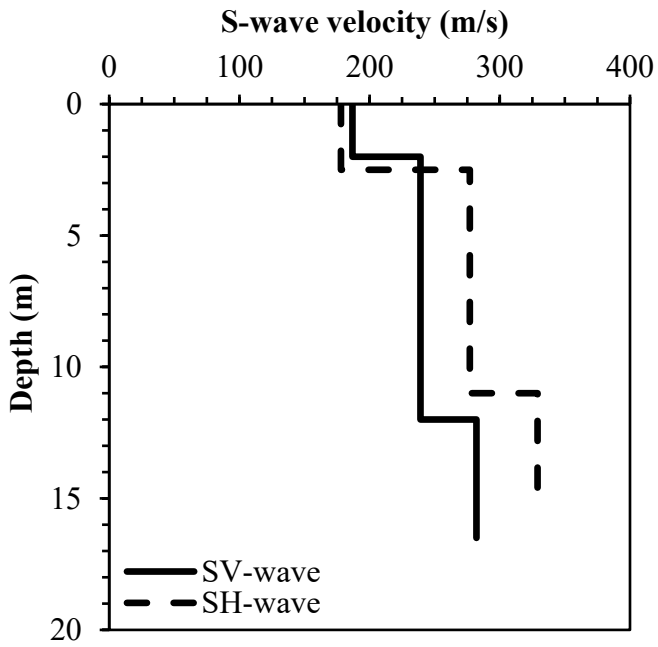

Figure 3-27: Shear wave comparison for Site 1: Denbela High School.

The ratio of S_V- and S_H-wave velocities, is a measure of soil anisotropy. A shear wave velocity ratio of less than unity implies a stiffer soil in the horizontal direction than in the vertical direction. Conversely, when $(S_V/S_H)>1$, the soil is stiffer in the vertical direction. The ratio varies between 0.86 to 1.05. Shear wave measurements at Site 1 indicate higher stiffness in the horizontal direction than in the vertical direction at depths between 2.5 m and 16.5 m.

3.3.1.3.2 Site 2: Amede Youth Center

Surface wave and seismic refraction field measurements were carried out inside the Amede Youth Center on the football field in the east of Adama on the 27th of August 2020. Seismic refraction (P-wave and S_H-wave) and surface wave (MASW and MAM) data were acquired.

The site first arrival picks, travel time curve, P-wave and S_H-wave velocity profile, dispersion image of MASW and MAM and the combined dispersion curve are shown in Appendix A.1-A.8.

The combined dispersion curve was inverted using an initial model with 15 layers. The layer thickness in the model gradually increased from 1 m to 5 m. The root-mean-square (RMS) error between the theoretical and experimental dispersion curve converged to within 1.86% after ten iterations. The P-wave velocity with twice the shear velocity and density vary from 1.6 to 2.1 g/cc were used during inversion.

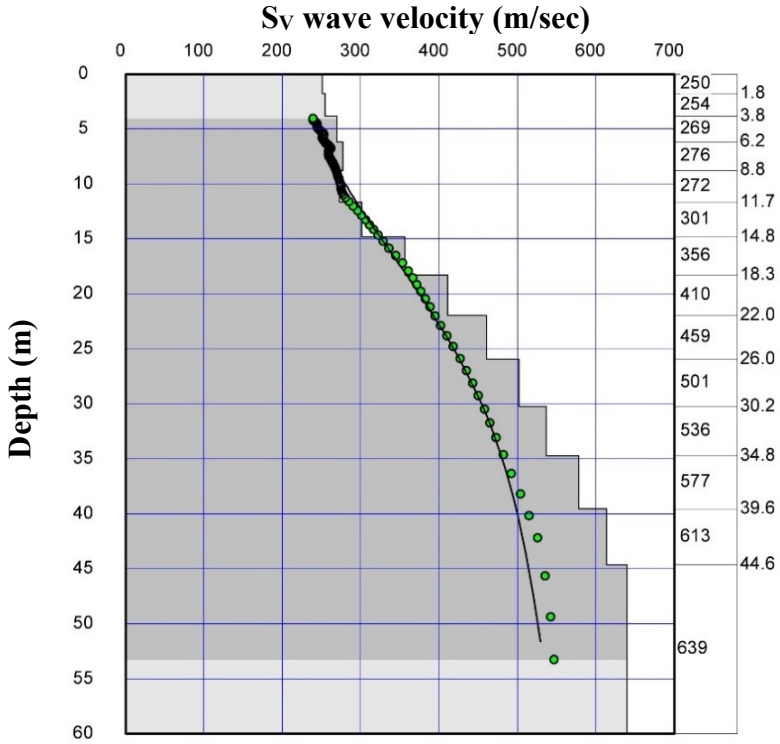

Figure 3-28: Shear wave velocity profiles obtained from the combined dispersion curves.

The velocity of the site increases gradually from 250 to 639 m/sec. The V_{S30} of the site is 332.5 m/sec, the site classifies as site class C according to Eurocode 8 and site class D according to NEHRP:2015.

The ratio between P-wave and S_V-wave was calculated and the P-wave and S_V-wave velocity is shown in Figure 3-29.

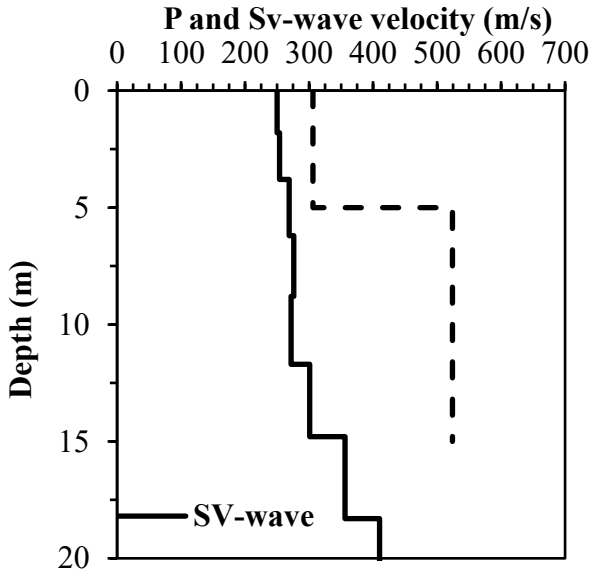

Figure 3-29: P-wave and S_V-wave comparison for Site 2: Amede Youth Center.

The ratio between P and S_V-waves between 5 and 15 m approximately is 1.924, and the corresponding Poisson's ratio is 0.32.

The ratio between S_H-wave and S_V-wave is calculated and the S_H-wave and S_V-wave velocity is shown in Figure 3-30.

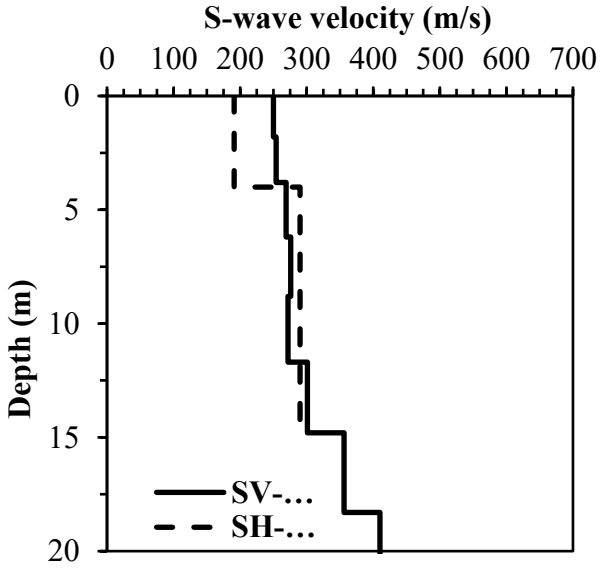

Figure 3-30: Shear wave comparison for Site 2: Amede Youth Center.

The ratio varies between 0.96 to 1.08. Shear wave measurements at Site 2 indicate higher stiffness in the horizontal direction than in the vertical direction at depths between 4 m and 11 m.

3.3.1.3.3 Site 3: Kebele 04 Youth Center

Seismic refraction field measurement was only carried out at inside the Kebele 04 Youth Center on the football field in the east of Adama on the 14th of April 2019. Seismic refraction (P-wave) data were acquired.

The site first arrival picks, travel time curve, P-wave velocity profile are shown in Appendix A.9-A.11.The results from time inversion, have given three layers and the first layer with an average thickness of 3.5 m and a velocity of 326 m/sec. The second layer has a velocity of 572 m/sec with thickness ranging from 3.5 to 10 m at the middle of the survey line. The third layer ranges in thickness from 10 to 14 m, and the velocity associated with this layer is 623 m/sec. The Root mean square **(**RMS) error is 1.35 msec.

3.3.1.3.4 Site 4: Doro Erbata

The Seismic refraction field measurement was carried out on a field near to Doro Erbata in the north of Adama on the 15th of April 2019. Seismic refraction (P-wave) data were acquired. The site first arrival picks, travel time curve, P-wave velocity profile are shown in Appendix A.12-A.14.

The results from time inversion , have given three layers and the first layer with an average thickness of 4 m and a velocity of 353 m/sec. The second layer has a velocity of 556 m/sec with thickness range from 4 to 10 m at the middle of the survey line. The third layer ranges in thickness from 10 to 25 m, and the velocity associated with this layer is 627 m/sec. The Root mean square **(**RMS) error is 0.83 msec.

On Site 3 and Site 4 only P-wave measurements were done and converted to shear wave by using the relationship between the compressional and shear wave:

$$V_S = \sqrt{\frac{(1-2\nu)}{2(1-\nu)}} V_P \tag{3-1}$$

Sharma et al. (1990) suggested silt soil's Poisson's ratio with a range of 0.3-0.35. The geotechnical reports found around these sites stated that the soil is sandy silt. The average Poisson's ratio of sandy silt range is 0.325, was used to calculate the shear wave velocity of the two sites. The converted shear wave results is shown in Table 3-5 with the measured P-wave.

Table 3-5: P-wave and S-wave of Site 3 and Site 4

	Site-3			Site-4	
Depth (m)	**Vp (m/sec)**	**Vs (m/sec)**	**Depth (m)**	**Vp (m/sec)**	**Vs (m/sec)**
3.5	326	142.86	3.5	353	154.69
10	572	250.67	10	524	229.63
15	623	273.02	16	633	277.40

3.3.1.4 Statical extrapolations

For Site 3 and 4, as their depth of measurements did not reach 30 m, V_{S30} had to be estimated by extrapolation. The four sites have similar geology which may be described as lacustrine sediments is shown Figure 3-31.

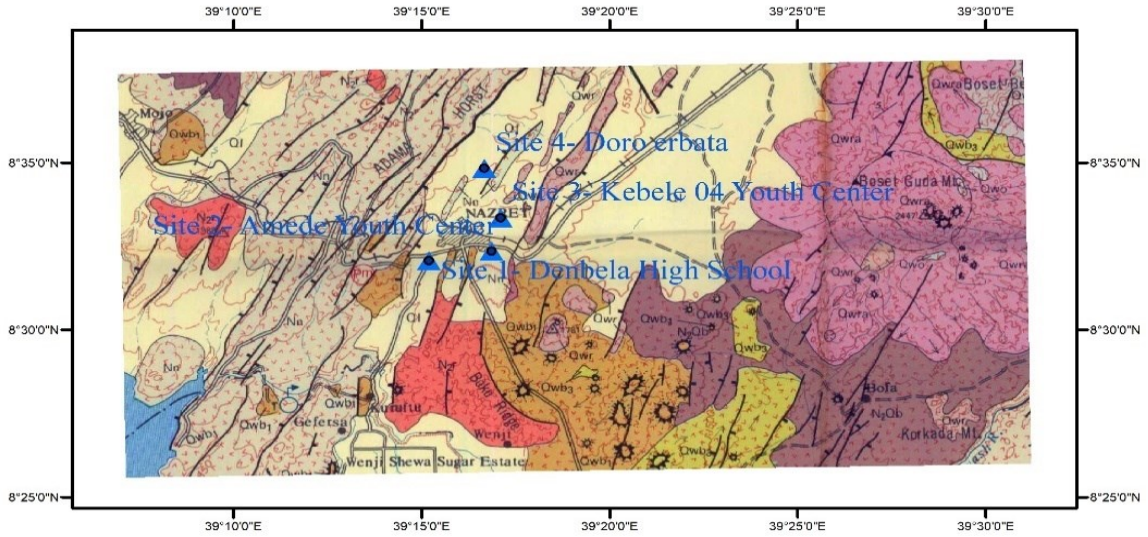

Figure 3-31: Geology of the four sites.

Direct measurements of shear wave velocity or those estimated from geotechnical data do not reach the required depth of 30m. In cases like these, it may be necessary to extrapolate shallow velocity data to estimate the V_{S30}. For the present the study Boore (2004) was used as the study area is also underlain by thick deposits.

Boore (2004) proposed a log–linear extrapolation method which is based on the statistical analysis of 135 boreholes for which the actual depths at least reached 30 m. Boore's model (Eq. (3-2)) involves a statistical correlation between V_{S30} and time-averaged velocity V_{Sd} to a depth d which is the last depth measurement that was made.

$$\mathrm{Log}V_{s30} = a + b \cdot \log V_{Sd} \qquad (3\text{-}2)$$

where a and b are regression coefficients and are presented in Appendix B.1 for depths ranging from 10 to 29 m. As depth increases, the estimated V_{S30} becomes more accurate.

The applicability of Boore (2004) extrapolation was first checked on the first two sites by taking the shear wave velocity up to a depth of 15 m depth and extrapolate this to a depth of 30 m. The V_{S30} obtained from the extrapolation for the two sites are 280.32 and 326.02 m/sec which show only small differences with the measured ones using surface wave which are 288.6 and 332.5 m/sec respectively. The extrapolated shear-wave velocity profiles of the Site 3 and Site 4 are shown in Table 3-6.

Table 3-6: Extrapolated shear-wave velocity profiles of the Site 3 and Site 4 profiles

Site 3		Site 4	
Depth (m)	**Vs (m/sec)**	**Depth (m)**	**Vs (m/sec)**
2	143	2	155
3.5	143	3.1	155
5	251	5	230
10	251	7	230
15*	273	8.8	230
16	278	16*	277
17	278	17	285
18	288	18	295
19	299	19	306
20	303	20	310
21	317	21	324
22	315	22	323
23	327	23	334
24	334	24	341
25	339	25	346
26	348	26	356
27	346	27	353
28	358	28	366
29	353	29	361
30	356	30	365

* indicate the maximum depth of the measured shear wave

The average shear wave velocity over the uppermost 30m of depth (V_{S30}) of the Site 3 and Site 4 are 260 m/sec and 265 m/sec respectively. The sites are classified as the site classes C according to the Eurocode 8 and site class D according to the NEHRP.

3.3.2 Data from Geotechnical Investigation

Geotechnical data was collected primarily from governmental agencies and private firms for various parts of the city. Standard penetration test (SPT) performed at different part of the city were used for determination of shear wave velocity and selection of dynamic properties of the soils. The investigations provided SPT blow counts along with laboratory index test results. The data collected from low-to medium- rise buildings and stadiums geotechnical investigations. The drilling depths varied between 10 to 40 m. Data with investigation depths less than 10m was filtered out. Statical extrapolation has been done for logs that did not reach the required depths of 30 m. A summary of the geotechnical data that was used in the study is shown in Table 3-7.

Table 3-7: A summary of relevant geotechnical reports for buildings and stadium in Adama

Project Name	Consulting Firm (that conducted the investigation)	Depth of Investigation (m)
G+5 Hotel Building	Addis Geosystems Plc	20
Moha Adama G+6 Mixed Use Building	Addis Geosystems Plc	10
G+8 Hotel Building	ARCON Design Build Plc	15
B+G+4 Office Building	ARCON Design Build Plc	10
Adama International Stadium	ARCON Design Build Plc	40
Adama Science and Technology University Stadium	Best Consulting Engineers Plc	10
G+4 Commercial Building	Best Consulting Engineers Plc	10
G+6 Arsema motel Building	Best Consulting Engineers Plc	15
G+7 Oromia Police College	Ethiopian Construction Design and Supervision Works Corporation	10
Horra Trading Plc	Radice Engineering Plc	10
Adama Medical College	SG Consulting Plc	15
Oda mixed use building	Jeroccia Geotechnical Engineering Plc	25
Zubeda Kedir Commerial Building	Ethiopian Institute of Architecture, Building Construction and City Development	15
Jerman Industrail Park	ARCON Design Build Plc	20

Figure 3-32: Location of all the boreholes from Adama city.

Figure 3-32 shows the location of all the boreholes chosen for the study. It can be seen that the density of the explorations was not uniform within a city. The center of the city has the most number of subsoil studies. Four boreholes were combined with geophysical measurements for site response analyses and five soil sites without geophysical measurement were selected for site response analyses to represent the spatial variability of subsoil conditions of Adama.

3.3.2.1 Correlation between SPT and shear wave

The SPT test procedure has inherent variability and uncertainty, the aforementioned problems have been overcome by applying proper corrections for SPT N-values otherwise may result in erroneous which may have serious impacts on the interpretation of the field data.

Martin et al. (1999) suggested the following equation for SPT N-values correction:

$$N_{60} = N_m C_N C_E C_B C_R C_S \quad (3\text{-}3)$$

where N_M = measured standard penetration resistance
C_E = hammer energy ratio (ER) correction factor
C_B = borehole diameter correction factor
C_R = rod length correction factor
C_S = correction factor for samplers with or without liners

An energy efficiency of 60% is considered to correct the blow count which is standard-of-practice across the world. Wair et al. (2012) states that for the purpose of site classification, it is not appropriate to normalize penetration resistance for overburden stress rather, the authors suggest that a correlation formula between shear wave and penetration resistance that includes overburden stress.

Martin et al. (1999) and suggested SPT correction parameters and are summarized in Appendix B.2.

Wair et al. (2012) developed equation to correlate shear wave velocity to the values of SPT blow counts which were corrected for all parameters except overburden pressure. A good overview of earlier work in this area is briefly discussed in the authors work. The following are reviewed in the authors work (Kanai (1966); Shibata (1970); Ohba & Toriuma (1970); Ohsaki & Iwasaki (1973); Ohta & Goto (1978); Imai & Tonouchi (1982); Seed et al. (1983); Sykora & Stokoe (1983); Lin et al. (1984); Jinan (1987); Lee (1992); Dickenson (1994); Sisman (1995); Iyisan (1996); Jafari et al. (1997); Pitilakis et al. (1999); Kiku et al. (2001); Jafari et al. (2002) and Hasncebi & Ulusay (2007)).

Wair et al. (2012) presented shear wave correlation equations based on combinations of N_{60}-value, effective stress, and geologic age for specific soils types (i.e., Clays & Silts, Sands and Gravels) or grouped together as All Soils and all sets are shown in Table 3-8.

Table 3-8: Recommended SPT–stress–V_S correlation equations (Wair et al.2012).

Soil Type	Shear Wave Velocity for Quaternary Soils (m/s)	Age Scaling Factors	
		Holocene	Pleistocene
All Soils	$30\ N_{60}^{0.215}\ \sigma'_v{}^{0.275}$	0.87	1.13
Clays & Silts	$26\ N_{60}^{0.17}\ \sigma'_v{}^{0.32}$	0.88	1.12
Sands	$30\ N_{60}^{0.23}\ \sigma'_v{}^{0.23}$	0.90	1.17
Gravels – Holocene	$53\ N_{60}^{0.19}\ \sigma'_v{}^{0.18}$	-	-
Gravels – Pleistocene	$115\ N_{60}^{0.17}\ \sigma'_v{}^{0.12}$	-	-

σ'_V is measured in kPa.

Table 3-9: Summarizes corrections and correlations of the five selected profiles.

(a) Site 5 (G+8 Hotel Building)

SPT sample number	Depth (m)	Measured N ER(55%)	C_E	C_B	C_R	C_S	N_{60}	V_s (m/s)
1	1.5	14	0.917	1	0.8	1	10.27	106.80
2	3	28	0.917	1	0.85	1	21.82	151.55
3	4.5	25	0.917	1	0.95	1	21.77	172.49
4	6	24	0.917	1	0.95	1	20.90	187.81
5	7.5	26	0.917	1	0.95	1	22.64	204.48
6	9	24	0.917	1	1	1	22.00	215.70
7	10.5	27	0.917	1	1	1	24.75	231.20
8	12	25	0.917	1	1	1	22.92	238.15
9	15	32	0.917	1	1	1	29.33	266.74

(b) Site 06 (G+5 Hotel Building)

SPT sample number	Depth (m)	Measured N ER(55%)	C_E	C_B	C_R	C_S	N_{60}	V_s (m/s)
1	3.5	29	0.917	1	0.85	1	22.60	160.17
2	5.5	39	0.917	1	0.95	1	33.96	198.37
3	8.3	34	0.917	1	0.95	1	29.61	221.07
4	11.6	24	0.917	1	1	1	22.00	233.95
5	14.7	26	0.917	1	1	1	23.83	255.83
6	17.75	28	0.917	1	1	1	25.67	275.19
7	19.5	25	0.917	1	1	1	22.92	278.18

(c) Site 07 (Adama International Stadium)

SPT sample number	Depth (m)	Measured N ER(55%)	C_E	C_B	C_R	C_S	N_{60}	V_s (m/s)
1	1.5	14	0.917	1	0.8	1	10.27	106.80
2	3	13	0.917	1	0.85	1	10.13	133.02
3	4.5	26	0.917	1	0.95	1	22.64	164.41
4	6	17	0.917	1	0.95	1	14.80	177.12
5	7.5	16	0.917	1	0.95	1	13.93	188.28
6	9	16	0.917	1	1	1	14.67	201.34
7	10.5	16	0.917	1	1	1	14.67	211.52
8	12	19	0.917	1	1	1	17.42	227.30
9	13.5	37	0.917	1	1	1	33.92	264.34
10	22.15	100	0.917	1	1	1	91.67	327.20
11	26	100	0.917	1	1	1	91.67	339.49
12	28.15	100	0.917	1	1	1	91.67	345.75
13	30	100	0.917	1	1	1	91.67	350.85

(d) Site 08 (Jerman Industrial Park)

SPT sample number	Depth (m)	Measured N ER(55%)	C_E	C_B	C_R	C_S	N_{60}	V_s (m/s)
1	2	13	0.917	1	0.8	1	9.53	120.08
2	4	33	0.917	1	0.9	1	25.71	177.44
3	6	37	0.917	1	1	1	32.22	209.92
4	8	71	0.917	1	1	1	61.83	257.13
5	10	75	0.917	1	1	1	68.75	281.19
6	12	88	0.917	1	1	1	80.67	306.29
7	14	100	0.917	1	1	1	91.67	328.85
8	16	100	0.917	1	1	1	91.67	343.21
9	18	100	0.917	1	1	1	91.67	356.39

(e) Site 09 (Oda Mixed-Use Building)

SPT sample number	Depth (m)	Measured N ER(60%)	C_E	C_B	C_R	C_S	N_{60}	V_s (m/s)
1	10	24	1	1	1	1	24	200.22
2	12	29	1	1	1	1	29	218.09
3	14	28	1	1	1	1	28	224.14
4	18	29	1	1	1	1	29	239.41

3.3.2.2 Statistical extrapolation

Many measurements of shear wave velocity or estimated from geotechnical data do not reach the required depth of 30 m. In cases like these, it may be necessary to extrapolate shallow velocity data to estimate the V_{S30}. For the present study, Boore (2004) was used because the study area was also underlain by thick deposits and it is also checked its applicability by the two sites.

The above extrapolation may be appropriate for sites with relatively uniform soil conditions. In contrast, this may lead to errors for sites with a velocity contrast within the upper 30 m. Geotechnical reports indicate that most of the locations in study area have been characterized by relatively uniform soil conditions with few velocity contrasts at few locations. It is worth using the recommended extrapolation method. Table 3-10 summarizes the extrapolation of five profiles, which are obtained from SPT-Vs correlation.

Table 3-10: Extrapolated shear-wave velocity profiles of five selected geotechnical sites

Site 05		Site 06		Site 07		Site 08		Site 09	
Depth (m)	Vs (m/s)	Depth (m)	Vs (m/s)	Depth (m)	Vs (m/s)	Depth (m)	Vs (m/s)	Depth (m)	Vs (m/s)
1.5	107	3.5	160	3.5	160	2	120	2	196
3	152	5.5	198	5.5	198	4	177	6	198
4.5	172	8.3	221	8.3	221	6	210	8	199
6	188	11.6	234	11.6	234	8	257	10	200
7.5	204	14.7	256	14.7	256	10	281	12	218
9	216	17.75	275	17.75	275	12	306	14	224
10.5	231	20*	278	20	278	14	329	18*	239
12	238	21	302	21	302	16	343	19	277
15*	267	22	300	22	300	18*	356	20	281
16	240	23	312	23	312	19	311	21	293
17	239	24	319	24	319	20	316	22	292
18	247	25	324	25	324	21	330	23	304
19	257	26	333	26	333	22	329	24	311
20	262	27	330	27	330	23	340	25	316
21	272	28	341	28	341	24	347	26	324
22	271	29	336	29	336	25	352	27	322
23	283	30	340	30*	340	26	362	28	332
24	290					27	360	29	327
25	295					28	373	30	330
26	302					29	368		
27	300					30	371		
28	309								
29	303								
30	306								

* indicate the maximum investigated depth

The V_{S30} of the sites are 225 m/sec, 248 m/sec, 236 m/sec, 270 m/sec and 241 m/sec for Site 5, Site 6, Site 7, Site 8 and Site 9 respectively. All sites are classified as the site class C according to the EN 1998:2015 and site class D according to the NEHRP. According to the EN 1998:2015, the site class C ranges from 180 m/sec to 360 m/sec, which is the range for site class D according to NEHRP:2015.

3.4 Shear Modulus Reduction and Damping curves

For the present study, the Darendeli (2001) model was used for the reason that it considers various parameters such as effective confining stress (σ'_m), plasticity index (PI) and over consolidation ratio (OCR) and can better represent the actual condition than other models.

3.4.1 Model Parameters

The site characteristics used in this study are based on shear wave measurement at site and geotechnical investigation conducted by private consultants. The site characteristics for Site 1: Denbela High School site used in the analysis are presented in Table 3-11 and Table 3-12.

The nonlinear soil properties were modeled using with twelve different nonlinear curves for each of the soil types of soil layer as shown in Table 3-11. The empirical model of Darendeli (2001) was used and the plasticity index, over consolidation ratio, and mean confining pressures used to generate these curves are listed in Table 3-12. The value of excitation frequency and number of cycles used in the model was 1 Hz and 10 cycles, respectively as recommended by Darendeli (2001), for all soils, since these represent average values of earthquake shaking.. The bedrock velocity and damping ratio were assumed to be 760 m/sec and 1%, respectively.

Table 3-11: The shear-wave velocity profile for the Site 1: Denbela High School site.

Depth (m)	Thickness (m)	Soil Type	Vs (m/s)
0	1.8	Sandy elastic silt	185
1.8	2	Sandy elastic silt	205
3.8	2.4	Sandy silt	243
6.2	2.6	Sandy silt	250
8.8	2.9	Sandy silt	249
11.7	3.1	Sandy silt	267
14.8	3.5	Sandy silt	311
18.3	3.7	Sandy silt	357
22	4	Sandy silt	388
26	4.2	Sandy silt	411
30.2	4.6	Sandy silt	438
34.8	4.8	Sandy silt	453
39.6	5	Sandy silt	465
44.6	7.4	Sandy silt	498
52		Bedrock	

Boore (2016) proposed an equation for obtaining the density (ρ) from the shear wave velocity and shown Eq. (3-4). The units of velocity are kilometers per second, and those of density are grams per cubic centimeter.

For V_S < 0.3 km/s (3-4)

$$\rho = 1 + \frac{1.53 V_S^{0.85}}{0.35 + 1.889 V_S^{1.7}}$$

For 0.30 km/s < Vs < 3.55 km/s

$$\rho = 1.74 V_P^{0.25}$$

in which

$$V_P = 0.9409 + 2.0947 V_S - 0.8206 V_S^2 + 0.2683 V_S^3 - 0.0251 V_S^4$$

Anbazhagan et al. (2016) proposed a relation which correlate the bulk density with shear wave velocity is shown in Eq. (3-5). Both relations have a good agreement with each other, Eq . (3-5) was used in this study to calculate the unit weight of the soil layer due to its simplicity. The effect of density almost negligible in the calculation of shear modulus.

$$\rho = 0.412 V_S^{0.262} \quad (3\text{-}5)$$

Table 3-12: The soil types and model parameters of the Site 1: Denbela High School site

Soil Type	Unit Wt. (kN/m^3)	Darendeli Parameters		
		σ'_m (atm)	PI	OCR
Sandy elastic silt (0.14 atm)	15.87	0.14	19	1
Sandy elastic silt (0.44 atm)	16.30	0.44	19	1
Sandy silt (0.81 atm)	17.04	0.81	12	1
Sandy silt (1.23 atm)	17.17	1.23	12	1
Sandy silt (1.70 atm)	17.15	1.70	11	1
Sandy silt (2.21 atm)	17.47	2.21	11	1
Sandy silt (2.79 atm)	18.18	2.79	0	1
Sandy silt (3.45 atm)	18.85	3.45	0	1
Sandy silt (4.18 atm)	19.27	4.18	0	1
Sandy silt (4.97 atm)	19.56	4.97	0	1
Sandy silt (5.83 atm)	19.89	5.83	0	1
Sandy gravel (6.75 atm)	20.07	6.75	0	1
Sandy gravel (7.73 atm)	20.20	7.73	0	1
Sandy gravel (8.98 atm)	20.57	8.98	0	1
Bedrock	24	-	-	-

The effective confining stress (σ'_m) is calculated and used together with plasticity index (PI) and over consolidation ratio (OCR) read from the geotechnical data to generate modulus reduction and damping curves is shown in Table 3-12.

As we can see from the Table 3-12 the PI value drops as we go down with depth and becomes zero after some depths. For geotechnical data that missed PI value at after some depths by observing the nature of the site, the PI value was assumed to be zero. The other sites characteristics used in the analyses are presented in Appendix C.

3.4.2 Shear Strength Evaluation

Shear strength is needed for GQ/H model. The target shear strength of the nonlinear G/G_{max} curves is constrained by a Mohr-Coulomb strength model using a friction angle and a cohesion intercept. The total shear strength of the material is described by

$$\tau_{target,implied} = c + \sigma'_v \tan(\phi) \quad (3\text{-}6)$$

The analysis of shear strength begins by considering the potential for cyclic strength degradation from pore pressure development (i.e., liquefaction of sands and cyclic softening of clays). If significant cyclic strength degradation is not expected, then more 'traditional' total stress methods (or undrained strength analyses; see Ladd (1991)) are appropriate. An important point in this regard is that if clay soil is below the ground water table, the shear strength that should be used for seismic analysis is the undrained shear strength. Above the ground water table, if the saturation is sufficiently low that significant pore pressure generation is not expected (this can be safely assumed to be the case if the saturations are below 90%), then drained shear strengths can be used. For sandy soils, whether above or below the ground water table (assuming no liquefaction), shear strength is typically expressed using the friction angle (Stewart et al., 2014).

For the study area, the water level is deep and all soil profiles is above the water table. Therefore the drained shear strength was used.

Early work on estimating drained friction angle (ϕ') from the N_{60} value attempted to make direct correlations. Meyerhof (1956) and Peck et al. (1974) tabulated recommended values for estimating ϕ'. Peck et al. (1974) published a graphical representation which was later approximated by the following equation by Wolff (1989) as cited by (Ameratunga et al., 2015).

$$\phi' = 27.1 + 0.3N_{60} - 0.00054N_{60}^2 \quad (3\text{-}7)$$

Hatanaka and Uchida (1996) proposed a relation drained angle of internal friction with normalized SPT blow count for 78% energy efficeincy. The relation adjusted for 60% energy efficiency is

$$\phi' = (17.14(N_1)_{60})^{0.5} + 20 \quad (3\text{-}8)$$

Uzielli et al. (2012) developed a relationship for ϕ' with shear wave velocity

$$\phi' = 3.9^0(V_{S1})^{0.44} \quad (3\text{-}9)$$

where $V_{S1}=V_S/(\sigma'_{vo/}\ \sigma_{atm})^{0.25}$= stress-normalized shear wave velocity (m/sec).

Hatanaka and Uchida (1996) and Uzielli et al. (2012) relationships were used to determine the drained friction angle which is used to calculate the shear strength of the soil. The estimated shear strength is for Site 1 for each layer is shown in Table 3-13. The other sites shear strength that used for GQ/H are presented in Appendix C.

Table 3-13: Shear strength of Site 1 that used for GQ/H model

Depth (m)	**Thickness** (m)	**Vs** (m/sec)	**Shear Strength (kPa)**
0	1.8	250	21.6
1.8	2	254	54.2
3.8	2.4	269	91.1
6.2	2.6	276	130.2
8.8	2.9	272	167.6
11.7	3.1	301	222.9
14.8	3.5	356	303.5
18.3	3.7	410	399.8
22	4	459	508.5
26	4.2	501	626.3
30.2	4.6	536	752.0
34.8	4.8	577	899.8
39.6	5	613	1055.3
44.6	7.4	639	1233.3
52			

3.5 Input Motions

One of the most critical steps in any site response analyses is the selection of input motions for the analyses. These include considerations for selecting input motions from available records according to certain filtering criteria. Proper filtering criteria should be applied for selecting motions from available records. The Pacific Earthquake Engineering Research Center (PEER) database is useful for use in a region such as Ethiopia, where strong motion records are unavailable. Ground motions were selected from the PEER database because the motions were recorded in similar geological and tectonic regimes with Ethiopia. Additionally, the PEER database has undergone significant reviews and revision and the search functions are extremely handy. In the following subsections the parameters used for selecting input motions are discussed in detail.

3.5.1 Tectonic Regime

Ground-motion prediction equation (GMPE) developed for particular tectonic regimes are expected to apply to regions with similar tectonic regimes. The reason for use of the PEER database is that, NGA west 2 is characterized by active shallow crustal sources similar to the Ethiopian main rift, which is also characterized by active continental regions and shallow crustal earthquake (Kebede and van Eck, 1997; Ayele, 2017).

3.5.2 Definition of Target Spectrum

In selecting for site response analyses, the first step to be performed is to develop a target spectrum. EN 1998:2015 recommends two types of response spectra depending on the characteristics of the most significant earthquake contributing to the local hazard: Type 1 for high and moderate seismicity regions with surface-wave magnitude, Ms, greater than 5.5 and Type 2 for low seismicity regions (Ms<= 5.5). Kebede and van Eck (1997) classified the horn of Africa into eight zones and Adama falls into zone two as a part of the Main Ethiopian Rift. Zone two was identified with a lower bound magnitude (Mo) of 4 and upper bound magnitude (Mmax) of 7. For this reason, the Type 1 spectrum is selected as it is appropriate for the site seismicity and only the current seismic code design spectrum is considered. Other codes spectrum like NEHRP is not chosen for the reason that the code is not adopted for local use. However the NEHRP design spectrum is not have much difference with EN 1998 Type 1 spectrum for site class A.

EN 1998:2015 requires the use of ground motions with a 10% probability of being exceeded over an interval of 50 years for design of structures. These ground motions are often termed the 10% in 50 years ground motions, which have an approximate return period of 475 years. GSHAP extracted acceleration which is 0.15g (0.147g) was used to plot the 5% damped horizontal response spectral acceleration at various periods (T) for ground type A (rock material).

According to the EN 1998:2015, for the horizontal components of the seismic action, the elastic response spectrum $S_e(T)$ is defined by the following expressions:

$$
\begin{aligned}
&0 \le T \le T_B: \quad S_e(T) = a_g \cdot S \cdot \left[1 + \frac{T}{T_B} \cdot (\eta \cdot 2.5 - 1)\right] \\
&T_B \le T \le T_C: \quad S_e(T) = a_g \cdot S \cdot \eta \cdot 2.5 \\
&T_C \le T \le T_D: \quad S_e(T) = a_g \cdot S \cdot \eta \cdot 2.5 \left[\frac{T_C}{T}\right] \\
&T_D \le T \le 4s: \quad S_e(T) = a_g \cdot S \cdot \eta \cdot 2.5 \left[\frac{T_C T_D}{T^2}\right]
\end{aligned}
\tag{3-10}
$$

where

$S_e(T)$ is the elastic response spectrum;

T is the vibration period of a linear single-degree-of-freedom system;

a_g is the design ground acceleration on type A ground ($a_g = \gamma_I . a_{gR}$);

T_B is the lower limit of the period of the constant spectral acceleration branch;

T_C is the upper limit of the period of the constant spectral acceleration branch;

T_D is the value defining the beginning of the constant displacement response range of the spectrum;

S is the soil factor;

η is the damping correction factor with a reference value of $\eta = 1$ for 5% viscous damping.

Table 3-14 shows the parameter values used to generate response spectra.

Table 3-14: Values of the parameters describing the recommended Type 1 elastic response spectra (ES EN 1998:2015)

Ground type	S	T_B(s)	T_C(s)	T_D(s)
A	1.0	0.15	0.15	2.0

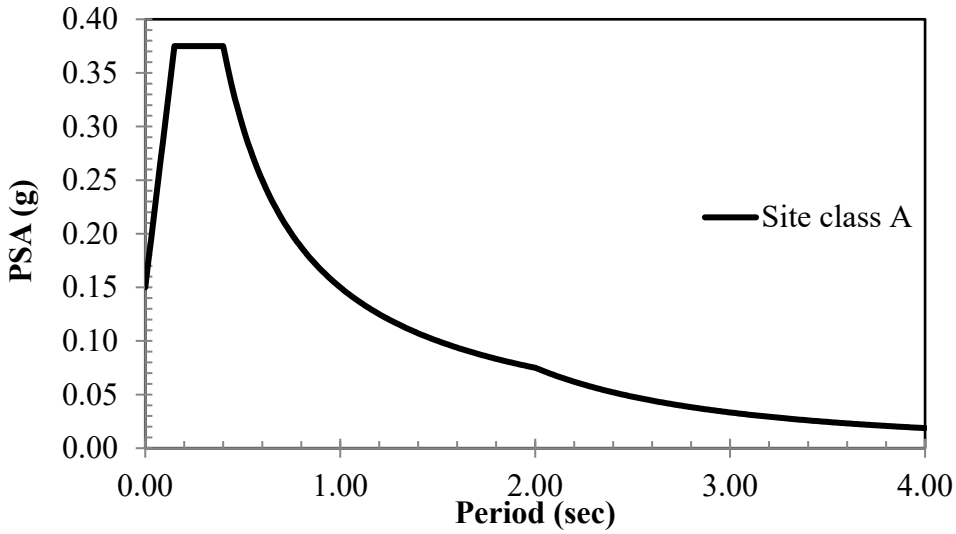

Figure 3-33: Recommended Type 1 elastic response spectra for ground types A (ES EN 1998:2015).

3.5.3 Range Magnitude

Kebede and van Eck (1997) grouped the horn of Africa into eight seismic source zones. Aswa shear zone belongs to zone 1; the southernmost rifts of Ethiopia and the main Ethiopian rift (MER) belongs to zone 2; zone 3 comprises the western margin of Afar depression; zone 4 comprises the Afar depression including the Djibouti area; zone 5 comprises the proposed transform fault (PTF) connecting northern Afar to the axial trough of the Red Sea; the southern part of the axial trough of the Red Sea belongs to zone 6; the western Gulf of Aden belongs to zone 7 and zone 8 comprises the region characterized by an extensional tectonics in Yemen. Most of the zones are located in the current Ethiopia.

zone 2 covers the southernmost rifts of Ethiopia and the main Ethiopian rift in which Adama is located. The zone is characterized with a lower bound magnitude of 4 and Upper bound magnitude of 7 with standard deviation of 0.2. These magnitude ranges were used as filtering criteria for PEER motions selections.

3.5.4 Site Conditions

Site conditions (V_{S30}) can be used as input for ground motion estimation but have already been addressed in the spectral shape used in time series scaling. The limits on site conditions should be reasonable and also not be preventive as to unreasonably limit the number of candidate motions. V_{S30} for the site for a range of 760-1500 m/sec, has been applied.

3.5.5 Duration of Magnitude Range

Several studies over the past decades have presented many definitions for strong ground motion duration, all of which attempt to isolate a certain portion of the records. It has been shown in Bommer et al. (2009) that all of these definitions can be grouped into one of three generic categories. The first category is bracketed duration, being simply the time interval between the first and last exceedance of ground acceleration above a particular threshold acceleration. The second category is uniform duration, which is the sum of the time intervals during which the acceleration level exceeds a specified threshold. The third category is significant duration, based on the interval over which a specified portion of Arias intensity is achieved.

Thresholds of 5–95% of the total energy were used to acquire the duration. The significant duration for the study is, according to the ground motion prediction equation (GMPE) of Bommer et al. (2009), is ~18.1 second. The duration was obtained using a rupture distance of 100 km and a shallow crustal earthquake magnitude of 7.0. An upper bound threshold (18 seconds) of the scaling factor was considered as a further criterion of selection.

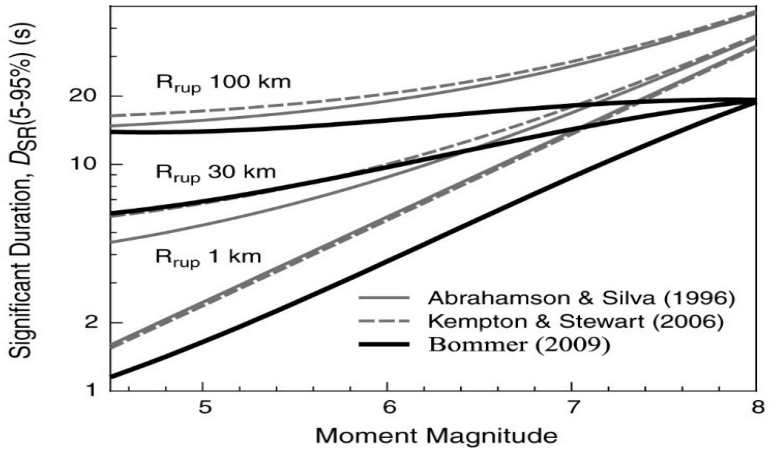

Figure 3-34: Comparison of empirical predictive models Abrahamson and Silva (1996), Kempton and Stewart (2006), and Bommer (2009) for significant duration by (Bommer et al., 2009).

3.5.6 Style of Faulting

Style of faulting is categorized into three different "end member" types that are: strike slip, normal, and reverse (or thrust) slip faulting. Kebede and van Eck (1997) reported that the main Ethiopian rift (MER) is dominated by normal faulting.

3.5.7 Time Series Scaling

It is often necessary to scale recorded ground motions in order to match the ground motion intensities associated with target spectra. In this context, scaling consists of simple multiplication of the time series by a constant (time-invariant) factor, which will increase its response spectra by the same amount. The objective is to select ground motions that match the target spectrum which consists of amplitude and frequency. The scaling procedure used for site response analysis and structural analysis are quite different because the latter one directly used to evaluate structural performance.

Two approaches for the coupled tasks of ground motion selection and scaling are considered to be suitable for site response analysis applications. (Stewart et al. 2014)

Approach 1–enforced matching of target over period range:

After earthquake motions are selected based on initial screening criteria, the median of ensemble ground motions matches the target response spectrum over a user-provided period range. The individual motions were then scaled to match the median of the ensemble motions. A process in which a real recorded earthquake ground motion is modified in some manner such that its response spectrum matches a desired target spectrum over a user-specified period range. A range based on the period of the structural system that is the subject of the overall ground motion analysis will generally be important.

Approach 2–matching target at single period:

The Ground motion selected and scaled at a defined period range is then used to match the target spectrum at a selected period. This approach consisted of records scaled such that their spectra match the design spectrum at a particular period. The scaled spectra are shown in Figure 3-35.

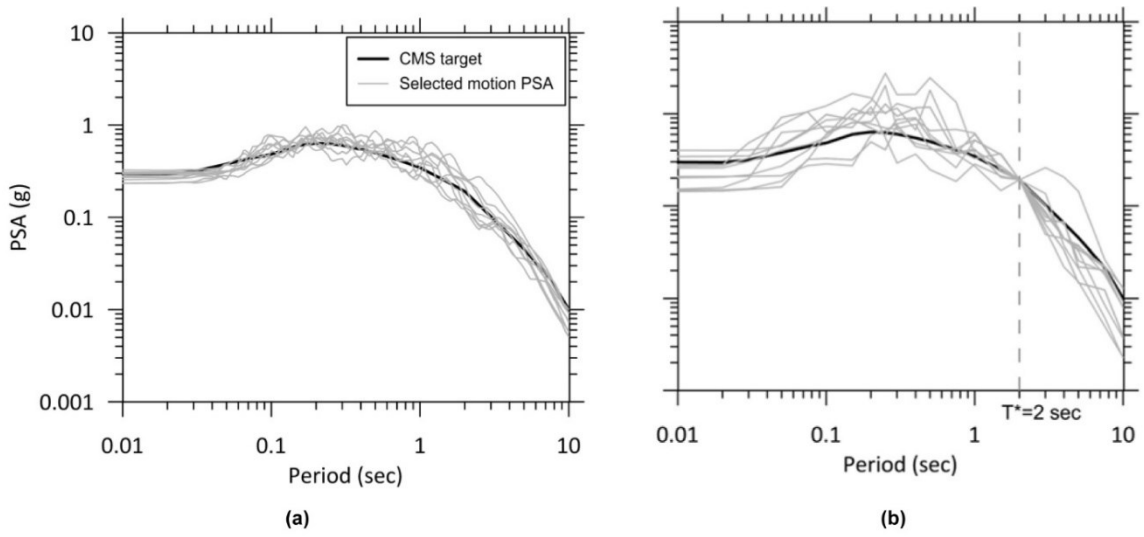

Figure 3-35: Conditional mean spectrum-based target spectrum and PSA for 11 selected and scaled motions. Part (a) is Approach 1, using a range of periods (0.01-10 sec). Part (b) is Approach 2, using a single matching period at 2.0 sec (Stewart et al. 2014).

In ES EN 1998:2015, this period range is taken from $0.2T_1$-$2.0T_1$, where T_1 is the fundamental period of a structure. In ground response applications, a similar range based on the period of the structural system that is the subject of the overall ground motion analysis will generally be important. The simplest way to take structural response into account is to scale the time series such that spectral acceleration at the fundamental period of the structure is equal to that of the target. The fundamental period of vibration of the building for lateral motion in the direction considered, T_1, is approximated by the following expression according to ES EN 1998:2015:

$$T_1 = C_t H^{3/4} \quad (3\text{-}11)$$

where: C_t =0.085, 0.075 for steel frame and reinforced building respectively and H= building height

The height ranges from 9 m to 63 m are considered for the building ranges between G+2 to G+20. The fundamental period of the building will be between 0.441sec and 1.9007sec. The period range for filtering is taken from $0.2T_1$-$2.0T_1$, a period range of 0.0882- 3.8154 sec was obtained. Accordingly, a period range of 0.1 - 3.854 is used as a filtering criterion. A scale factor limit of approximately 0.25 to 4.0 is not uncommon (Haselton et al., 2017). In the current selection, a factor of three that is with minimum and maximum value of 0.333 and 3 respectively was selected.

BSSC (2015) recommended the maximum largest spectral value that is RotD100 for the multi-component response spectrum definition during PEER database selection; However, Stewart et al. (2014) stated that this is conservative for site response analyses and suggested RotD50 which is the median value over all rotation angles for target spectral matching.

Each potential ground motion is scaled to match the target spectrum on average over the period range of interest and then to minimize squared errors between the ground motion spectrum and the target spectrum, weight function is applied with a value of 1,1 for the period range of 0.1, 3.9 seconds respectively.

Ground motion records are archived as sets of two horizontal components and one vertical component. For site response analysis, only horizontal records are of interest, and only a single component is required (Stewart et al., 2014). Overall, a single recording event should not dominate the suite of records. Only one record was selected for the Loma Prieta earthquake from five available records during the filtering. From the five, the set with the lowest root-mean-square error of median response spectrum to target response spectrum was selected.

The input motions in NGA west 2 are already bandpass filtered and baseline corrected, so only scaling to 0.15g was applied on the selected motions. A minimum of seven ground motions needed for site response analysis and for the present study 8 motions were selected. The selected ground motion records and their characteristic parameters are listed in Table 3-15. As depicted in Figure 3-36, the selected motions scaled to 0.15g which is PGA of Adama.

Table 3-15: Selected Input Motions from PEER database

Result ID	Record Sequence Number	Scale Factor	5-95% Duration (sec)	Earthquake Name	Magnitude	V_{S30} (m/sec)
1	80	1.5169	14.1	"San Fernando"	6.61	969.07
2	146	2.2405	6.8	"Coyote Lake"	5.74	1428.14
3	680	2.1773	6.2	"Whittier Narrows-01"	5.99	969.07
4	804	1.7136	12.1	"Loma Prieta"	6.93	1020.62
5	1091	0.8960	8.3	"Northridge-01"	6.69	996.43
6	3954	0.7504	12.8	"Tottori_ Japan"	6.61	967.27
7	4083	1.2748	8.8	"Parkfield-02_ CA"	6	906.96
8	8167	2.3904	16.9	"San Simeon_ CA"	6.52	1100

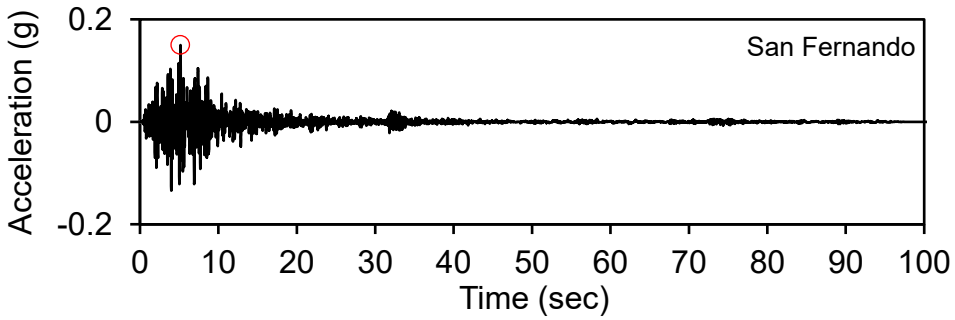
San Fernando
Acceleration (g)
0.2
0
-0.2
0 10 20 30 40 50 60 70 80 90 100
Time (sec)

(a)

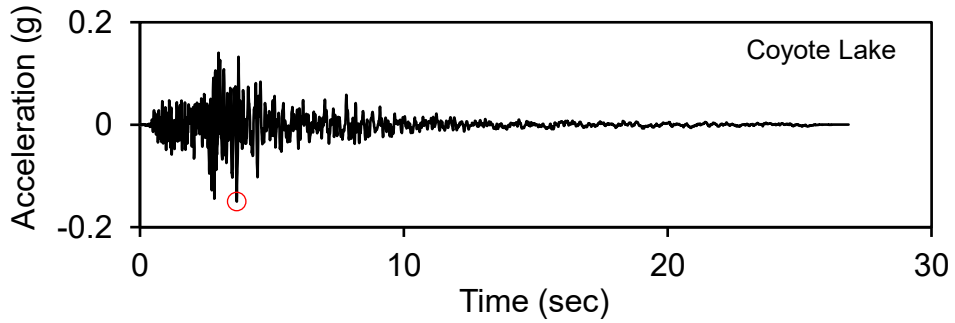
Coyote Lake
Acceleration (g)
0.2
0
-0.2
0 10 20 30
Time (sec)

(b)

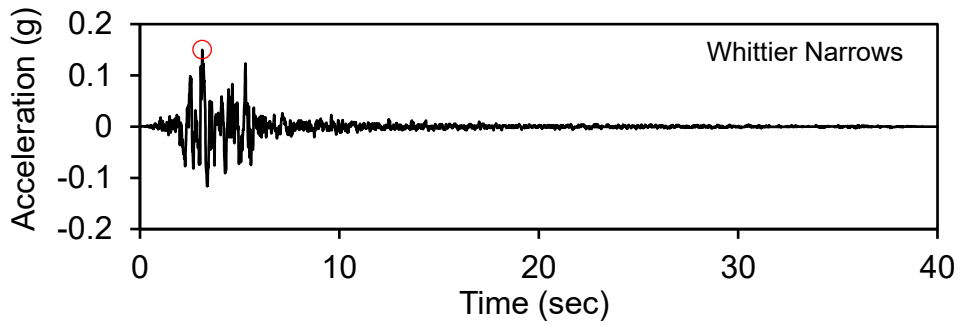
Whittier Narrows
Acceleration (g)
0.2
0.1
0
-0.1
-0.2
0 10 20 30 40
Time (sec)

(c)

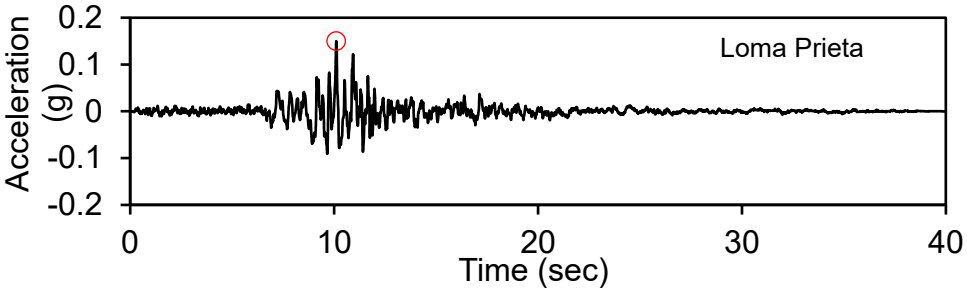
Loma Prieta
Acceleration (g)
0.2
0.1
0
-0.1
-0.2
0 10 20 30 40
Time (sec)

(d)

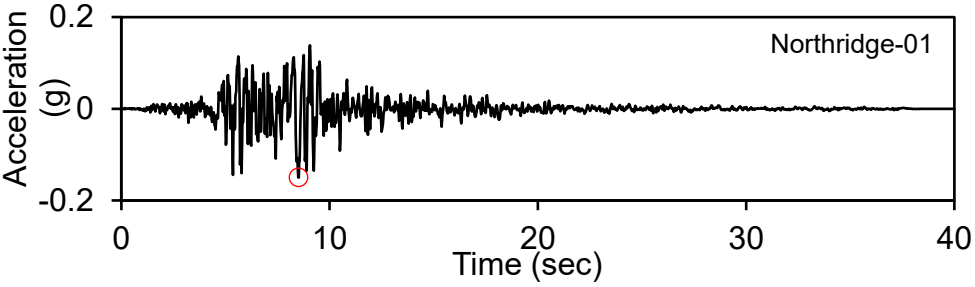
Northridge-01
Acceleration (g)
0.2
0
-0.2
0 10 20 30 40
Time (sec)

(e)

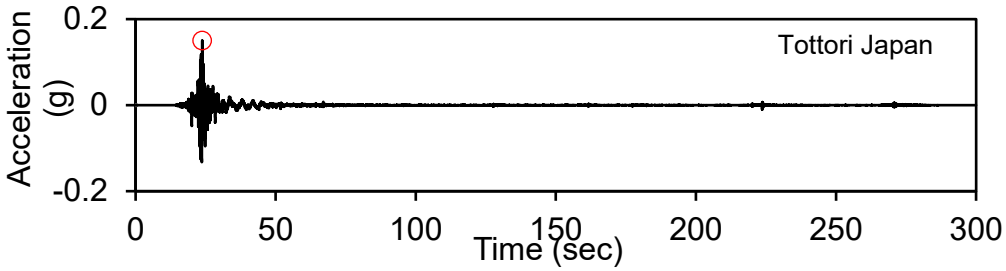

(f)

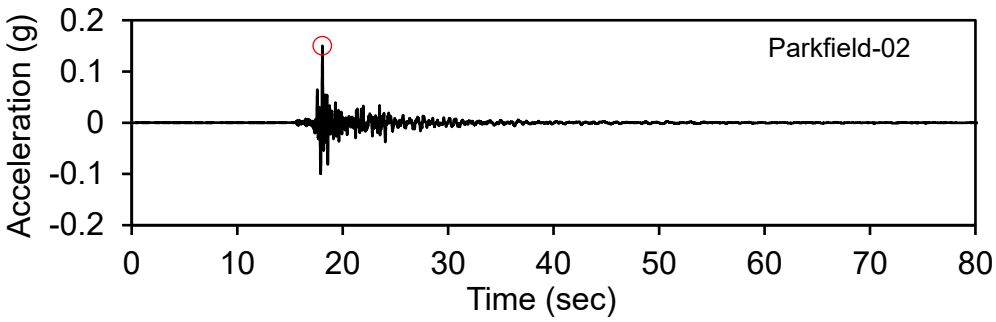

(g)

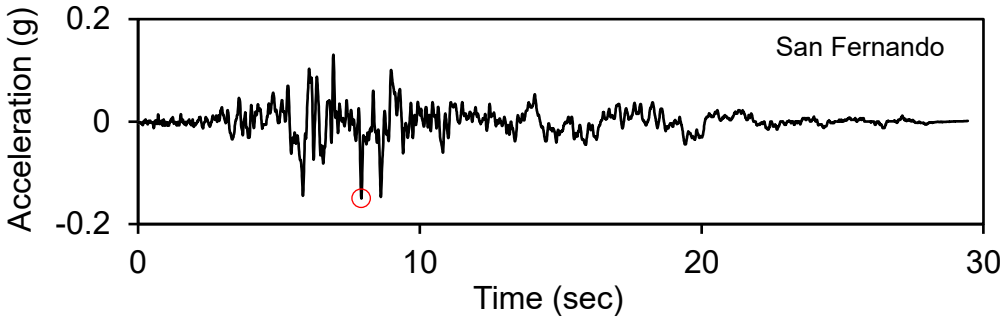

(h)

Figure 3-36: The acceleration time histories for the scaled San Fernando (a) Coyote Lake (b) Whittier Narrows-01 (c) Loma Prieta (d) Northridge-01 (e) Tottori Japan (f) Parkfield-02 (g) San Simeon (h) motions.

3.6 Model Analysis

One site response analysis models and procedures described in detail in section 2.2.2. For this study, the program DEEPSOILv7 was used for all site response analyses, and the author has acquired official permission from the developer. Both equivalent linear and nonlinear were performed in this study.

In equivalent linear analysis for defining the dynamic soil properties of soil i.e (the shear modulus and damping ratio curves) discrete points were used in the DEEPSOIL software. For nonlinear analysis MKZ and GQ/H models were used for defining backbone curve together with MRDF approach for defining hysteretic damping. Frequency independent damping was used as viscous damping at small strain in time domain analysis. For nonlinear

analysis, soil profiles in this study were subdivided such that the maximum frequency of the soil profile was 50 Hz. The ground motions in section 3.5 used in conjunction with an elastic base.

CHAPTER 4
RESULTS AND DISCUSSION

One-dimensional ground response analyses are the most widely used method to assess the response of soil deposits by ground motion propagation through soil deposits. It is based on some assumptions as all boundaries are horizontal, and the shear waves propagate vertically from the underlying bedrock, and the soil and bedrock are assumed to be infinitely extended in the horizontal direction (Kramer, 1996).

Over the years, different site response analysis techniques have been developed to account for the influence of sites over the motion applied at bedrock. The nonlinear response of the soil can be characterized either through the EQL approach or through the fully nonlinear approach. DEEPSOIL is used perform one-dimensional site response analyses of layered media. The results of the analysis are presented and discussed here.

4.1 Analysis Results

The average shear wave velocity value (i,e V_{S30}) is used for site characterization as per both Eurocode 8 and the National Earthquake Hazard Reduction Program (NEHRP). The average shear wave velocity at the top 30 m (V_{S30}) of the study area varied from 225 to 332.5 m/sec. The study area was classified as site class C according to EN 1998:2015 and site class D according to NEHRP. According to the Eurocode 8, the site class C Vs_{30} ranges from 180 m/sec to 360 m/sec and According to the NEHRP, the site class D Vs_{30} ranges from 180 m/sec to 360 m/sec.

4.1.1 Summary of Profiles

4.1.1.1 Summary of PGA Profiles

The result of the one dimensional analyses using equivalent linear and nonlinear (MKZ and GQ/H) models are presented in the form of PGA profiles, displacement profiles, strain profiles and response spectra. Profiles are separated as geophysical and geotechnical profiles based on their acquisition.

(a) Geophysical profiles

The results of analysis of the geophysical profiles showed significant amplification in all the profiles and all of which were calculated for the top of each layer. All the profiles, obtained from DEEPSOIL, for an input PGA of 0.15g are shown in Appendix D.1-D.3. It has been found that the various selected ground motions at bedrock level are amplified and their PGA values using EQL and NL analyses at the surface are tabulated in Table 4-1. The amplification ratio of these sites clearly indicate the amplification potential of local soil and geological conditions. The MKZ and GQ/H model resulted in lesser amplification.

Table 4-1: PGA values at the surface for Site 1, Site 2, Site 3 and Site 4

	PGA at the surface		
	EQL	**MKZ**	**GQ/H**
Site 1	0.24 to 0.33g	0.22 to 0.25g	0.23 to 0.26g
Site 2	0.23 to 0.35g	0.20 to 0.27g	0.20 to 0.29g
Site 3	0.27 to 0.41g	0.20 to 0.27g	0.23 to 0.31g
Site 4	0.26 to 0.44g	0.20 to 0.28g	0.22 to 0.29g

PGA values in profile Site 1 and Site 2 were less than those in Site 3 and Site 4. The reason for that may be due to the difference of soil column height above the bedrock in the two sites which resulted in stiffer soils. Additionally, there was no significant velocity contrast between the bottom of the soil column and bedrock on these sites. In Site 1 and Site 2 the depth of shear wave profiles more than 50 m which represents the real conditions of the sites, thus the result is more reliable.

Different motions give different picks on the same site as shown in Appendix D.1-D.3. This difference of peak acceleration values at the surface was due to the relative strong and weak Fourier amplitude of different motions near the fundamental frequency of the site. Tottori motion gives higher amplification in all four sites. It is noted that the predominant period of the profiles ranges from 0.45-0.61 sec, the motion has high-energy content for this period range.

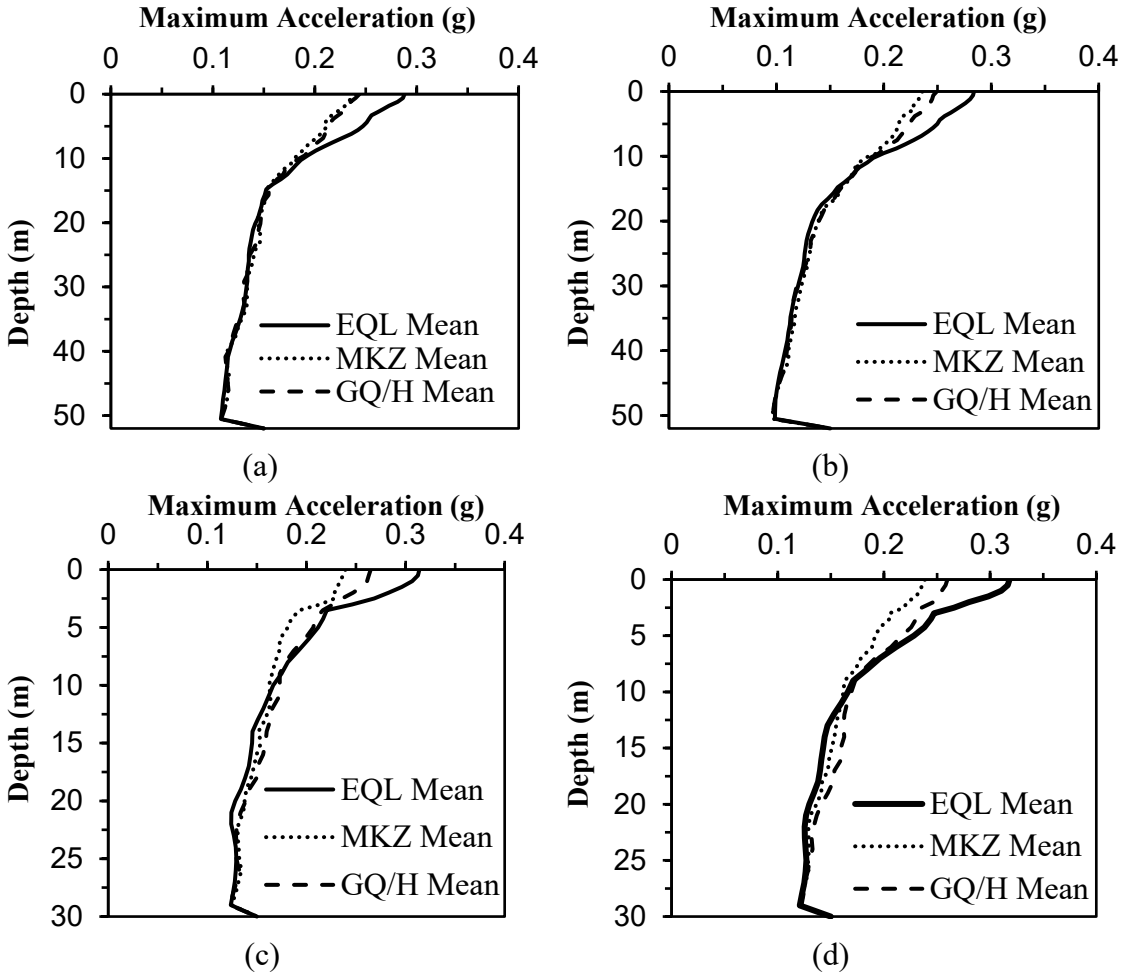

Figure 4-1: Mean peak ground acceleration profiles for (a) Site 1 (b) Site 2 (c) Site 3 (d) Site 4.

In Figure 4-1, the mean PGA of the eight motions from the EQL is compared with the nonlinear mean PGA of the MKZ and GQ/H models. The PGA values show almost similar results in the depth range up to 10 m for all three analyses. Above 10 m, the three lines started to split up and resulted in a significant variation between EQL and nonlinear models; the nonlinear models give lower values of PGA compared to EQL at the surface. This is due to the fact that the nonlinear models will undergo hysteretic damping.

The MKZ and GQ/H models shows similar PGA results in Site 1 and Site 2, for the reason that they predicted similar strain profile while they predicted a slightly different strain profiles in Site 3 and Site 4, resulted in a slightly different PGA. The MKZ model allows more energy dissipation as compared to GQ/H, which resulted in lesser PGA values than GQ/H.

(b) Geotechnical profiles

The results of analysis of the geotechnical profiles showed significant amplification in all the profiles. All the profiles, obtained from DEEPSOIL, for an input PGA of 0.15g are shown in are shown in Appendix D.4-D.6. It has been found that the various selected ground motions at bedrock level are amplified and their PGA values at the surface are tabulated in Table 4-2.

Table 4-2: PGA value at the surface for Site 5, Site 6, Site 7, Site 8 and Site 9

	PGA at the surface		
	EQL	**MKZ**	**GQ/H**
Site 5	0.26 to 0.38g	0.20 to 0.27g	0.23 to 0.26g
Site 6	0.25 to 0.36g	0.20 to 0.26g	0.21 to 0.25g
Site 7	0.28 to 0.56g	0.19 to 0.30g	0.23 to 0.31g
Site 8	0.31 to 0.50g	0.21 to 0.30g	0.25 to 0.35g
Site 9	0.20 to 0.28g	0.17 to 0.23g	0.19 to 0.26g

In Table 4-2, the mean PGA of the eight motions from the EQL is compared with the nonlinear mean PGA of the MKZ and GQ/H models. The PGA values show almost similar results in the depth range up to 10 m for all three analyses. The upper 10 m soil deposit contributes to the amplification of the motions. Above 10 m, the three lines started to split up and resulted in a significant variation between EQL and nonlinear models; the nonlinear models give lower values of PGA compared to EQL at the surface. This is due to the fact that the nonlinear models will undergo hysteretic damping.

The EQL analysis resulted high PGA value at Site 7. Because the EQL method is based on equivalent linear properties, this induces spurious peaks in the Fourier spectra of the responses obtained via this method. These peaks are caused by the coincidence of a strong component of an input motion with one of the natural frequencies of the EQL Site 7 soil deposit, resulting in artificial amplification near the fundamental frequencies of the soil. For nonlinear analyses and field responses, because the stiffness of soil actually changes during earthquakes, these spurious peaks are rare (Kramer, 1996).

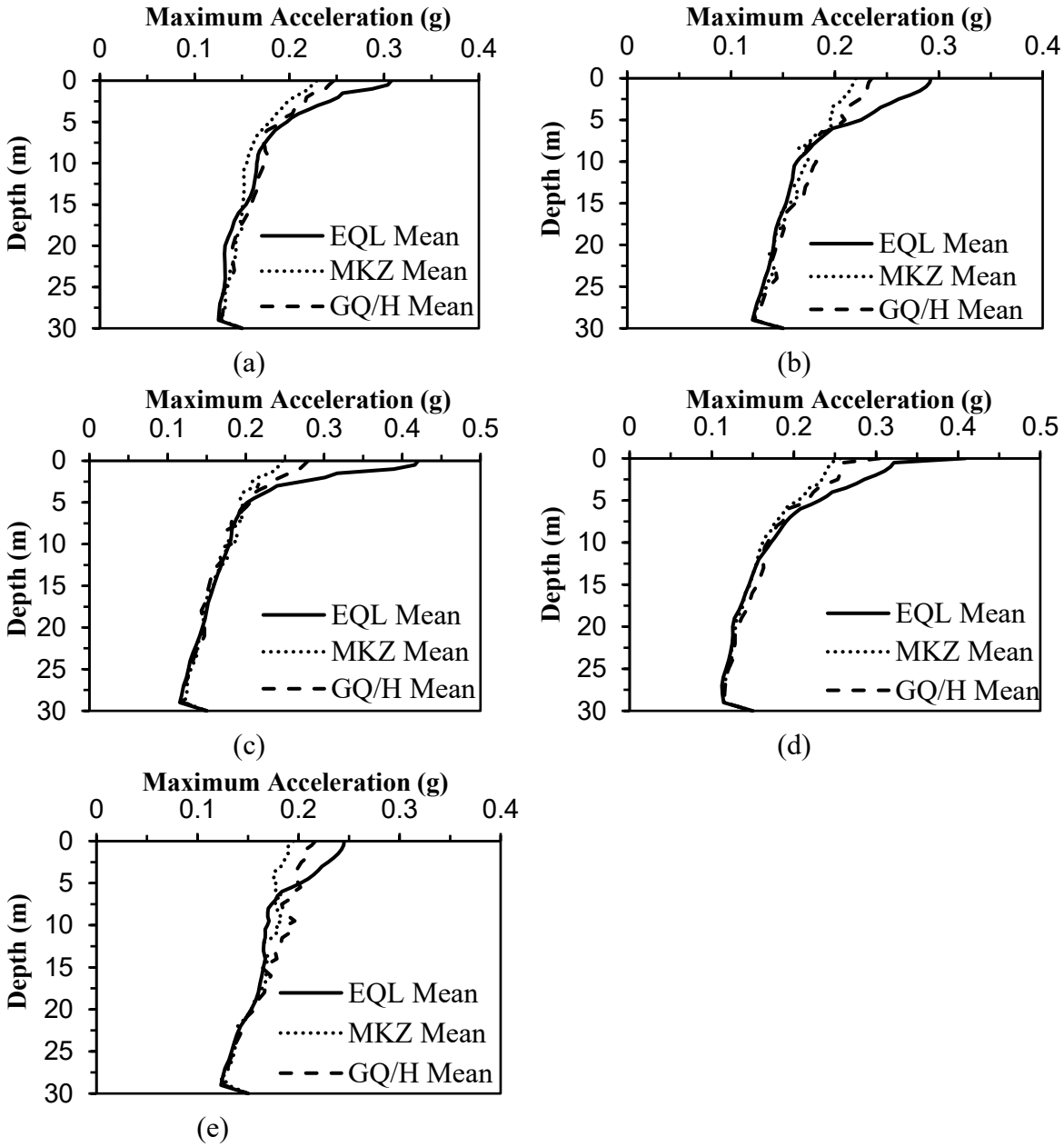

Figure 4-2: Mean peak ground acceleration profiles for (a) Site 5 (b) Site 6 (c) Site 7 (d) Site 8 (e) Site 9 sites.

4.1.1.2 Summary of Displacement Profiles

(a) Geophysical profiles

The results of analyses of the geophysical profiles showed the significant peak displacement in all the profiles and all of which were calculated for the top of each layer as are shown in Appendix D.7-D.12. After ground response analyses, it has been found that mean peak displacements at the ground surface are high as shown in Figure 4-3. The displacement is reduced below the ground surface and zero at the bedrock level.

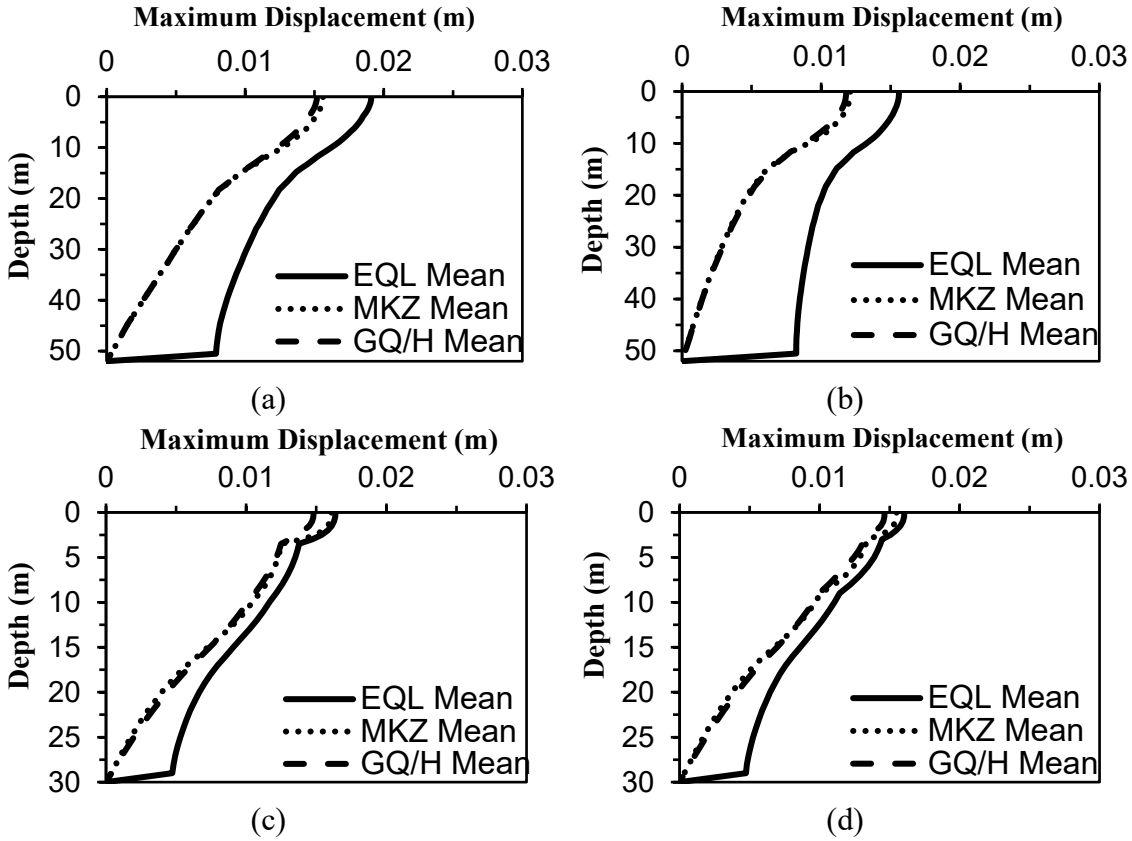

Figure 4-3: Mean peak displacement profiles for (a) Site 1 (b) Site 2 (c) Site 3 (d) Site 4 sites.

(b) Geotechnical profiles

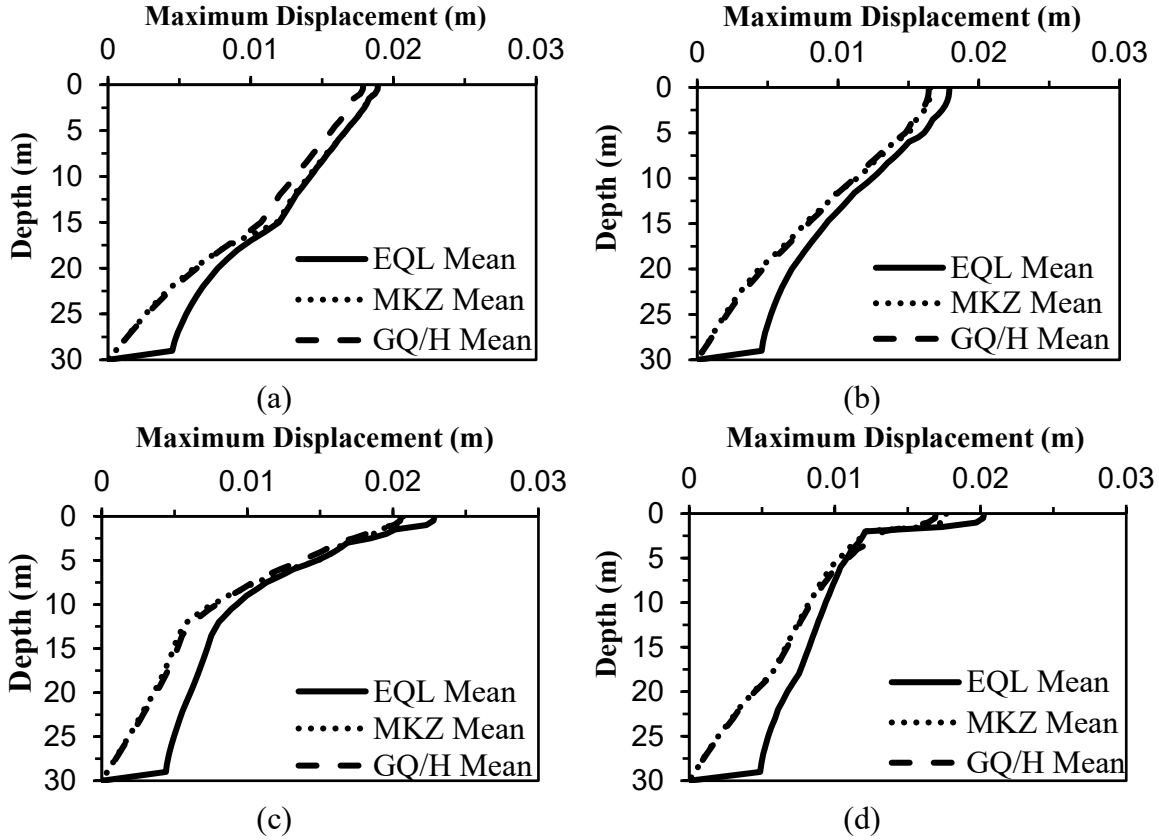

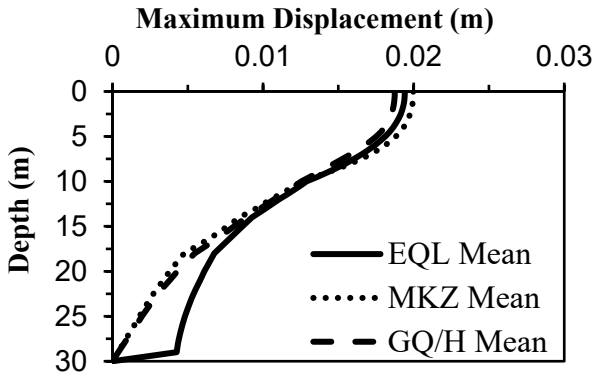

(e)

Figure 4-4: Peak displacement profiles for (a) Site 5 (b) Site 6 (c) Site 7 (d) Site 8 (e) Site 9.

All the models resulted in similar mean peak ground displacement (PGD), the nonlinear model gave a slightly lower PGD value as compared to the EQL model, as shown in Figure 4-3 and Figure 4-4. It can be observed from Figure 4-3 and Figure 4-4 that the nonlinear models show no to minimal variation in the lower depth, but the EQL model shows sudden variations at the bottom-most depth. This is due to the fact that the low frequency motion filtered out during the double integration of acceleration time histories for the nonlinear models.

4.1.1.3 Summary of Strain Profiles

(a) Geophysical profiles

The maximum shear strain is defined as the largest peak shear strain within the soil column. Appendix D.13-D.15. shows the maximum shear strain results obtained from the site response analysis and the mean of the shear strain profiles from the eight motion for three analyses shown in Figure 4-5. The maximum shear strain are tabulated in Table 4-3.

Table 4-3: Maximum shear strain for Site 1, Site 2, Site 3 and Site 4

	Maximum shear strain (%)		
	EQL	**MKZ**	**GQ/H**
Site 1	0.12	0.20	0.11
Site 2	0.12	0.20	0.11
Site 3	0.51	0.67	0.19
Site 4	0.46	0.60	0.14

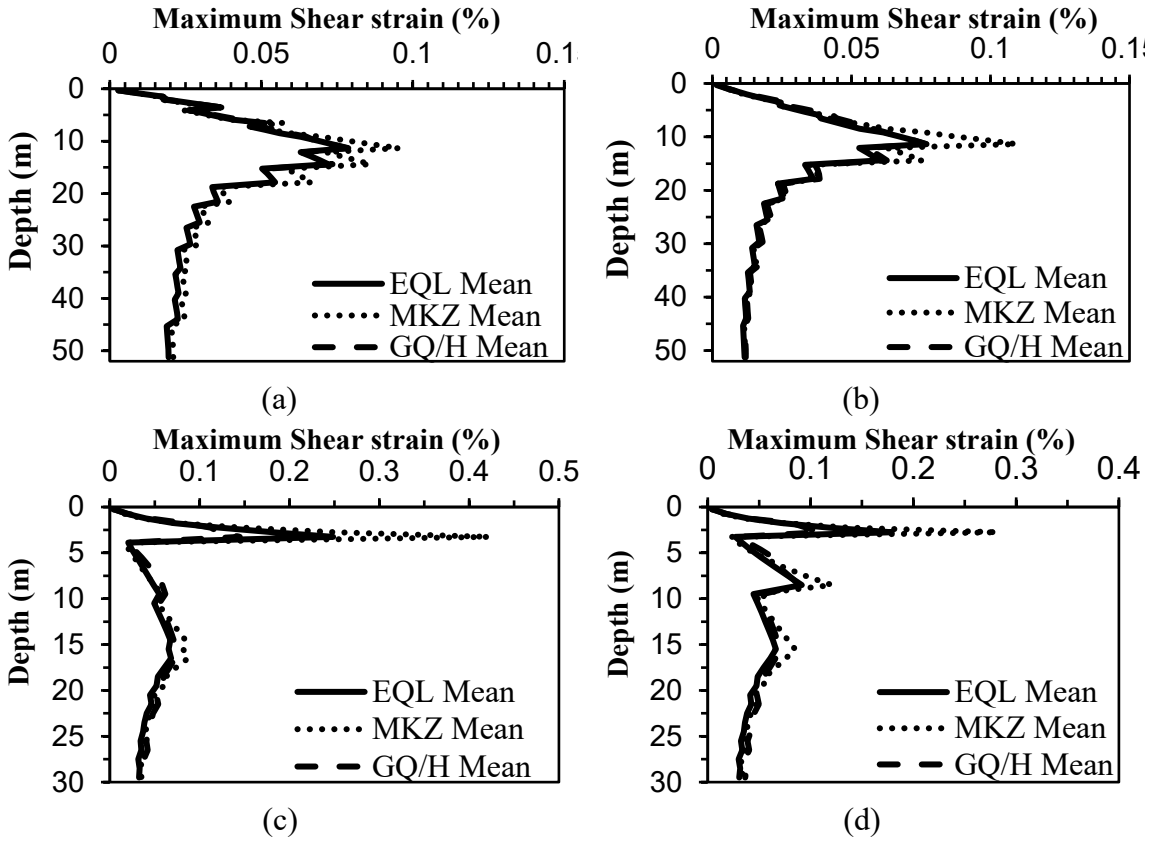

Figure 4-5: Mean strain profiles for (a) Site 1 (b) Site 2 (c) Site 3 (d) Site 4.

(b) Geotechnical profiles

Appendix D.16-D.18. shows the maximum shear strain results obtained from the site response analysis and the mean of the shear strain profiles from the eight motion for three analyses shown in Figure 4-5The maximum shear strain are tabulated in Table 4-4.

Table 4-4: Maximum shear strain for Site 5, Site 6, Site 7, Site 8 and Site 9

	Maximum shear strain (%)		
	EQL	**MKZ**	**GQ/H**
Site 5	0.20	0.33	0.20
Site 6	0.23	0.39	0.22
Site 7	0.90	0.69	0.46
Site 8	0.32	0.49	0.31
Site 9	0.29	0.45	0.25

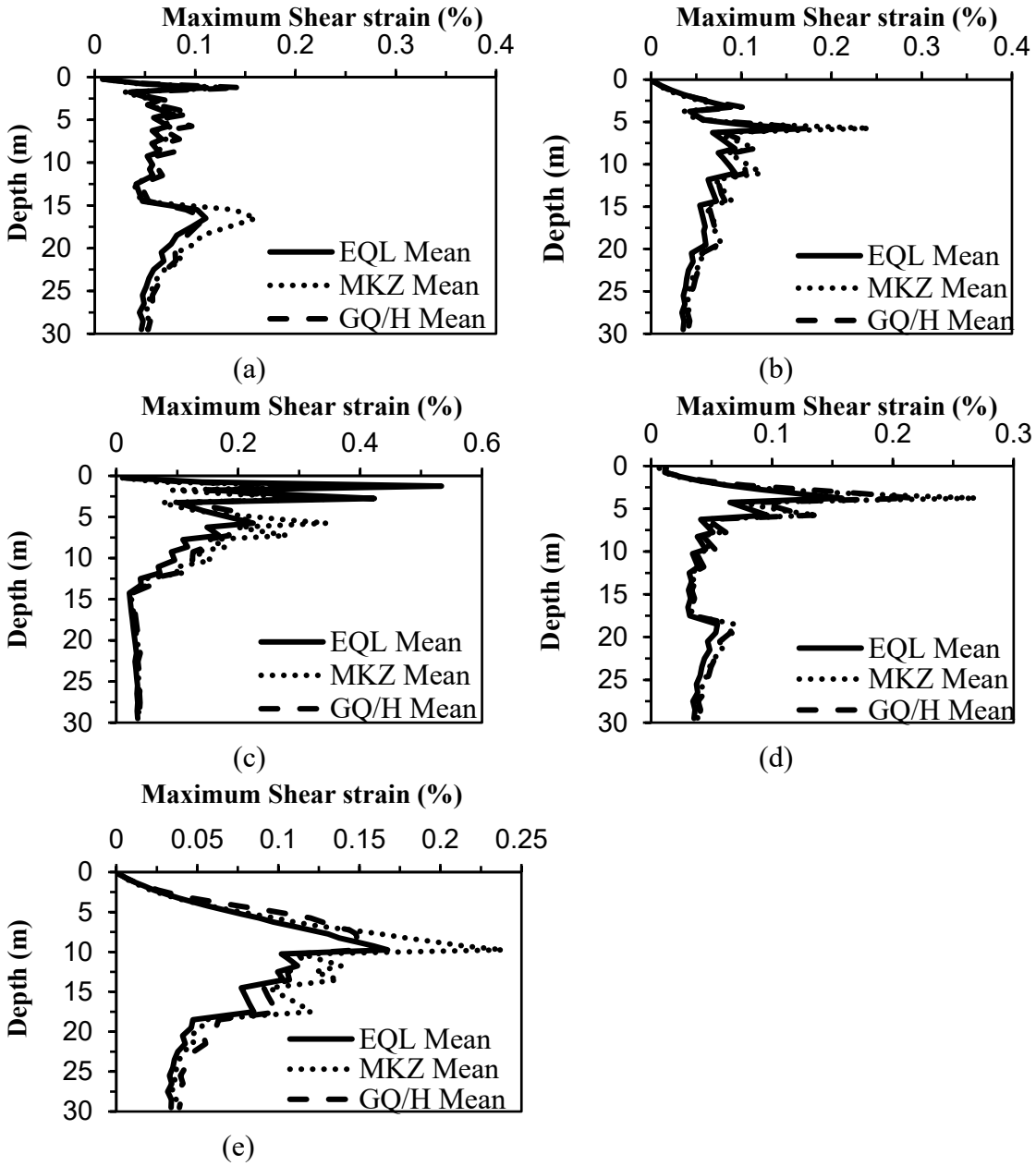

Figure 4-6: Mean strain profiles for (a) Site 5 (b) Site 6 (c) Site 7 (d) Site 8 (e) Site 9 sites.

The shapes of the strain profiles are the same for all analyses are shown in Figure 4-5 and Figure 4-6 in the mean strain profiles. All analyses captured a noticeable increase of the induced shear strain started from 20 m depth with the maximum shear strain with the upper 15 m.

In most site, the nonlinear analyses predict higher strain than the EQL analyses. In Site 07, only the EQL analysis predicts a higher strain value than the nonlinear analyses, 0.9%. The use of effective shear strains and the iterative procedure in equivalent linear analyses may not always guarantee converged solutions and can also lead to over-softened and

overdamped systems. This happens if the peak shear strain is much larger than the remainder of the shear strains as shown Figure 4-7 (Kramer, 1996).

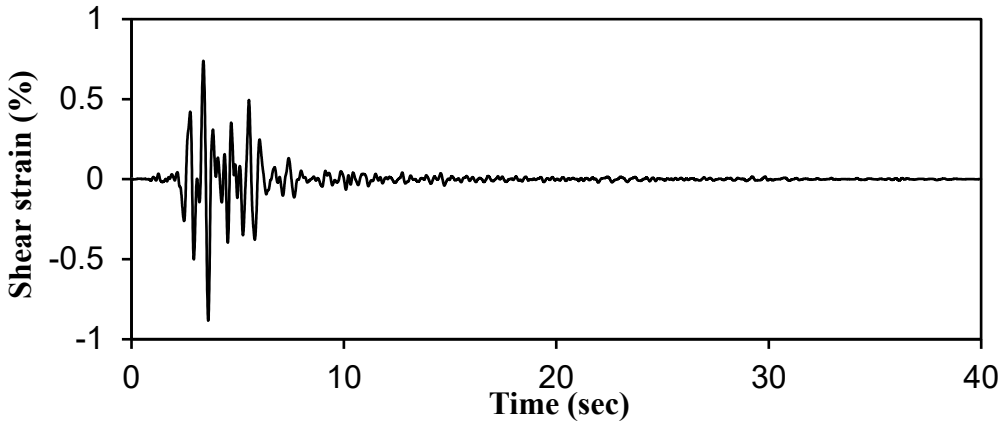

Figure 4-7: Shear strain time history for Site 7 at 2.5 m.

The MKZ model predicts maximum strains up to 0.67%, whereas the maximum strain calculated by the GQ/H model is 0.46%. For the MKZ model, the largest strain occurs at a depth immediately above the interface between the top two layers with high impedance contrast. The high impedance contrast at the interface causes a large amplification. The MKZ model reveals a distinct underestimation of the strength, whereas the GQ/H fitting procedure provides a favorable fit with the target shear strength, and at the same time matches well with the reference Darendeli (2001) normalized modulus reduction and damping ratio curves. The underestimation of the shear strength in the layer above the interface results in a very soft soil response, inducing an unrealistic level of shear strain to develop. The large shear strain also has an important influence on the PGA profiles. For the MKZ model compared with GQ/H, there is a drop in the calculated PGA in the profiles, obviously caused by the excessive dissipation of energy near the interface.

An Acceptable agreement is found between the EQL results and the nonlinear results for sites the maximum shear strain of less than 0.4%; which is in line with the study of Kaklamanos et al. (2013); recommended that for EQL analysis, the value of between 0.2-0.4% is acceptable.

4.1.2 Response Spectral Analysis

A total of nine sites from both geophysical and geotechnical profiles were used in site response analysis for calculating response spectra analysis, and the corresponding response

spectra with 5% structural damping are shown in Appendix D.19,22., D.20,23. and D.21,24 for EQL, MKZ and GQ/H models respectively.

In this section, the response spectra at the ground surface from the equivalent response analysis are compared with response spectra at the bedrock level to evaluate the amplification potential of the soil. In all profiles, the response spectra are amplified by a significant amount which indicates the amplification potential of the sites. It was observed a significant amplification for all eight motions in all sites. Response spectra of eight records with EQL, MKZ and GQ/H models are shown in Appendix D.19-D.24. Among the eight earthquakes, Northridge earthquake produces the highest (1.54g) pseudo spectral acceleration (PSA) with EQL, 1.36g with MKZ and 1.44g with GQ/H for Site 1 and San Simeon earthquake produces the lowest (0.73g) peak spectral acceleration (PSA) with EQL, 0.62g with MKZ and 0.63g with GQ/H. Similarly, Northridge record peak a maximum PSA for Site 2 as well, with a value of 2.0g with EQL, 1.6g with MKZ, 1.78g with GQ/H at 0.39sec. For Site 3, the maximum PSA value encountered was 1.52g with EQL, 1.46g with MKZ, 1.52g with GQ/H at a period of 0.39 sec for the Northridge record. Site 3 has a relatively wide range of predominant period, which was 0.19-0.39 sec. Site 4 showed a similar trend with Site 3 whereby a predominant period in the range of 0.22-0.39 sec with peak PSA of 1.57g with EQL, 1.39g with MKZ, 1.56g with GQ/H for Northridge record.

Coyote Lake and Tottori Japan records peaked 1.59g and 1.55g of PSA with a short period difference at 0.19 and 0.21 sec for Site 5 with EQL and similarly the MKZ and GQ/H peaked 1.31 g and 1.19g; 1.32g and 1.25g for the two records respectively at similar periods with EQL. Site 6 showed a predominant period in the range of 0.2 - 0.4 sec, with a peak spectral acceleration 1.32g with EQL, 1.09g with MKZ and 1.217g with GQ/H. Tottori record peak a maximum PSA for Site 7 with a value of 2.0g at 0.36 sec with EQL. Northridge record peak a maximum PSA for Site 8 with a value of 1.97g with EQL, 1.75g with MKZ and 1.74g with GQ/H at 0.39 sec. Site 9 showed the lowest amplification value of all sites with a maximum PSA value of 1.2g with EQL, 0.95g with MKZ and 1.1g with GQ/H.

All of the three analyses are plotted together for comparison and the mean of response spectra of eight motions from the three analyses are calculated and shown in Appendix D.25-26.

A similar pattern was observed in all sites on the response spectra. It was found that the nonlinear analysis predicted less amplification than the EQL analysis for small periods (0.03 sec) due to the phase incoherence introduced at high frequencies, greater amplification for periods between 0.03 and 0.2 sec. This difference is caused by: (1) high-frequency amplification in the NL analysis caused by instantaneous changes in stiffness upon stress reversal and (2) over-damping of high frequencies in EQL analysis at larger strains. The NL predicted lesser amplification than the EQL analysis at the natural period of the sites. This difference is caused by the continuously-varying softened properties used in nonlinear analysis as opposed to constant, strain-compatible properties used by EQL analysis (Rathje and R., 2011).

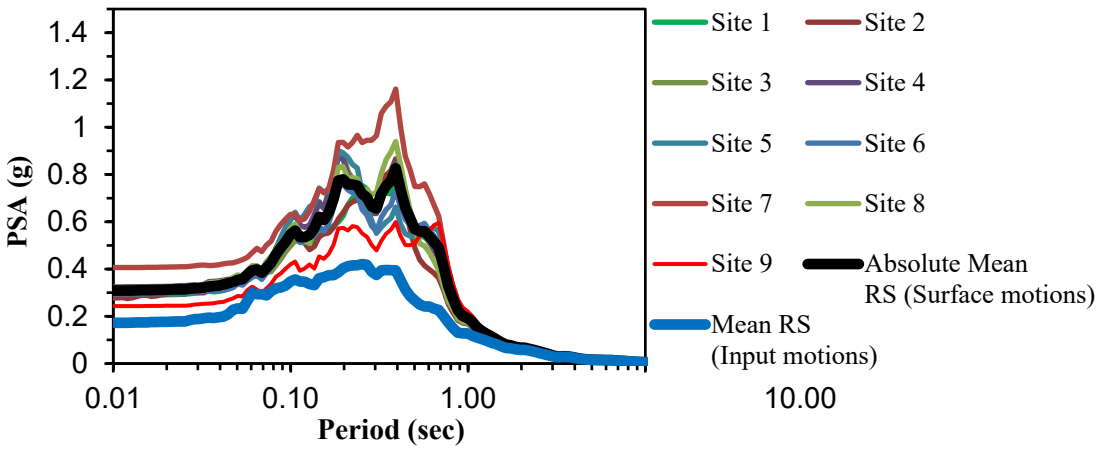

(a)

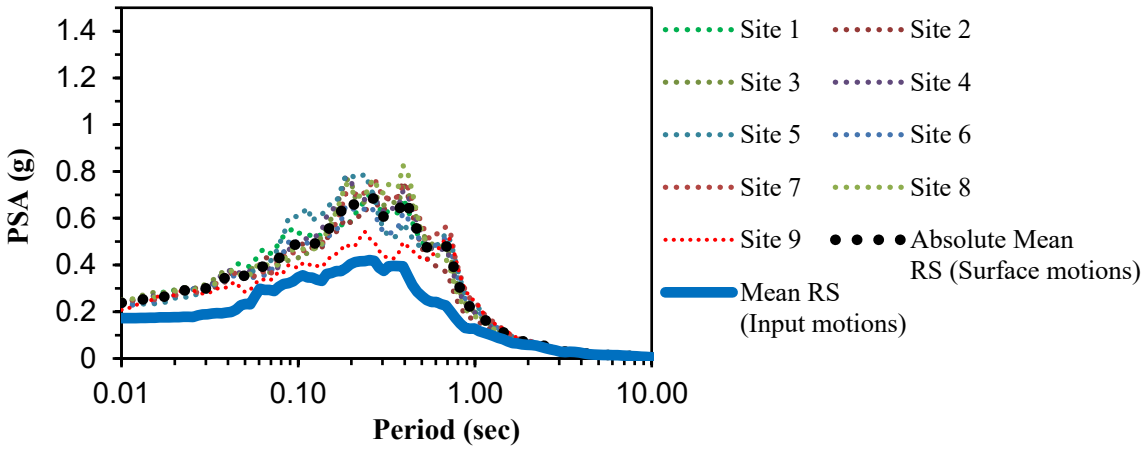

(b)

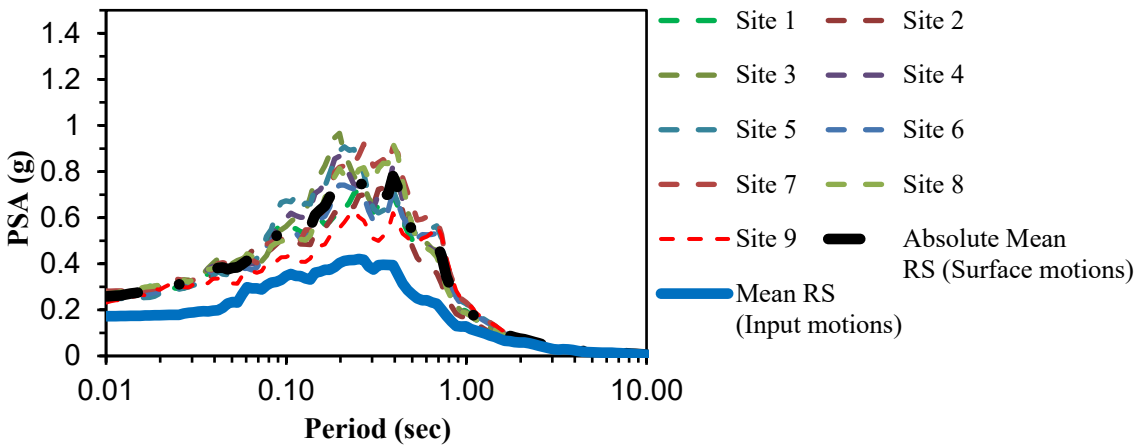

(c)

Figure 4-8: Mean response spectra of all sites with (a) EQL (b) MKZ (GQ/H) analyses.

A similar trend is observed for almost all mean response spectra of the sites, as shown in Figure 4-8. The predominant period is in the range of 0.1-0.5 sec, and no amplification is observed after 2 sec.

4.1.3 Comparison with Code Specified Design Spectra

Based on the V_{S30} values from Site 1 to Site 9 can be classified as site class C. Absolute mean response spectra were obtained after combining all sites' mean response spectra at the surface. Figure 4-9 shows a comparison of the absolute mean response spectra with the design spectra of EN 1998:2015 and NEHRP 2015 for the corresponding site class C.

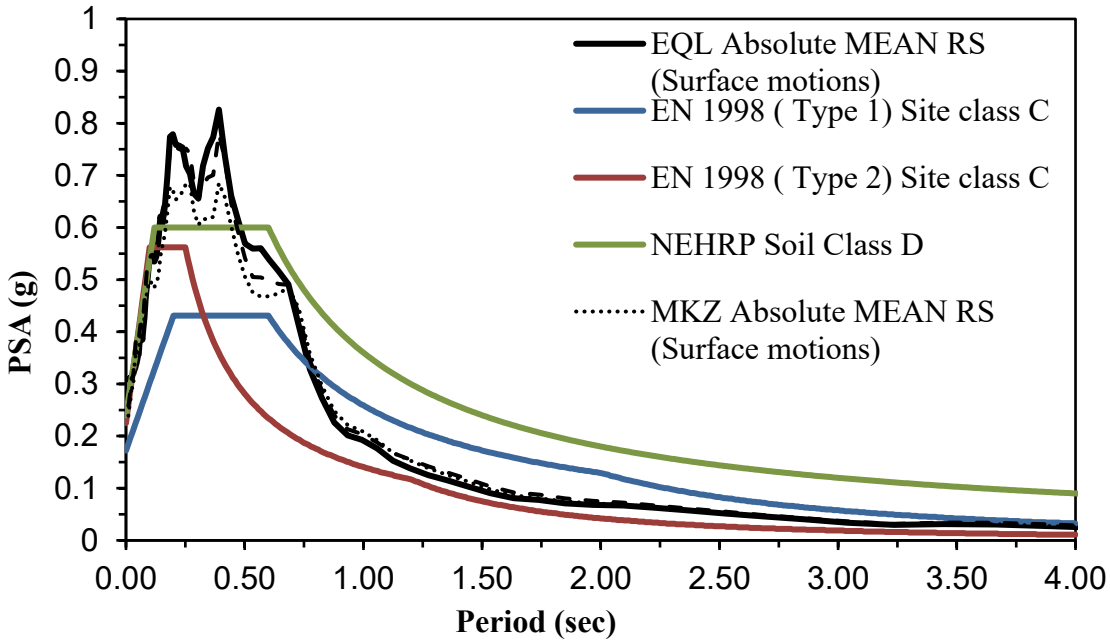

Figure 4-9: Comparison of the absolute mean response spectra against the codes design spectra.

The response spectra by the EQL analysis is greater of both MKZ and GQ/H models with period ranging from 0.01 to 0.82 sec, lesser between 0.82 and 1.97 sec and the same after 2 sec. GQ/H model gives less spectra value at period of 0.01 sec than EQL and the difference is not observed when we go towards to the right. GQ/H model lie close to the EQL response spectra in most period ranges. MKZ model gives lesser spectral value than both EQL and GQ/H models. The nonlinear with MKZ model response spectra is lower than the EQL and nonlinear with GQ/H model response spectra and at some points even matches with the design spectra of NEHRP:2015. It can be concluded that the nonlinear analysis with MKZ model gives lesser spectral values than the two models for the reason that it will allow energy dissipation in the analysis.

Design response spectra EN 1998:2015 have two different levels of seismic action: Type 1 spectra recommended for regions with earthquakes that contribute to a surface magnitude Ms greater than 5.5 and Type 2 spectra recommended for regions with Ms ≤5.5. Type 1 spectra has more energy in a long period motions while Type 2 spectra has less energy in long period motions and has greater spectral amplitude magnitude at short periods.

The response spectra of the three analyses is greater of both the design response spectra of EN 1998:2015 and NEHRP:2015 between a period of 0.12 and 0.68 sec. It is shown that the design response design spectra of both codes underestimate the spectral acceleration considerably and becomes more pronounced with a period of range of 0.14-0.56 sec. The response spectra of the three analyses is less than the design spectra of EN 1998:2015 (Type 1) and NEHRP:2015 period after 0.82 sec while it is still greater than the design response spectra of EN 1998:2015 (Type 2). As a result both design spectra (EN 1998:2015 (Type 1) and NEHRP:2015) tend to become conservative while moving towards long periods and underestimate at short periods. The design spectra of NEHRP:2015 is more close to the absolute mean spectra than that of EN 1998:2015. Worku (2014) showed that the NEHRP design spectra supported by evidence by reviewing authors works (Borcherdt 1994; Rodriguez-Marek et al1999; Borcherdt & Fumal 2000; Dobry et al 2000; Dobry & Susumu 2000; Borcherdt 2002; Crouse & McGuire 2002; Stewart et al 2003).

The response spectra of the analyses showed that the codes failed to provide the representative spectral for buildings ranging from one to seven stories (periods from 0.1 to 0.76 sec); these kind of buildings are dominating in the study area and will aggravate the problem.

CHAPTER 5
CONCLUSIONS AND RECOMMENDATIONS

5.1 Conclusions

One-dimensional equivalent linear and nonlinear site response analyses have been conducted at nine sites in Adama. The shear wave profiles of the sites were acquired using geophysical tests, which were incorporated into the DEEPSOIL model. Geotechnical data that was collected from different organizations, including information on soil type and penetration resistance, were also used to estimate the shear wave velocity and the dynamic soil properties of the different soil layers. Input ground motions were selected from areas having the same geological and seismic conditions as the sites. According to the obtained results, the following conclusions have been drawn:

- By combining refraction, MASW, and MAM, shear wave profiles up to a depth of 50 m were acquired – whereas MASW mapped the top shear wave velocity profiles, MAM mapped the bottom shear wave profiles. The horizontal polarized shear wave velocity was obtained without correlating with the P-wave, and the transverse anisotropy of the sites were mapped. Using all the geophysical methods together increased the reliability of the results, boosted the advantages of each single method, and the methods were shown to be coherent with each other.
- The average shear wave velocity for a depth of 30 m (V_{S30}) of the four geophysical and the five geotechnical sites varied from 225 to 332.5 m/sec and were used for site classification as per EN 1998:2015 and NEHRP:2015. All the sites are classified as site class C according to EN:1998 and site class D according to NEHRP.
- Poisson's ratio was estimated using the relation between compressional and shear waves. The Poisson's ratio of the sites were in the range of 0.3-0.35, which falls under the category of silty soil, according to Sharma et al. (1990) and agrees with geotechnical investigations.
- All the sites showed significant amplification - input ground motions of 0.15g at bedrock level were amplified to the range of 0.20g to 0.56g, 0.17g to 0.30g and 0.19g to 0.35g for EQL, MKZ and GQ/H model respectively. In other words, an amplification factor in the range of 1.30 to 3.73, 1.15 to 2.00, 1.25 to 2.36 was

observed for EQL, MKZ and GQ/H model. The MKZ and GQ/H models resulted in lesser amplification reflecting the energy dissipation associated with large strains.

- The displacement profiles of the sites were increased from zero at the bedrock level and reached its peak value ranging from 0.43 to 3.51 cm, 0.32 to 3.65 cm, 0.32 to 3.51 cm for EQL, MKZ and GQ/H model respectively, at the top of the layer.
- The shear strain profiles have shown noticeable changes after 15 m, and sharp peak maximum shear strains were obtained in the range from 0.12% to 0.90%, 0.20% to 0.67%, 0.11% to 0.46% for EQL, MKZ and GQ/H respectively, for depths between 15 and 0.5 m for all evaluated sites. The nonlinear models predict strain profiles of the soil deposits that are in contrast with EQL results and simulate the actual mechanism of dissipation of energy.
- The MKZ model underestimate the shear strength of the layers unlike GQ/H model which induces high strain than the GQ/H model at a depth immediately above the interface between the top two layers with high impedance contrast.
- An acceptable agreement is found between the EQL results and the nonlinear results for sites, where the maximum shear strain is less than 0.4%; which is in line with the study of Kaklamanos et al. (2013), who recommended that the EQL analysis is can be used for strains value of between 0.2-0.4% in absence of nonlinear analysis.
- The ES EN 1998:2015 and NEHRP:2015 building code design response spectra were used for comparison with the average site response spectra of the sites. Both code design response spectra underestimate the response of the sites for periods in the range of 0.21-0.39 sec. It may thus be suggested that the design response spectrum of ES EN 1998:2015 needs revisiting at least for site class C as established for the sites

5.2 Recommendations

Further analyses could be conducted to investigate the potential bias introduced in our results by: the scaling of the input motions used within site response analysis, correlation of SPT value to get shear wave velocities and shear strength of soil, representing the city with fewer sites, assumed PI value at some sites depths and using of secondary data. Despite these limitations the selected sites showed amplification potential of the soil which underestimated by the EN 1998:2015 design spectra for an important range of periods

representing most structures. We recommend, a detailed and city-wide investigation that could lead to a microzonation map useable for development plans.

REFERENCES

Aki, K. and Richards, P. G. (1980). Quantitative seismology. Sausalito, CA, University Science Books.

Alula, D. (1992). Geological map of the Nazret-Dera Region (main Ethiopian rift). [Firenze], S.E.L.C.A.

Ameratunga, J., Sivakugan, N. and Das, B. M. (2015). Correlations of Soil and Rock Properties in Geotechnical Engineering, Springer.

Anbazhagan, P., Uday, A., Moustafa, S. S. R. and Al-Arifi, N. S. N. (2016). "Correlation of densities with shear wave velocities and SPT N values." Journal of Geophysics and Engineering 13(3): 320-341.

Asfaw, L. M. (1998). "Environmental hazard from fissures in the Main Ethiopian Rift." Journal of African Earth Sciences 27(3): 481-490.

Ayele, A. (2017). "Probabilistic seismic hazard analysis (PSHA) for Ethiopia and the neighboring region." Journal of African Earth Sciences 134: 257-264.

Boccaletti, M., Bonini, M., Mazzuoli, R., Abebe, B., Piccardi, L. and Tortorici, L. (1998). "Quaternary oblique extensional tectonics in the Ethiopian Rift (Horn of Africa)." Tectonophysics 287(1): 97-116.

Bommer, J., Stafford, P. and E. Alarcon, J. (2009). Empirical Equations for the Prediction of the Significant, Bracketed, and Uniform Duration of Earthquake Ground Motion.

Boore, D. (2004). "Estimating s(30) (or NEHRP Site Classes) from Shallow Velocity Models (Depths < 30 m)." Bulletin of the Seismological Society of America 94: 591-597.

Boore, D. (2016). "Determining generic velocity and density models for crustal amplification calculations, with an update of the Boore and Joyner (1997) Generic Site Amplification for Graphic Site Amplification." Bulletin of the Seismological Society of America 106(1): 316-320.

BSSC (2015). NEHRP Recommended seismic provisions for new buildings and other structures. Building Seismic Safety Council, Federal Emergency Management Agency, Washington D.C, in press. .

Celebi, M., Prince, J., Dietel, C., Onate, M. and Chavez, G. (1987). "The Culprit in Mexico City—Amplification of Motions." Earthquake Spectra 3(2): 315-328.

Central Statistical Authority (CSA) (2012). "Population and Housing Census of Ethiopia: Administrative Report By Central Statistical Authority, (April).".

Chávez-García, F. and Faccioli, E. (2000). "Complex site effects and building codes: Making the leap." Journal of Seismology 4: 23-40.

Darendeli, B. M. (2001). Development of a new family of normalized modulus reduction and material damping curves. PhD dissertation, University of Texas at Austin,Texas, USA.

Darendeli, M. (2001). Development of New Family of Normalized Modulus Reduction and Material Damping Curves.

EBCS-8 (1995). Code of Standards for Seismic Loads. Ministry of Works and Urban Development, Addis Ababa, Ethiopia.

ES EN 1998:2015 Ministry of Construction Design of structures for earthquake resistance. Ethiopian Standards based on Euro Norms (EBCS EN 1998:2015), Addis Ababa.

Furi, W., Razack, M., Haile, T., Abiye, T. A. and Legesse, D. (2011). "The hydrogeology of Adama-Wonji basin and assessment of groundwater level changes in Wonji wetland, Main Ethiopian Rift: results from 2D tomography and electrical sounding methods." Environmental Earth Sciences 62(6): 1323-1335.

Geometrics, I., 2016, SeisImager manual—windows software for analysis of surface waves, ver. 1.2: Geometrics, Inc.,74 p.

Getahun, K. (1987). "Hydrogeology of Nazreth area, NC 37-15 Ethiopian Institute of Geological Surveys." Ministry of Mines and Energy (unpublished report). .

Giardini, D. (1999). The Global Seismic Hazard Assessment Program (GSHAP)-1992/1999.

Gibbs, J. F., Fumal, T. E., Boore, D. M. and Joyner, W. B. (1992). Seismic velocities and geologic logs from borehole measurements at seven strong-motion stations that recorded the 1989 Loma Prieta earthquake. Open-File Report.

Gibbs, J. F., Fumal, T. E., Boore, D. M. and Joyner, W. B. (1992). "Seismic Velocities and Geologic Logs from Borehole Measurements at Seven Strong-Motion Stations That Recorded the Loma Prieta Earthquake," U. S. Geological Survey Open-File Report 92-287, Menlo Park, California.

Groholski, D., R., Hashash, Y., M. A., Kim, B., Musgrove, M., Harmon, J. and Stewart Jonathan, P. (2016). "Simplified Model for Small-Strain Nonlinearity and Strength in 1D Seismic Site Response Analysis." Journal of Geotechnical and Geoenvironmental Engineering 142(9): 04016042.

Haines, S. S. (2007). A Hammer-Impact, Aluminum, Shear-Wave Seismic Source. Open-File Report.

Hasbrouck, W. P. (1983). Sketches of a hammer-impact, spiked-base, shear-wave source. Open-File Report.

Haselton, C. B., Baker, J. W., Stewart, J. P., Whittaker, A. S., Luco, N., Fry, A., Hamburger, R. O., Zimmerman, R. B., Hooper, J. D., Charney, F. A. and Pekelnicky, R. G. (2017). "Response History Analysis for the Design of New Buildings in the NEHRP Provisions and ASCE/SEI 7 Standard: Part I - Overview and Specification of Ground Motions." Earthquake Spectra 33(2): 373-395.

Hashash, Y. M. A., Musgrove, M. I., Harmon, J. A., Ilhan, O., Xing, G., Groholski, D., Phillips, C. A. and Park, D. (2020). DEEPSOIL V7.0, User Manual. Urbana, IL, Board of Trustees of University of Illinois at Urbana-Champaign.

Hashash, Y. M. A. and Park, D. (2001). "Non-linear one-dimensional seismic ground motion propagation in the Mississippi embayment." Eng. Geol., 62(1–3), 185–206.

Hatanaka, M. and Uchida, A. (1996). "Empirical Correlation Between Penetration Resistance and Internal Friction Angle of Sandy Soils." Soils and Foundations 36(4): 1-9.

Kaklamanos, J., Bradley, B. A., Thompson, E. M. and Baise, L. G. (2013). "Critical Parameters Affecting Bias and Variability in Site-Response Analyses Using KiK-net Downhole Array Data." Bulletin of the Seismological Society of America 103(3): 1733-1749.

Kausel, E. and Roësset, J. M. (1981). "Stiffness matrices for layered soils." Bulletin of the Seismological Society of America 71(6): 1743-1761.

Kebede, F. and van Eck, T. (1997). "Probabilistic seismic hazard assessment for the Horn of Africa based on seismotectonic regionalisation." Tectonophysics 270: 221-237.

Kondner, R. L. and Zelasko, J. S. (1963). "Hyperbolic stress-strain formulation of sands." 2nd pan American Conf. on Soil Mechanics and Foundation Engineering, Associação Brasileira de Mecânica dos Solos, São Paulo, Brazil.

Kramer, S. L. (1996). Geotechnical earthquake engineering. Prentice Hall, Upper Saddle River.

Lee, N. K. J. (1993). Experimental Study of Body Wave Velocities in Sand Under Anisotropic Conditions. Ph.D. Dissertation, University of Texas at Austin.

Martin, G., Lew, M., Arulmoli, K., Baez, J., Blake, T., Earnest, J., Gharib, F., Goldhammer, J., Hsu, D., Kupferman, S., O'Tousa, J., Real, C., Reeder, W., Simantob, A. and Youd, T. (1999). "Recommended Procedures For Implementation of DMG Special Publication 117 Guidelines for Analyzing and Mitigating Liquefaction Hazard in California." Los Angeles, USA: The Southern California Earthquake Center.

Masing, G. (1926). "Eigenspannungen und Verfestigung beim Messing." 2nd Int. Congress on Applied Mechanics, Orell FüssliZurich.

Matasovic, N. (1993). Seismic response of composite horizontally-layered soil deposits.

Mohr, P. A. (1963). "Geological Map of the Horn of Africa, Scale 1:2,000,000." London, Philip and Tacey.

Newmark, N. M. (1959). A method of computation for structural dynamics, American Society of Civil Engineers.

Park, C. and Carnevale, M. (2010). Optimum MASW survey - Revisit after a Decade of Use.

Park, C., Miller, R. and Miura, H. (2002). "Optimum Field Parameters of an MASW Survey." SEG-J, Tokyo.

Park, C., Miller, R., Ryden, N., Xia, J. and Ivanov, J. (2005). "Combined Use of Active and Passive Surface Waves." Journal of Environmental and Engineering Geophysics 10: 323-334.

Park, C., Miller, R. and Xia, J. (1998). "Imaging dispersion curves of surface waves on multi-channelrecord." SEG Expanded Abstracts 17.

Park, C., Miller, R. and Xia, J. (1999). "Multichannel analysis of surface waves (MASW)." Geophysics 64.

Park, C. and Shawver, J. B. (2009). MASW survey using multiple source offsets.

Park, C. B. (2019). "Data acquisition. Retrieved 23 May, 2019." from http://www.masw.com/DataAcquisition.html.

Phillips, C. and Hashash, Y. (2009). "Damping formulation for nonlinear 1D site response analyses." Soil Dynamics and Earthquake Engineering 29: 1143-1158.

Pyke, M. (1979). "Nonlinear Soil Models for Irregular Cyclic Loadings." Journal of the Geotechnical Engineering Division 105(6): 715-726.

Rathje, E. M. and R., K. A. (2011). "Relative differences between equivalent-linear and nonlinear site response methods. ." 5th International Conference on Earthquake Geotechnical Engineering. Santiago, Chile.

Richart, F. E., Hall, J. R. and Woods, R. D. (1970). Vibrations of soils and foundations. Englewood Cliffs, N.J., Prentice-Hall.

Schnabel, P. B., Lysmer, J., Seed, H. B., University of California, B., College of, E., University of California, B., Earthquake Engineering, C. and National Science, F. (1972). SHAKE: a computer program for earthquake response analysis on horizontally layered sites. Berkeley, University of California College of Engineering.

Seed, H. B., Wong, R. T., Idriss, I. M. and Tokimatsu, K. (1986). "Moduli and Damping Factors for Dynamic Analyses of Cohesionless Soils." Journal of Geotechnical Engineering 112(11): 1016-1032.

Seed, R. B., Dickenson, S. E., Riemer, M. F., Bray, J. D., Sitar, N., Mitchell, J. K., Idriss, I. M., Kayen, R. E., Kropp, A., Harder, L. F., Power , J. and Power, M. S. (1990). Preliminary Report On the Principal Geotechnical Aspects of the October 17, 1989 Loma Prieta Earthquake, University of California, Berkeley Earthquake Engineering Research, Center.

Sharma, H. D., Dukes, M. T. and Olsen, D. M. (1990). Field Measurements of Dynamic Moduli and Poisson's Ratios of Refuse and Underlying Soils at a Landfill Site. A. Landva and G. D. Knowles. West Conshohocken, PA, ASTM International: 57-70.

Sheriff, R. E., 1991, Encyclopedic dictionary of exploration geophysics: Soc. Expl. Geophys.

Sjogren, B. (1984). Shallow Refraction Seismics. USA, Chapman and Hall.

Stewart, J., Afshari, K. and Hashash, Y. (2014). Guidelines for performing hazard-consistent one-dimensional ground response analysis for ground motion prediction.

Stewart, J. P. (2008). Benchmarking of nonlinear geotechnical ground response analysis procedures. Berkeley, Calif. :, Pacific Earthquake Engineering Research Center.

Stone, W. C., United, S. and National Bureau of, S. (1987). Engineering aspects of the September 19, 1985 Mexico earthquake. Gaithersburg, MD; Washington, DC, U.S. Dept. of Commerce, National Bureau of Standards ; For sale by the Supt. of Docs., U.S. G.P.O.

Uzielli, M., Mayne, P. and Cassidy, M. (2012). Probabilistic assignment of design strength for sands from in-situ testing data: 214-227.

Vucetic, M. and Dobry, R. (1991). "Effect of Soil Plasticity on Cyclic Response." Journal of Geotechnical Engineering 117(1): 89-107.

Wair, B., DeJong, J. and Shantz, T. (2012). "Guidelines for Estimation of Shear Wave Velocity Profiles." Pacific earthquake engineering research center.

Wolfenden, E., Ebinger, C., Yirgu, G., Deino, A. and Ayalew, D. (2004). "Evolution of the northern Main Ethiopian rift: birth of a triple junction." Earth and Planetary Science Letters 224(1): 213-228.

Woods, R. D. (1978). Measurement of Dynamic Soil Properties, State of the Art Report: Proceedings of the ASCE Geotechnical Engineering Division Specialty Conference, Earthquake Engineering a nd Soil Dynamics, Pasadena, CA. 1, 91-178.

Worku, A. (2011). "Recent developments in the definition of design earthquake ground motions calling for a revision of the current Ethiopian seismic code - EBCS 8: 1995." Zede - Journal of EEA 28: 1-15.

Worku, A. (2014). "The status of basic design ground motion provisions in seismic design codes of sub-Saharan African countries: A critical review." Journal of the South African Institution of Civil Engineering 56: 40-52.

Xia, J. (2014). "Estimation of near-surface shear-wave velocities and quality factors using multichannel analysis of surface-wave methods." Journal of Applied Geophysics 103.

Xia, J., Miller, R. and Park, C. (1999). "Estimation of near-surface shear-wave velocity by inversion of Rayleigh waves." Geophysics 64.

Xia, J., Miller, R., Xu, Y., Luo, Y., Chao, C., Liu, J., Ivanov, J. and Zeng, C. (2009). "High-frequency Rayleigh-Wave method." Journal of Earth Science 20: 563-579.

Xia, J., Miller, R. D., Park, C. B., Hunter, J. A., Harris, J. B. and Ivanov, J. (2002). "Comparing shear-wave velocity profiles inverted from multichannel surface wave with borehole measurements." Soil Dynamics and Earthquake Engineering 22(3): 181-190.

Yoshida, N. (2015). Seismic Ground Response Analysis. Dordrecht, Springer.

Zeng, C., Xia, J., Miller, R., Tsoflias, G. and Wang, Z. (2012). "Numerical investigation of MASW applications in presence of surface topography." Journal of Applied Geophysics 84: 52–60.

APPENDIX A

GEOPHYSICAL INVESTIGATION RESULTS

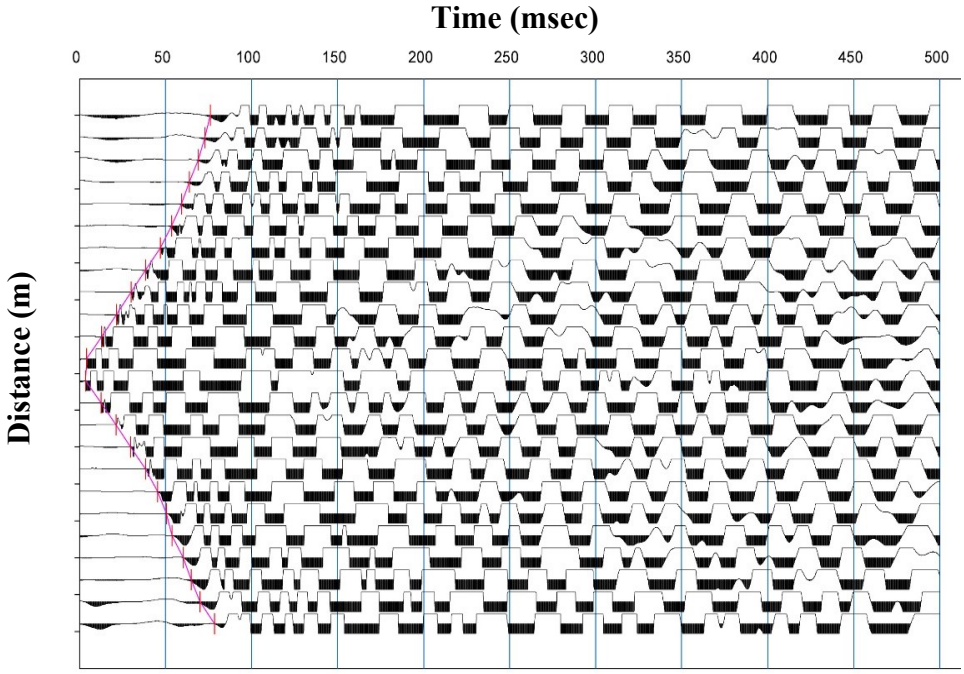

Figure A.1: First-arrival picks of P-wave represented by red lines for the shot location at 34.5 m for Site 2.

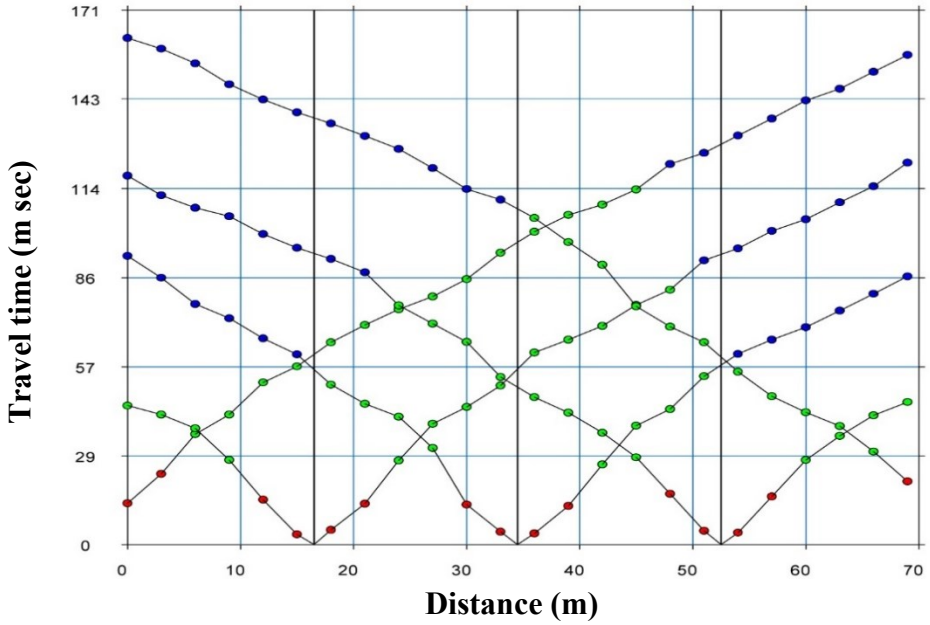

Figure A.2: Travel time curves of P-wave for all field shots at Site 2-Amede youth center.

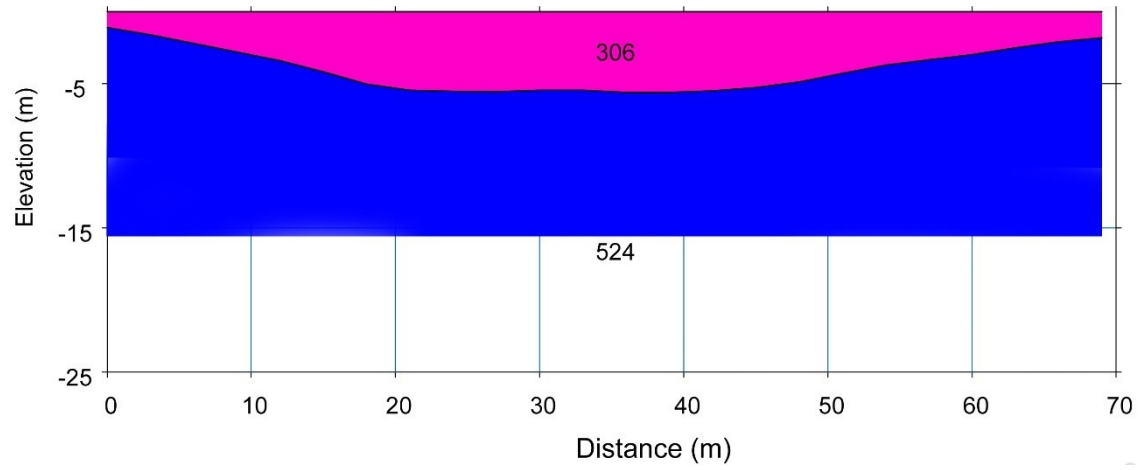

Figure A.3: P-wave velocity of Site 2: Amede Youth Center site using time-term inversion.

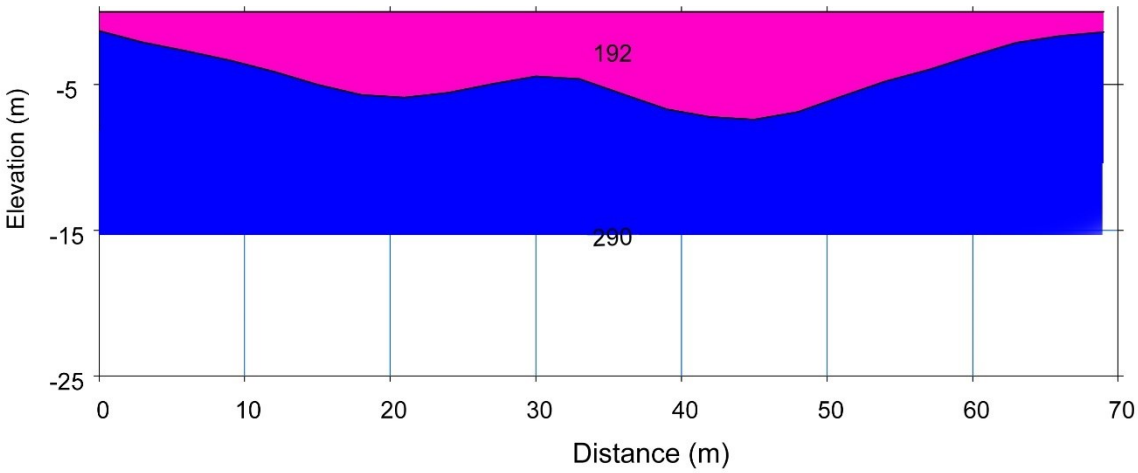

Figure A.4: S_H-wave velocity of Site 2: Amede Youth Center site using time inversion.

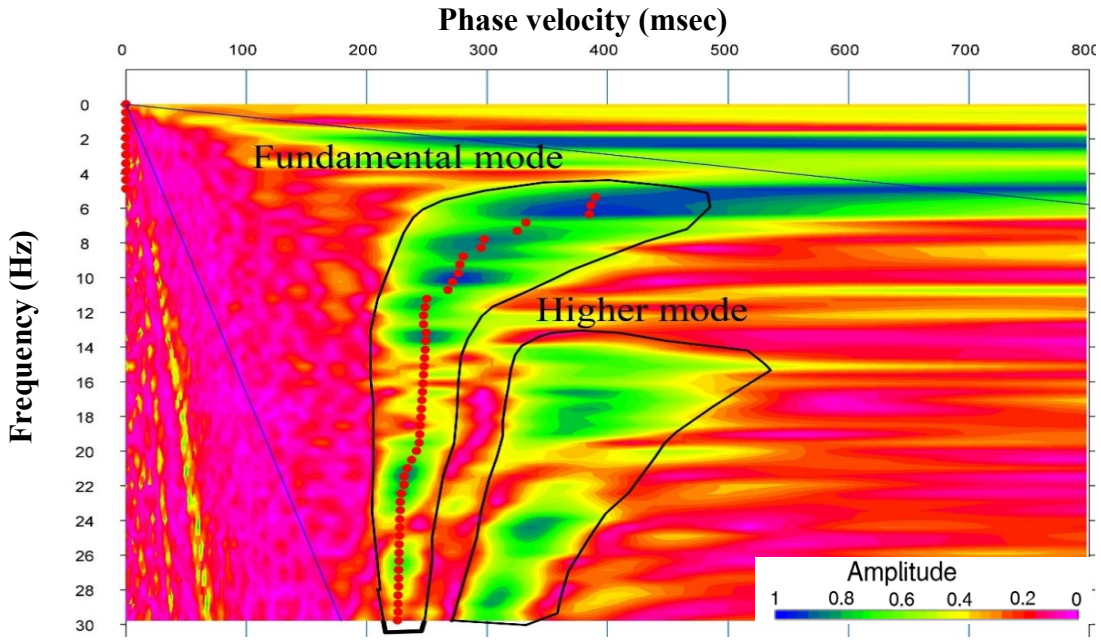

Figure A.5: Dispersion image of Site-2: Amede Youth Center using MASW.

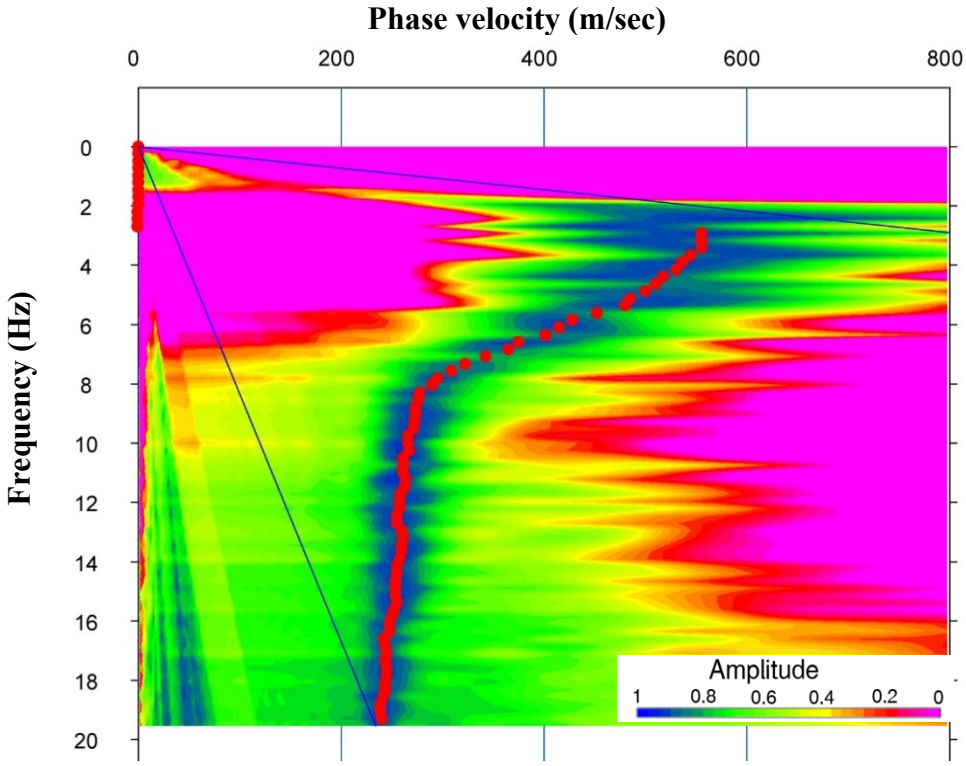

Figure A.6: Dispersion image of Site-2: Amede Youth Center using linear MAM.

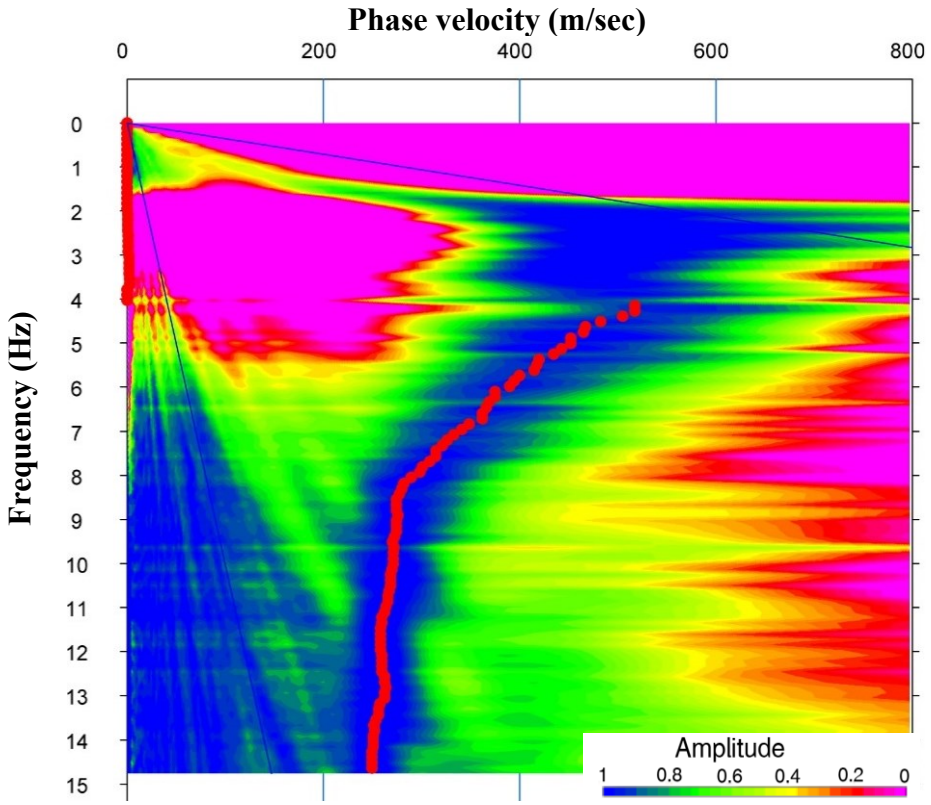

Figure A.7: Dispersion image of Site-2: Amede Youth Center using L-shape MAM.

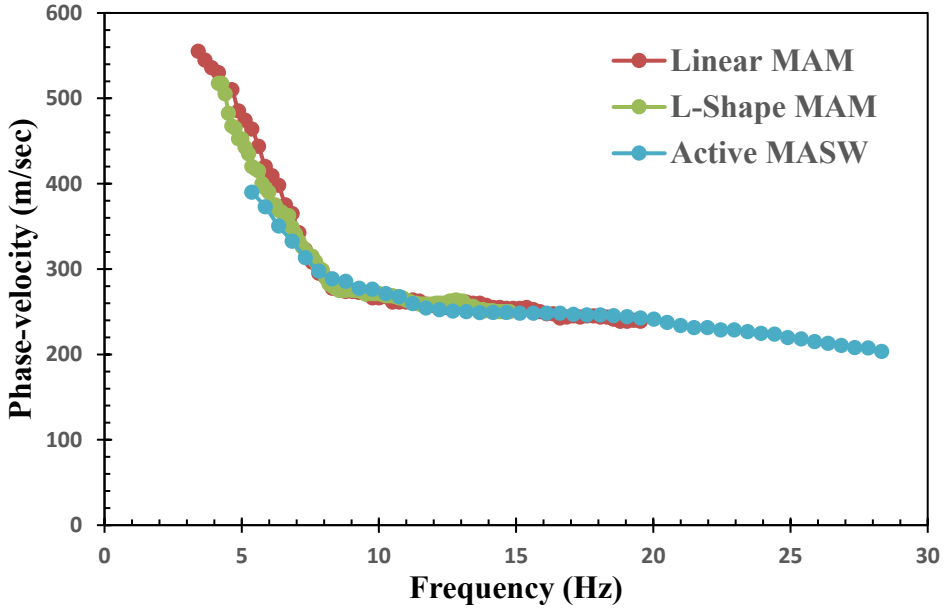

Figure A.8: Dispersion curve of active MASW, linear MAM, and L-shape MAM for Site 2.

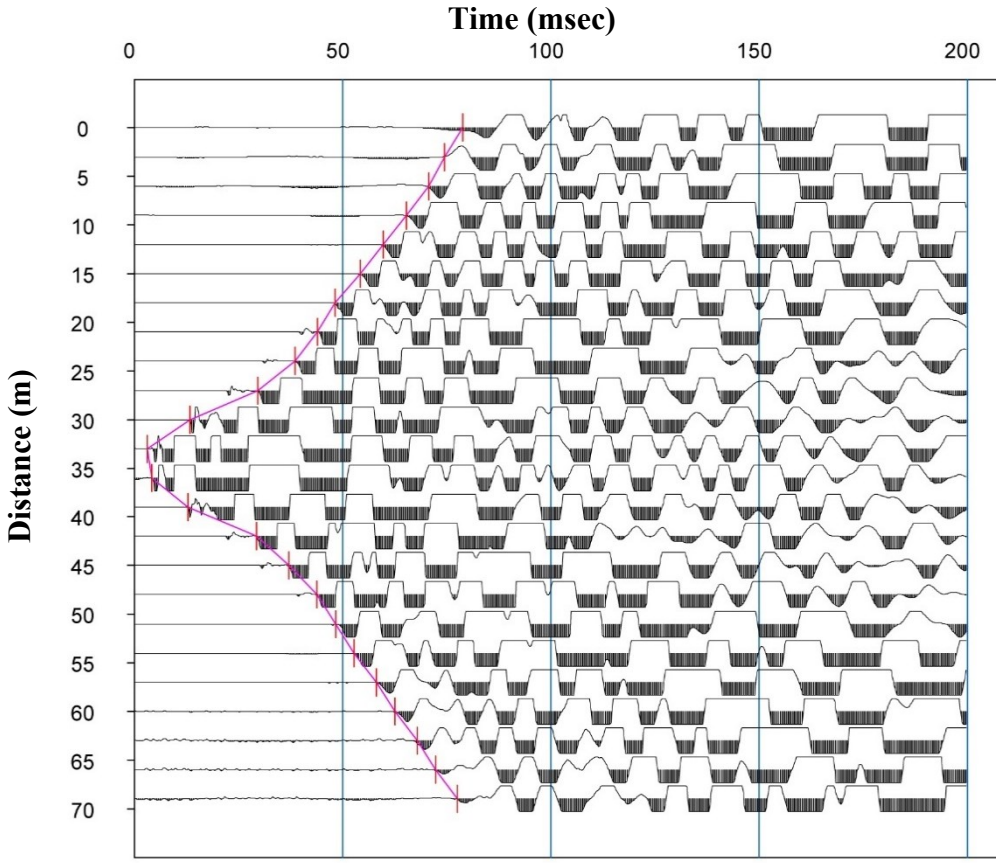

Figure A.9: First-arrival picks represented by red lines for the shot location at 34.5m for Site 3.

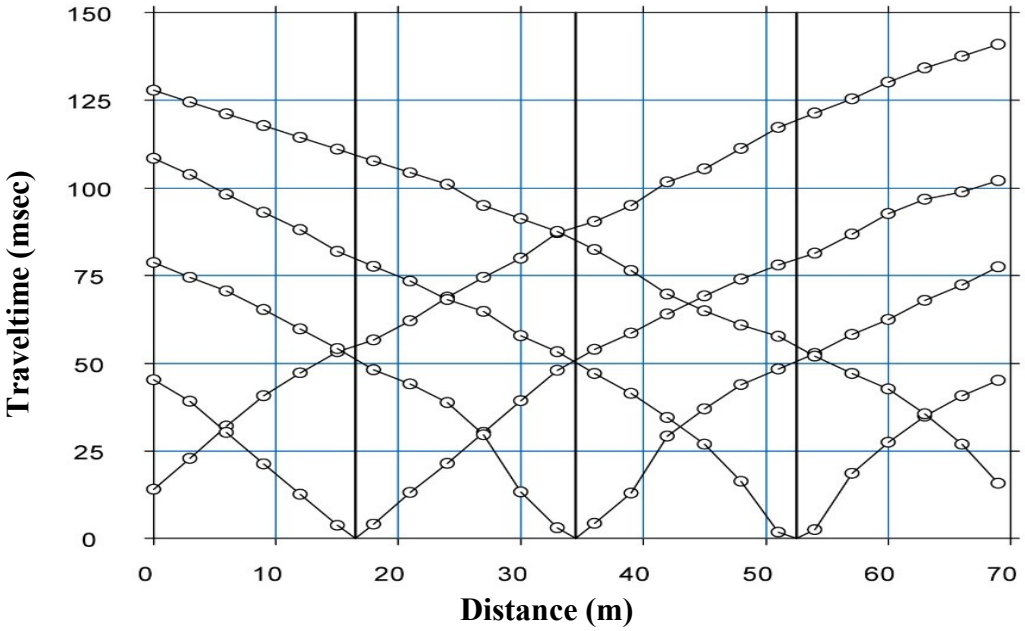

Figure A.10: Travel time curves of P-wave for all field shots at Site 3: Kebele 04 Youth Center.

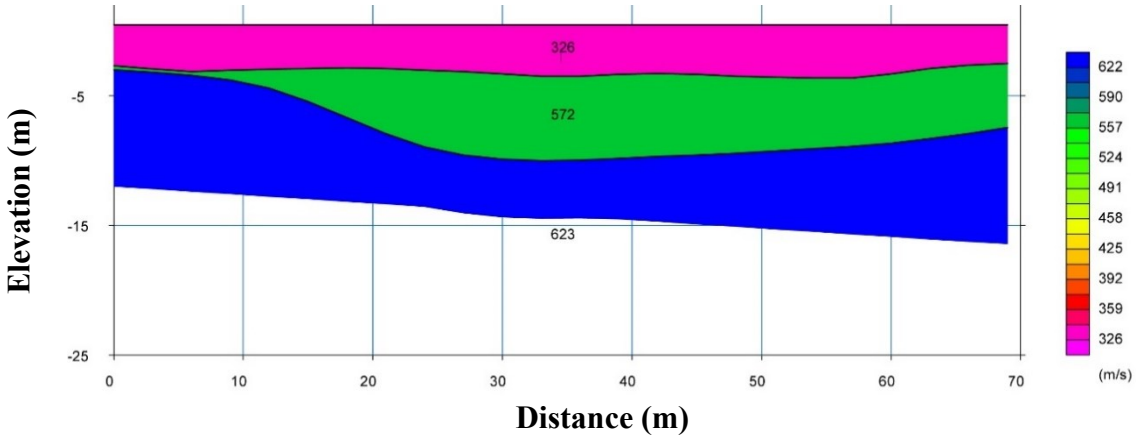

Figure A.11: P-wave velocity of Site 3: Kebele 04 Youth Center site using time inversion. Time (msec).

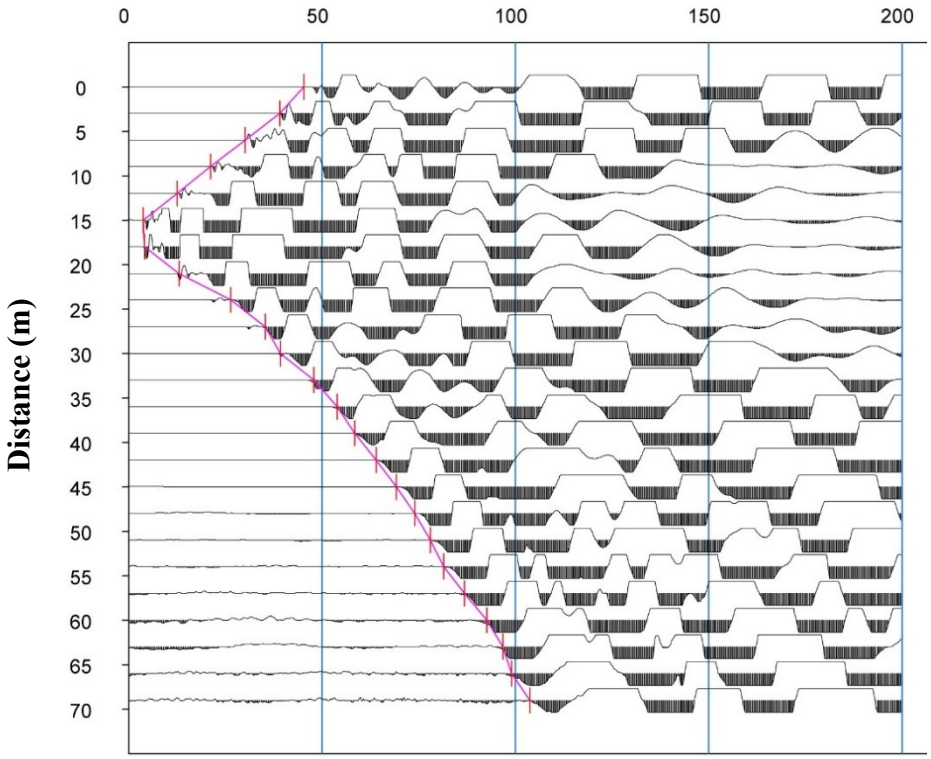

Figure A.12: First-arrival picks represented by red lines for the shot location at 34.5m for Site 4.

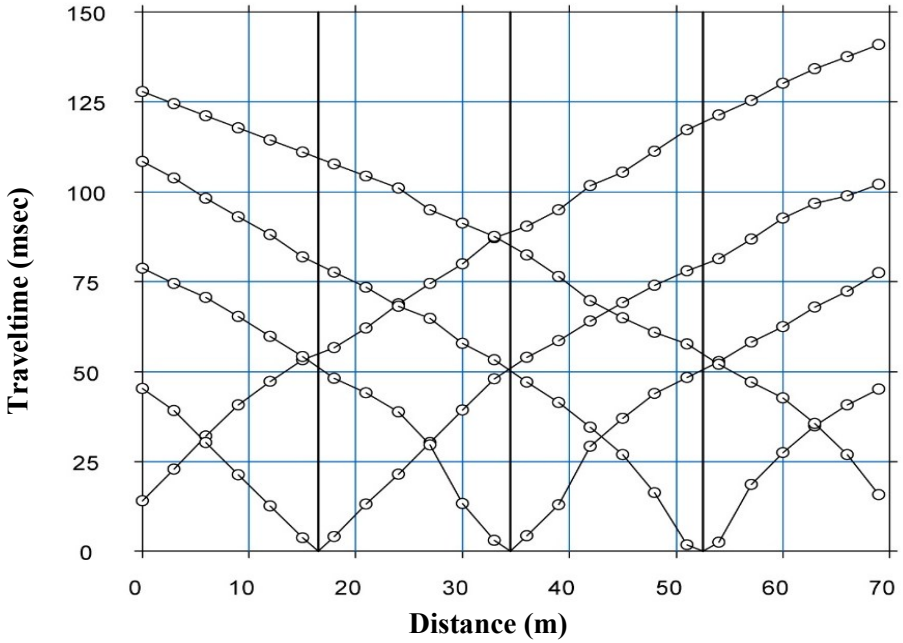

Figure A.13: Travel time curves of P-wave for all field shots at Site 4: Doro Erbata.

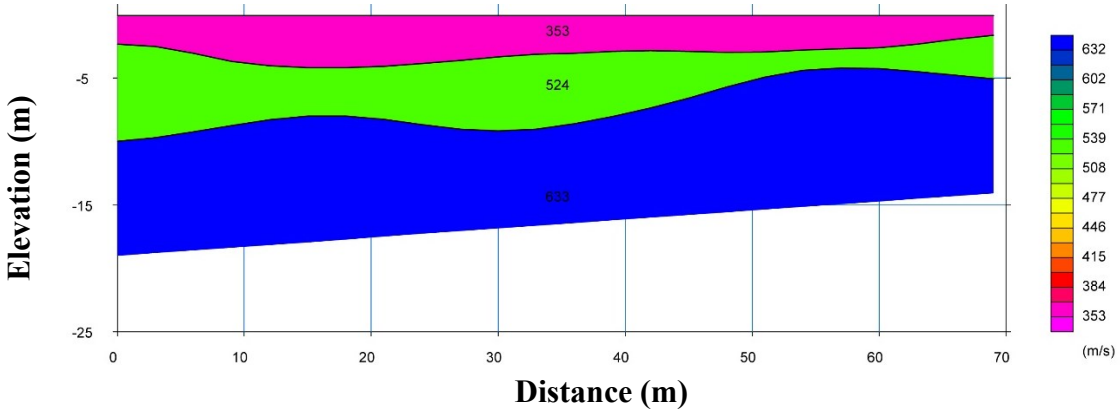

Figure A.14: P-wave velocity of Site 4-Doro Erbata site using time-term inversion.

APPENDIX B

REFERENCE TABLES

Table B.1: Boore [2004] regression coefficients.

Depth (m)	Regression Coefficients	
	a	b
10	4.21E-02	1.03E+00
11	2.21E-02	1.03E+00
12	1.26E-02	1.04E+00
13	1.42E-02	1.03E+00
14	1.23E-02	1.03E+00
15	1.38E-02	1.03E+00
16	1.39E-02	1.02E+00
17	1.96E-02	1.02E+00
18	2.49E-02	1.01E+00
19	2.56E-02	1.01E+00
20	2.54E-02	1.01E+00
21	2.53E-02	1.01E+00
22	2.69E-02	1.00E+00
23	2.22E-02	1.00E+00
24	1.69E-02	1.00E+00
25	1.15E-02	1.00E+00
26	6.56E-03	1.00E+00
27	2.52E-03	1.00E+00
28	7.73E-04	1.00E+00
29	4.31E-04	1.00E+00

Table B.2:Corrections to Field SPT N-Values (Martin et al., 1999)

Factor	Equipment Variable	Term	Correction
Overburden Pressure		C_N	$(P_a / \sigma'_{vo})^{0.5}$; $0.4 \leq C_N \leq 2$ *
Energy Ratio	Safety Hammer Donut Hammer Automatic Trip Hammer	C_E	0.60 to 1.17 0.45 to 1.00 0.9 to 1.6
Borehole Diameter	65 mm to 115 mm 150 mm 200 mm	C_B	1.0 1.05 1.15
Rod Length**	3 m to 4 m 4 m to 6 m 6 m to 10 m 10 m to 30 m >30 m	C_R	0.75 0.85 0.95 1.0 <1.0
Sampling Method	Standard Sampler Sampler without liners	C_S	1.0 1.2

APPENDIX C
DEEPSOIL INPUT PARAMETERS

Site characteristics that used in site response analysis.

Table C.1: The shear-wave velocity profile for the Site 2: Amede High School site.

Depth (m)	Thickness (m)	Soil Type	Vs (m/s)	Shear Strength (kPa)
0	1.8	Sandy silt	250	21.6
1.8	2	Sandy silt	254	54.2
3.8	2.4	Sandy silt	269	91.1
6.2	2.6	Sandy silt	276	130.2
8.8	2.9	Sandy silt	272	167.6
11.7	3.1	Sandy silt	301	222.9
14.8	3.5	Sandy silt	356	303.5
18.3	3.7	Sandy silt	410	399.8
22	4	Sandy gravel	459	508.5
26	4.2	Sandy gravel	501	626.3
30.2	4.6	Sandy gravel	536	752.0
34.8	4.8	Sandy gravel	577	899.8
39.6	5	Sandy gravel	613	1055.3
44.6	7.4	Sandy gravel	639	1233.3
52		Bedrock		

Table C.2: The soil types and model parameters of the Site 2: Amede High School site.

Soil Type	Unit Wt. (kN/m^3)	Darendeli Parameters		
		σ'_m (atm)	PI	OCR
Sandy silt	17.17	0.15	0	1
Sandy silt	17.24	0.48	0	1
Sandy silt	17.50	0.85	0	1
Sandy silt	17.62	1.29	0	1
Sandy silt	17.56	1.77	0	1
Sandy silt	18.03	2.30	0	1
Sandy silt	18.84	2.90	0	1
Sandy silt	19.55	3.58	0	1
Sandy gravel	20.14	4.34	0	1
Sandy gravel	20.60	5.16	0	1
Sandy gravel	20.97	6.07	0	1
Sandy gravel	21.38	7.05	0	1

Sandy gravel	21.72	8.10	0	1
Sandy gravel	21.96	9.44	0	1
Bedrock	24	-	-	-

Table C.3: The shear-wave velocity profile for the Site 3: Kebele 04 Youth Center site.

Depth (m)	**Thickness** (m)	**Soil Type**	**Vs** (m/s)	**Shear Strength (kPa)**
0	2	Sandy silt	143	13.72
2	1.5	Sandy silt	143	32.17
3.5	1.5	Sandy silt	251	68.48
5	5	Sandy silt	251	114.51
10	5	Sandy silt	273	190.36
15	1	Sandy silt	278	232.84
16	1	Sandy silt	278	246.02
17	1	Sandy silt	288	265.09
18	1	Sandy silt	299	285.34
19	1	Sandy silt	303	301.60
20	1	Sandy silt	317	324.84
21	1	Sandy silt	315	337.54
22	1	Sandy silt	327	360.29
23	1	Sandy silt	334	379.90
24	1	Sandy silt	339	398.28
25	1	Sandy silt	348	420.14
26	1	Sandy gravel	346	433.23
27	1	Sandy gravel	358	458.21
28	1	Sandy gravel	353	468.72
29	1	Sandy gravel	356	486.15
30		Bedrock		

Table C.4: The soil types and model parameters of the Site 3: Kebele 04 Youth Center site.

Soil Type	**Unit Wt.** (kN/m^3)	**Darendeli Parameters**		
		σ'_m (atm)	**PI**	**OCR**
Sandy silt	14.83	0.15	10	1
Sandy silt	14.83	0.40	8	1
Sandy silt	17.19	0.64	8	1
Sandy silt	17.19	1.19	6	1
Sandy silt	17.57	2.05	0	1
Sandy silt	17.66	2.58	0	1
Sandy silt	17.66	2.75	0	1
Sandy silt	17.82	2.93	0	1

Sandy silt	18.00	3.10	0	1
Sandy silt	18.06	3.28	0	1
Sandy silt	18.27	3.46	0	1
Sandy silt	18.24	3.64	0	1
Sandy silt	18.42	3.82	0	1
Sandy silt	18.53	4.01	0	1
Sandy silt	18.60	4.19	0	1
Sandy silt	18.73	4.37	0	1
Sandy gravel	18.70	4.56	0	1
Sandy gravel	18.87	4.74	0	1
Sandy gravel	18.80	4.93	0	1
Sandy gravel	18.84	5.12	0	1
Bedrock	24	-	-	-

Table C.5: The shear-wave velocity profile for the Site 4: Doro-erbata site

Depth (m)	**Thickness** (m)	**Soil Type**	**Vs** (m/s)	**Shear Strength (kPa)**
0	2	Sandy silt	155	14.7
2	1.1	Sandy silt	155	32.3
3.1	1.9	Sandy silt	230	62.9
5	2	Sandy silt	230	89.0
7	1.8	Sandy silt	230	113.3
8.8	7.2	Sandy silt	277	191.1
16	1	Sandy silt	285	250.5
17	1	Sandy silt	295	269.8
18	1	Sandy silt	306	290.4
19	1	Sandy silt	310	306.9
20	1	Sandy silt	324	330.4
21	1	Sandy silt	323	344.1
22	1	Sandy silt	334	366.4
23	1	Sandy silt	341	386.3
24	1	Sandy silt	346	404.9
25	1	Sandy silt	356	427.9
26	1	Sandy gravel	353	440.4
27	1	Sandy gravel	366	466.5
28	1	Sandy gravel	361	477.3
29	1	Sandy gravel	365	495.9
30		Bedrock		

Table C.6: The soil types and model parameters of the Site 4: Doro-erbata site

Soil Type	Unit Wt. (kN/m^3)	Darendeli Parameters		
		σ'_m (atm)	PI	OCR
Sandy silt	15.15	0.15	0	1
Sandy silt	15.15	0.38	0	1
Sandy silt	16.80	0.62	0	1
Sandy silt	16.80	0.95	0	1
Sandy silt	16.80	1.26	0	1
Sandy silt	17.64	2.04	0	1
Sandy silt	17.77	2.76	0	1
Sandy silt	17.93	2.93	0	1
Sandy silt	18.11	3.11	0	1
Sandy silt	18.17	3.29	0	1
Sandy silt	18.38	3.47	0	1
Sandy silt	18.36	3.65	0	1
Sandy silt	18.53	3.84	0	1
Sandy silt	18.63	4.02	0	1
Sandy silt	18.70	4.20	0	1
Sandy silt	18.84	4.39	0	1
Sandy gravel	18.80	4.58	0	1
Sandy gravel	18.98	4.76	0	1
Sandy gravel	18.91	4.95	0	1
Sandy gravel	18.96	5.14	0	1
Bedrock	24	-	-	-

Table C.7: The shear-wave velocity profile for the Site 5

Depth (m)	Thickness (m)	Soil Type	Vs (m/s)	Shear Strength (kPa)
0	1.5	Sandy elastic silt	107	8.4
1.5	1.5	Sandy elastic silt	152	27.2
3	1.5	Sandy elastic silt	172	46.3
4.5	1.5	Sandy silt	188	66.3
6	1.5	Sandy silt	204	87.5
7.5	1.5	Sandy silt	216	108.6
9	1.5	Sandy silt	231	131.8
10.5	1.5	Sandy silt	238	152.9
12	3	Sandy silt	267	194.4
15	1	Sandy silt	240	206.0
16	1	Sandy silt	239	217.1
17	1	Sandy silt	247	233.4

18	1	Sandy silt	257	251.4
19	1	Sandy silt	262	266.7
20	1	Sandy silt	272	285.5
21	1	Sandy silt	271	297.3
22	1	Sandy silt	283	318.2
23	1	Sandy silt	290	336.1
24	1	Sandy silt	295	352.9
25	1	Sandy silt	302	371.4
26	1	Sandy silt	300	383.0
27	1	Sandy silt	309	403.5
28	1	Sandy silt	303	411.6
29	1	Sandy silt	306	427.3
30		Bedrock		

Table C.8: The soil types and model parameters of the Site 5

Soil Type	Unit Wt. (kN/m^3)	Darendeli Parameters		
		σ'_m (atm)	PI	OCR
Sandy elastic silt	13.75	0.10	19	1
Sandy elastic silt	15.07	0.32	19	1
Sandy elastic silt	15.57	0.54	19	1
Sandy silt	15.94	0.78	12	1
Sandy silt	16.28	1.02	12	1
Sandy silt	16.53	1.26	12	1
Sandy silt	16.82	1.51	12	1
Sandy silt	16.95	1.76	11	1
Sandy silt	17.47	2.14	11	1
Sandy silt	16.99	2.49	11	1
Sandy silt	16.97	2.65	0	1
Sandy silt	17.12	2.82	0	1
Sandy silt	17.30	2.99	0	1
Sandy silt	17.38	3.16	0	1
Sandy silt	17.56	3.34	0	1
Sandy silt	17.54	3.51	0	1
Sandy silt	17.74	3.68	0	1
Sandy silt	17.85	3.86	0	1
Sandy silt	17.93	4.04	0	1
Sandy silt	18.04	4.22	0	1
Sandy silt	18.01	4.39	0	1
Sandy silt	18.15	4.57	0	1
Sandy silt	18.06	4.75	0	1
Sandy silt	18.11	4.93	0	1

Bedrock	24	-	-	-

Table C.9: The shear-wave velocity profile for the Site 6

Depth (m)	**Thickness** (m)	**Soil Type**	**Vs** (m/s)	**Shear Strength (kPa)**
0	3.5	Sandy silt	160	24.2
3.5	2	Sandy silt	198	61.9
5.5	2.8	Sandy silt	221	96.8
8.3	3.3	Sandy silt	234	138.7
11.6	3.1	Sandy silt	256	187.9
14.7	3.05	Sandy silt	275	237.2
17.75	2.25	Sandy silt	278	273.4
20	1	Sandy silt	302	310.3
21	1	Sandy silt	300	322.5
22	1	Sandy silt	312	344.6
23	1	Sandy silt	319	363.6
24	1	Sandy silt	324	381.4
25	1	Sandy silt	333	402.7
26	1	Sandy silt	330	414.5
27	1	Sandy silt	341	437.9
28	1	Sandy silt	336	447.9
29	1	Sandy silt	340	465.6
30		Bedrock		

Table C.10: The soil types and model parameters of the Site 6

Soil Type	**Unit Wt.** (kN/m^3)	**Darendeli Parameters**		
		σ'_m (atm)	**PI**	**OCR**
Sandy silt	15.28	0.26	15	1
Sandy silt	16.15	0.69	15	1
Sandy silt	16.63	1.08	15	1
Sandy silt	16.88	1.58	0	1
Sandy silt	17.28	2.12	0	1
Sandy silt	17.61	2.66	0	1
Sandy silt	17.66	3.12	0	1
Sandy silt	18.04	3.40	0	1
Sandy silt	18.01	3.58	0	1
Sandy silt	18.20	3.76	0	1
Sandy silt	18.30	3.94	0	1
Sandy silt	18.38	4.12	0	1
Sandy silt	18.51	4.30	0	1

Sandy silt	18.47	4.49	0	1
Sandy silt	18.63	4.67	0	1
Sandy silt	18.56	4.86	0	1
Sandy silt	18.61	5.04	0	1
Bedrock	24	-	-	-

Table C.11: The shear-wave velocity profile for the Site 7

Depth (m)	**Thickness** (m)	**Soil Type**	**Vs** (m/s)	**Shear Strength (kPa)**
0	1.5	Sandy silt	107	8.4
1.5	1.5	Sandy silt	133	24.7
3	1.5	Sandy silt	164	44.4
4.5	1.5	Sandy silt	177	63.0
6	1.5	Sandy silt	188	82.1
7.5	1.5	Sandy silt	201	102.5
9	1.5	Sandy silt	212	122.9
10.5	1.5	Sandy silt	227	146.4
12	1.5	Sandy silt	264	180.8
13.5	8.65	Sandy silt	327	286.2
22.15	3.85	Silty sand with gravel	339	386.8
26	2.15	Silty sand with gravel	346	435.8
28.15	1.85	Silty sand with gravel	351	469.4
30		Bedrock		

Table C.12: The soil types and model parameters of the Site 7

Soil Type	**Unit Wt.** (kN/m^3)	**Darendeli Parameters**		
		σ'_m (atm)	**PI**	**OCR**
Sandy silt	13.74	0.10	11	1
Sandy silt	14.56	0.31	10	1
Sandy silt	15.39	0.53	10	1
Sandy silt	15.69	0.76	0	1
Sandy silt	15.94	1.00	0	1
Sandy silt	16.23	1.24	0	1
Sandy silt	16.44	1.48	0	1
Sandy silt	16.75	1.73	0	1
Sandy silt	17.43	1.98	0	1
Sandy silt	18.43	2.90	0	1
Silty sand with gravel	18.61	4.04	0	1
Silty sand with gravel	18.69	4.59	0	1
Silty sand with gravel	18.77	4.96	0	1

Bedrock	24	-	-	-

Table C.13: The shear-wave velocity profile for the Site 8

Depth (m)	**Thickness** (m)	**Soil Type**	**Vs** (m/s)	**Shear Strength (kPa)**
0	2	Sandy silt	120	11.8
2	2	Sandy silt	177	39.2
4	2	Sandy silt	210	69.3
6	2	Sandy silt	257	107.6
8	2	Sandy silt	281	143.8
10	2	Sandy silt	306	183.2
12	2	Sandy silt	329	224.4
14	2	Sandy silt	343	263.1
16	2	Sandy silt	356	302.5
18	1	Sandy silt	311	297.5
19	1	Sandy silt	316	314.9
20	1	Sandy silt	330	338.8
21	1	Sandy silt	329	352.6
22	1	Sandy silt	340	375.2
23	1	Sandy silt	347	395.4
24	1	Sandy silt	352	414.3
25	1	Sandy silt	362	437.5
26	1	Sandy silt	360	451.0
27	1	Sandy silt	373	477.5
28	1	Sandy silt	368	488.4
29	1	Sandy silt	371	506.4
30		Bedrock		

Table C.14: The soil types and model parameters of the Site 8

Soil Type	**Unit Wt.** (kN/m^3)	**Darendeli Parameters**		
		σ'_m (atm)	**PI**	**OCR**
Sandy silt	14.17	0.14	0	1
Sandy silt	15.69	0.44	0	1
Sandy silt	16.41	0.75	0	1
Sandy silt	17.30	1.09	0	1
Sandy silt	17.71	1.43	0	1
Sandy silt	18.11	1.79	0	1
Sandy silt	18.45	2.15	0	1

Sandy silt	18.66	2.52	0	1
Sandy silt	18.84	2.89	0	1
Sandy silt	18.18	3.16	0	1
Sandy silt	18.26	3.34	0	1
Sandy silt	18.47	3.52	0	1
Sandy silt	18.45	3.71	0	1
Sandy silt	18.61	3.89	0	1
Sandy silt	18.71	4.07	0	1
Sandy silt	18.78	4.26	0	1
Sandy silt	18.92	4.45	0	1
Sandy silt	18.89	4.63	0	1
Sandy silt	19.07	4.82	0	1
Sandy silt	19.00	5.01	0	1
Sandy silt	19.04	5.20	0	1
Bedrock	24	-	-	-

Table C.15: The shear-wave velocity profile for the Site 9

Depth (m)	**Thickness** (m)	**Soil Type**	**Vs** (m/s)	**Shear Strength (kPa)**
0	2	Silt with Sand	196	18.3
2	4	Silt with Sand	198	58.1
6	2	Silt with Sand	199	93.4
8	2	Silt with Sand	200	115.9
10	2	Silt with Sand	218	145.1
12	2	Silt with Sand	224	170.6
14	4	Silty sand and some gravel	239	212.9
18	1	Silty sand and some gravel	277	265.2
19	1	Silty sand and some gravel	281	280.6
20	1	Silty sand and some gravel	293	301.5
21	1	Silty sand and some gravel	292	314.1
22	1	Silty sand and some gravel	304	335.8
23	1	Silty sand and some gravel	311	354.5
24	1	Silty sand and some gravel	316	372.0
25	1	Silty sand and some gravel	324	392.2
26	1	Silty sand and some gravel	322	404.5
27	1	Silty sand and some gravel	332	426.7
28	1	Silty sand and some gravel	327	436.5
29	1	Silty sand and some gravel	330	453.0
30		Bedrock		

Table C.14: The soil types and model parameters of the Site 9

Soil Type	Unit Wt. (kN/m^3)	Darendeli Parameters		
		σ'_m (atm)	PI	OCR
Silt with Sand	16.11	0.16	0	1
Silt with Sand	16.15	0.64	0	1
Silt with Sand	16.18	1.12	0	1
Silt with Sand	16.20	1.44	0	1
Silt with Sand	16.57	1.76	0	1
Silt with Sand	16.69	2.09	0	1
Silty sand and some gravel	16.97	2.59	0	1
Silty sand and some gravel	17.64	3.01	0	1
Silty sand and some gravel	17.71	3.19	0	1
Silty sand and some gravel	17.90	3.37	0	1
Silty sand and some gravel	17.89	3.54	0	1
Silty sand and some gravel	18.08	3.72	0	1
Silty sand and some gravel	18.18	3.90	0	1
Silty sand and some gravel	18.26	4.08	0	1
Silty sand and some gravel	18.38	4.26	0	1
Silty sand and some gravel	18.35	4.44	0	1
Silty sand and some gravel	18.50	4.63	0	1
Silty sand and some gravel	18.42	4.81	0	1
Silty sand and some gravel	18.47	4.99	0	1
Bedrock	24	-	-	-

APPENDIX D

SITE RESPONSE ANALYSIS RESULTS

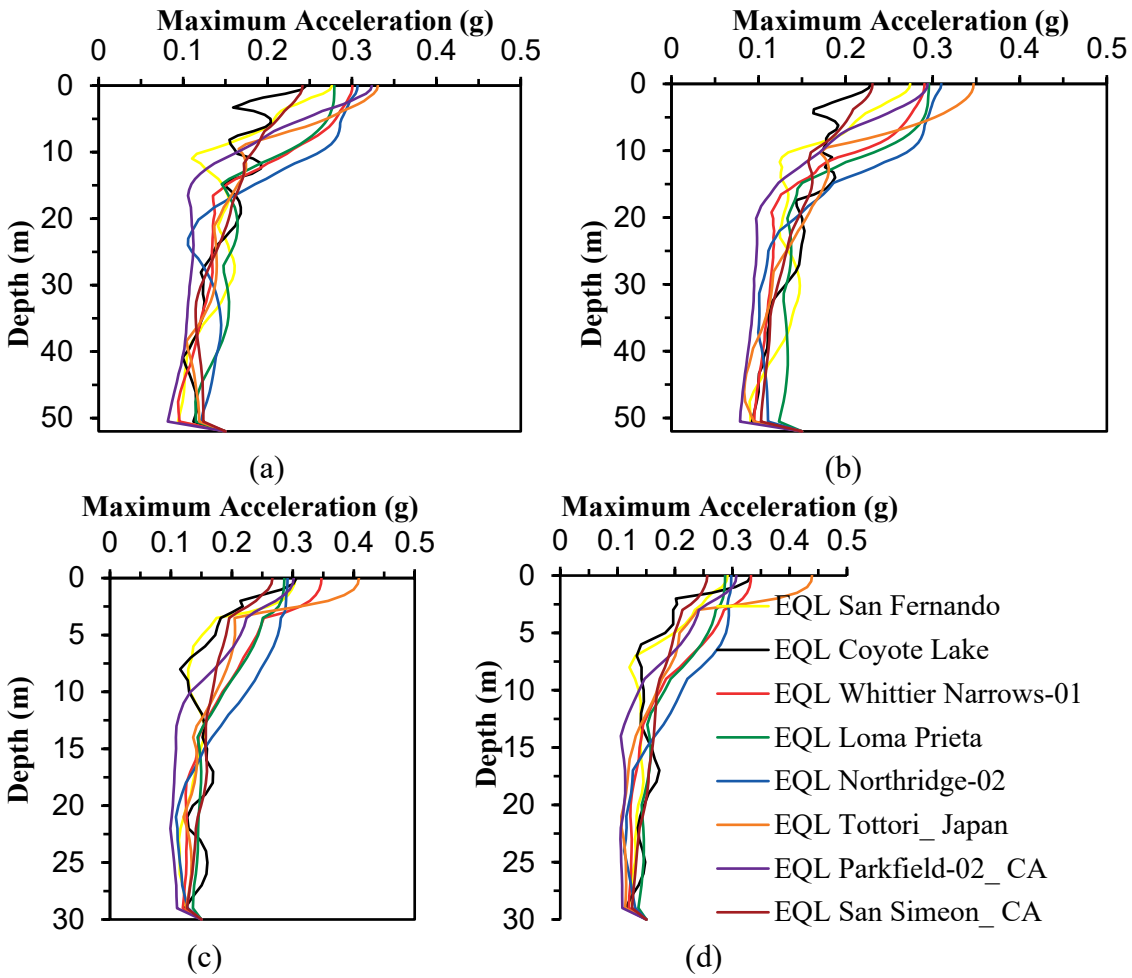

Figure D.1: Peak ground acceleration profiles for (a) Site 1 (b) Site 2 (c) Site 3 (d) Site 4 sites using EQL.

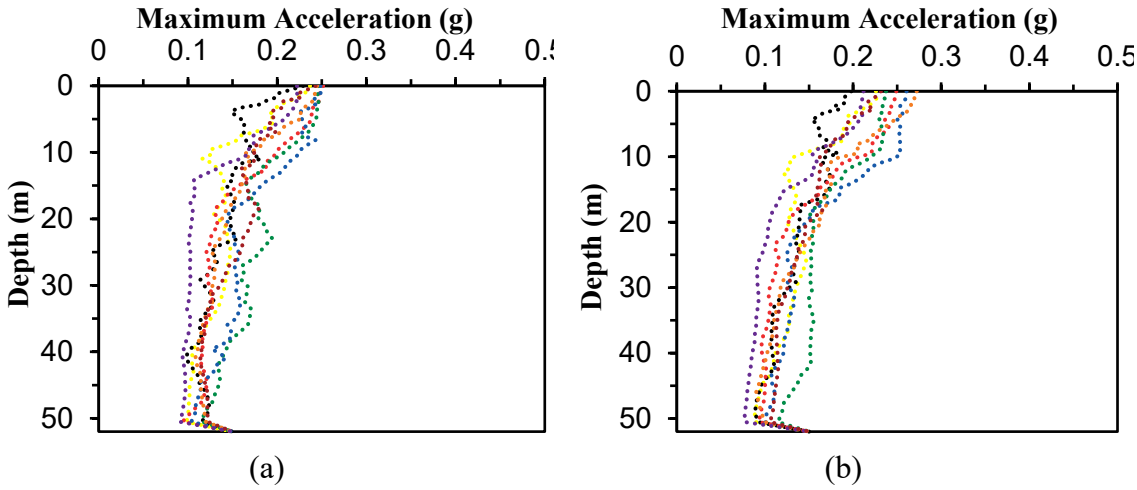

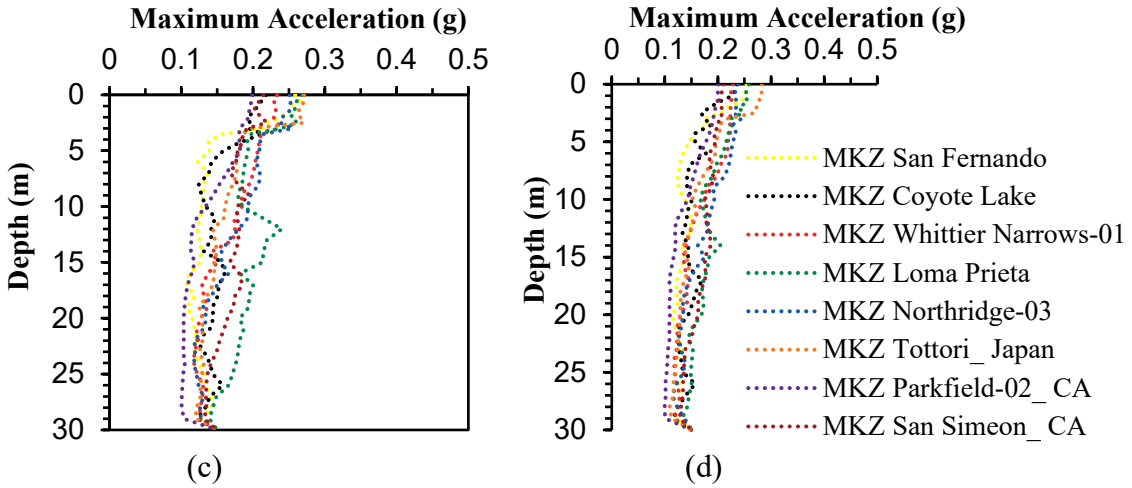

Figure D.2: Peak ground acceleration profiles for (a) Site 1 (b) Site 2 (c) Site 3 (d) Site 4 using MKZ.

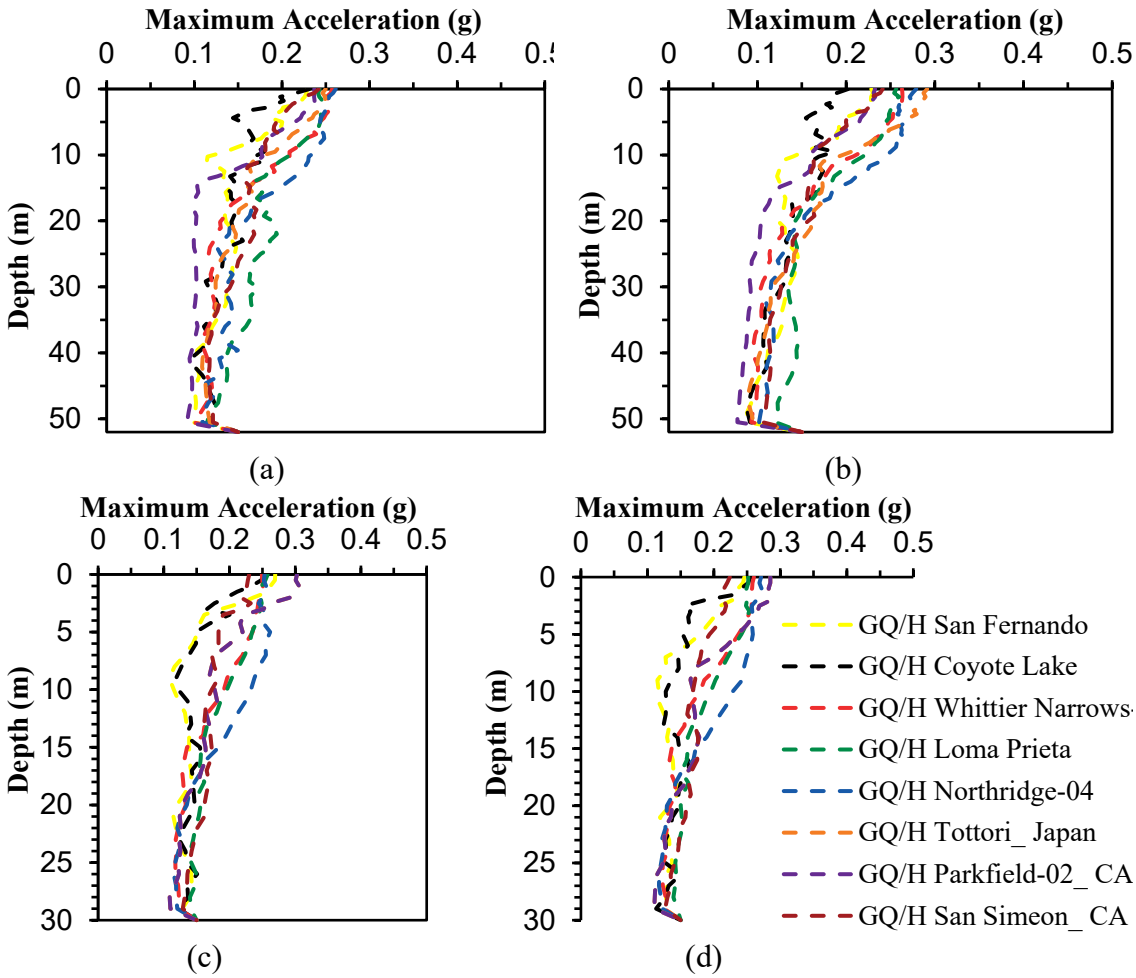

Figure D.3: Peak ground acceleration profiles for (a) Site 1 (b) Site 2 (c) Site 3 (d) Site 4 using GQ/H.

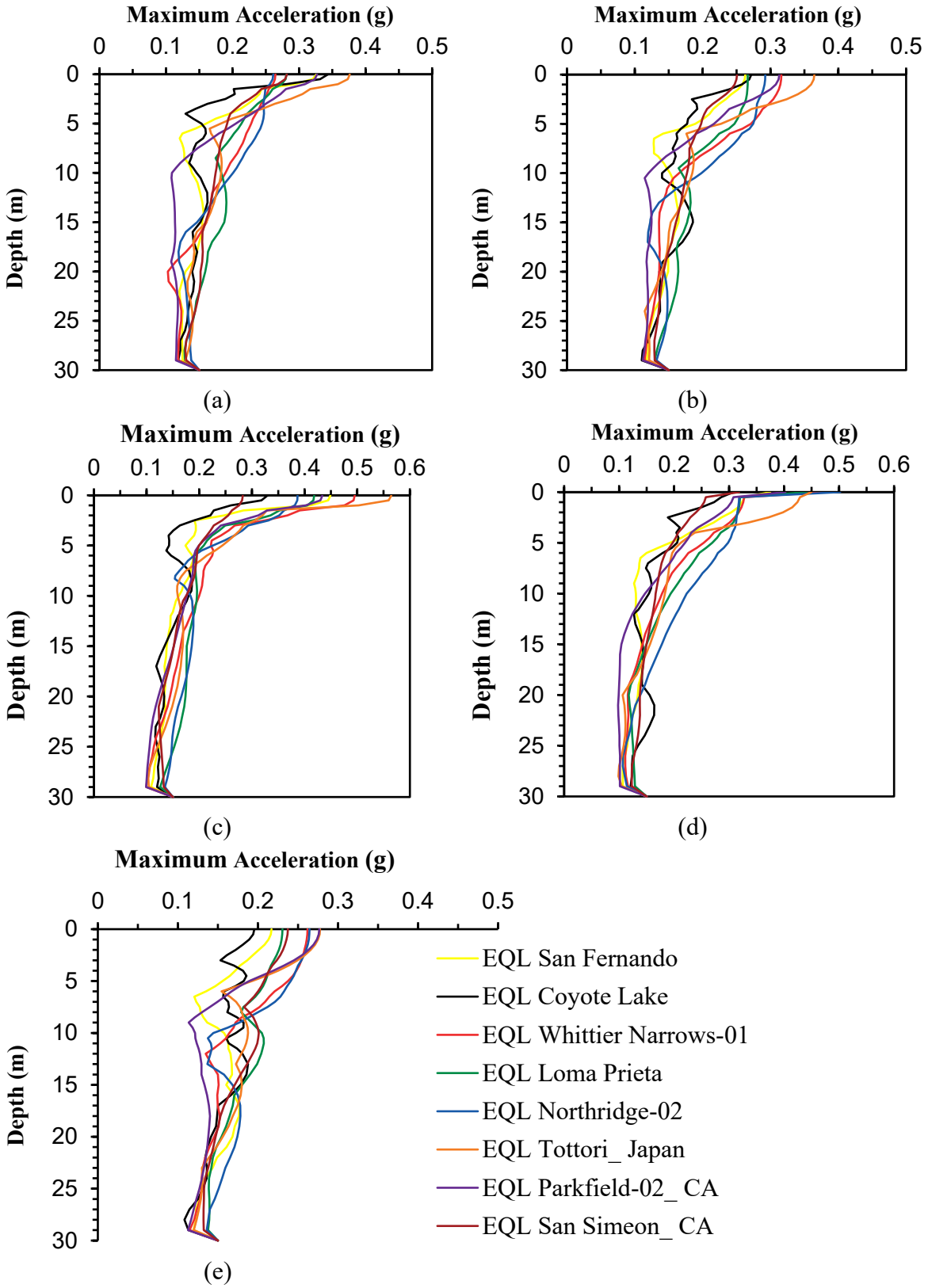

Figure D.4: Peak ground acceleration profiles for (a) Site 5 (b) Site 6 (c) Site 7 (d) Site 8 (e) Site 9 using EQL.

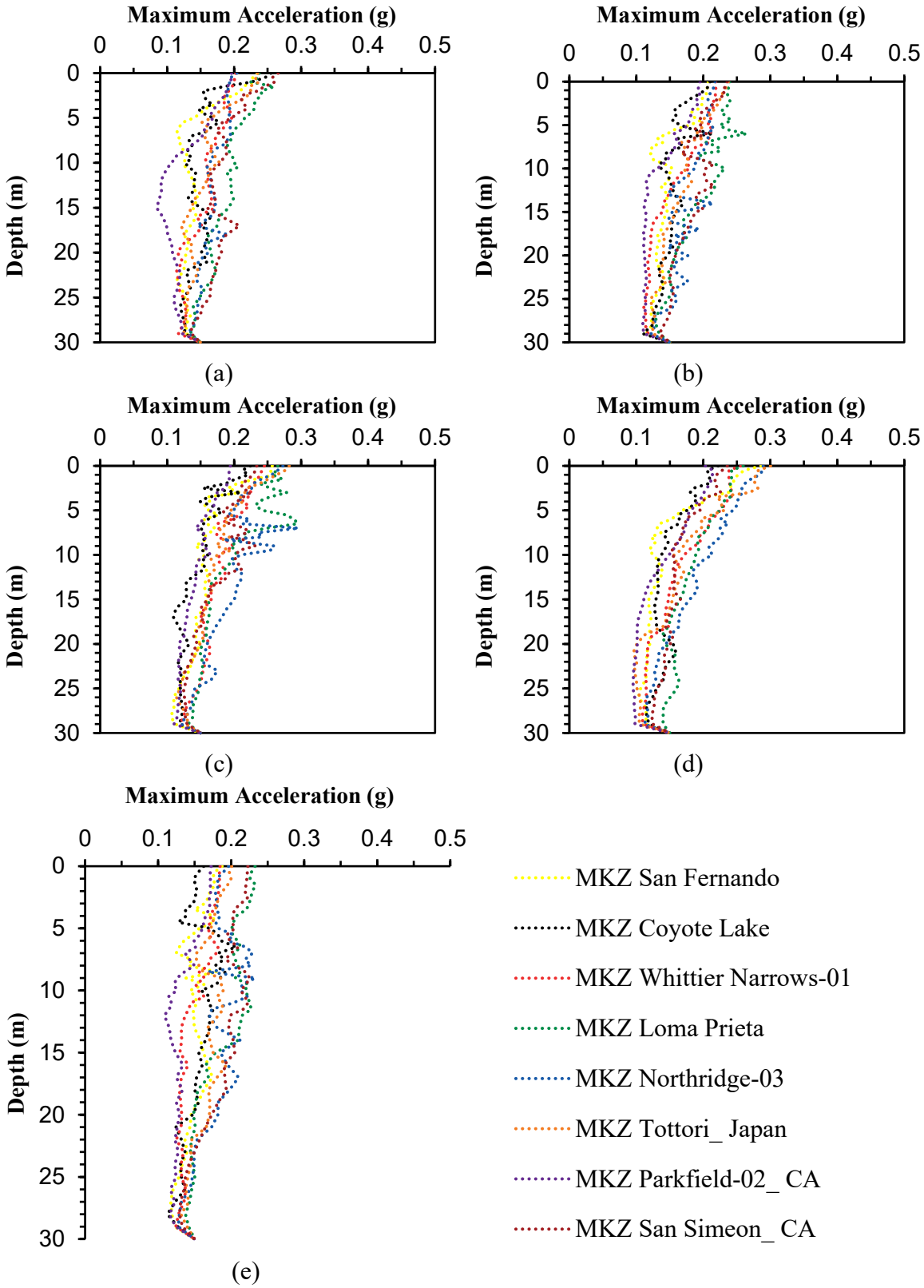

Figure D.5: Peak ground acceleration profiles for (a) Site 5 (b) Site 6 (c) Site 7 (d) Site 8 (e) Site 9 sites using MKZ.

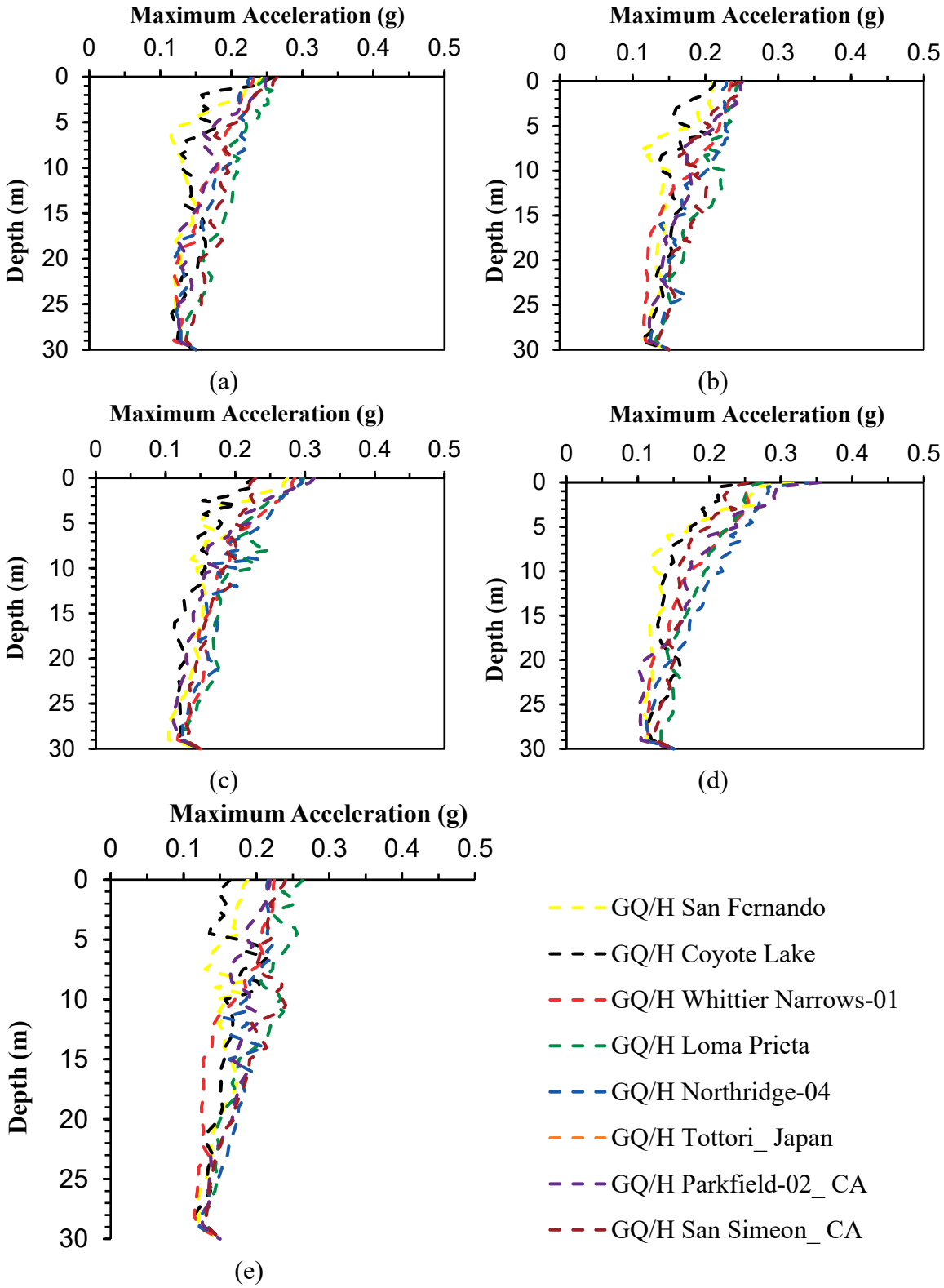

Figure D.6: Peak ground acceleration profiles for (a) Site 5 (b) Site 6 (c) Site 7 (d) Site 8 (e) Site 9 using GQ/H.

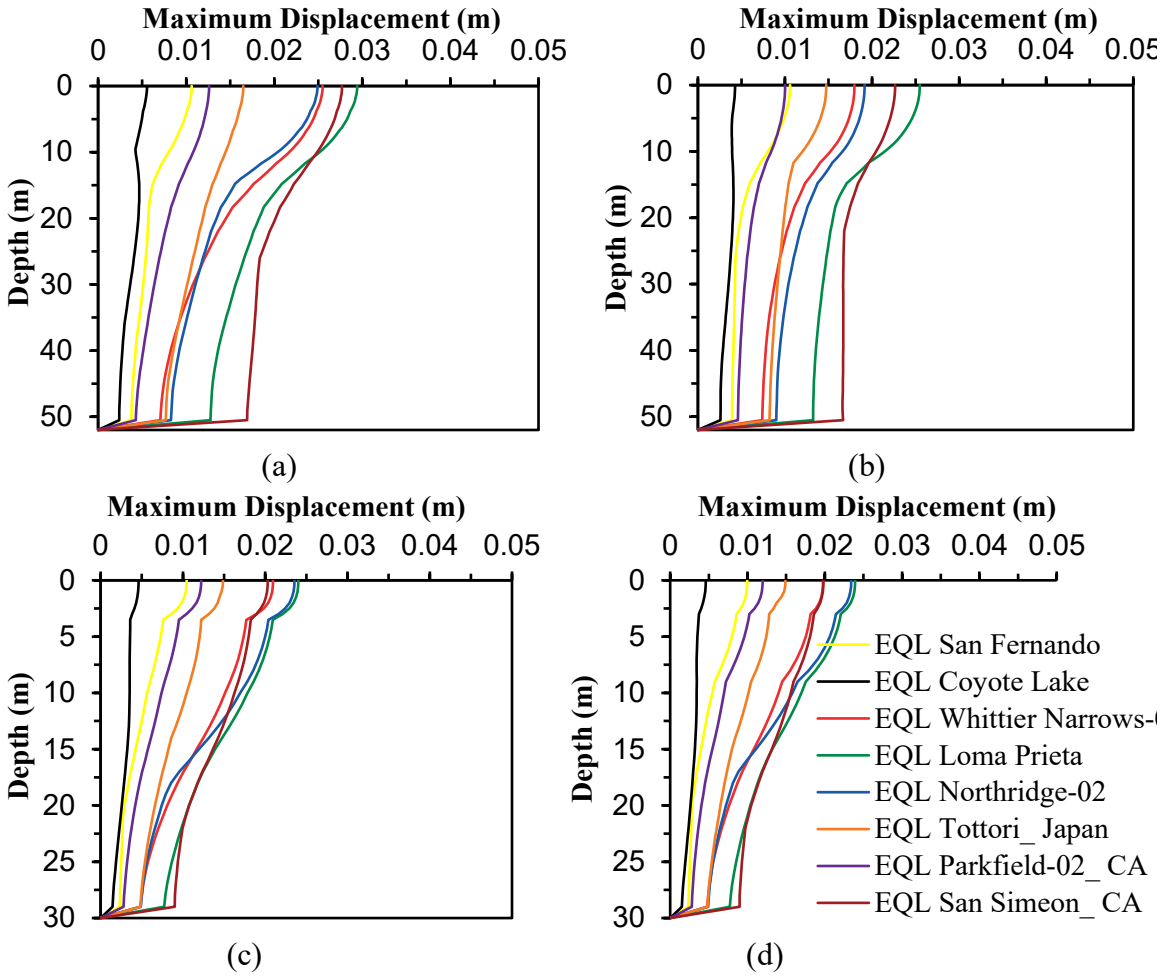

Figure D.7: Peak displacement profiles for (a) Site 1 (b) Site 2 (c) Site 3 (d) Site 4 using EQL.

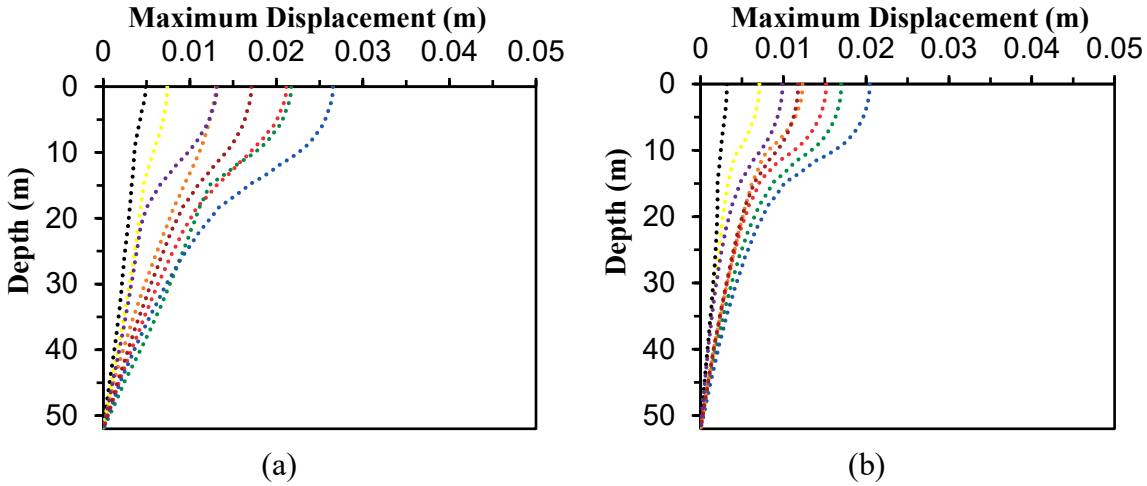

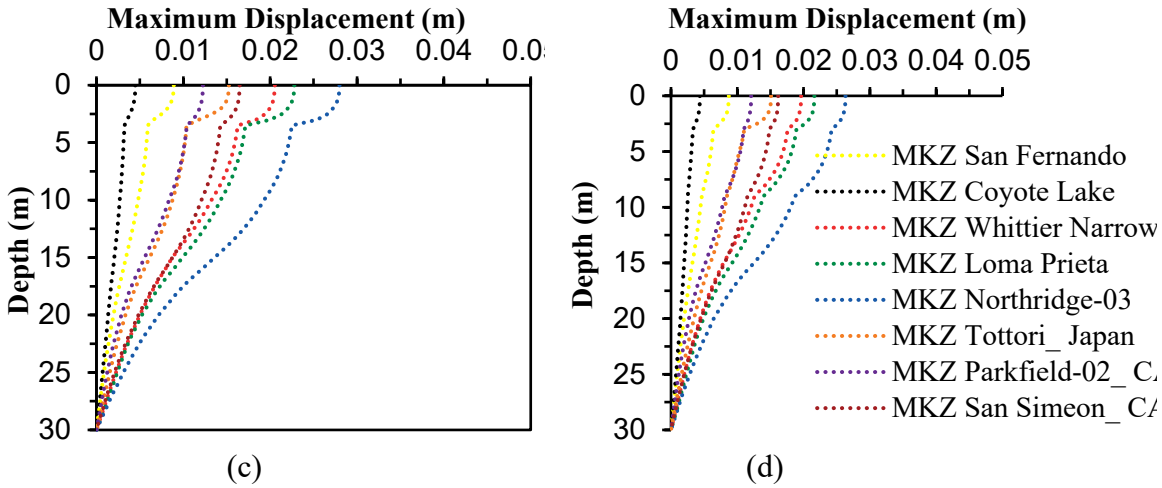

Figure D.8: Peak displacement profiles for (a) Site 1 (b) Site 2 (c) Site 3 (d) Site 4 sites using MKZ.

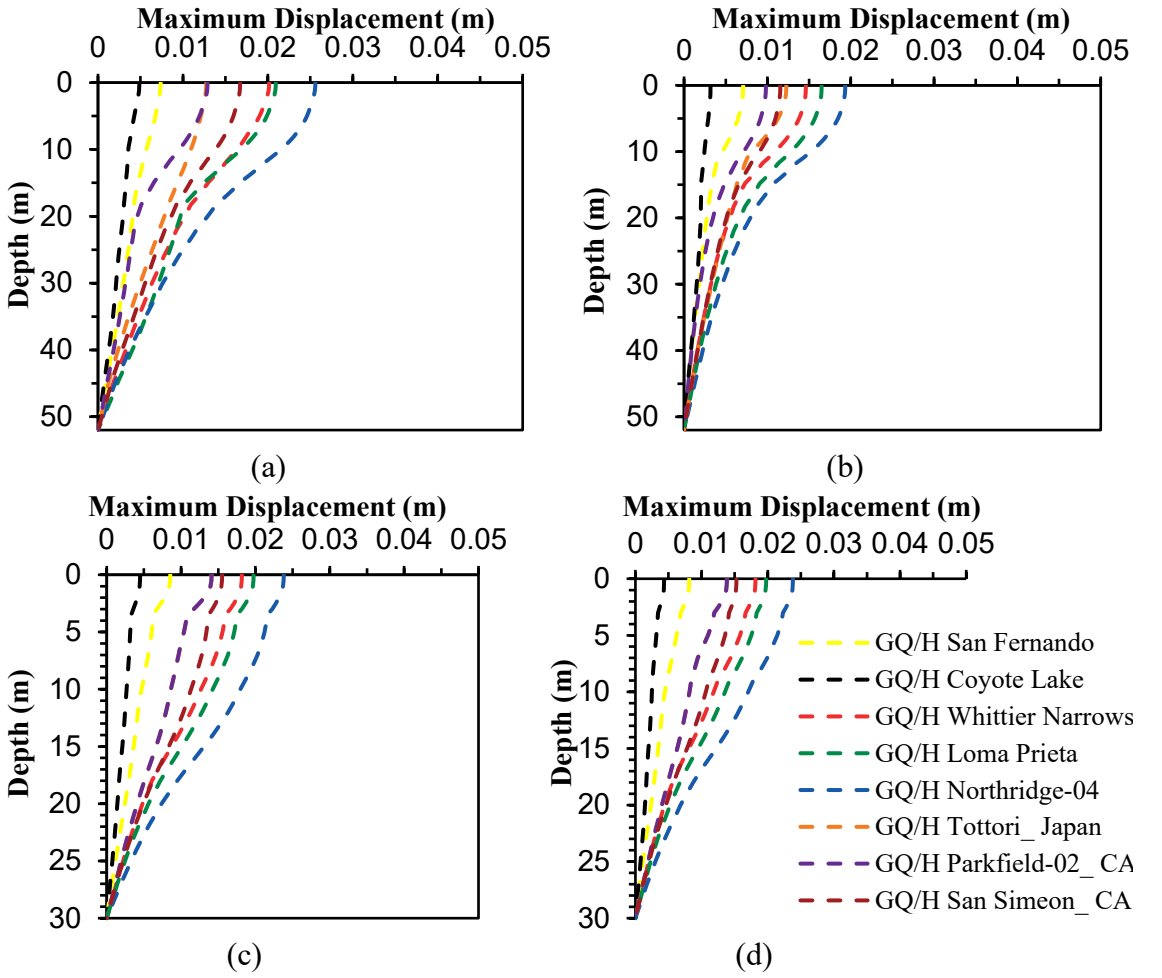

Figure D.9: Peak displacement profiles for (a) Site 1 (b) Site 2 (c) Site 3 (d) Site 4 sites using GQ/H.

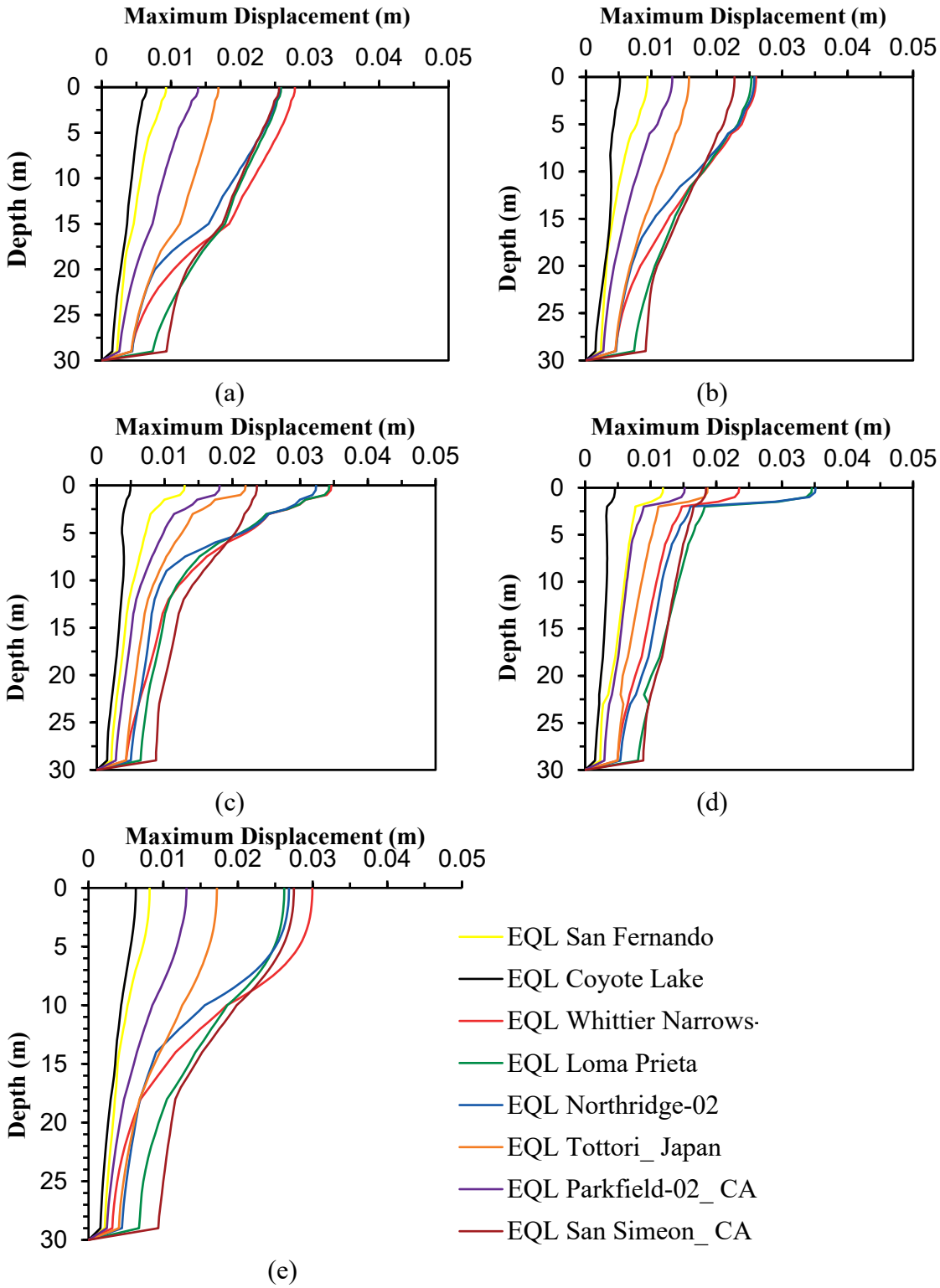

Figure D.10: Peak displacement profiles for (a) Site 5 (b) Site 6 (c) Site 7 (d) Site 8 (e) Site 9 using EQL.

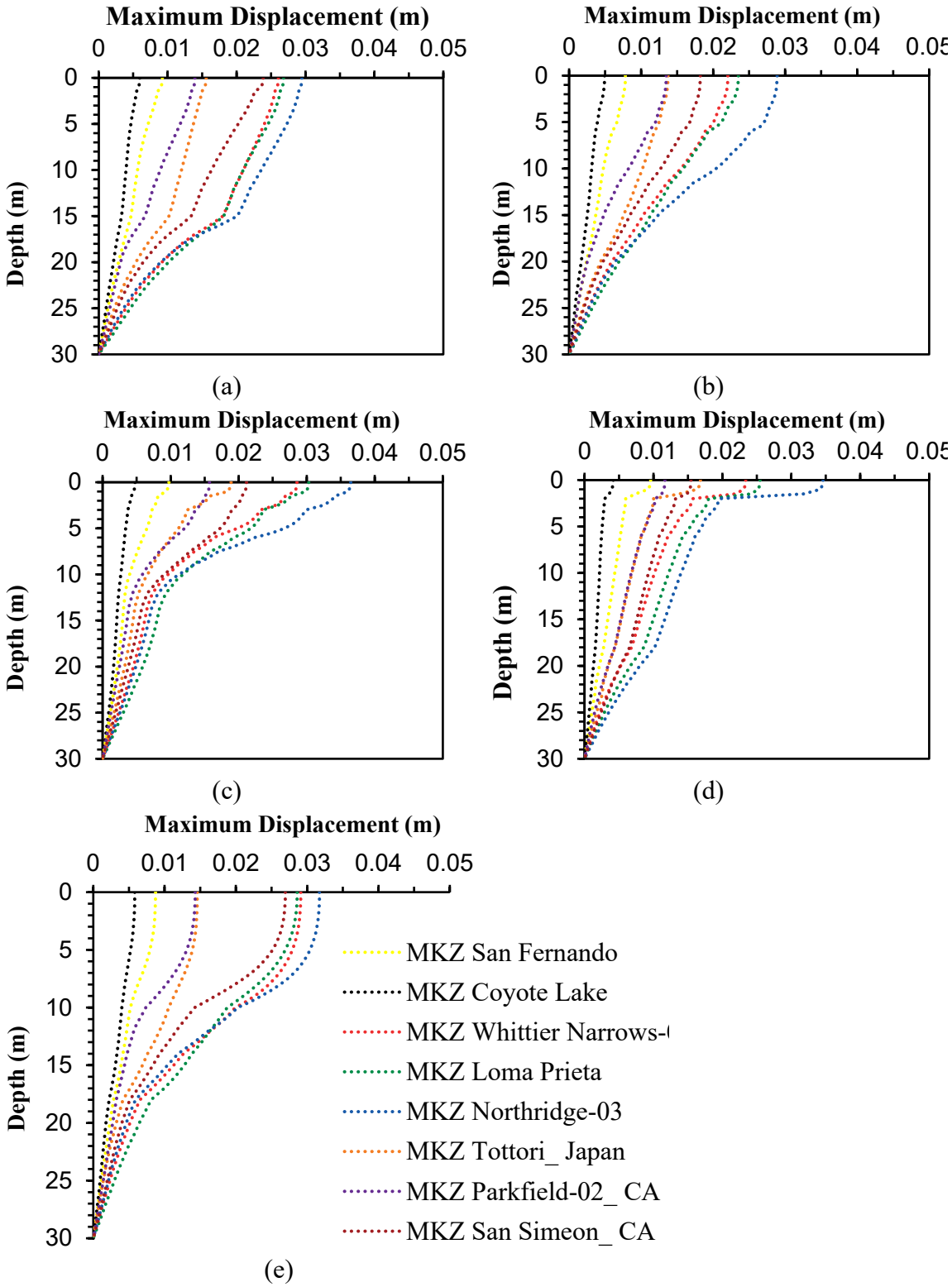

Figure D.11: Peak displacement profiles for (a) Site 5 (b) Site 6 (c) Site 7 (d) Site 8 (e) Site 9 using MKZ.

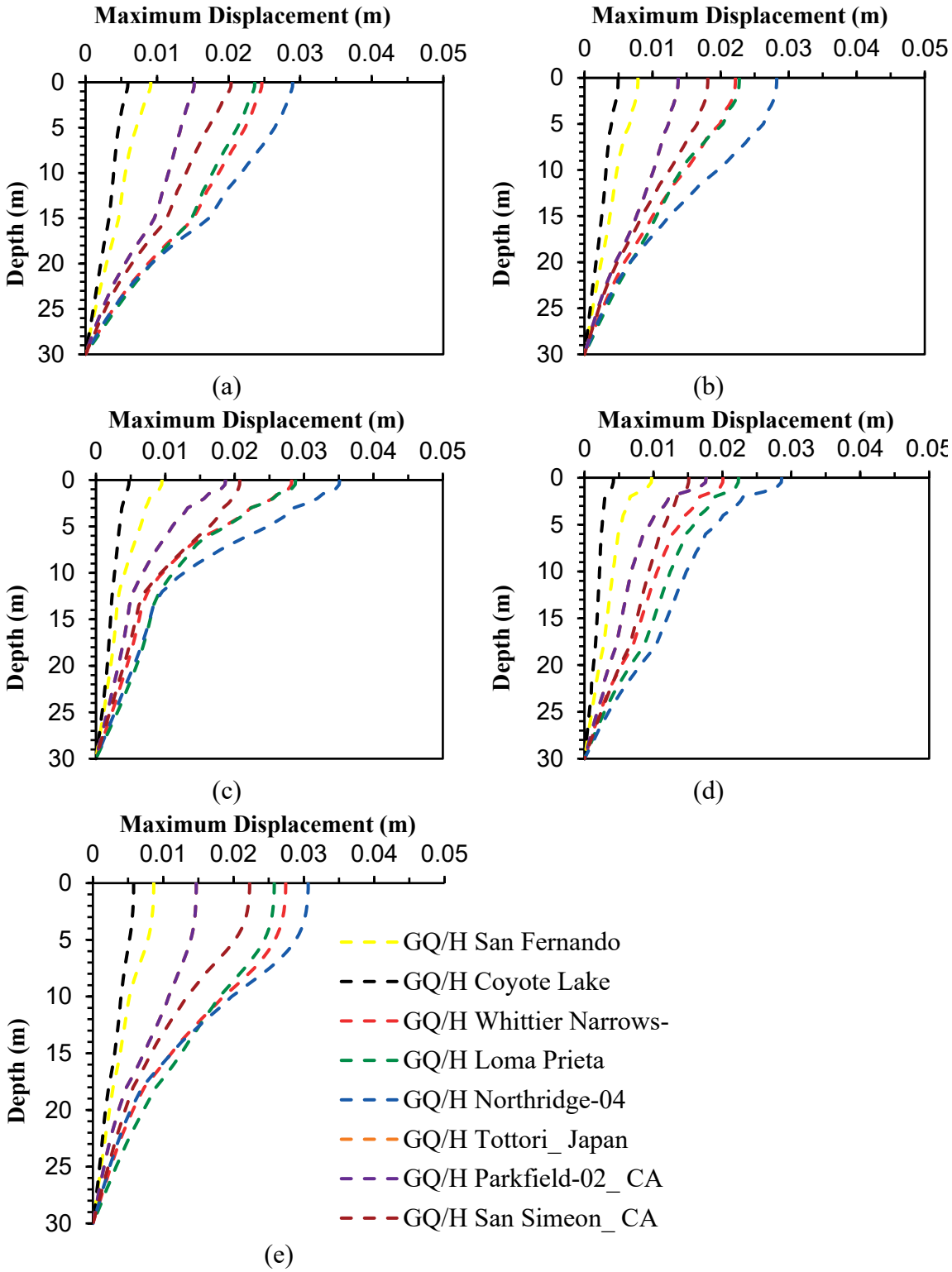

Figure D.12: Peak displacement profiles for (a) Site 5 (b) Site 6 (c) Site 7 (d) Site 8 (e) Site 9 using GQ/H.

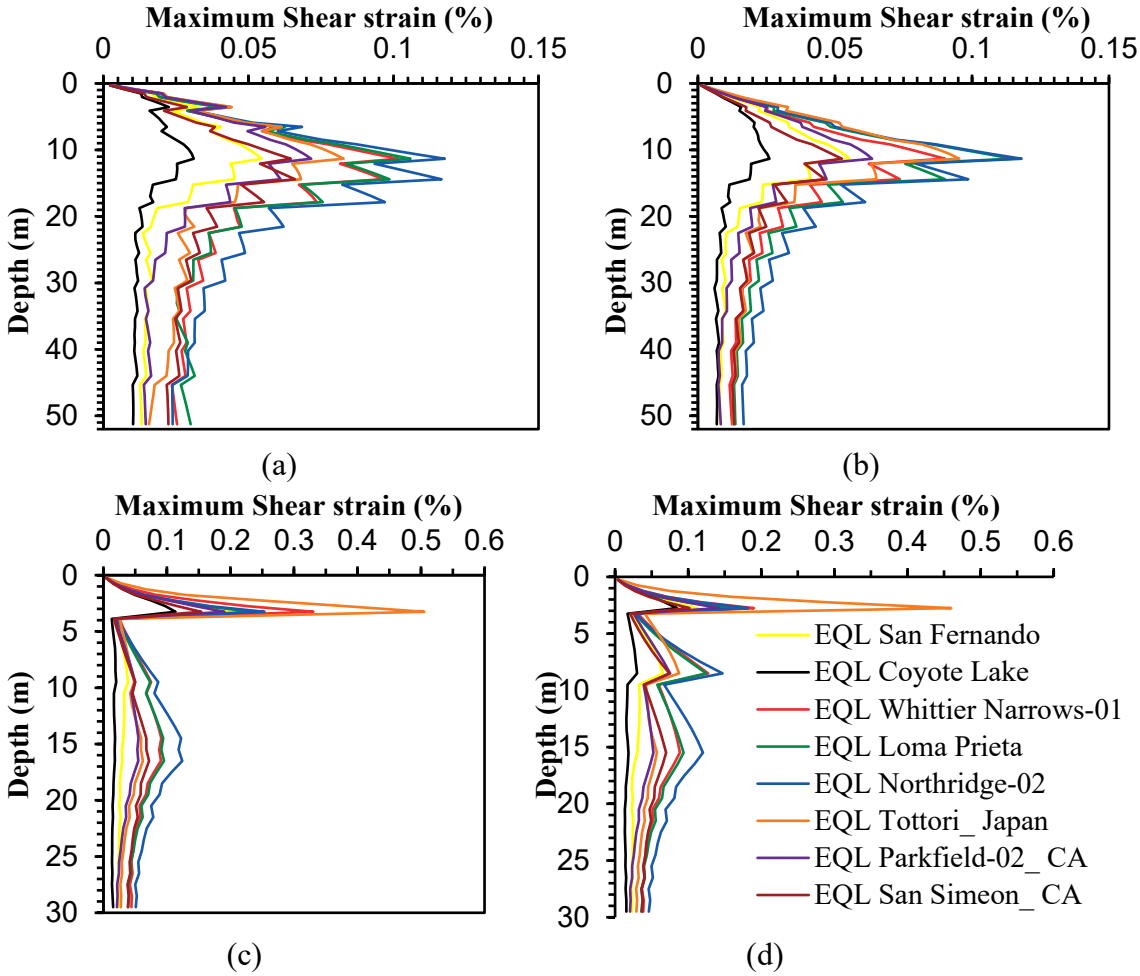

Figure D.13: Strain profiles for (a) Site 1 (b) Site 2 (c) Site 3 (d) Site 4 using EQL.

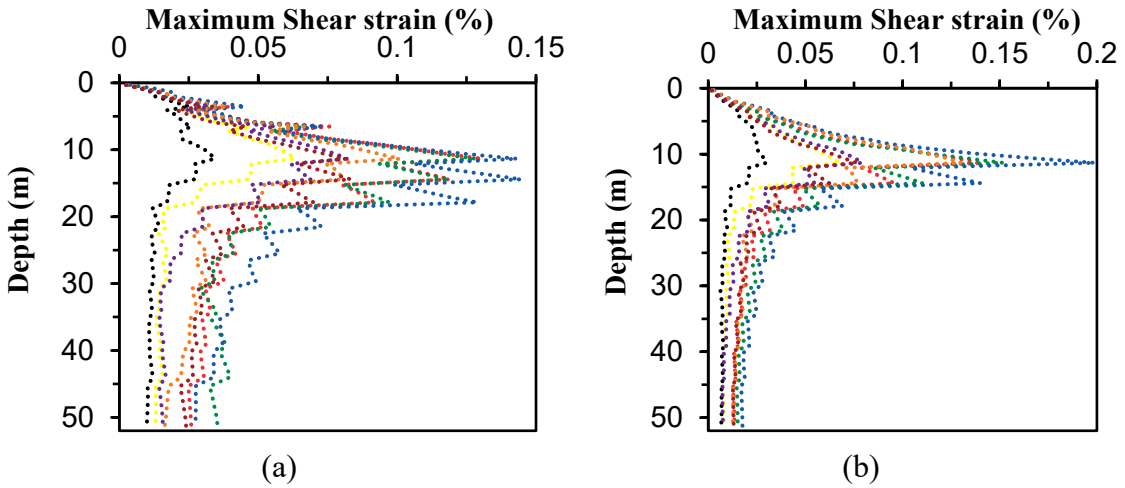

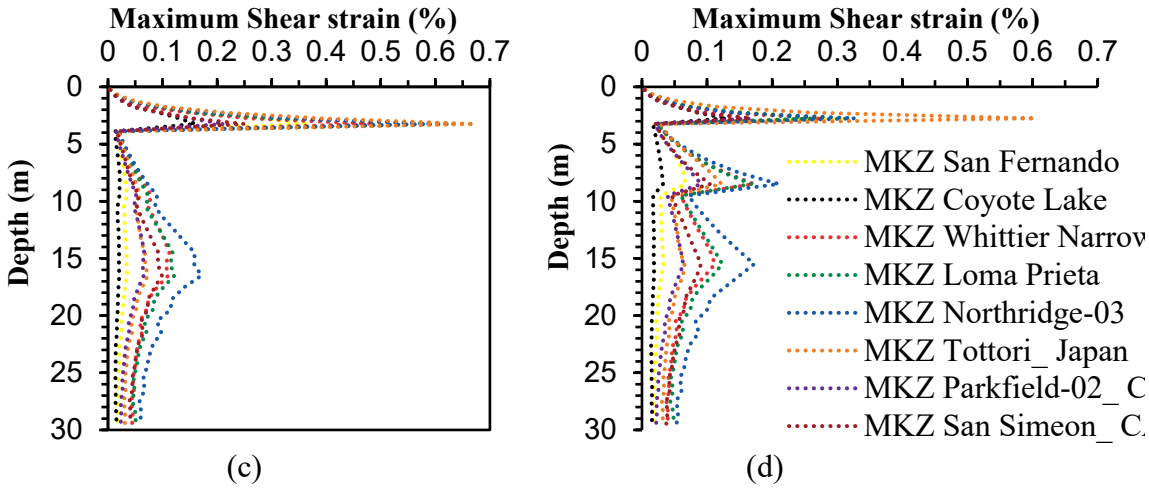

Figure D.14: Strain profiles for (a) Site 1 (b) Site 2 (c) Site 3 (d) Site 4 using MKZ.

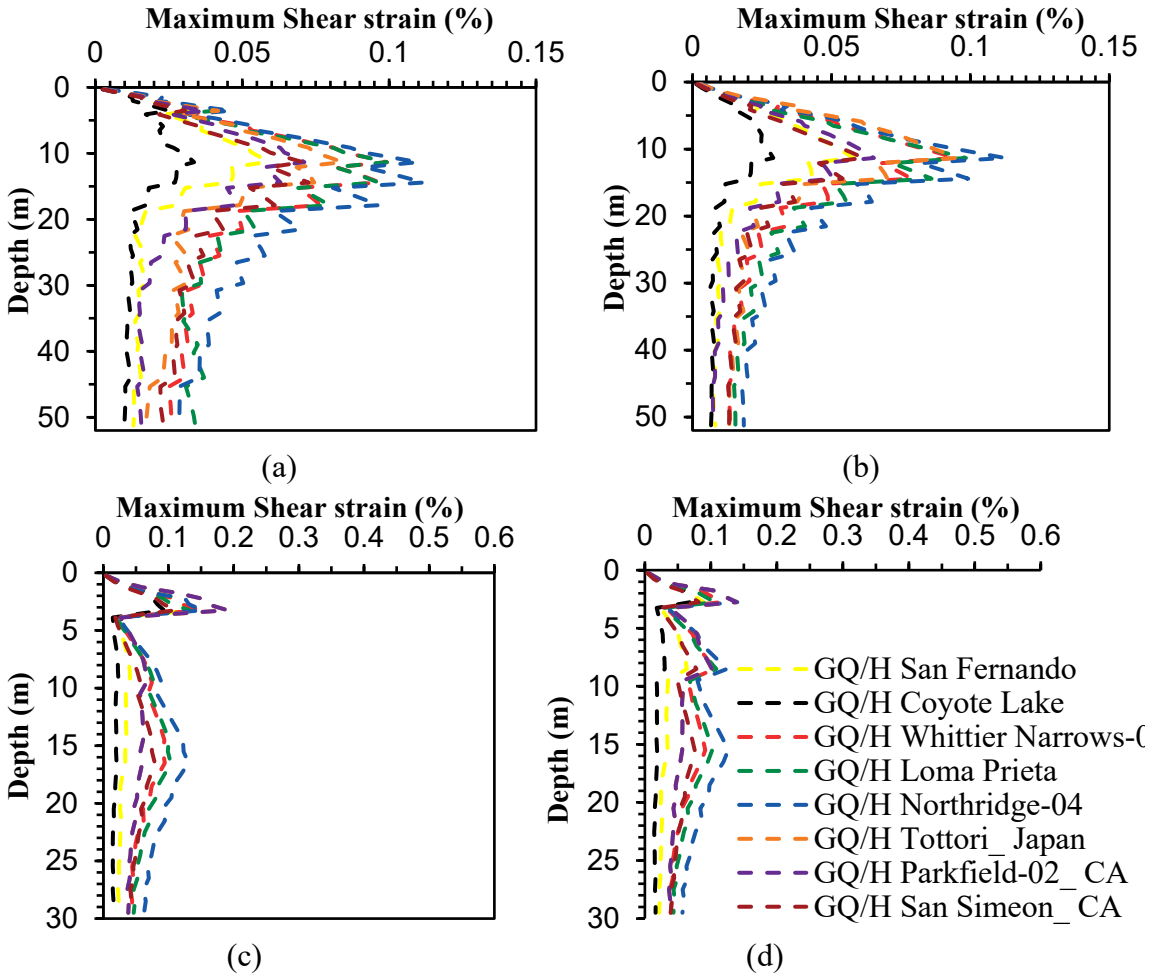

Figure D.15: Strain profiles for (a) Site 1 (b) Site 2 (c) Site 3 (d) Site 4 using GQ/H.

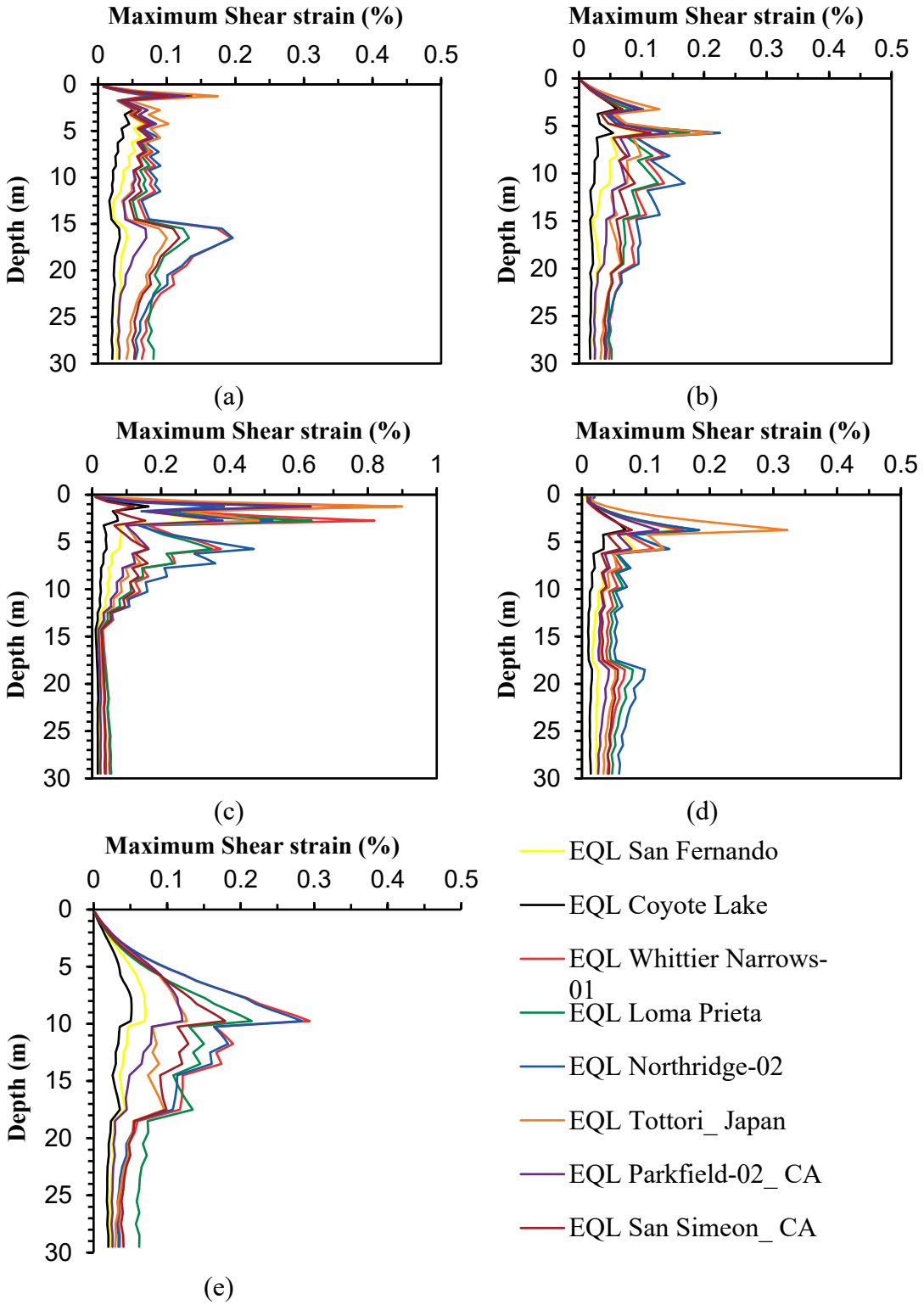

Figure D.16: Strain profiles for (a) Site 5 (b) Site 6 (c) Site 7 (d) Site 8 (e) Site 9 using EQL.

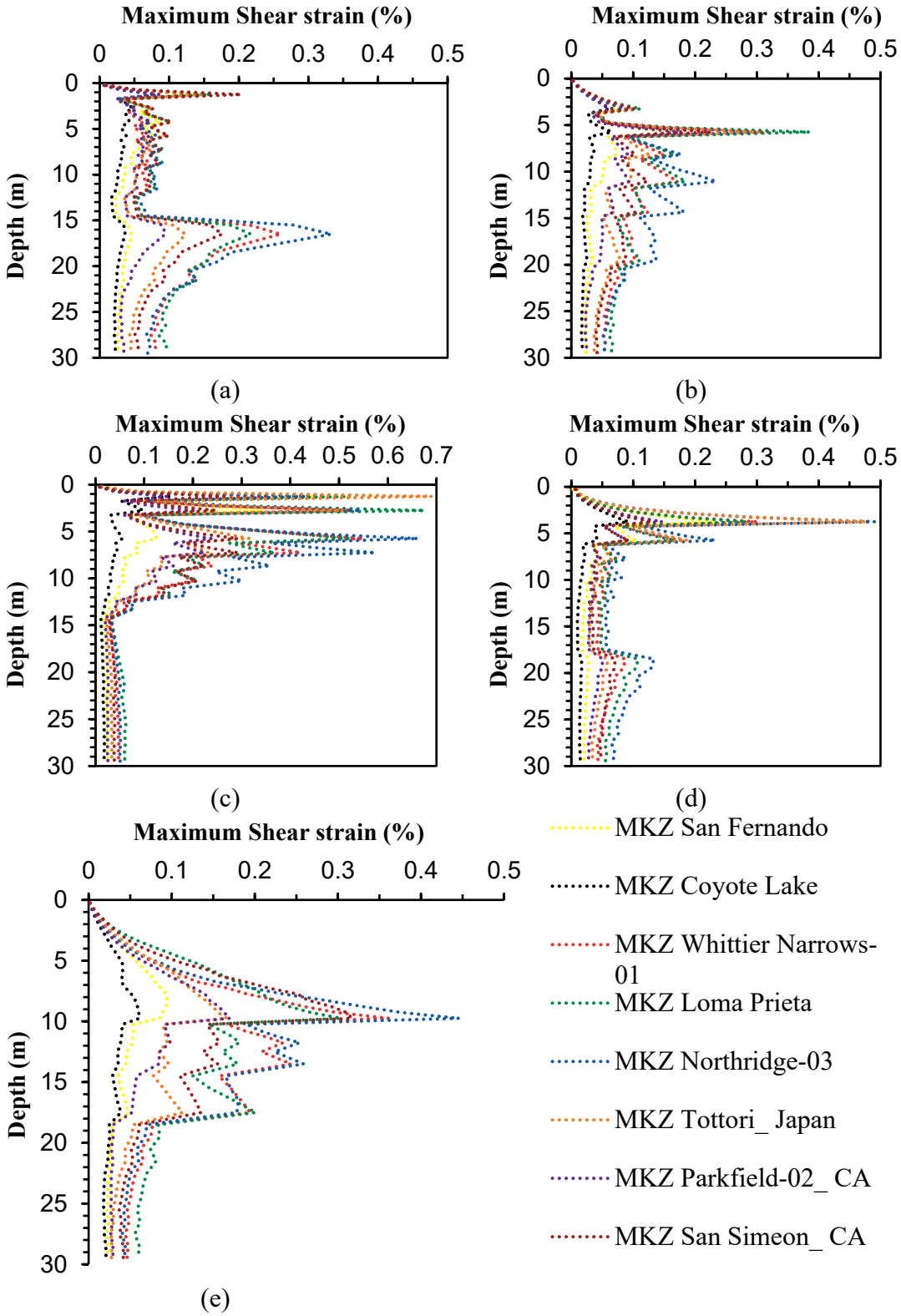

Figure D.17: Strain profiles for (a) Site 5 (b) Site 6 (c) Site 7 (d) Site 8 (e) Site 9 using MKZ.

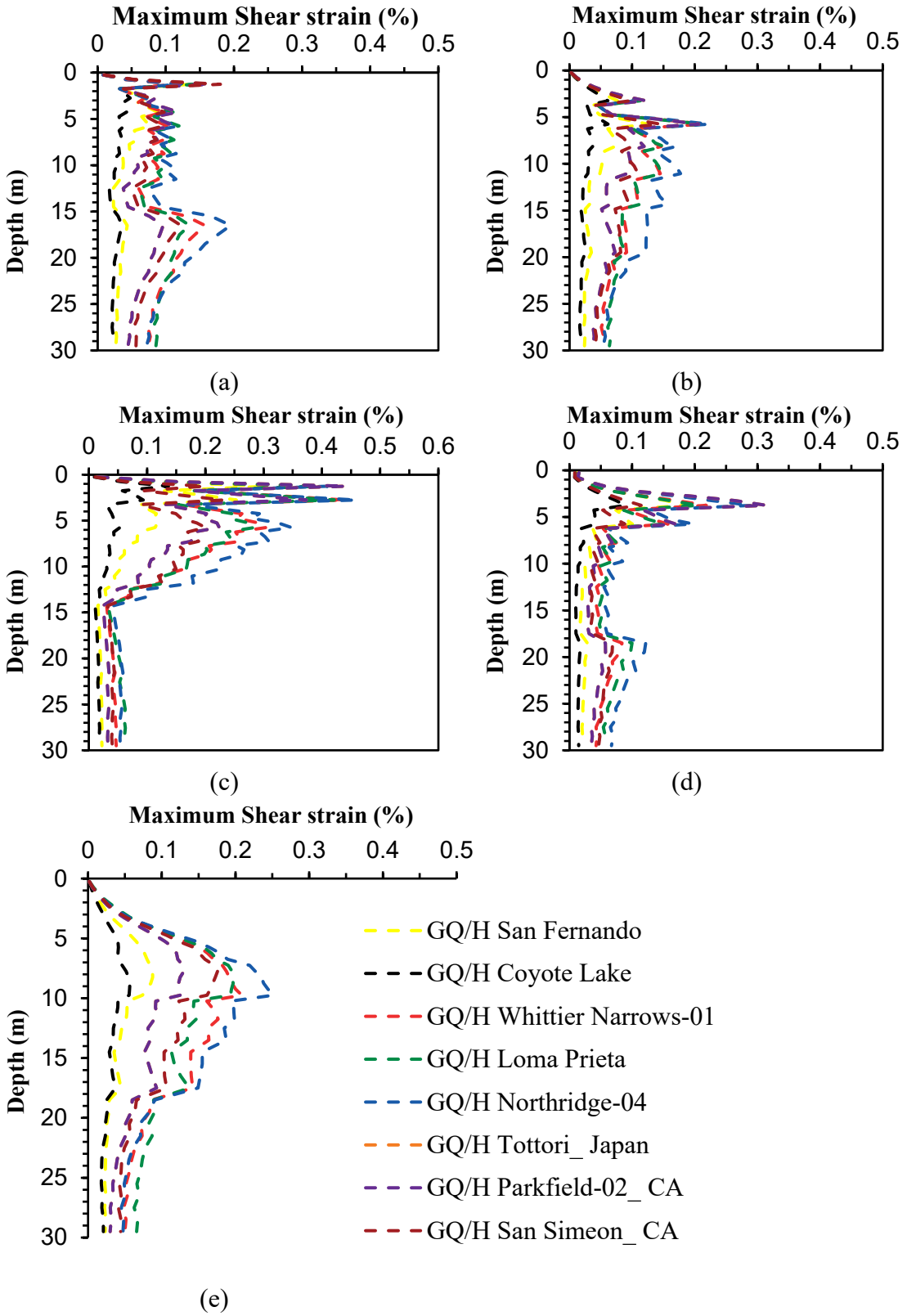

Figure D.18: Strain profiles for (a) Site 5 (b) Site 6 (c) Site 7 (d) Site 8 (e) Site 9 using GQ/H.

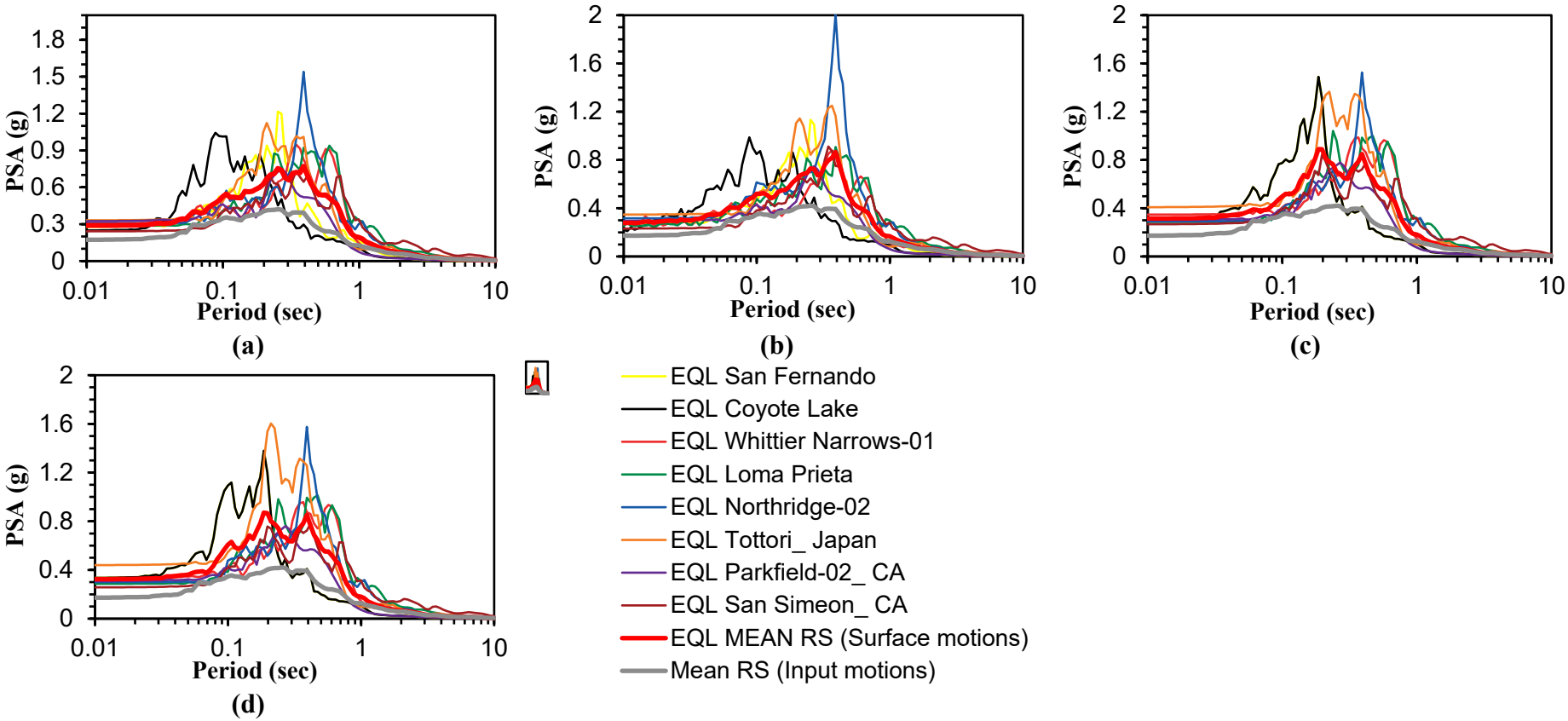

Figure D.19: Response spectra analysis at the surface for (a) Site 1 (b) Site 2 (c) Site 3 (d) Site 4 using EQL.

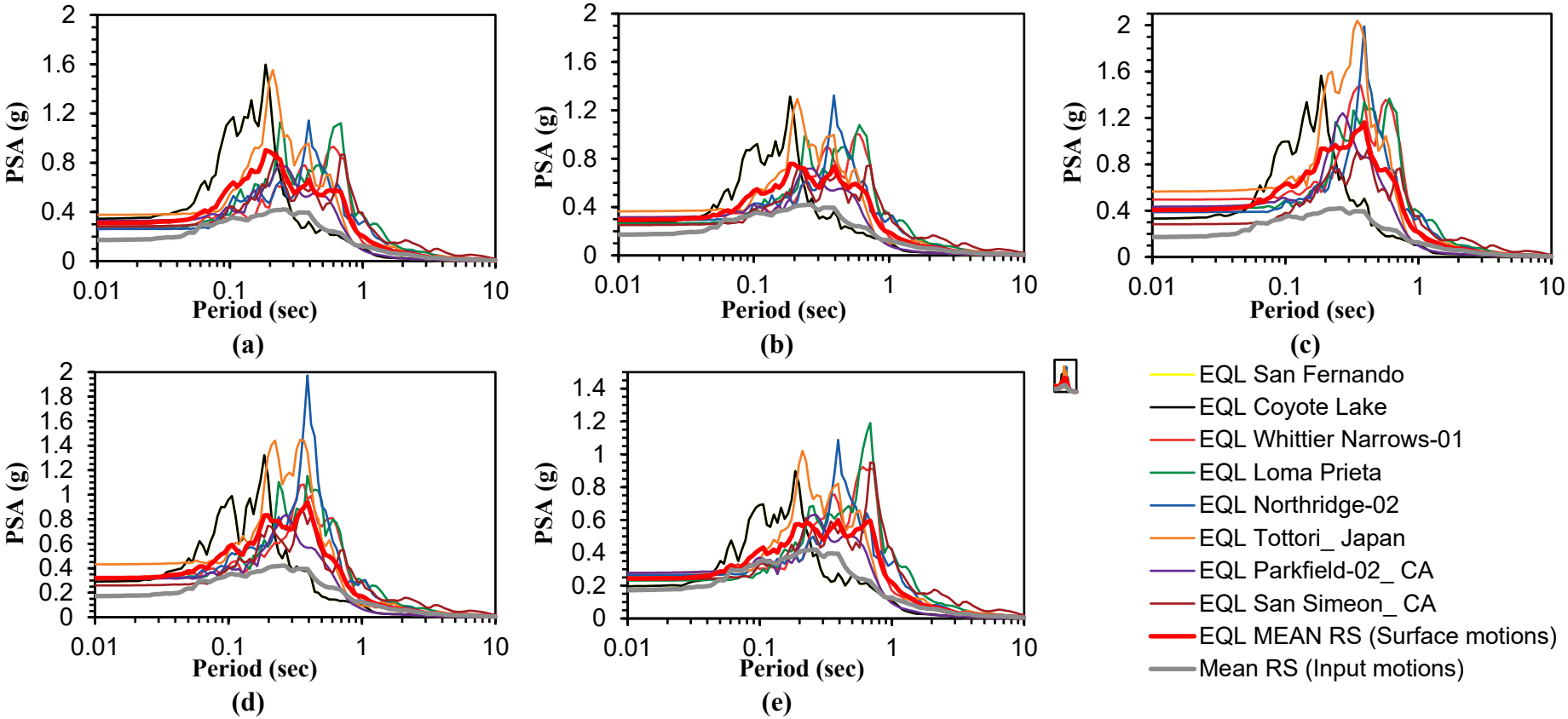

Figure D.20: Response spectra analysis at the surface for (a) Site 5 (b) Site 6 (c) Site 7 (d) Site 8 (e) Site 9 using EQL.

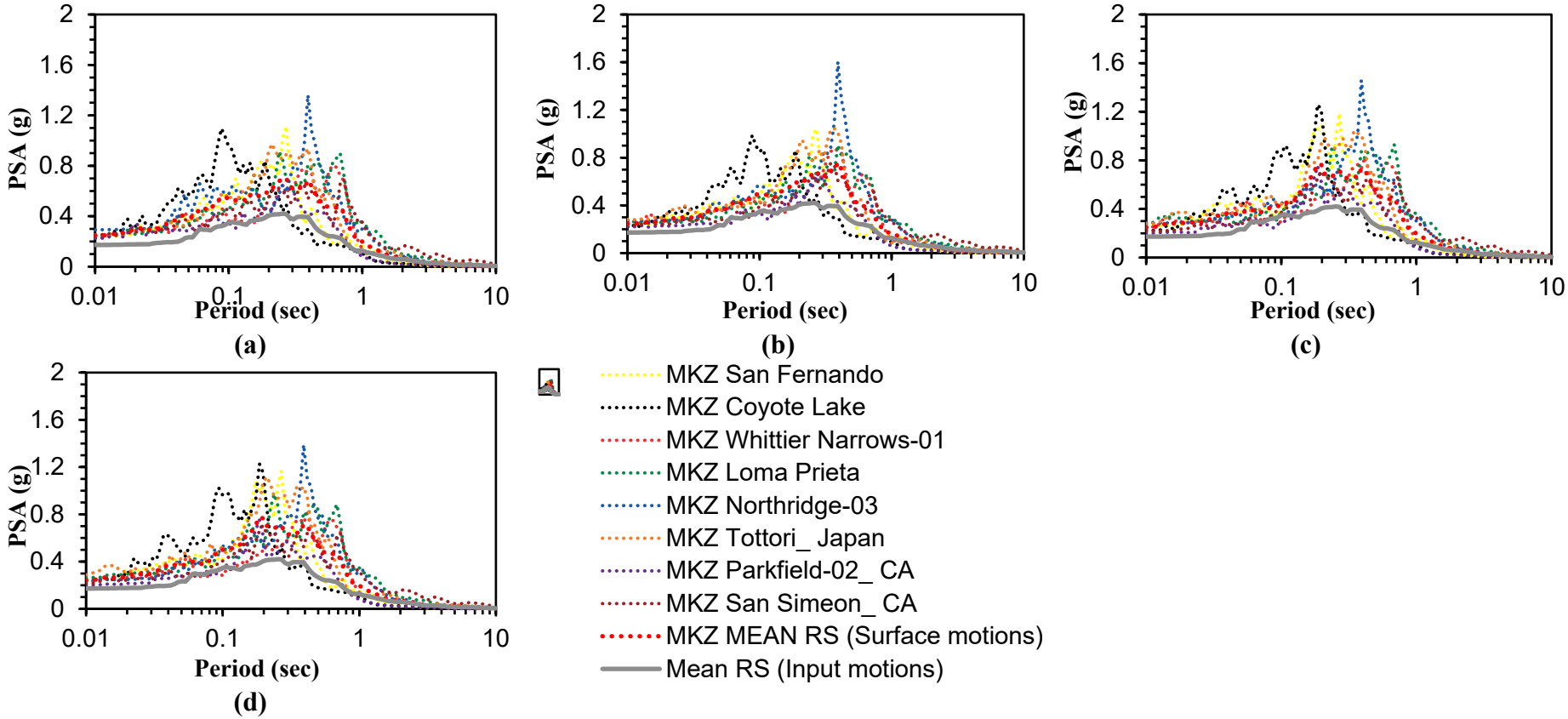

Figure D.21: Response spectra analysis at the surface for (a) Site 1 (b) Site 2 (c) Site 3 (d) Site 4 using MKZ.

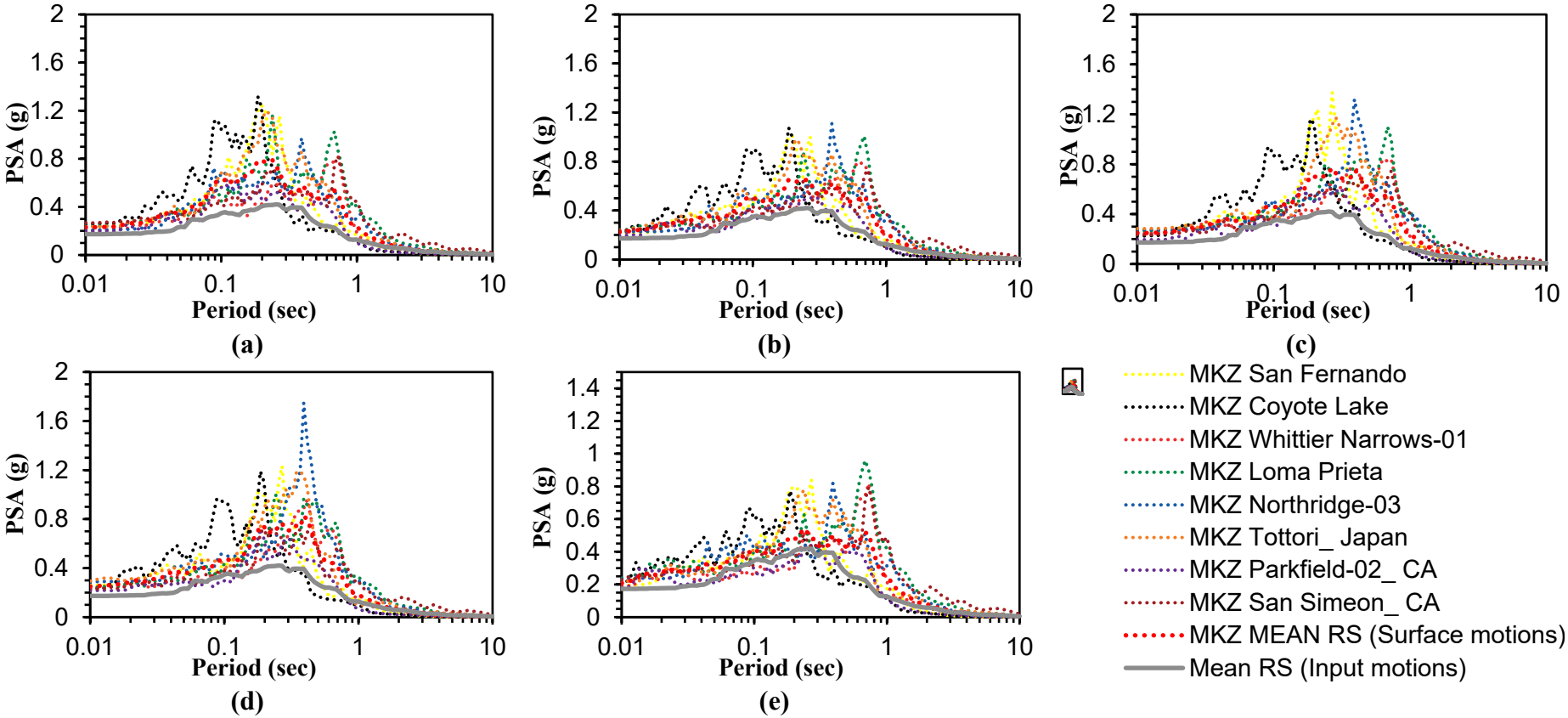

Figure D.22: Response spectra analysis at the surface for (a) Site 5 (b) Site 6 (c) Site 7 (d) Site 8 (e) Site 9 using MKZ.

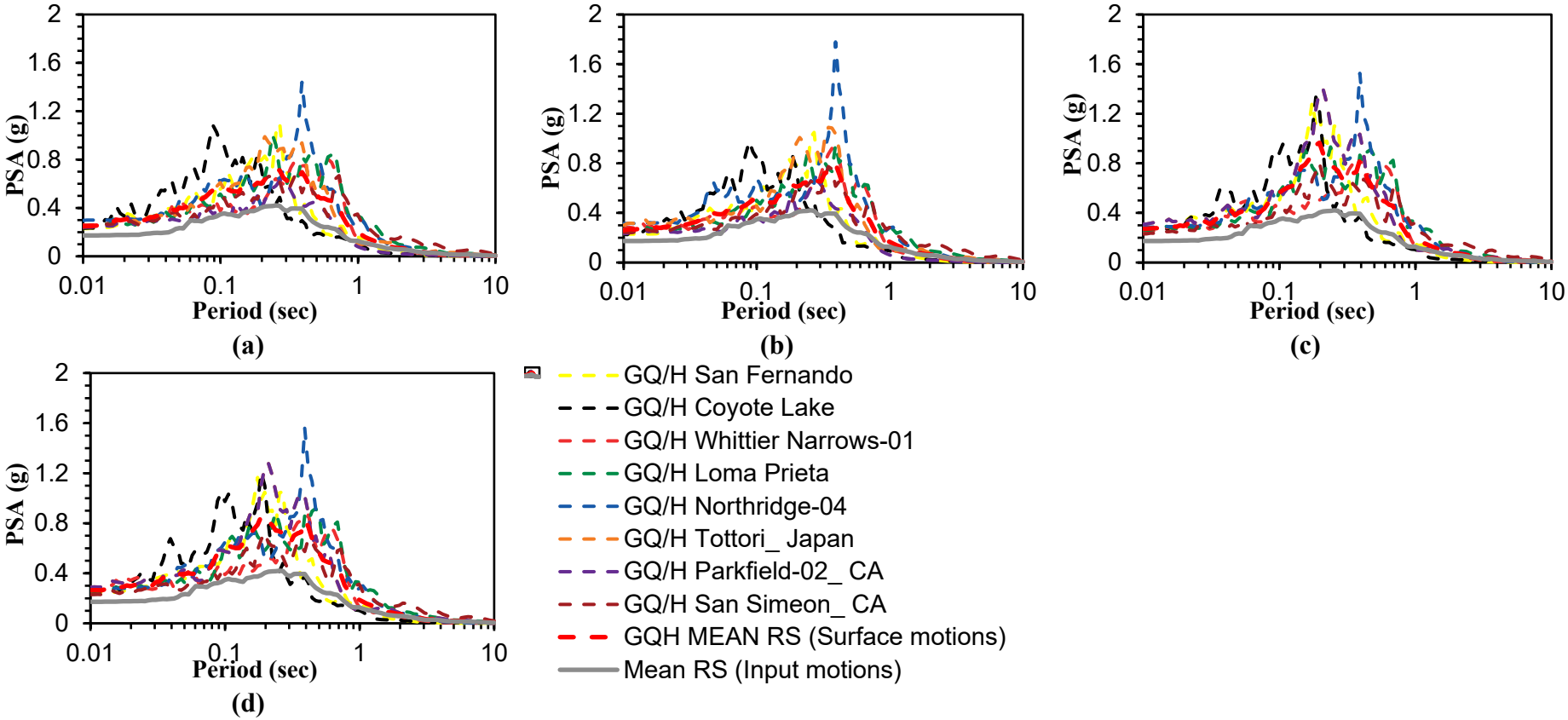

Figure D.23: Response spectra analysis at the surface for (a) Site 1 (b) Site 2 (c) Site 3 (d) Site 4 using GQ/H.

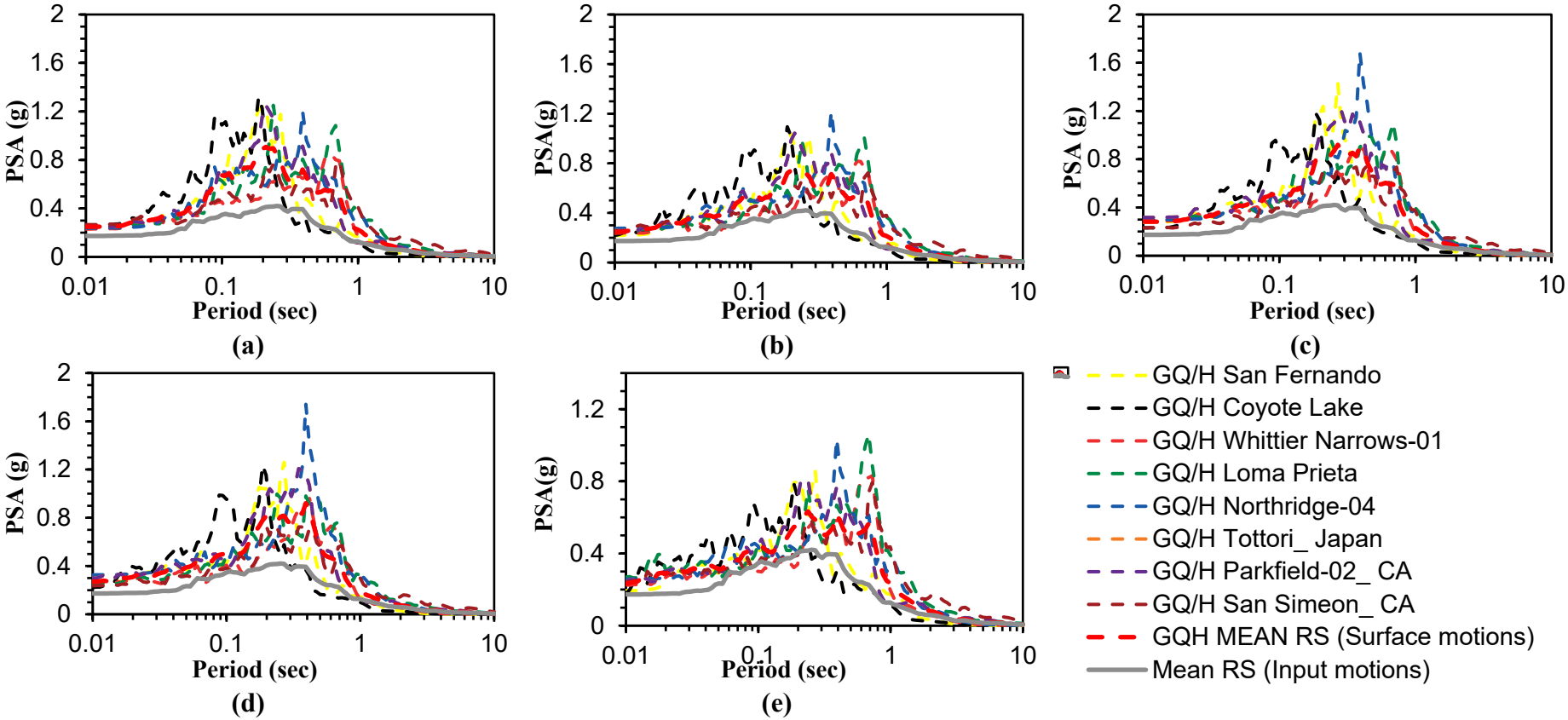

Figure D.24: Response spectra analysis at the surface for (a) Site 5 (b) Site 6 (c) Site 7 (d) Site 8 (e) Site 9 using GQ/H.

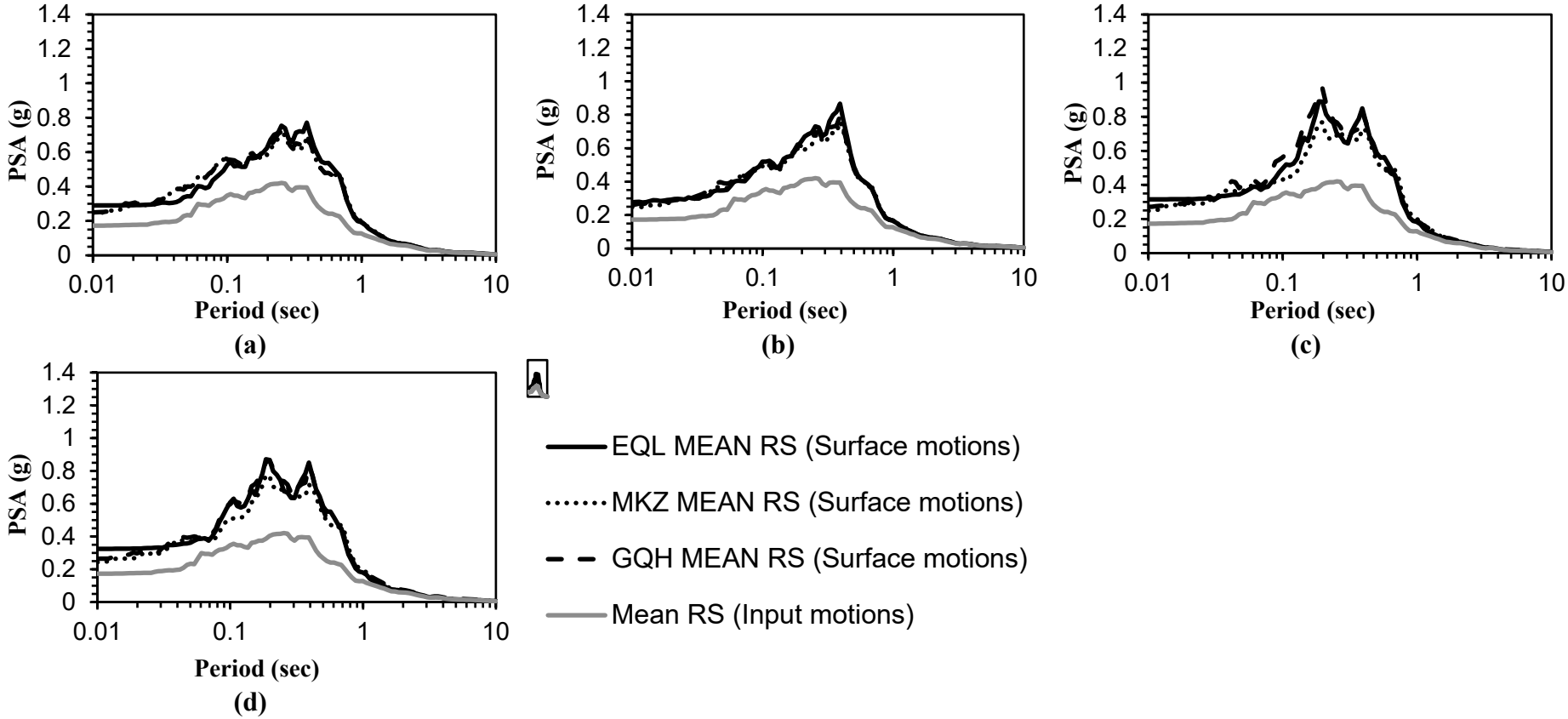

Figure D.25: Mean response spectra at the surface for (a) Site 1 (b) Site 2 (c) Site 3 (d) Site 4.

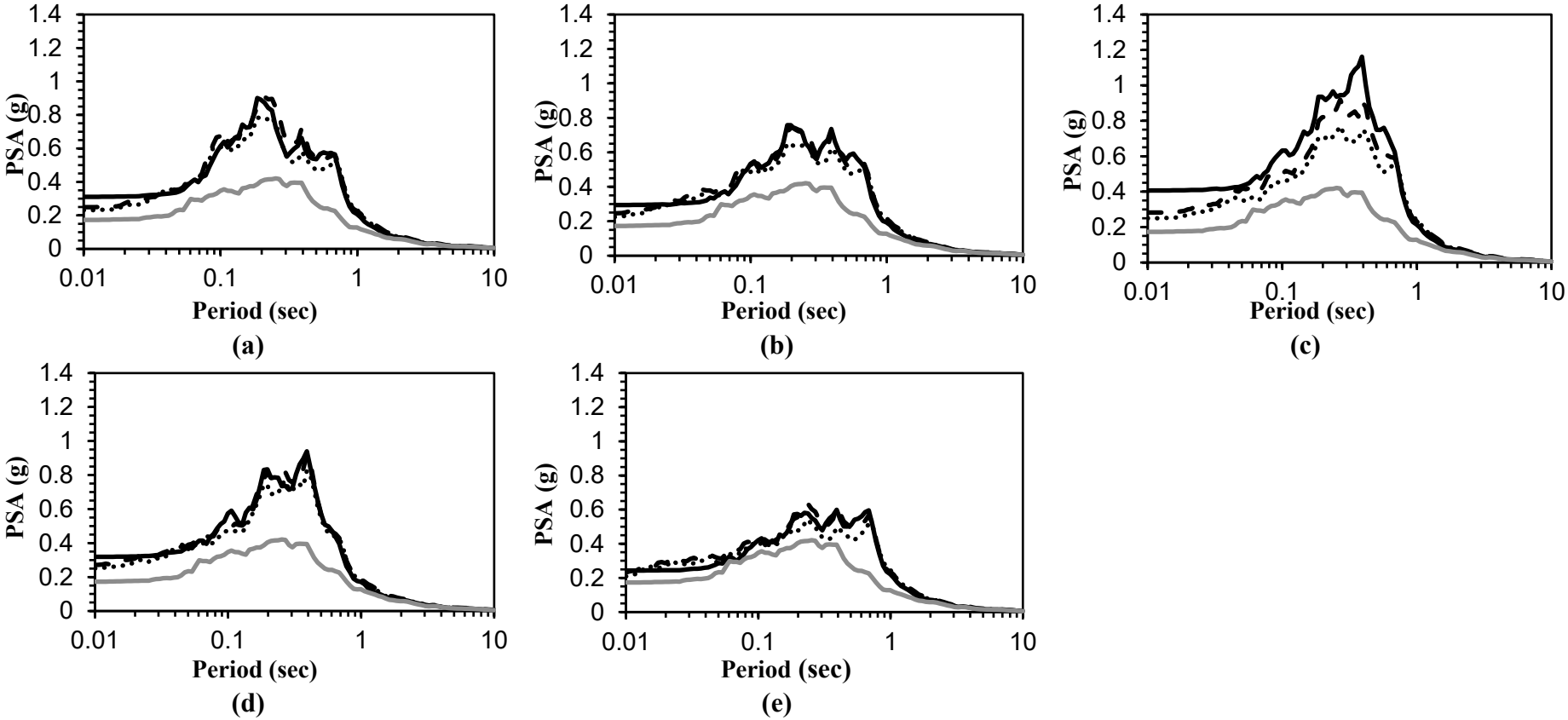

Figure D.26: Mean response spectra at the surface for (a) Site 5 (b) Site 6 (c) Site 7 (d) Site 8 (e) Site 9.